NUMERICAL AND EXPERIMENTAL STUDY ON COMPOSITE STRUCTURES UNDER A CRUSHING LOAD

Ngai Sum Louis CHIU

Submitted in fulfilment of the requirements for the award of
Doctor of Philosophy

2015

Department of Mechanical and Aerospace Engineering
Monash University, Clayton, Australia

Summary

Crashworthiness of aerostructures is one of the most important factors in their design. Energy absorbing structures within the airframe can contribute substantially to crash protection. The move towards fibre reinforced composite materials, due to their improved performance, presents both opportunities and challenges to the design of energy absorbing structures. The multitude of damage mechanisms of composite structures increase energy absorption capability while making analysis significantly more difficult than those of traditional metallic structures. Currently, the design process of composite structures is heavily dependent on expensive and time consuming physical testing, which can be reduced by the use of validated virtual testing capability. Unfortunately, currently available numerical models have not been able to meet this demand.

The aim of this study is to develop and validate a comprehensive, predictive material damage model for the analysis of composite laminate structures under a crushing load, which can be used for virtual testing within the design process for energy absorbing composite structures. A robust damage model, to simulate the response of composite structures subjected to a crushing load, was developed to overcome limitations in commercially available composite damage models. This work makes a significant contribution to the analysis of damage in composite structures by the improved modelling of:

- The nonlinear material response,

- The unloading and load reversal behaviour,

- Physically based damage mechanisms,

- Damage mode interactions, and

- The characteristic length.

The superior predictive capability of this material damage model has been demonstrated in this work. This model only requires physically measurable parameters as input and artificial manipulation of

these parameters is not necessary. The model was implemented into Abaqus/Explicit as a VUMAT subroutine and validated against theoretical expectations.

An experimental program was conducted to probe rate dependent behaviour and to provide data for subsequent validation work. A set of tulip-triggered cylindrical tube specimens were tested at a range of nominal strain rate between 2×10^{-4} to $100 \ s^{-1}$. Overall, the material response was found to be rate independent. Consistent force responses and damage morphologies were observed for all the strain rates investigated. The standard deviation of the results for each strain rate was less than 8%, demonstrating that good reliability was achieved in the experiments.
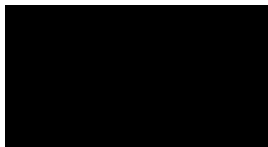
The effectiveness of the material damage model was assessed using experimental data obtained from experimental testing as well as the literature. Results showed that the model can accurately predict the force response of a range of different crushed composite structures. The simulated energy absorption of each test case was within 4% to 12% of the experimental value. The experimentally observed post-crush deformation and the damage morphologies were also accurately predicted by the model. The results have demonstrated the effectiveness of this new model in predicting the crush response of composite structures. This model can be applied in industry to reduce costly and time consuming physical testing during the design process of components, thus reducing cycle time and/or increasing performance of the end product.

Declaration

I hereby declare that the work presented in this thesis is solely my own work and to the best of my knowledge is original except where indicated by reference to other authors. No part of this work has been submitted for any other degree or diploma.

Ngai Sum Louis Chiu

Date: 25/06/2015

Acknowledgement

Publications

Conference publications

1. Chiu LNS, Falzon BG, Boman R. A Continuum Damage Mechanics Model for the Analysis of the Crashworthiness of Composite Structures: A work in progress. Australian International Aerospace Congress. Melbourne, Australia 2013.

2. Chiu LNS, Falzon BG, Boman R, Chen B, Yan W. Verification of a novel material model to predict damage in composite structures. 8th International Conference on Structural Integrity and Fatigue. Melbourne, Australia 2013.

Journal publications

1. Chiu, L.N.S., B.G. Falzon, R. Boman, B. Chen, and W. Yan, Finite element modelling of composite structures under crushing load. Composite Structures, 2015. 131(0): p. 215-228.

2. Chiu, L.N.S., B.G. Falzon, D. Ruan, S. Xu, R.S. Thomson, B. Chen, and W. Yan, Crush responses of composite cylinder under quasi-static and dynamic loading. Composite Structures, 2015. 131(0): p. 90-98.

3. Chiu, L.N.S., B.G. Falzon, R. Boman, B. Chen, and W. Yan, Evaluating a 3D solid damage model for composite structures under crushing loads, [pending review: Composite structures].

4. Tan W, Falzon BG, Chiu LNS, Price M. Predicting low velocity impact damage and Compression-After-Impact (CAI) behaviour of composite laminates. Composites Part A: Applied Science and Manufacturing. 2015;7:212-26.

Table of contents

List of figures

List of tables

Nomenclature

2D	Two dimensional
3D	Three dimensional
C3D8R	8 node linear reduced integration solid element (in Abaqus)
GFRP	Glass fibre reinforced plastics
CFRP	Carbon fibre reinforced plastics
CDM	Continuum damage mechanics
FRP	Fibre reinforced plastics
FE	Finite element
FEA	Finite element analysis
FM	Fracture mechanics
FPCS	Fracture plane coordinate system
GCS	Global coordinate system
IDM	Intralaminar damage model
MCS	Material coordinate system
SEA	Specific energy absorption
VUMAT	User defined material response subroutine
ASTM	American Society of Testing and Materials
BC	Boundary conditions
DCB	Double cantilever beam
ENF	End notch flexure
CT	Compact tension test
CC	Compact compression test
QS	Quasi-static

Material properties

E_{11}	Elastic modulus in the fibre direction (11)
E_{22}	Elastic modulus in the transverse direction
E_{33}	Elastic modulus in the thickness direction
v_{12}	Longitudinal-transverse Poisson's ratio
v_{13}	Longitudinal-thickness Poisson's ratio
v_{23}	Transverse-thickness Poisson's ratio
G_{12}	Longitudinal-transverse (in-plane) shear modulus
G_{13}	Longitudinal-thickness shear modulus
G_{23}	Transverse-thickness shear modulus
X^T	Longitudinal tensile strength
X^C	Longitudinal compressive strength
Y^T	Transverse tensile strength
Y^C	Transverse compressive strength

S_{12}	In-plane shear strength
G_{fib}^{T}	Critical energy release rate for fibre tensile fracture
G_{fib}^{C}	Critical energy release rate for fibre compressive fracture
G_{mat}^{T}	Critical energy release rate for matrix tensile fracture
G_{mat}^{C}	Critical energy release rate for matrix compressive fracture
G_{mat}^{12}	Critical energy release rate for in-plane shear fracture
G_{mat}^{13}	Critical energy release rate for longitudinal-thickness shear fracture
G_{mat}^{23}	Critical energy release rate for transverse-thickness shear fracture
Shear ij: c_1	1st coefficient for ij direction cubic shear response
Shear ij: c_2	2nd coefficient for ij direction cubic shear response
Shear ij: c_3	3rd coefficient for ij direction cubic shear response
ρ	Density
σ_I^{max}	Mode I interlaminar strength
σ_{II}^{max}	Mode II interlaminar strength
σ_{III}^{max}	Mode III interlaminar strength
G_{int}^{I}	Mode I interlaminar fracture toughness
G_{int}^{II}	Mode II interlaminar fracture toughness
G_{int}^{III}	Mode III interlaminar fracture toughness
μ	Friction coefficient

Damage initiation and propagation

σ_{ij}	Damaged stress in the ij direction
$\bar{\sigma}_{ij}$	Elastic stress in the ij direction
γ_{ij}	Shear strain
$\gamma_{ij,el}$	Elastic shear strain
$\gamma_{ij,in}$	Inelastic shear strain
γ_r	Resultant shear strain on fracture plane
Λ	Fracture plane total volumetric strain energy
σ_r	Resultant shear stress on fracture plane
g_i^{j}	Volumetric critical energy release rate for damage mode i in direction j
l_i	Characteristic length for damage mode i
F_i^{j}	Damage initiation criteria for damage mode i in direction j
ε_i^{OT}	Tensile damage initiation strain for damage mode i
ε_i^{OC}	Compressive damage initiation strain for damage mode i
ε_i^{FT}	Tensile failure strain for damage mode i
ε_i^{FC}	Compressive failure strain for damage mode i
d_i^{j}	Damage parameter for damage mode i in direction j
θ_{fp}	Fracture plane angle
μ_{1N}	Fracture plane pseudo-friction coefficient in the longitudinal direction
μ_{NT}	Fracture plane pseudo-friction coefficient in the transvers direction

Chapter 1
Introduction

1.1 Motivation

Composite material is a structural material composed of two (or more) distinct macroscopic constituents [1]. Typically, a discrete reinforcing phase is embedded into a continuous matrix phase. Fibre reinforced plastics (FRP) are a widely used composite, which comprise of fibres, typically carbon or glass, embedded into a polymer matrix. In particular, continuous carbon fibre reinforced plastics (CFRP) have been receiving increasing attention due to their superior specific strength and stiffness. As a result, CFRP are progressively replacing traditional metallic materials in the construction of aerostructures.
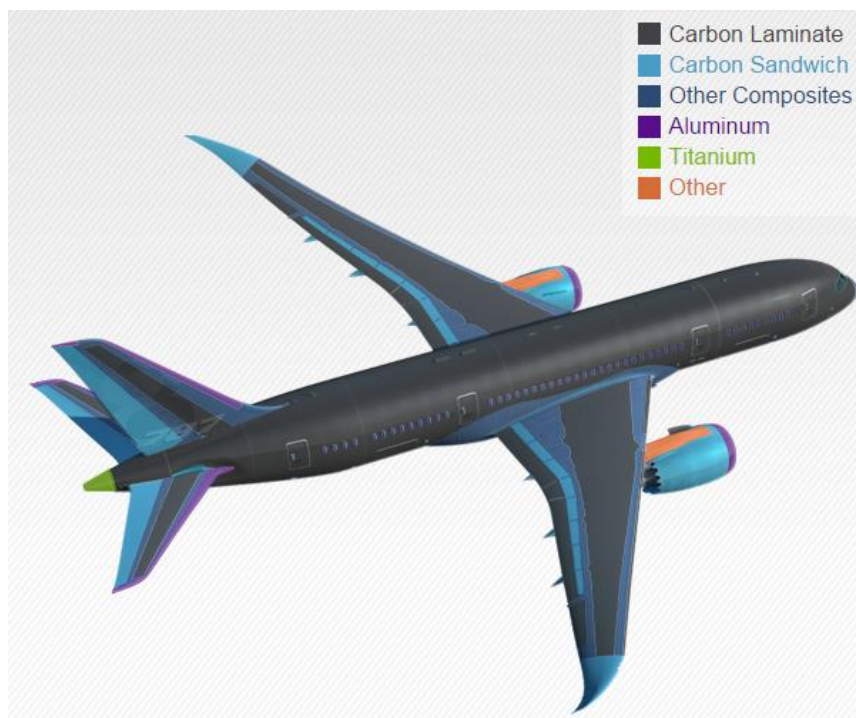
Figure 1.1: Widespread use of FRP in the construction of the Boeing 787 Dreamliner [2].

Safety has always been a priority in the design of aircraft. An important aspect of aircraft safety is the crashworthiness of aircraft, which is the aircraft's ability to protect the occupants from serious injury in a potentially survivable crash [3]. This is achieved through limiting the accelerations the occupant is exposed to in a crash situation. Maximum allowable acceleration experienced by the occupant in a

crash is specified in design guidelines [3] and standards [4]. The load path from the impact to the occupant is shown in Figure 1.2. Each part in the load path can contribute to the total force attenuation.
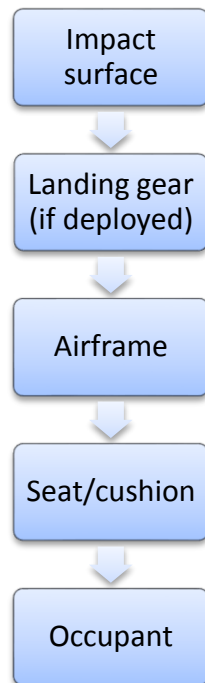
Figure 1.2: Load path for impact forces.

In particular, the airframe is a convenient region to place energy absorbing structures. Unlike the landing gear and the seat, the airframe offers ample space for the inclusion of energy absorbing structures in an unobtrusive manner. In the event of a crash, the energy absorbing structures deform and break, which absorb the impact energy and reduce the transmitted force. Containing the crush elements within the airframe also reduces the potential for debris to enter the cabin.

Different materials have been proposed for the construction of energy absorbing structures. Weight is a major consideration in many applications, particularly for aerostructures. Composite materials offer superior potential as energy absorbing structures due to their high specific strength and the multitude of possible different energy-dissipating damage modes [5], which is a result of the bi-phasic nature of CFRP.

3

The geometry of the energy absorbing element has a direct effect on the load attenuation characteristics of the element. The multitude of damage mechanisms, coupled with the complex geometry of the airframe structures, creates significant challenges for the design in optimising for energy absorption in the airframe. As a result, the design process relies on a large amount of physical testing at the subcomponent level. By replacing physical tests with virtual testing, substantial saving can be realised (Figure 1.3). Furthermore, an accurate numerical model is able to show details during the crushing process, particularly at the crush front, which may not be readily observable in an experimental test.
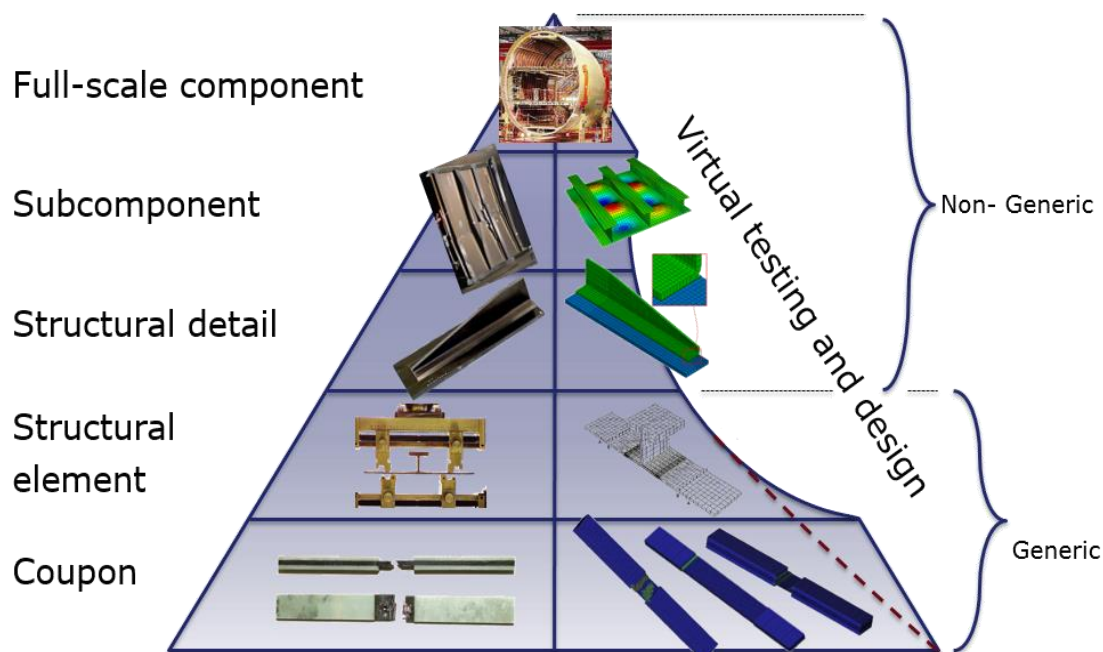
Figure 1.3: Comparison of testing requirement with (right) and without (left) the use of validated virtual testing techniques.

Current commercially available material models [6, 7] are insufficient for predicting the multiple concurrent failure modes and their interactions within an energy absorber being crushed [8, 9]. This lack of robust and predictive capability of current numerical modelling tools has negative implications for the design of these energy absorbing structures. Analysis of these components relies heavily on physical testing, which is both time consuming and expensive. Furthermore, the use of these models relies on significant simplifications such as the use of shell elements [6, 7].

Subsequent advances [10] in the field of composite damage modelling have been focussing on developing models to describe different phenomena observed during physical testing. These advances have steadily improved the predictive capability of composite material models [11-14]. Therefore, there is an opportunity to integrate the current and novel modelling techniques into a comprehensive damage model implemented for a commercially available finite element analysis package to achieve a general, reliable and predictive virtual testing capability. This work will contribute to the virtual testing capability that can:

1. Provide a better understanding of the crushing process in composite structures, and
2. Substantially reduce the reliance of the design process on physical testing on the subcomponent and part level.

1.2   Aims of research

The development of a validated predictive modelling capability to assess crush behaviour of composite structures can reduce the cost of development of these energy absorbing structures. The main aim of this project is to develop and validate a material model capable of predicting the damage response of composite structures under crush loading so that the reliance on physical testing can be reduced. There are three main objectives in this study:

- Develop a reliable and predictive composite material damage model;
- Conduct a testing program to assess the crushing behaviour at different speeds;
- Verify the developed damage model against experimental data.

In order to achieve the first objective, an extensive literature survey was conducted to assess the available techniques for assessing damage within the composite laminate. The developed material model required only the applied loading, structural geometry and measured material properties to calculate the crush response due to the physically-based nature of the model, which includes:

- A full 3D formulation,

- A robust method for characteristic length determination, and

- A physically based model of material behaviour which can predict the:

  - Behaviour under unloading and load reversal,

  - Nonlinear material response, and

  - Interaction between damage mechanisms within each phase of the composite,

The experimental testing conducted in this project provided a comprehensive set of data to understand the damage process as well as to provide data for subsequent validation work. The three main aims of the experimental program are summarised below:

1. Understand the damage processes in the crush structure;

2. Measure force response during crushing;

3. Measure extent of dependence on strain rate.

Finally, in order to demonstrate the effectiveness of the developed damage model, evaluation was completed by benchmarking the numerical solution of the damage model against experimental data of representative energy absorbing structures. The results of the damage model were assessed both quantitatively and qualitatively in terms of damage morphology, force response and total energy absorption.

The final result of this research program was the creation of a validated predictive model for evaluating composite structures undergoing crush loading, which can improve the optimisation of energy absorbing capability of composite structures for crash protection applications.

1.3 Thesis outline

This introductory chapter is followed by a literature review in Chapter 2, which begins with a brief introduction to crashworthiness. The current metrics employed in the measurement of crash protection offered by composite energy absorbing structures is then introduced. The current approaches to the construction of composite energy absorbers are outlined to highlight the complexity encountered in

the analysis of these structures. This is followed by a critical assessment of the modelling capability currently available for assessment of damage response in composite structures. The limitations of these models, particularly those that are commercially available, are presented here. The final section outlines the various experimental methods for the measurement of material properties required in numerical modelling of composite structures, particularly properties that are not part of an accepted standard.

A detailed description of the theory behind the developed damage model is given in Chapter 3. In this chapter, the theory underpinning the proposed model is presented in detail. These include quantification of damage, calculation of characteristic length to achieve mesh independence, assessment of damage initiation as well as evolution of damage. Numerical aspects are also covered, including deletion of elements and optimisation of code sections. The implementation of the model into an Abaqus/Explicit VUMAT is discussed. A brief outline of the other inbuilt Abaqus models used in conjunction with the proposed model is also presented.

The numerical implementation of the material model is validated and its sensitivities are explored in Chapter 4. The chapter begins by presenting the single element models, which were used to check the constitutive response for monotonic and cyclic loading. This is followed by the use of coupon models to validate macroscopic features of the model. These include the formation of fracture planes and testing the overall energy dissipation. The sensitivity of the proposed model to variation in the input parameters is then explored. These parameters include material properties such as the transverse strengths and friction coefficients as well as numerical parameters such as the mesh density, numerical controls and mass scaling.

The experimental program is presented in Chapter 5 in order to assess strain rate sensitivity as well as to provide data for subsequent validation of the developed model. A set of specimens, which is representative of typical energy absorbing structural designs, was developed and manufactured. These specimens were tested under crushing loads at different loading rates. The force response and the damage morphologies of these specimens were analysed. Four metrics (specific energy absorption,

crush efficiency, peak and steady-state crush loads) characterising energy absorption performance have been used to establish strain rate sensitivity for the tested configuration.

The evaluation of the material model against experimental data is presented in Chapter 6. This work incorporates data from the experimental program as well as experimental data from the literature. Four different test cases were used and the test geometries were modelled numerically using the material damage model developed in this study. The force response, damage morphology and overall energy absorption were compared against experimental records to demonstrate the capability of the developed model.

This thesis concludes with Chapter 7. The main outcomes of this project are presented along with their contribution to the current state of the art.

Chapter 2
Literature review

2.1 Introduction

Composite materials are an attractive option for many applications. In particular, the high specific stiffness and strength properties of carbon fibre reinforced plastics (CFRP) [1] are ideal for civil airframe manufacturers in their pursuit of a lighter structure to reduce operating costs. One critical aspect of airframe design is the crashworthiness of the aerostructure. Regulations and standards set out the compliance requirements for airframes in terms of the limitation of load transmitted to the occupants in an impact scenario [4, 15-18]. These have been driving the development of energy absorbing structures to reduce the severity of an impact event through attenuation of the loading felt by the occupants of the aircraft. Existing numerical modelling methods cannot reliably predict the complex damage interaction and evolution in the composite material. Thus, the design of these structures relies heavily on experimental testing which is both expensive and time consuming. A robust predictive modelling capability would provide greater detail and reduce the cost involved in the design of energy absorbing structures.

This literature review begins by introducing crashworthiness and discusses the methods with which it is assessed. The energy absorbing structures that are used for crash protection purposes are then reviewed. The desirable features of energy absorbing structures and the metrics used to characterise their performance are outlined. The variety of different configurations of composite structures used for crash protection explored in the literature is highlighted.

The current theory and practices in the modelling of damage response of composite materials are then outlined. In particular, various currently available finite element material models for composite materials are critically reviewed and their limitations, when applied to the analysis of crushing structures, are outlined.

Accurate material property data underpins the ability to predict the structural response under loading. The methods for obtaining the required property data are detailed and the relevant standards are

summarised. For properties whose measurement is not governed by a standard, the currently accepted methods are presented. This chapter concludes with a brief summary of key elements in each section.

2.2 Airframe crashworthiness

The crash protection requirement for aircraft systems have been specified in various regulations [15-18], standards [4] and guidelines [3]. This applies to both light fixed-wing and rotary-wing aircraft. Crashworthiness is defined as the "ability of an airframe structure to maintain a protective shell around occupants during a crash and minimize accelerations applied to the occupiable portion of the aircraft during crash impacts" in MIL-STD-1290A(AV) [4]. It also sets out the impact conditions for which protection should be designed.

2.2.1 Crash protection assessment

JSSG-2010-7 [3] lists some of the possible injury types that occur during a crash situation. The first is "whole body acceleration induced injuries". As its name suggest, this type of injuries is due to the sudden increase in acceleration experienced by the body of the occupant in a crash. The magnitude and direction of acceleration experienced can be related to the potential for injury.

Figure 2.1 shows the tolerable limits for the upwards acceleration that is prominent in aircraft crash situations. As well as whole body accelerations, tolerance limits have also been specified for specific locations on the human body, such as the lumbar and neck loads.
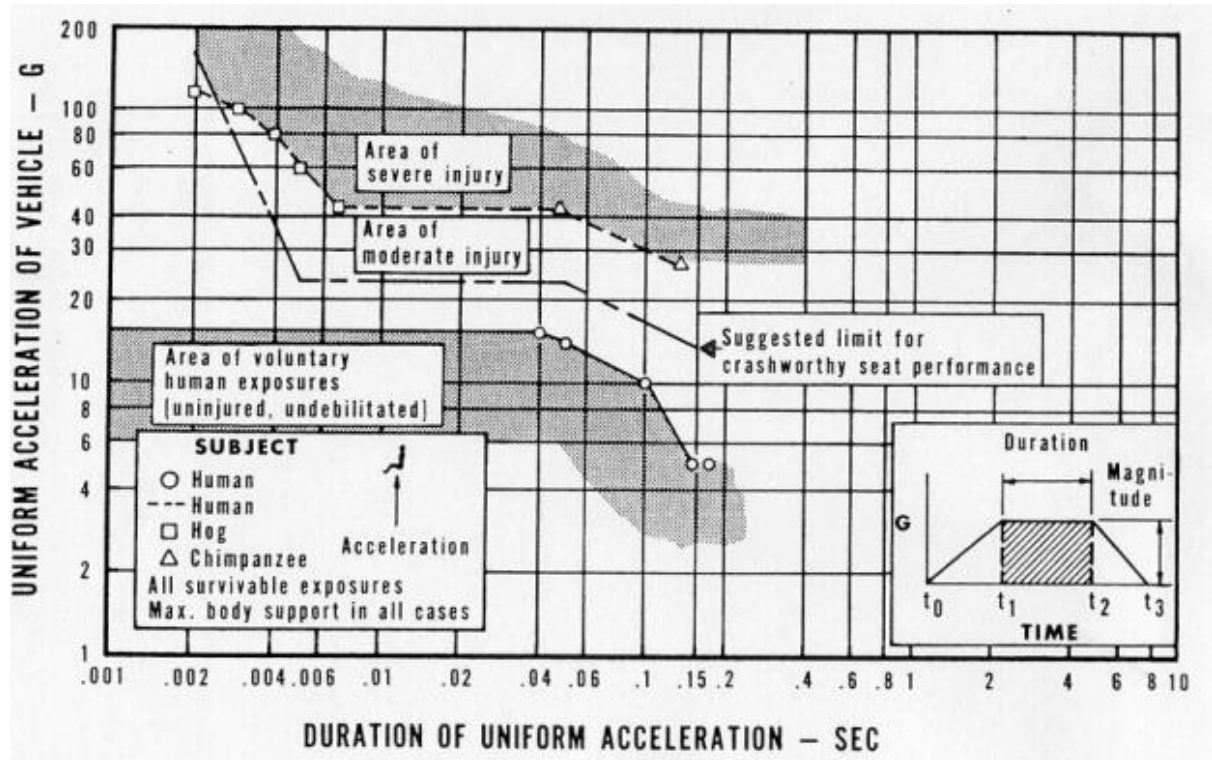
Figure 2.1: Tolerable limits for head-ward acceleration [4].

Another prominent metric for evaluation of the potential for injury is the head injury criterion, HIC, (Eq. (2.1)). This relationship is developed from experimentally measured data related to skull fractures and correlate the acceleration (a) – time (t) response to injury potential [3].

$$HIC = (t_2 - t_1) \left(\frac{1}{t_2 - t_1} \int_{t_1}^{t_2} a(t) \, dt \right)^{2.5} \tag{2.1}$$

From these criteria, it is clear that injury potential is closely related to the acceleration experienced by the occupant. Hence, reduction of transmitted impact acceleration is vital to crash protection.

2.2.2 Methods of crash load reduction

Crash protection is achieved via the attenuation of impact loading transmitted to the occupants. This can be done at different stages of the load path from the site of impact to the occupant. Each component along the load path from the impact to the occupant plays a role in the absorption of impact energy. From the point of impact, the forces travel up the landing gear (if deployed) and into

the aircraft structure. Collapse of the landing gear begins to absorb the impact energy. When the lower fuselage makes contact with the surface, it begins to deform and absorb energy (Figure 2.2). Typically, the subfloor structure undergoes substantial damage and hence absorbs a large amount of energy to protect the occupants. The impact loading then travels through the seat and passes through to the occupant through the seat cushion. Stroking seats and cushions [19] add to the energy absorbing capability and are the last line of defence before the impact loadings reach the occupant.
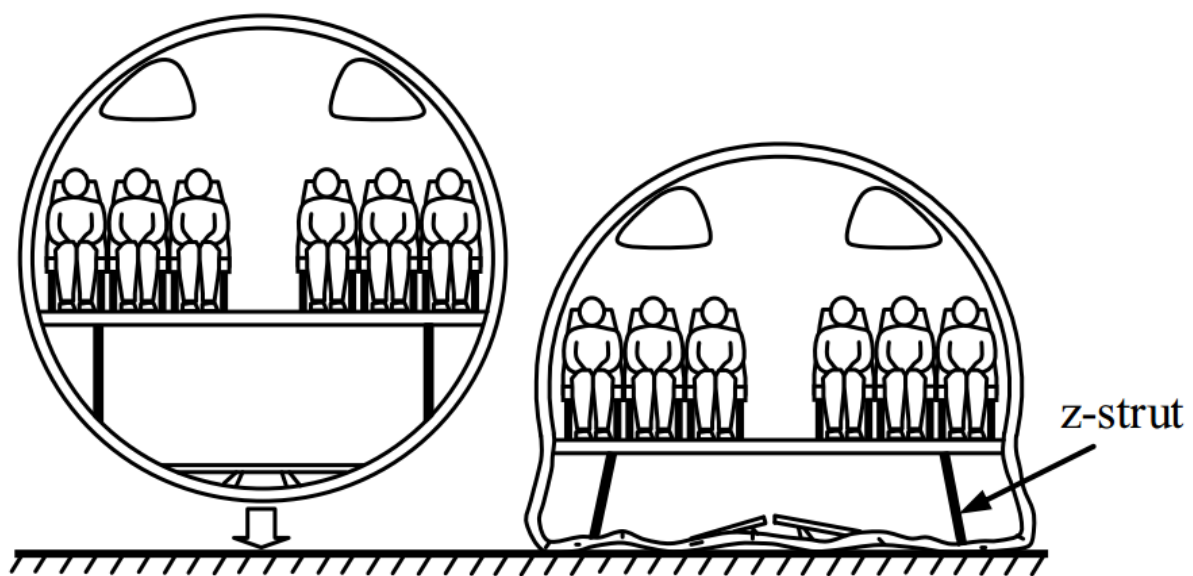
Figure 2.2: Deformation of the airframe to absorb impact [20].

In particular, the performance of the subfloor structure in the fuselage is vital to the overall performance of the airframe. Relative to the other locations, there is ample amount of space in the subfloor region, which aids the integration of energy absorbing elements into the structure (Figure 2.3).
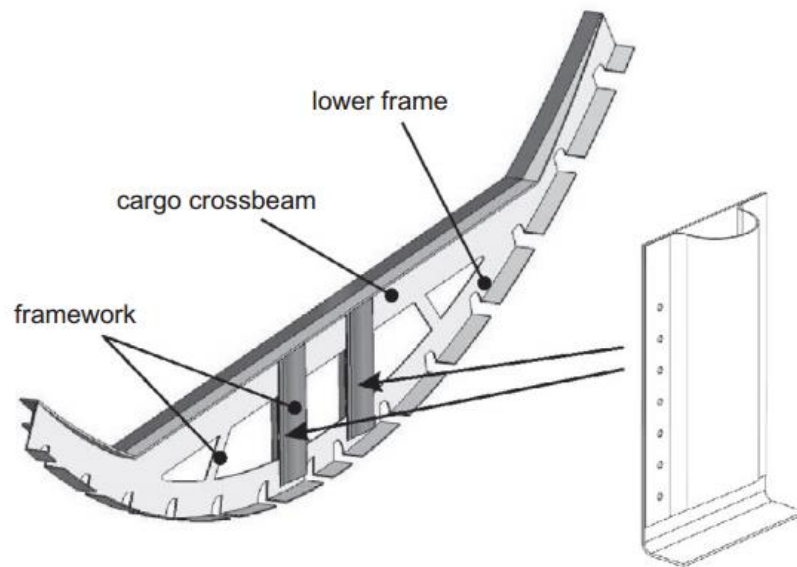
Figure 2.3: Energy absorbing elements integrated into the subfloor structure [21].

In order to maximise the energy absorption in the subfloor, the performance of these energy absorbing elements will need to be assessed.

2.3 Energy absorbing structures

The role of the energy absorbing structure is to attenuate the transmitted forces through deformation and fracture of the structure. This section provides an introduction to the measurement of energy absorber performance as well as gives an overview of different configurations seen in the literature.

2.3.1 Features of an idealised energy absorbing device

The idealised force-displacement response of a well-designed energy absorber undergoing crushing displays three distinct phases as shown in Figure 2.4.
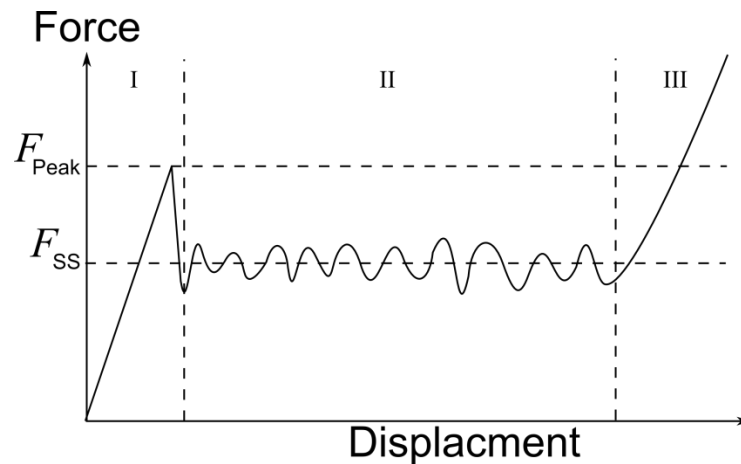
Figure 2.4: Three phases of loading during the crushing of an energy absorber.

Region I begins with elastic loading, followed by damage initiation and progression leading to peak load (F_{peak}). The point of damage initiation depends on whether a trigger mechanism is present and on its specific geometry. The force grows with increasing stroke up to the peak force. This peak force dictates the maximum acceleration felt by the occupants. After peak force occurs, crushing stabilises which signals the interface between region I and II.

Region II is characterised by a force plateau during the steady-state crushing of the energy absorbing device. In this region, the steady-state crush force, F_{SS}, is measured. This phase is where most of the energy absorption occurs. Good designs aim to maximise the magnitude of this force plateau while keeping fluctuations in the force to a minimum.

Region III follows where a dramatic increase in force is observed. This phenomenon is known as "bottoming out". This occurs when the energy absorbing device is completely consumed. Typically, it is undesirable for the energy absorber to be completely consumed due to this sharp rise in the transmitted force. The bottoming out characteristic is heavily dependent on the support structure rather than on the energy absorbing structure itself. Hence, in general, experimental investigation of energy absorbers will terminate before this stage has been reached.

The characteristics of the force response have a direct impact on the crash protection performance. Design of composite energy absorbing structures requires the optimisation of this force response to achieve the protection required.

2.3.2 Key assessment metrics

Four main metrics (peak and steady-state crush loads, specific energy absorption and crush efficiency) give quantitative measure of energy absorber performance, which forms the basis for comparison of different energy absorbing structures.

2.3.2.1 Peak load

The peak load (F_{peak}) is defined as the maximum force transmitted through the energy absorbing device. Typically, it occurs at the end of the trigger region just before the onset of steady state crushing for progressive damage modes at the point of transition between regions I and II in Figure 2.4. In the context of crash protection, this quantity has a direct impact on the peak acceleration that the occupant experiences in a crash situation.

2.3.2.2 Steady-state load

The steady-state load (F_{SS}) is the averaged, sustained loading during the steady-state crushing of the bulk of the energy absorbing structure. This quantity is closely related to the total energy absorption of the absorber device.

2.3.2.3 Specific energy absorption

The amount of energy absorbed (E_{abs}) is directly related to the crash protection offered by the device [22]. The kinetic energy of the vehicle is absorbed by the damage processes within the crush structure. An increasing in the total energy absorption of the structure affords an increase to the speed range at which the crash protection is effective. This quantity can be calculated through integration of the area under the force (F) – displacement (x) curve as the structure undergoes crushing, i.e.:

$$E_{abs} = \int_{start}^{end} F \ dx \tag{2.2}$$

Eq. (2.3) shows the specific energy absorption (SEA) which is the energy absorption (E_{abs}) normalised via the total crushed mass ($m_{curshed}$) [22]. This quantity is more useful for when comparing the performance of designs with differing geometry, configuration and materials.

$$SEA = \frac{E_{abs}}{m_{crushed}} \tag{2.3}$$

This quantity also gives an indication of the efficiency of the absorber design. This is particularly important consideration in weight sensitive applications such as aerospace and automotive.

2.3.2.4 Crush efficiency

The crush efficiency is the ratio between steady-state and peak loads [23], and serves as an indicator of how progressive the crushing process is.

$$CE = \frac{F_{SS}}{F_{peak}} \tag{2.4}$$

Progressive crushing is desired in crash protective structures as this maximises the energy absorption. Design of energy absorbing structure is generally bound by the amount of acceleration that can be tolerated by the occupants.

Figure 2.5 shows two similar force response curves with difference crush efficiencies. For the same peak allowable load, the top curve (high crush efficiency) can absorb more energy per length of structure. Consequently, for a given crash situation, the required structure can be smaller, which can mean considerable cost and weight savings. This is particularly important for highly weight sensitive applications such as aerostructures.
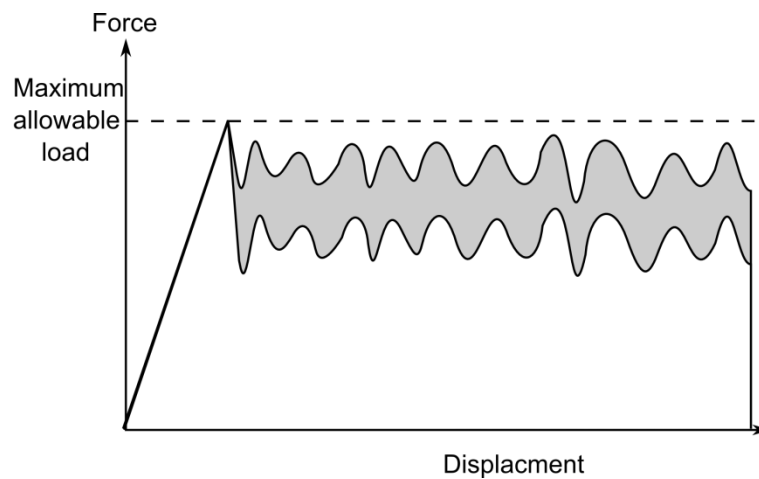
Figure 2.5: Reduction of overall energy (grey region) due to a low crush efficiency.

2.3.3 Energy absorbing structures in the literature

Energy absorbing structures have been studied extensively in the literature. A very large range of materials, geometries and configurations have been explored by different authors. This section gives an overview of the combinations that have been experimentally tested in the literature. The variety and freedom in the design of energy absorbing structures are summarised to highlight the challenges present in the optimisation of these structures.

2.3.3.1 Materials used in energy absorber construction

Steel, aluminium, foam and composite laminates can all be used to construct energy absorbing structures. Metallic materials such as steel [24] and aluminium [19] have traditionally been used extensively as structural materials. Naturally, they are also used for the attenuation of impact loading. However, due to their high density, metallic structures are increasingly being replaced by composites in weight sensitive applications such as aerospace structures.

Composite materials are increasingly being utilised in aircraft structures due to their superior specific strength and stiffness, corrosion and fatigue resistance. Their complex failure modes facilitate a high level of energy dissipation making them suitable for use in energy absorbing structures to meet crash protection requirements. Composite laminates can either be used alone or in conjunction with other materials. Pitarresi et al. [25] compared the crush performance of composite sandwich structures,

some of which contained foam inserts between composite sheets. Taher et al.[26] investigated the crush performance of a keel beam consisting of composite panel sandwiching foam core. Nonetheless, most designs reported in the literature do not use foam, i.e. they are monolithic. This study will focus on the use of monolithic continuous fibre reinforced polymer composite laminates.

2.3.3.2 Various types of geometric configurations

A large number of geometries have been examined in the literature. Garner and Adam [22] listed commonly used cross-sectional geometries in their review. These geometries can be broadly categorised into open (Figure 2.6: c, d, e, f, g, i) and closed sections (Figure 2.6: a, b, h).
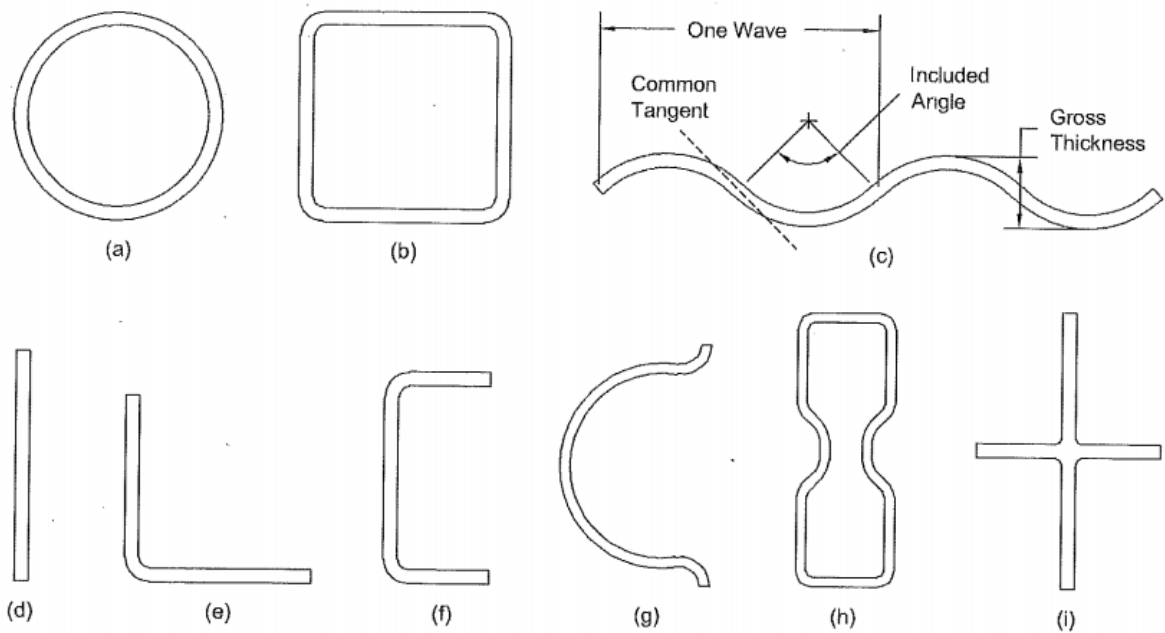
Figure 2.6: Cross-sectional geometries investigated for use in composite energy absorbers [22].

Closed sections reported in the literature are general either circular (Figure 2.6a) [27-29] or rectangular (Figure 2.6b) [30-32] in cross section. Jacob et al.[5] noted in their review that circular tubes were more energy absorbent than rectangular tubes. It was suggested that this was due to the stress concentrations at the corners of the rectangular section [22]. Other shapes such as a hexagon

have also been studied. Jackson et al.[33, 34] developed deployable honeycomb-like composite energy absorbers. The hexagonal cross section was used so that the entire structure can be folded away when not in use.

The simplest open section is a flat panel (Figure 2.6d). This geometry is very easy to produce and yields relatively simple damage mechanisms, which is suitable for probing the initiation and evolution of damage. However, the flat plate is not a free standing structure and is prone to buckling when placed under crushing loads, so additional support structure is required [35, 36]. The addition of bends to the flat plate to form angle (Figure 2.6e) [36] and channel sections (Figure 2.6f) [37] creates free standing structures. Feraboli et al.[38] compared the energy absorbing capability of these flat, angle, channel and rectangular tube sections and remarked on the affect the section geometry has on the SEA. The C-section (Figure 2.6g) was developed by Johnson and David [39] as a free standing specimens that was easy to manufacture and yielded reproducible results. The corrugated web (Figure 2.6c) has been used extensively in energy absorbing applications [40, 41] as it can be readily integrated into existing beam or subfloor structures. More complex geometries such as the corrugated sandwich [42] and laterally loaded honeycomb [33] have also been studied in the literature.

Structures with changing cross sections along their length have also been studied by many authors. Palanivelu et al.[43] tested a range of geometries shown in Figure 2.7, which include hourglass and conical configurations. It was noted that the hourglass and conical specimens displayed more progressive crushing behaviour than the hexagonal and square cross-sections. However, these complex geometries also resulted in lower SEA compared to plain circular cross-sections.
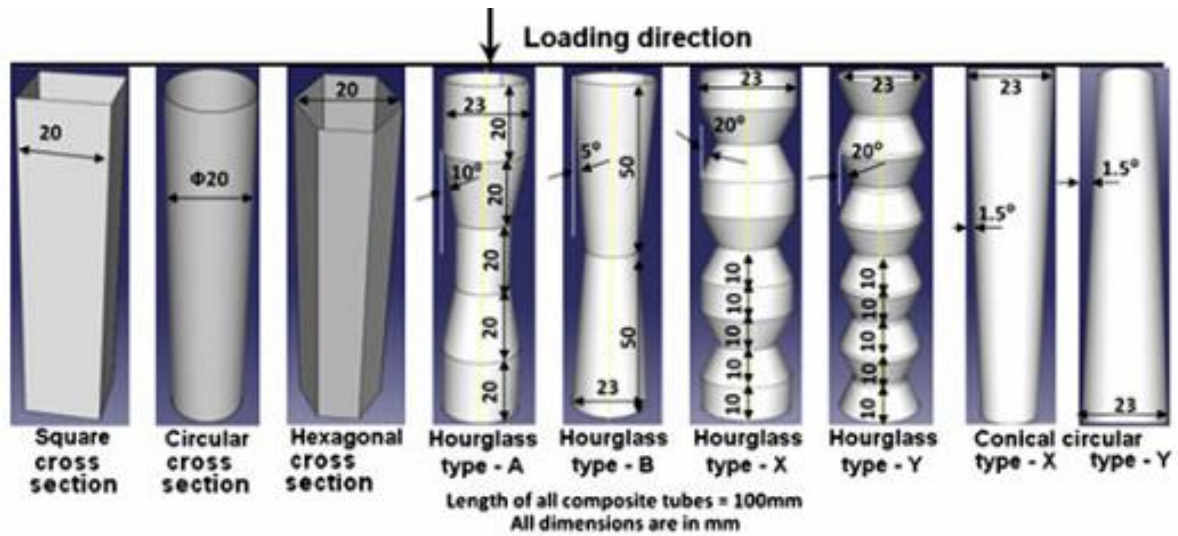
Figure 2.7: Designs that vary the cross-sectional geometry [43].

Integrating energy absorbers into actual structures adds considerable complexity and hence is more difficult to analyse. Jackson et al.[44] studied a variety of different energy absorbing subfloor structures using scale models. These configurations include monolithic foam blocks, laterally loaded tubes, trusses and composite sandwich layers. Good correlation was achieved between the scale test and the numerical analysis. McCarthy et al.[45] studied the performance of sine wave webs used in subfloor box structures for energy absorbing purposes. It was found that adjustments based on test results were required for the numerical result to achieve a close correlation with experimental observations.

In summary, the geometry is chosen based on a range of considerations. Chiefly, promotion of steady and multi-mode damage evolution is given priority as this can enhance the energy absorption.

2.3.3.3 Trigger mechanism to promote desirable damage progression

Various authors have noted the importance of a trigger mechanism in the subsequent progress of the crush behaviour for a given structure [5, 22, 46]. Trigger regions are intentional regions of weakness in the structure to encourage damage initiation so that a progressive crushing process can be achieved by controlling where and how failure occurs. The weak region avoids the transmission of the high initial load and prevents catastrophic collapse of the structure by promoting damage initiation early on.

There are many methods for creating such a weakness in the structure. The simplest method is to remove a portion of the composite structure to create an artificially weakened region. For example, the use of a chamfered loading edge (Figure 2.8 left) is very common [27, 30, 31, 43]. This trigger mechanism is very simple and easy to produce.
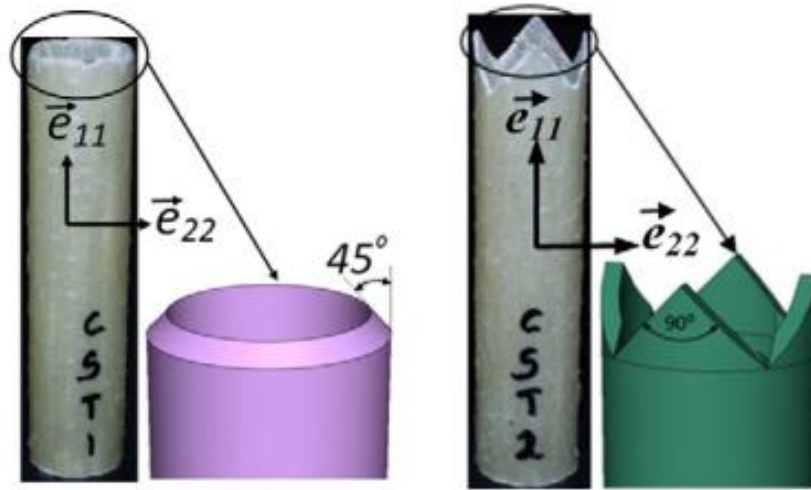
Figure 2.8: Chamfer trigger (left) and tulip trigger (right) [43].

However, chamfering creates a trigger region that is limited in length. In some cases, it is desirable to have a larger trigger region so that the transition between region I and II in the force response can be as smooth as possible. The tulip trigger (Figure 2.8 right), which is a series of sawtooth peaks, has been used by many authors [43, 47, 48]. By altering the number of peaks, the length of the trigger region can be customised to suit the needs of the intended application. A similar design is the steeple trigger (Figure 2.9) where a single peak is used rather than a series of peaks [49]. Another variable trigger design is the crown trigger where semi-circular sections are cut out of the loading surface (Figure 2.9 right) [27]. Similar to the tulip trigger, the crown and steeple triggers can be tailored to suit the expected loading.
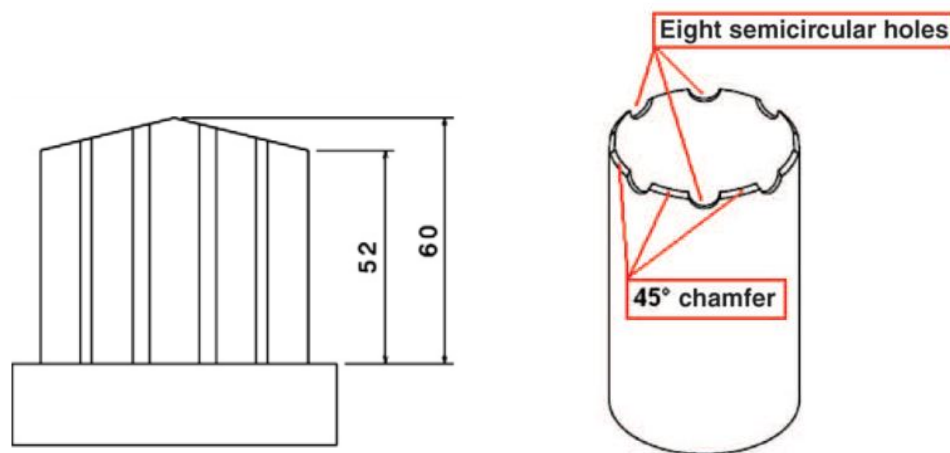
Figure 2.9: Steeple trigger (left) [49] and crown trigger (right) [27].

Another method to create trigger regions is to use embedded ply drops, illustrated in Figure 2.10, which are intentional breaks in the laminate created by terminating one or more plies. Despite the additional complexity in the manufacture of structures with such a trigger, it leaves a continuous surface so that the energy absorbing element can be more easily attached to other structures.
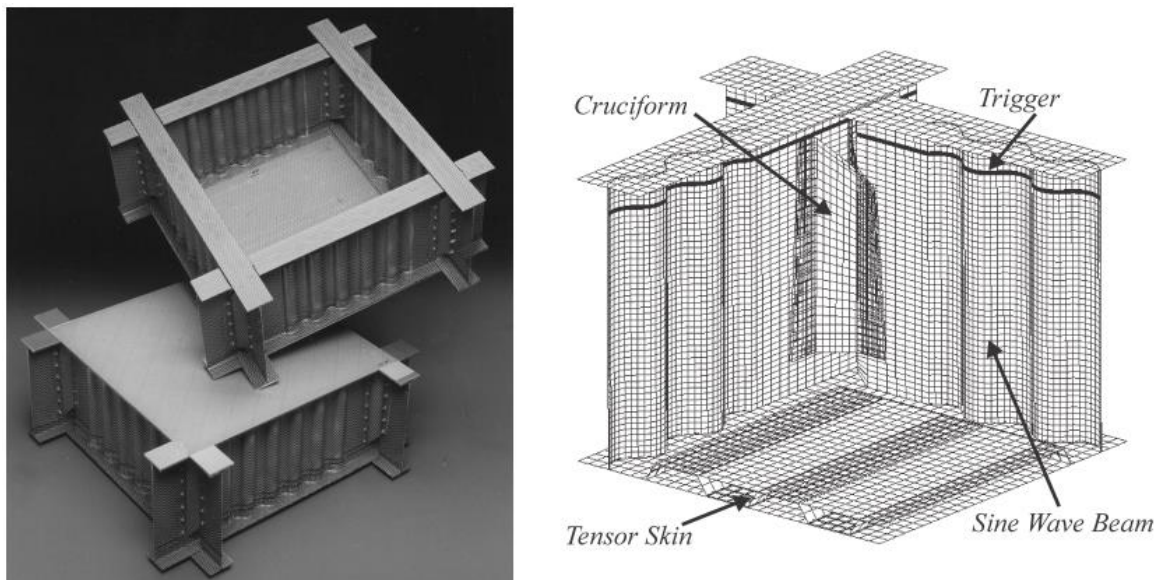
Figure 2.10: Ply drop triggering embedded into the sine web [41].

Alternatively, triggering can also be achieved through the use of external structures which bend [35] or cut [20] the composite material. Siromani et al.[50] studied the use of crush-caps (Figure 2.11) to

promote splaying in composite tubes. The effect of the cap radius was investigated and the performance was comparable with a chamfer trigger.
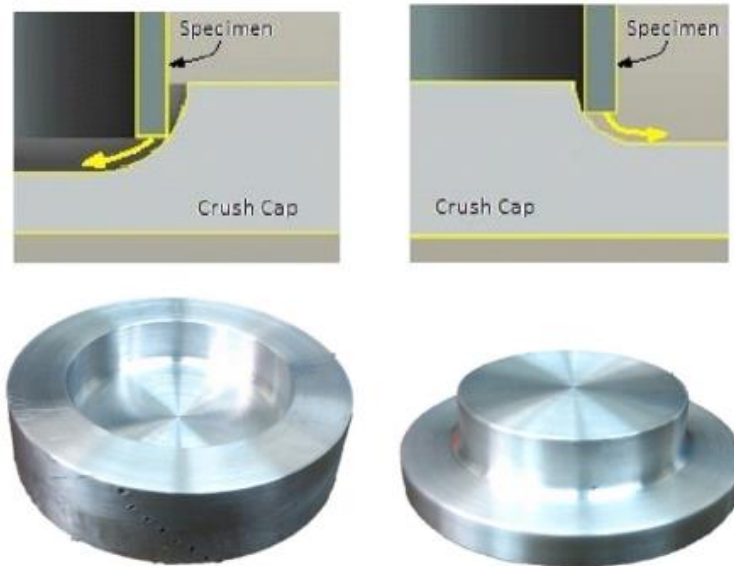
Figure 2.11: Crush-cap to promote splaying of the composite tube [50].

Heimbs et al.[20] studied the use of an absorber device to cut through a composite tube as a means of energy dissipation (Figure 2.12). This design can ensure reproducible results for a variety of loading conditions. However, the use of external devices, which are typically metallic, leads to increased weight of the overall structure.
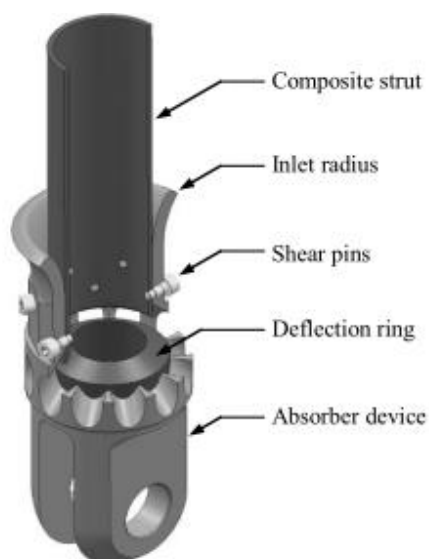
Figure 2.12: Triggering via cutting and deflection of the composite tube [20].

Untriggered [32] or poorly triggered structures tend to collapse catastrophically and/or crush with minimal damage, which leads to a reduced SEA. Hence triggering is vital to the performance of energy absorbing members. A properly triggered structure crushes in a progressive manner and the damage is spread as evenly as possible through the structure, resulting in optimal energy absorption.

The analysis of the damage and deformation of the trigger is critical as it dictates the subsequent progression of damage through the structure.

2.3.3.4 Effect of strain rate on energy absorber performance

Currently, disagreement remains in the literature over the effect of loading rate between 0.1 and 100 s^{-1} on the response of composite structures. Available experimental results span a wide variety of materials, layup configurations and geometries, which makes direct comparisons difficult.

Material and layup configuration were examined to assess their effect on rate sensitivity. Farley [51] noted that Kevlar-epoxy $[0/\pm \theta]_2$ cylindrical tube specimens exhibited increasing SEA with increasing test speed while carbon-epoxy tubes were not rate sensitive. On the other hand, Brighton et al. [52] reported a decrease in SEA for chamfered carbon-epoxy tubes with a $[0/90]_4$ layup when the test speed was increased. It was also noted that the chamfered 4 ply glass-polypropylene fabric tubes showed greater rate dependence but the trend cannot be established due to the magnitude of the scatter observed.

Work by Thornton [53] probing different factors that affect energy absorption of cylindrical tubes have suggested rate independence for glass and graphite-epoxy cylindrical tubes. Farley [51] noted that for chamfered cylinders, $[0/\pm \theta]_2$ graphite-epoxy specimens were rate insensitive, but $[\pm\theta]_3$ graphite-epoxy specimens displayed increased SEA as the testing speed increased.

Different cross-section geometries were also examined. Palanivelu et al. [23] found the SEA of specimens with a circular cross-section were rate insensitive, whereas those with a square cross-section increased slightly with crush speed. Work done on rectangular tubes by Mamalis et al. [32]

has found that both the SEA and peak force of square tubes increased with respect to increasing strain rate. On the other hand, crush testing conducted by Jackson et al. [54] on chamfered C-section found an approximately 10% reduction in SEA for specimens impacted at 8.5 m/s when compared, with those crushed at 20 mm/s. This was confirmed by David et al. [55] who also observed a reduced SEA on dynamically tested C-section specimens with a $[(0/90)_2/0/(90/0)_2]$ layup.

Furthermore, in order to establish the reliability of a measured trend, a sufficiently large sample size is required to quantify the scatter in the experimental data. Brighton et al. [52] noted that variations in the specimens caused by the manufacturing process has a significant effect on the specimen response, which leads to increased scatter that can mask potential strain rate dependency. Unstable collapse of specimens [32] also presented challenges in their measurement due to the presence of high force spikes in the resulting force response. The unstable crushing response is more dependent on any microscopic defects or weak points within the structure, which are random in nature. In order for a conclusion to be drawn with confidence, the observed trend must be compared with the size of the scatter inherent in the experimental results

As a result of the disagreement in the literature regarding whether a composite structure is loading rate sensitive, more work is required. A suitably detailed experimental program can help shed light on the mechanisms behind strain rate dependency of composite structures. This knowledge can then aid the design of composite energy absorbing structures.

2.4   Modelling damage in composites

Sections 2.3.3.1 to 2.3.3.3 presented complexities in the analysis of crush structures. Numerical modelling of the initiation and evolution of damage within the composite structures is a good way to understand and optimise the design of composite energy absorbers. The definition of damage put forward by Talreja [56] has been adopted for the purpose of this study:

- A damage entity is an individually identifiable change in the microstructure constitution of a solid, which is brought about by an internal energy dissipative mechanism.

- A damage mode is a collective reference to a subset of damage entities, which on account of their geometric feature and local driving forces, evolve in a similar fashion.

- Damage is defined as a collection of all damage entities, or equivalently, as the set of all damage modes present in a body.

Many different techniques have been developed to model the initiation and progression of damage through a structure. These can be broadly separated into two categories, fracture mechanics and continuum damage mechanics.

Fracture mechanics stems from the work of Griffith [57] which reconciled the theoretical and measured strength of materials. In the process, it was discovered that small cracks within the material are the cause of this reduction in strength. Fracture mechanics describe the propagation of cracking through a bulk material from a small initial crack. Further development over many has refined the description of crack growth into include plasticity as well as the dependence on fracture toughness [58]. Fracture mechanics is generally used for analysis of a single crack, but it can also be extended to analyse a small number of cracks at the expense of greatly increased complexity. Furthermore, fracture mechanics does not allow for the creation of cracks, hence the location of the crack will need to be known or assumed at the beginning of the analysis.

In order to describe the behaviour of materials with a large number of microscopic cracks and voids, Kachanov, Chaboche [59]and Lemaître [60] developed continuum damage mechanics (CDM). CDM was developed to describe material behaviour in the presence of microscopic imperfections before the onset of macroscopic crack initiation, as shown in Figure 2.13. Talreja applied CDM concepts to derive a set of constitutive equations describing the effect of small damage on the overall response of a composite laminate. These equations have subsequently been validated against experimental data [61].
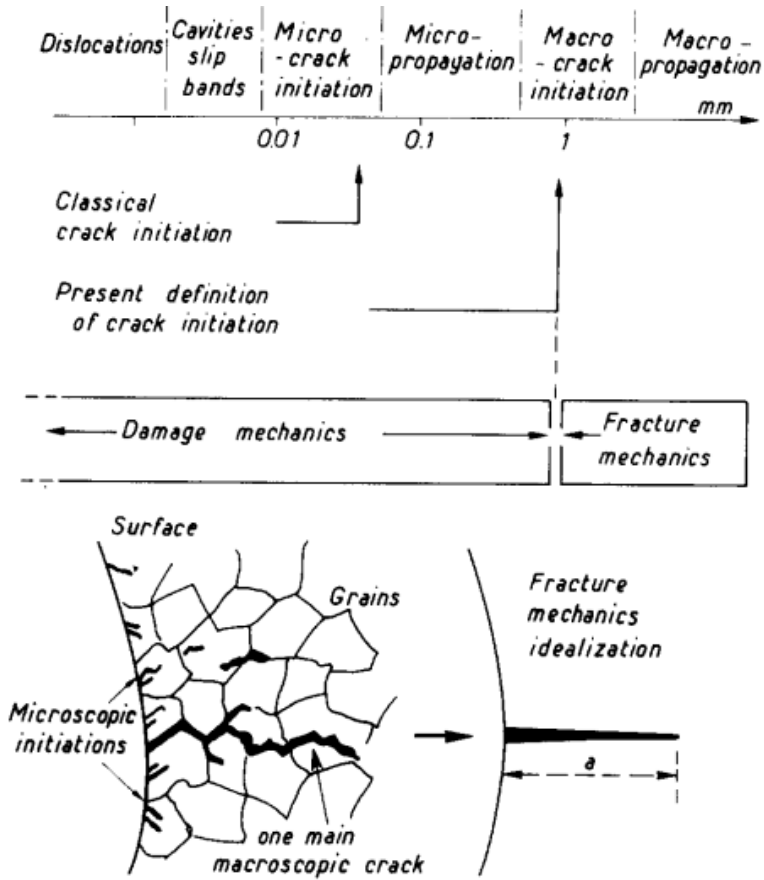
Figure 2.13: Relationship between continuum damage mechanics and fracture mechanics [59].

2.4.1 Continuum damage mechanics

CDM was first proposed by Kachanov and further developed by Chaboche [59] and Lemaître [60].

Rather than describing discrete cracks, which was the approach adopted in fracture mechanics, CDM

assumed that the material is homogenous and continuous. Despite the absence of macroscopic

cracking in the body, CDM assumes that numerous microscopic damage entities can exist within a

volume of material. CDM provides a way to model the initiation and evolution of cracks and voids

within the body, which are assumed to be small and hence can be effectively smeared over a small

volume of the material. The damage in the body is quantified by one or more damage parameters,

which controls the constitutive response of the material, which generally has the form in Eq. (2.5).

$$\vec{\sigma} = \left[\hat{C}(C, d_i, \dots)\right] \cdot \vec{\varepsilon} \qquad (2.5)$$

The damaged stiffness matrix ($\left[\hat{C}\right]$ in Eq. (2.5)) describes the modification of the elastic stiffness

matrix ($[C]$) by the existence of damage as quantified by the damage parameters (d_i, where i denotes

the damage mode). The progression of the damage parameters are a function of loading conditions

and material properties such as the fracture toughness. The main advantage of this approach is that the

volume is treated as continuous and homogenous. This allows continuum mechanics to be applied. In

particular, this method can be used with conventional finite element analysis.

2.4.2 Finite element analysis

Finite element analysis (FEA) approaches have been used extensively to capture and simulate

composite structural response. In FEA, the body being considered is discretised into a connected

series of elements. Each element consists of a series of interconnected nodes. The notion of the nodes

can be described as a function of the material stiffness (K), damping (C) and mass (M) in reaction to

an external load (F) [62].

$$M\ddot{u} + C\dot{u} + Ku = F \qquad (2.6)$$

There are two main categories of FEA: implicit and explicit integration. The implicit integration

method is an iterative process.

$$g\big(u(t + \Delta t), \dot{u}(t + \Delta t), u(t), \dot{u}(t), \ddot{u}(t)\big) = 0 \qquad (2.7)$$

This is in contrast to the explicit integration method where the state variables of the system (in this

case, the nodal displacements u) in the next increment are only dependent on the state of the system in

the current increment.

$$u(t + \Delta t) = f_u\big(u(t), \dot{u}(t)\big) \qquad (2.8)$$

$$\dot{u}(t + \Delta t) = f_{\dot{u}}\big(\dot{u}(t), \ddot{u}(t)\big) \qquad (2.9)$$

The main advantage of the implicit method is its unconditional stability for a large time step. To

achieve this stability, an iterative process is used to ensure convergence of the solution. This requires

the inverse of the global stiffness matrix, which is difficult to obtain in the presence of nonlinearity in the system. On the other hand, the explicit method is only stable where the time increment is below a critical threshold, but does not require the inverse of the stiffness matrix. It can deal with nonlinearity readily as the stiffness matrix can be updated at each increment. The intended application of this work is the modelling of crush response, which is typically dynamic and involves significant deformation and damage within the structure. The highly nonlinear nature of this application makes the implicit scheme unsuitable. Hence, the discussion will be focussed on the explicit integration FEA scheme.

Operating on the principle of virtual work [63], the internal and external virtual work on a given infinitesimal volume must be equal. The internal virtual work (δW_{int}) is the virtual strain energy, while the external virtual work (δW_{ext}) consists of the work done by body forces (f_i) as well as the surface tractions (t_i):

$$\delta W_{int} = \int_{Vol} \sigma_{ij}\, \delta\varepsilon_{ij}\, dV = \delta W_{ext} = \int_{Vol} f_i\, \delta u_i\, dV + \int_{Surf} t_i\, \delta u_i\, dS \qquad (2.10)$$

The FEA progresses by determining the stress (σ_{ij}) due to strains (ε_{ij}) involved in deformation applied to an element.

2.4.3 Modelling approaches for composite structures

There are a number of commercially available numerical models that provide for the modelling of damage in composite structures. However, these are generally basic and require some form of calibration. Subsequent developments have introduced nonlinear material response as well as more physically based damage mechanisms and damage interactions [11, 14, 64]. These have contributed to the improvement in performance of impact damage modelling [12]. However, existing studies modelling composite structures under crushing loads were generally completed using commercially available codes [8, 30, 45, 49, 65] and adopted an empirical approach. Hence, integrating physically based modelling approaches into a comprehensive model for the analysis of damage in composite

structures allows the performance of composite structures under crush loading to be predicted with greater fidelity as well as eliminating the need for calibration.

2.4.3.1 Commercially available models

Various damage models are available in commercial finite element packages. One example is material model type 54 (Mat54), a shell-based formulation implemented in LS-DYNA [7] for arbitrary orthotropic materials which can either utilise failure criteria developed by Chang and Chang [66] or those developed by Tsai and Wu [67]. This model is based on an elastic response until failure is detected via a set of stress-based failure criteria. These criteria can account for the effect of combined loading. The damage evolution is assumed to be instantaneous, i.e., the element is deleted as soon as one of the failure criteria is met. This has led to numerical artefacts as elements are deleted. This phenomenon necessitates in numerical input parameters (such as SOFT, FBRT and YCFAC) which soften the elements adjacent to the deleted elements to smooth the response. However, these parameters require tuning against test data of the complete structure [8]. LS-DYNA also offers Mat58 for use with composite fabric laminates which is based on the work of Matzenmiller et al.[68] and implemented for shell elements. It is a CDM model that uses a purely stress-based response after damage initiation. Like Mat54, Mat58 also requires non-physical parameters such as SLIMxx, TSMD and SOFT factor to control response post-damage.

The ply type 7 model, based on Ladeveze and Le Dantec's [69] work, is implemented for shell elements in PAM-CRASH. This model assumes an elastic compliance matrix with a damage parameter controlling reductions in the elastic moduli. The evolution of the damage parameter is dependent on the respective energy release rates. The ply type 7 model does not adequately represent the more complex damage modes that occur in a crush structure and neglects interaction between damage modes. Similar to Mat54, some input parameters required substantial calibration against experimental test data in order for this material model to produce the desired response [9]. These include the initial damage limit, ultimate damage fracture limit, critical damage limit and the

maximum allowed damage, which are empirical parameters controlling element softening and removal.

Abaqus also has a progressive damage model, for use with continuum shell elements, based on the work of Hashin [70] and Matzenmiller et al.[68]. This model utilises Hashin's failure criteria to detect the initiation of damage. Damage progression is controlled by the energy dissipated due to failure. The maximum degradation can be used to manipulate the calculated response. In the explicit implementation of this model, element deletion is employed to prevent damaged elements from undergoing excessive distortions that can lead to the termination of the simulation.

These commercially available models have been developed to use plane stress shell elements, which assume that through thickness stresses are negligible. This assumption cannot be made for structures being crushed as the loading on a typical section of material in a crushing structure is highly complex and three-dimensional. Furthermore, the interactive damage mechanisms and material non-linearity are not well handled by these models. Loads that induce damage also cause loading and unloading in the local region, which is not captured by these models [31]. As a result, these commercially available models rely on calibration against whole-structure test data in order to achieve good results and thus lack predictive capability.

2.4.3.2 Current developments

The complexity of composite crushing invariably results in highly localised and rapid load redistribution and consequently the damage process needs to take into account the loading history on the material. Much of the commercially available models do not properly account for the effect of loading/unloading and load reversal, particularly for the inelastic shear behaviour of the matrix material. In this section, subsequent developments which have addressed some of these deficiencies [12, 64, 71-73] are discussed.

In cases where complete failure and disintegration of the structure occurs, there is generally more than one damage mode involved. To accurately model the structures to failure, this interaction needs to be

addressed. The CODAM model developed by Williams et al.[71] was based on CDM, using a strain based damage function to control the residual stiffness $\left(\frac{E}{E_0}\right)$ in the constitutive equations. This model adopted a bilinear residual stiffness progression law, which allowed two different damage phases to occur one after another, for example, the matrix breakage occurs before fibre failure due to the higher strength of the fibres. The damage growth functions are determined through experimental determination of failure strains. This approach enables damage mode interaction during the evolution of damage.

Raimondo et al. [72] developed an energy-based, interactive approach that took into account the contribution of each loading direction to the overall energy balance within each element. This allows load from multiple directions to contribute to the same damage mode. However, this damage model did not account for loading and reloading which may have contributed to the over prediction of the force response during the impactor rebound phase after impact, while still in contact with the composite plate. However, this model makes use of a crack saturation density parameter, which can only be obtained by trial and error, and in essence becomes a "calibration" parameter.

Donadon et al. [64] and later Faggiani and Falzon [12] developed damage models which are considerably more physically based. Due to the failure of neighbouring material, unloading and reloading is expected in the crushing structure and must be account for. Furthermore, a nonlinear shear profile was adopted which enabled a more accurate representation of the matrix material. Egan et al [74] developed a 3D composite damage model which includes the interaction between damage and material nonlinearity in the in-plane shear response of composite plies. Their models also utilised Puck and Schürmann's approach to assessing matrix damage [11]. Puck and Schürmann's phenomenological assessment of matrix damage included interactions of local stresses on a fracture plane, which was compared with the material's resistance to determine damage initiation. This approach mirrors the experimentally observed fracture plane for matrix-dominated failure modes. These two models were able to give good predictions of the impact response for a simple composite plate and a stiffened composite panel, respectively.

A major issue with the use of a damage softening model is damage localisation, which leads to mesh non-objectivity in the FEA. As element size becomes infinitesimal, the resulting dissipated energy approaches zero, which is clearly unrealistic. Bazant [75] pioneered the concept of a crack band which is a characteristic length scale of the fracture. The requirement for an accurate estimate of the characteristic length to achieve mesh independence for a CDM based smeared crack FE damage model has been analytically demonstrated by Oliver [76]. However, much of the existing composite damage models use a coarse estimate of this quantity. The Abaqus in-built progressive damage model for composite laminates, for example, approximates the characteristic length as the cube root of the elemental volume, which is increasingly inaccurate as the aspect ratio increases. Donadon et al's [64] model tackled this issue by calculating the characteristic length directly from the shape functions of the element. This approach will yield an accurate characteristic length regardless of the aspect ratio of the element. However, the implementation restricts the fracture plane that can be represented, i.e., the fibre direction of the laminate must align with one axis of the element so that the material coordinate system and the elemental coordinate system are not completely independent of each other. A more general algorithm is required to determine the characteristic length for the full spectrum of possible orientations of the fracture plane.

Table 2.1 shows a summary of the features of the damage models found in the literature, highlighting the gaps in the current capabilities. By integrating these advanced techniques as well as new approaches, a material model that comprehensively capture the complete response of the composite structure can be created. The resulting model would be well placed to predict the complexities that arise during the analysis of composite structures under crush loading.

Table 2.1: Summary of comparison between existing models and the present model.

Model	Element formulation	Robust characteristic length*	Nonlinear shear	Load reversal	Damage interaction	
					Fibre	Matrix
Commercially available models						
PAM-CRASH ply type 7 [69]	2D	N	Y	Unloading/ reloading only	N	Y
LS-DYNA Mat 54 [7]	2D	N	N	N	N	N
LS-DYNA Mat 58 [7]	2D	N	Y	N	N	N
Abaqus Hashin Damage [6]	2D	N	N	N	Y	Y
Recently published models						
William et al. [71]	2D	N	N	N	Y	Y
Donadon et al. [64]	3D	N	Y	Unloading/ reloading only	Y	Y
Faggiani and Falzon [12]	3D	N	Y	Unloading/ reloading only	N	Y
Raimondo et al. [72]	3D	N	Y	N	Y	Y
Shi et al. [73]	3D	N	Y	N	Y	Y
Proposed model	3D	Y	Y	Y	Y	Y

* Capable of accurately assessing characteristic length for a fracture plane in an arbitrary orientation with respect to both the material and the elemental coordinate system

2.4.4 Modelling crushing in composite structures

Many authors have studied the response of composite structure under crushing loads numerically through FEA [8, 49, 77]. A majority of these studies were completed using commercially available software. A common theme present in these studies is the use of shell elements in the FE analysis.

LS-DYNA [7] has been a popular choice for researchers. It offers two similar material models for use with composite structures, Mat54 and Mat58. Mat54 was used by Feraboli et al. [8] to model the collapse of a corrugated web specimen. In general, the simulated results agreed well with the experimental observations. However, substantial oscillations were observed in the numerical force response. Many of the input parameters must also be calibrated via trial and error against the

experimental response [8]. This model was not capable of reproducing the complex deformation that occurs to the structure, such as the splaying and fragmentation of the composite laminates [8]. Mat58 was used by Kakogiannis et al.[47] to analyse the crush response of tulip triggered cylindrical tubes with 30 and 60 degree peaks driven by explosive charges. Agreement with experiment for the overall shape and magnitude of the force response was achieved after manual calibration. Despite calibration, simulated results of some specimens were not satisfactory. Xiao [31] demonstrated that the unloading behaviour of the composite material is important to the overall response. It was shown that modifying the Mat58 material model to better capture the unloading and reloading response yields more accurate results in terms of a more realistic splaying of the plies as well as an SEA that is closer to the test value [31].

The ply type 7 material model implemented for a stacked shell approach in PAM-CRASH was used by Joosten et al. [49] to simulate the response of hat-shaped sections. Both the force response and the final deformation were in good agreement with experimental observations. However, substantial calibration was required in order for the desired simulated response to occur. Not only were the damage limits adjusted, the material properties, which were measured physically, were manipulated to obtain the desired response. Similarly, when Johnson and David [39] simulated C-shaped channel sections under crushing loads, a numerical trigger was required in the simulation to promote the development of the desired crush progression. For these hat and C-shaped sections, the model was only able to capture realistic deformation when the desired response is known and appropriate steps were taken to encourage the correct response, which limits the range of potential applications that the stacked shell based ply type 7 model can be applied to.

Subsequent developments tended towards a more physically based approach. Israr et al.[78] used a pseudo 2D model based on work by Hongkarnjanakul et al.[79] and Bouvet et al.[80]. The model depends only on material property parameters. The simulated force responses closely matched experimental observations. It was able to capture the damage mechanisms individually for the 0 and 90 degree plies, and hence the deformation of the damaged plies was very well represented. However,

the pseudo 2D nature of the material model restricted the types of structures it can simulate. The authors [78] have yet to be extend the model into 3D.

Sokolinsky et al.[77] used the shell based CDM model developed by Johnson [81] to model a corrugated web specimen. The energy absorption was well predicted by the simulation. However, the force response has a slight initial offset from the experimental observation. The extent of damage was more pronounced in the simulation than experimental observations, with large cracks running along the side of the specimens rather than the splaying confined to the crush front seen in the tests.

The CODAM material model is one of the more successful models in this area. McGregor et al.[82] used it to simulate the crushing of square tubes with and without a plug initiator. Good correlation was achieved between simulated and experimental results both in terms of force response as well as the damage deformation. An artificially debris wedge was required in the simulation without the plug initiator to promote splaying of less constrained plies. The model works well for thin composite structures [82, 83] but is untested for more typical composite structures which are generally thicker.

Currently, there is opportunity for continuing work in the simulation of composite structures under crush loading due to the limitations in the models used in analysis. A model that can capture the physical damage and deformation will be beneficial to the design and development of energy absorbing composite structures by providing a more detailed representation of the damage process.

2.5   Measurement methods for material properties for composite laminates

A damage model requires a set of material property parameters to determine the structural response, which has a significant impact on the accuracy of the numerical simulation. CDM based material models requires a large number of parameters, which characterise each aspect of material behaviour ranging from the stiffness and strengths to fracture energies. These parameters can be obtained from a range of standardised and non-standard tests. The test setup and the coupon used are briefly discussed,

particularly those which are not a part of an accepted standard. Challenges in the measurement of these properties are highlighted.

2.5.1 Statically measured composite material properties

Material characterisation is generally done under quasi-static conditions where dynamic effects are not present. The measurement of elastic material properties and some critical energy release rates are governed by the ASTM standards.

2.5.1.1 Normal direction elastic properties

ASTM D3039 [84] describes the coupons tests for determination of tensile strength, modulus and Poisson's ratio. Both longitudinal and transverse properties can be determined via appropriate orientation of layup directions. The thickness properties are usually taken to be the same as the transverse properties due to the orthotropic assumption applied to the composite plies. Coupon specimens as described in Figure 2.14 are placed in grips attached to a testing machine in tension. The force and displacement histories of the specimen under loading are analysed to yield the desired quantities.
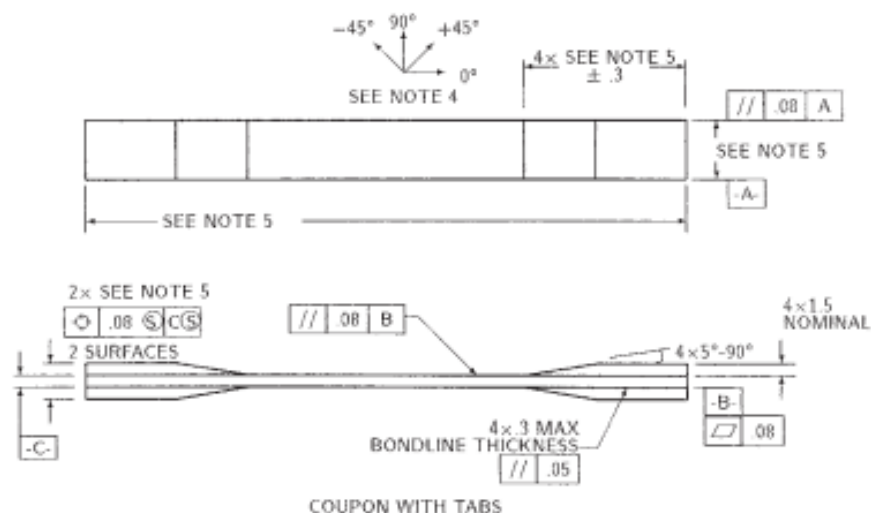
Figure 2.14: Tensile coupon specification [84].

ASTM D3410 [85] describe a similar coupon test which yields the compressive strength and modulus. Again, the longitudinal and transverse properties are measured through layup of 0 or 90 degree ply in the test direction. The coupons used are shown in Figure 2.15.
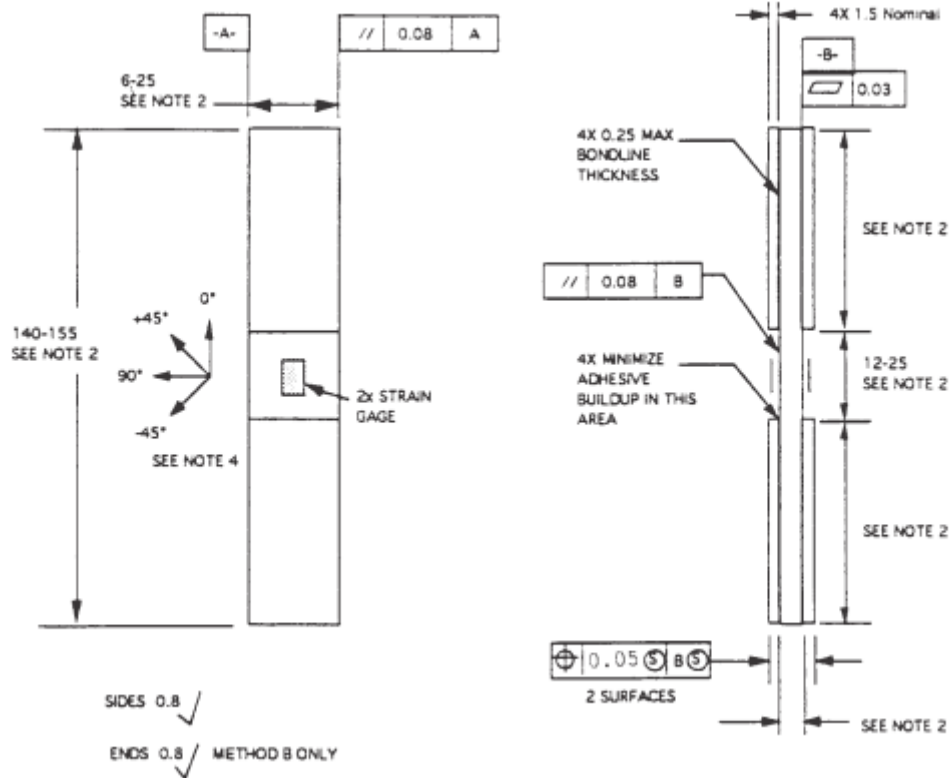
Figure 2.15: Compressive coupon specification [85].

However, the transverse properties obtained using these standards do not account for in-situ effects. It was shown by Chang and Chen [86] that shear failure within a composite laminate is dependent on the orientation, thickness and number of surrounding plies. This is due to the potential confining and supporting effect of surrounding plies. As a result, the local transverse compression and shear strengths have been shown to be dependent on the ply configuration. This is the in-situ strength and is typically higher than that of the unidirectional strength [87]. For the purposes of input to the material model, the unidirectional value is used as a conservative estimate in order to reduce the number of input parameters required and to reduce the complexity of the model implementation.

2.5.1.2 Shear properties

ASTM D3518 [88] defines the testing method for the shear profile and strength measurement of a unidirectional composite ply. This standard describes a test similar to ASTM D3039. Rather than the unidirectional laminates used in ASTS D3039, this standard calls for ±45 degree layup for the coupon specimen as shown in Figure 2.16.
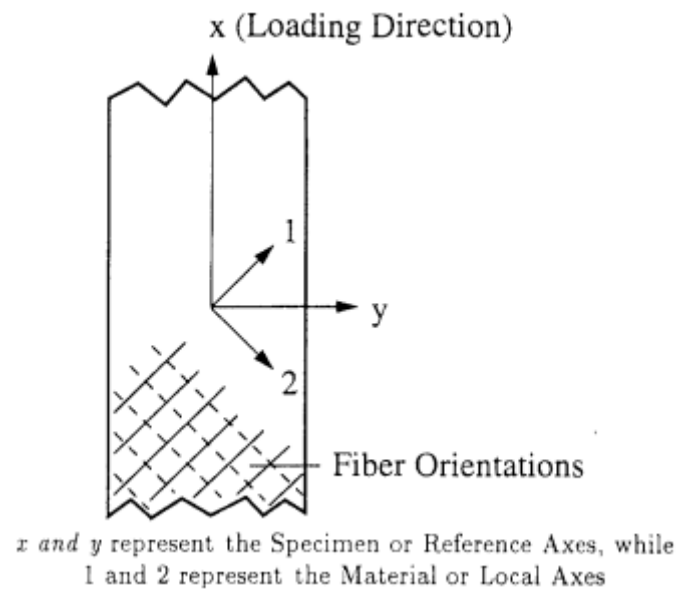
Figure 2.16: Shear testing coupon layup specification [88].

Test methods also exist for the measurement of shear properties in other directions. These include the ASTM D4255 [89] rail shear method, the ASTM D7078 [90] V-Notched rail shear method and ASTM D5379 [91] V-notched beam method. ASTM D3518 provides a fast and simple measurement of the in-plane shear properties while the other methods allow the measurement of shear properties in the transverse and thickness directions.

2.5.1.3 Intralaminar critical energy release rate

Methods describing the measurement of intralaminar critical energy release rates are not as well established. Compact specimens described in ASTM E399 [92] and E1820 [93] (Figure 2.17), originally designed for the testing of metallic materials, can be adapted for the determination of both

tensile and compressive fibre-dominated critical energy. This approach is also similar to the single

edge notch test method described in ASTM E1922 [94], which applies only to tensile energy release

rate.
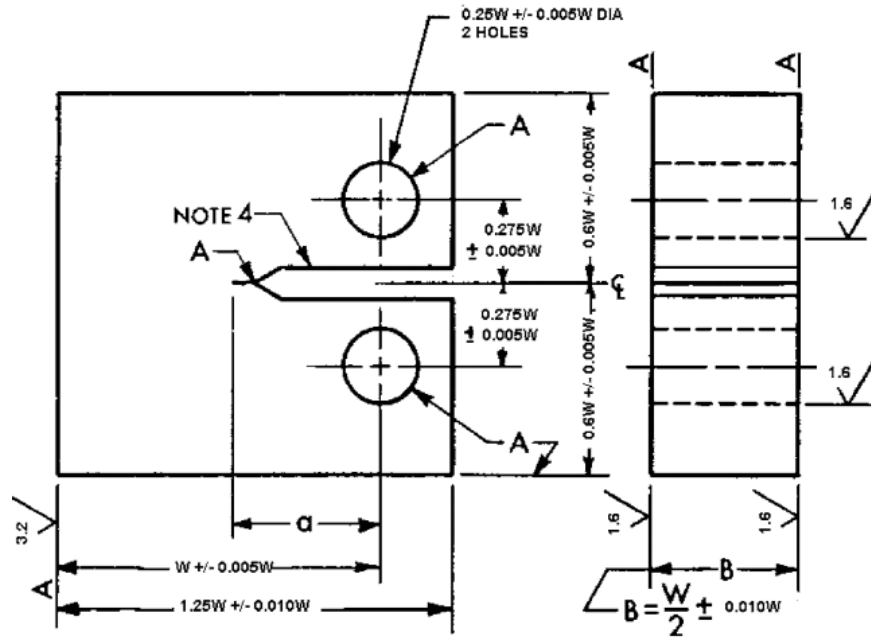
Figure 2.17: Compact specimen (CT) described in ASTM E399 [92].

ASTM E399 was originally intended for use in determining the fracture toughness of metallic

materials release rates. Pinho et al.[95] demonstrated that the data reduction method used was not

suitable as it depended on the stress intensity factor for isotropic materials. An alternative FE based

method was proposed to account for the significant anisotropy in composite laminates. This result was

validated against experimental data. Laffan et al.[96] compared five different data reduction methods

for the measurement of mode I fracture energy. The modified compliance calibration method was

adopted for their subsequent studies as it did not require the measurement of crack length, which was

performed optically and thus could be unreliable. Coupons described in ASTM E399 can also be

applied to the matrix-dominated energy release rates in tension and compression by rotating the

orientation of the laminate. The same analysis process as the tensile coupon can be performed to

obtain the compressive value using an appropriately laid up specimen. There are currently no direct

methods to measure the intralaminar shear energy release rates. The mode II interlaminar energy

release rate is an appropriate approximation of the intralaminar shear energy release rates, as mode II interlaminar failure is caused by the shear failure of the laminar interface, which is similar to the shear failure within the matrix material. The value of Mode II interlaminar critical energy release rate is likely to be lower than the critical energy release rate in shear for the matrix due to the ply interface, forming a conservative estimate.

Similar to the transverse compression and shear strength, some in-situ effects have also been observed in mode I critical energy release rate [97]. When multiple 0 degree plies are blocked together, an increase in fibre pull-out is observed, which results in an increased apparent fracture toughness. However, the current state of intralaminar fracture is immature and substantial variations exist in the approaches of different authors [98]. Given this uncertainty, possible in-situ effects in the intralaminar fracture energies are neglected.

2.5.1.4 Interlaminar strength and critical energy release rate

In contrast, methods to obtain mode I, mode II and mixed-mode interlaminar critical energy release rates for unidirectional composite laminate are well specified. ASTM standards D5528 [99] describe the widely accepted double cantilever beam specimen (Figure 2.18) for determination of mode I energy.
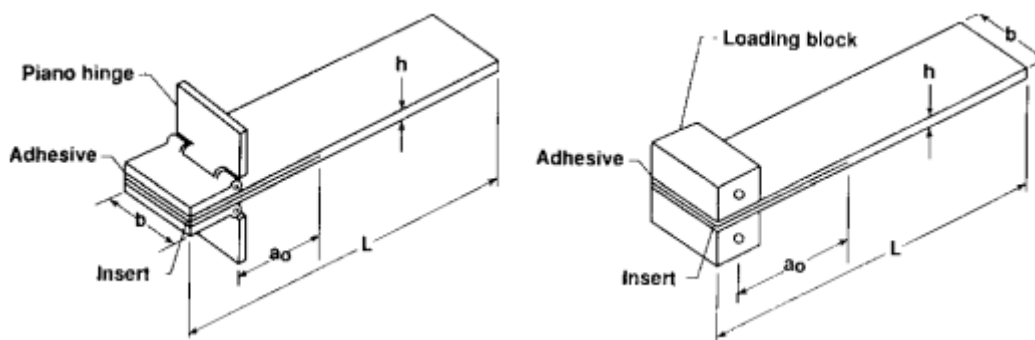
Figure 2.18: Double cantilever beam specimen [99].

The ASTM D6617 [100] standard describes the mixed mode bending test (Figure 2.19) which is designed to measure the mixed mode I/mode II energy release rate. Through this test, the mode II energy can be found. Mode mixing parameters can also be calculated from the results.
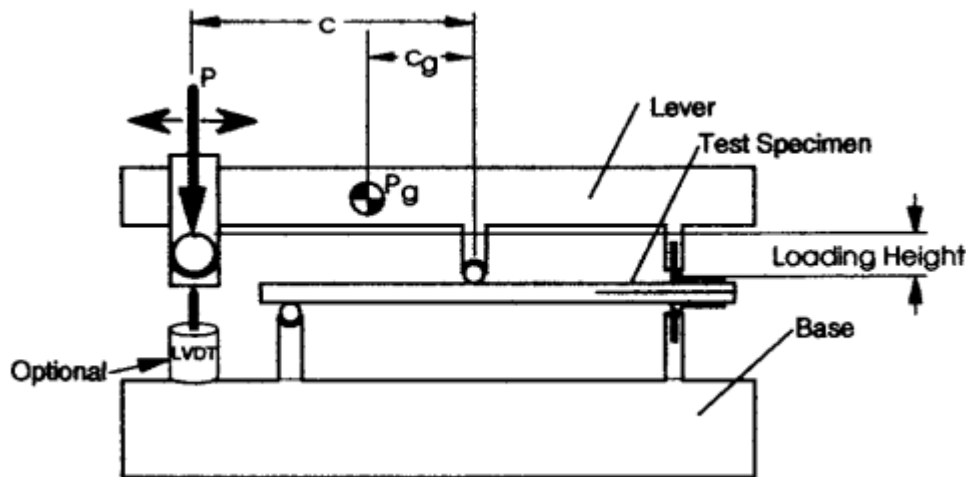
Figure 2.19: Mixed mode bending test setup using the end notch flexure specimen [100].

The mode III energy is assumed to be the same as that of mode II.

2.5.2 Dynamically measured composite material properties

Composite energy absorbing structures are intended for use in the attenuation of crash loading. MIL-STD-1290A(AV) specified that the aircraft should be designed so that the loading on the occupant remains at an acceptable level for a crash with 13m/s vertical speed. Consequently, the energy absorber would be expected to perform under dynamic loading. Any material rate dependency will need to be measured. Measurement of material properties is difficult for high rates of loading and generally not a part of an accepted standard. Special equipment is typically required and the results often contain significant spread.

2.5.2.1 Normal and shear direction properties

Numerous researchers have explored strain rate effect on material properties. ASTM standard D4762 [101] mentioned some of the standards relating to the testing of composites under dynamic loading. However, this standard focussed on impact and fatigue testing. In his review, Sierakowski [102]

discussed the different test methods for obtaining elastic material properties at high strain rates. The difficulties encountered in trying to understand the high rate behaviour of composite materials was also noted. Four main approaches were discussed. Explosive impact testing (Figure 2.20) utilised a pressure pulse generated by an explosive to achieve high speed loading on the test specimen, which is a thin ring. Both tension and compression properties can be tested using this method. The ring undergoes deformation with rotational symmetry, giving rise to uniform loading in the circumferential direction. The attainable strain rates are limited by the wave propagation characteristics of specimen [102].
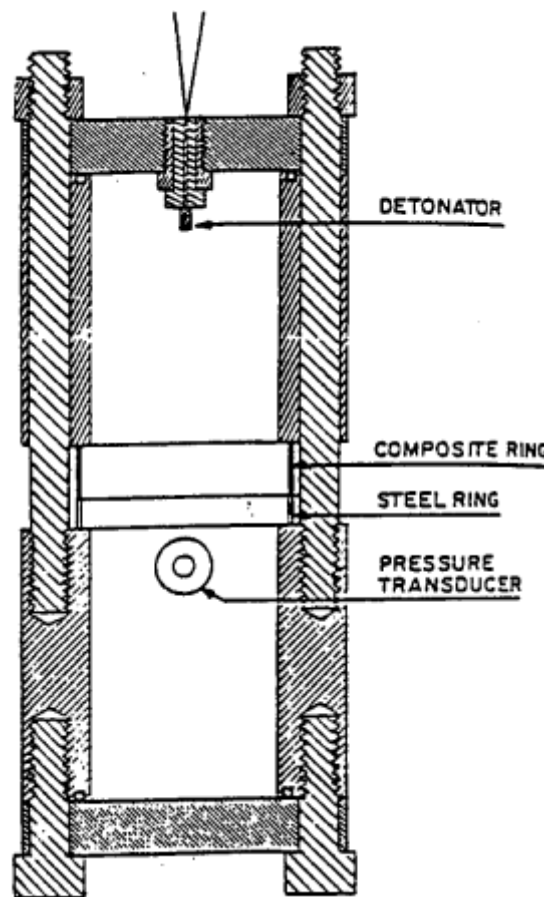
Figure 2.20: Explosive expanding ring tester [102].

Another method to achieve accelerated rates of loading is drop weight impact testing (Figure 2.21). A large mass is dropped onto the fixture containing the specimen to be tester. The deceleration of the mass provides the forces necessary to load the specimen. A similar approach is the split Hopkinson

44

pressure bar testing (SHPB, Figure 2.22) [103]. The SHPB works by using a striker bar, typically fired out of a gas gun, to impact on the incident bar and generate a pressure wave. This wave then travels through the specimen and into the transmission bar. The strain history is captured both before and after passing through the specimen. A pulse shaper is normally used to ensure the loading on the specimen is uniform and at a constant strain rate. The SHPB approach has been widely used in the literature for the testing of composite material properties at elevated strain rates [102].
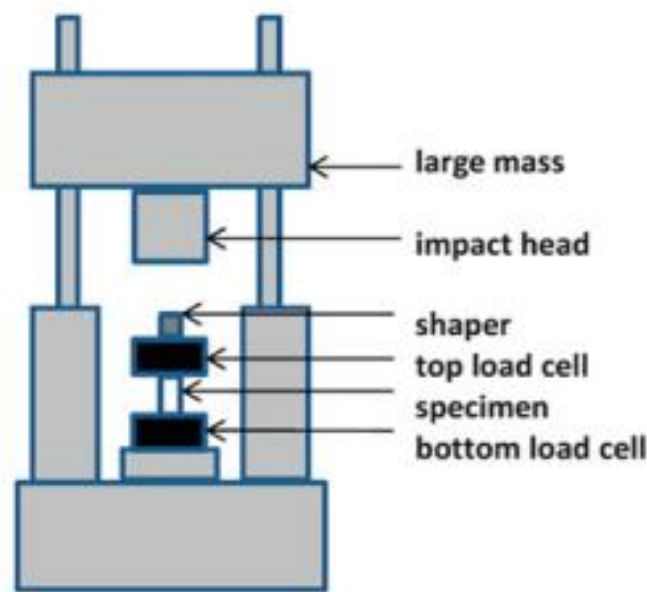
Figure 2.21: Drop weight impact tester (DWIT) [104].
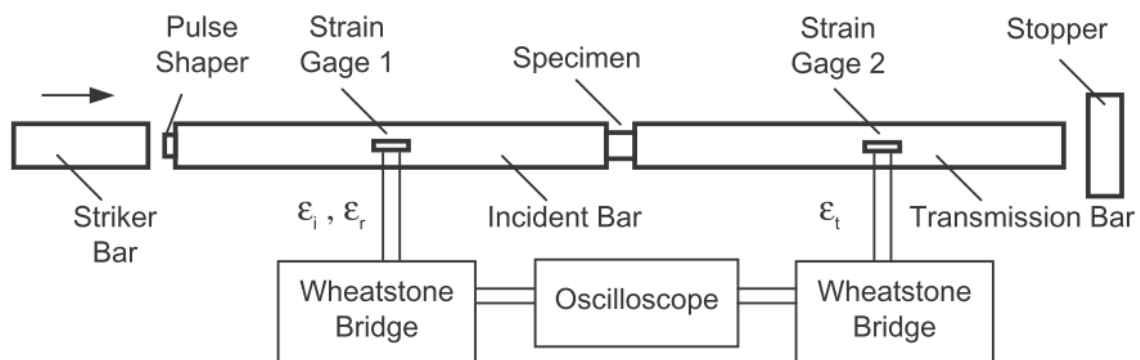
Figure 2.22: Split Hopkinson pressure bar (SHPB, or alternatively, Kolsky bar) for high rate measurement of

material properties [105].

Both the DWIT and SHPB make use of fixtures to ensure that the loading is applied correctly to the specimen. Fixtures have been developed for compressive (Figure 2.23), tensile (Figure 2.24) and shear (Figure 2.25) testing.

(a)   (b)
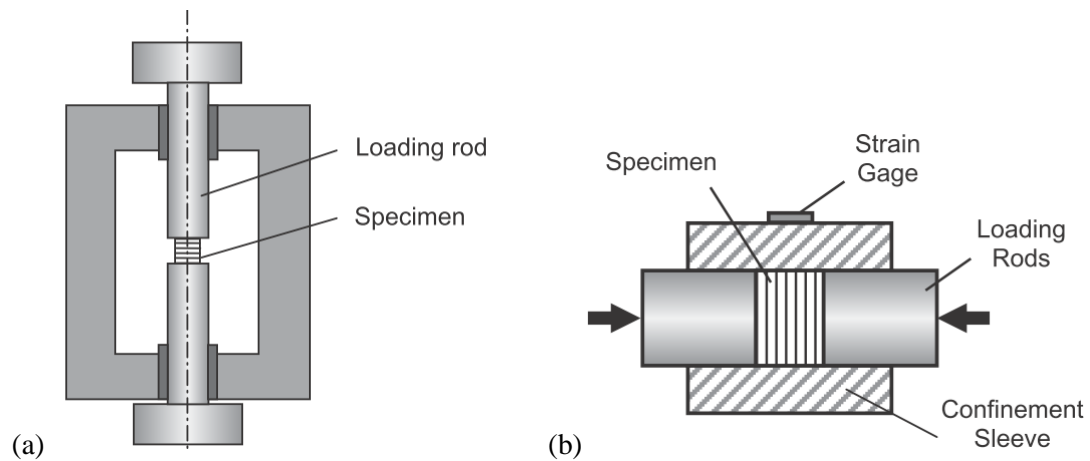
Figure 2.23: Fixture for compressive for uniaxial (a) and multi-axial (b) dynamic testing [105].
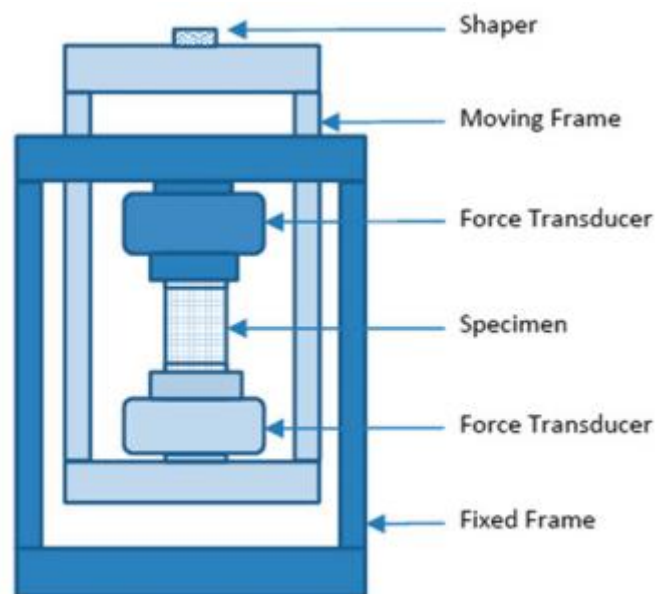
Figure 2.24: Fixture for tensile dynamic testing [104].
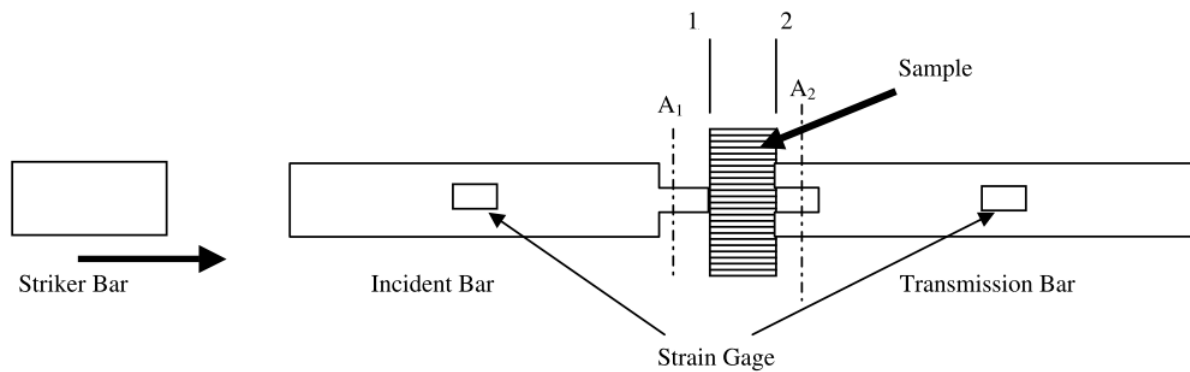
Figure 2.25: Fixture for dynamic punch shear test [106].

Increased rates of loading can also be achieved through a servo-hydraulic testing setup (Figure 2.26). A hydraulic jack is used to provide the forces to the fixture. This method is generally used for low to intermediate strain rates. Attainable strain rates are limited by the inertial effects of the load cell and fixture.
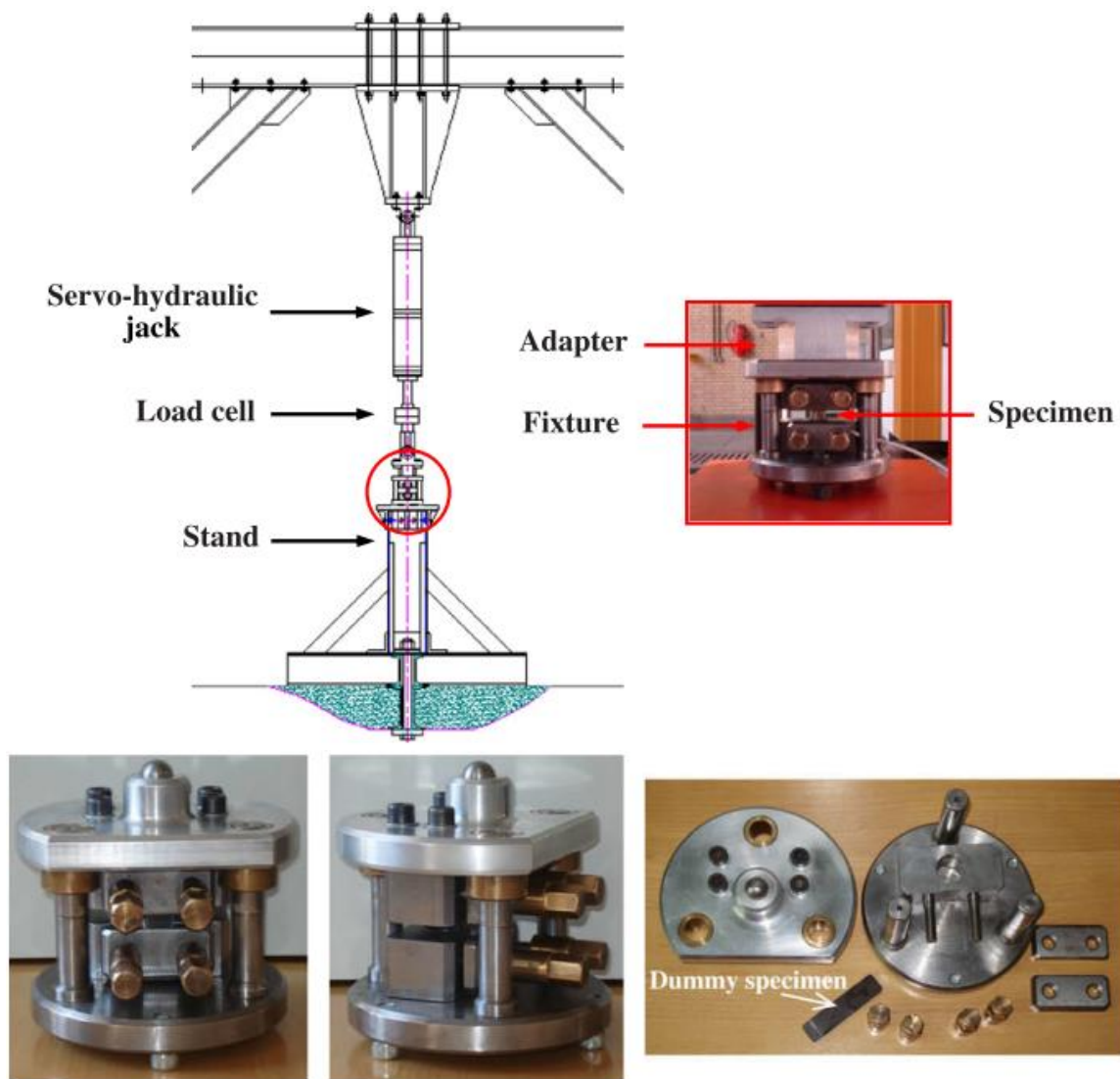
Figure 2.26: Servo-hydraulic setup and fixture for intermediate strain rate testing [107].

2.5.2.2 Critical energy release rate

The critical energy release rates at increased strain rates are much more difficult to obtain than the elastic properties due to the unsteady nature of the crack propagation. Much of the test methods used for dynamic testing are based on test methods established for static testing. Cantwell and Blyton [108] reviews existing techniques for the measurement of interlaminar fracture energies under dynamic loading. The test specimens used are generally some variation of the double cantilever beam specimen used in the static mode I tests. Similarly, the measurement of mode II and mixed mode tests are conducting using notched flexure type specimens. An alternative was proposed by Sun and Han [109],

who used the wedge loaded compact tension specimen (WLCT, Figure 2.27) with a SHPB setup
(Figure 2.28) to measure Mode I interlaminar energy release rate.
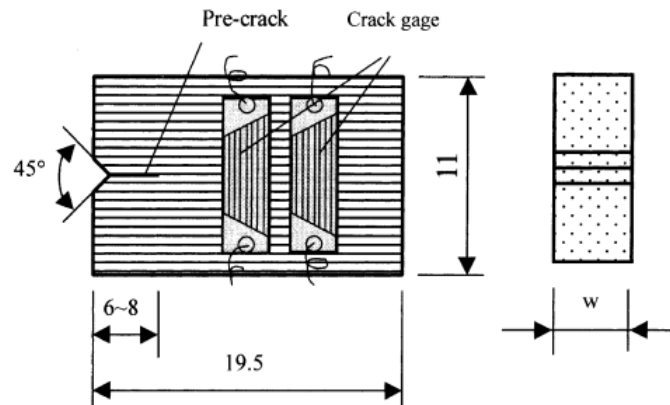
Figure 2.27: Wedge loaded compact tension specimen (WLCT) [109].
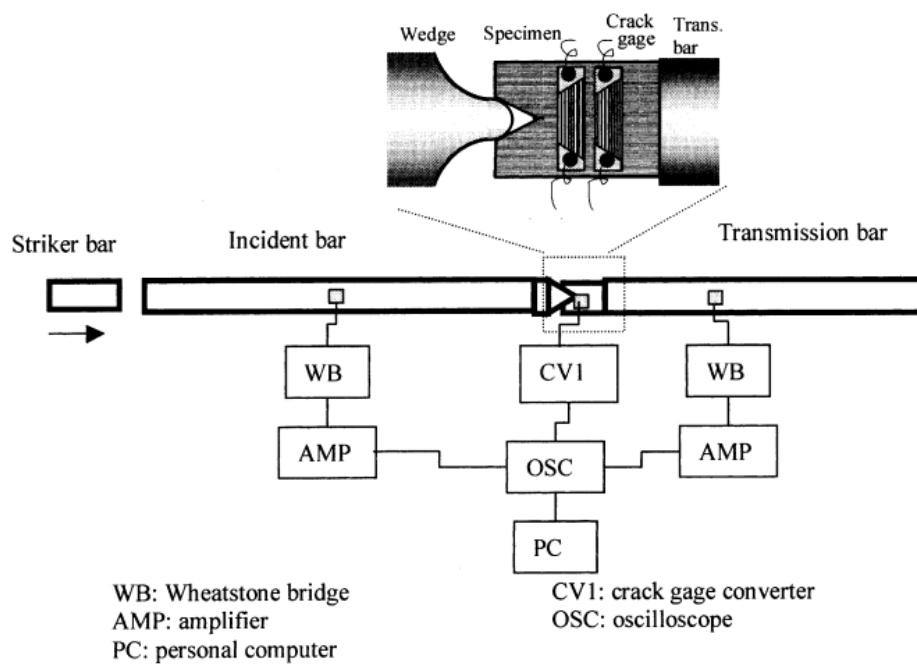
Figure 2.28: WLCT used with a SHPB setup [109].

As the WLCT specimens are very similar to the compact tension specimens used in the measurement
of intralaminar critical energy release rates, the WLCT specimens can potentially be used in the same
manner for testing under high loading rates.

2.5.2.3 Observed trends on strain rate effect on material properties

Sierakowski [102] also noted that the strain rate behaviour is dependent on the complex interaction between the fibre and the matrix which changes as the strain rate increased, leading to a changing response. It was noted by Hsiao and Daniel [110] that waviness in the fibres tows generate significant nonlinearity in the high rate response. Jacob et al.[111] reviewed property dependence on strain rate for tensile, compressive and shear moduli and strengths for composite laminates. It was concluded that significant disagreement exist in the literature.

Koerber et al. [112] showed rate dependence in the matrix-dominated material properties beyond 200 s^{-1} and rate independence in fibre-dominated longitudinal compressive modulus [113] for a carbon-epoxy material system. This supports the view that the strain rate effects are primarily driven by the response of the matrix in this instance. However, this does not apply to other composites. The glass fibre composite used in Shokrieh and Omidi's test showed substantial strain rate effects on longitudinal tensile [114] and compressive [107] as well as transverse [115] properties.

Cantwell and Blyton [108] surveyed the literature for interlaminar energy release rates measured under increased loading rates. For the mode I test data surveyed, systems with brittle polymer matrix were generally rate insensitive or increased slightly with loading rate. Similarly, mixed mode I/II tests reported constant or slightly increasing energy rates with increasing loading rate. However, thermoplastics and rubber-modified exhibited reduced mode I energy release rate with increased speed. On the other hand, consensus has not been reached in the literature over the rate sensitivity of pure mode II critical energy release rate.

2.6   Summary

Composite materials are suitable for use in aircraft structures due to their superior specific strength and stiffness. Increasing regulatory pressure to improve safety has been driving the development of energy absorbing structures in improve protection offered to the occupant by the airframe. These

energy absorbing structures are designed to reduce the acceleration experienced by the occupants. However, the freedom of design choices and the complexity of the crushing behaviour places increased demands on analysis.

2.6.1 Energy absorbing structures

Energy absorbing structures generally exhibit three phases when subjected to crush loading. Region I is marked by a quick rise in transmitted force up to the peak force. Subsequently, the force reduces when steady-state crushing is established in Region II. When the structure is completely consumed, another sharp rise in the transmitted force occurs which marks Region III. Four main metrics (peak load, the steady-state load, the crush efficiency and the specific energy absorption) are generally used to quantify the performance of energy absorbers.

Energy absorbing structures can be constructed using a variety of materials. This study will focus on structures composed of purely continuous fibre reinforced plastic laminates. A brief survey was conducted on the variety of geometries adopted for energy absorbing crush structures found in the literature. In particular, the different trigger mechanisms used for manipulating the crush initiation and progression was discussed. The disagreement within existing work on crushing at elevated rates of loading was also discussed, promoting further work on assessing dynamic response of energy absorbing structures.

2.6.2 Modelling energy absorbing structures

The biphasic nature of composite laminates leads to complex damage mechanisms when the structure is crushed. While this increases the potential energy absorption, it also makes the analysis and design of composite energy absorbing structures difficult. Finite element analysis has been extensively employed in the study of composite structures. Coupled with continuum damage mechanics, FEA has been used in simulating damage in composite structures. Commercially available composite damage material models in LS-DYNA, PAM-CRASH and Abaqus were developed for use with shell element and do not include complex damage mechanisms. As a result, these models [8] typically require

calibration of input parameters in order to accurate capture structural response. Subsequent developments have moved onto a 3D formulation as crushing induces complex multi-axial loading on the structure [12, 64, 71-73], as well as material nonlinearity, unloading / load reversal, physically based damage mechanisms and damage interactions. These more advanced modelling approaches have not yet been extensively applied to the modelling of composite structures under crush loading. This presents an opportunity to develop a predictive material model, which integrates a range of new and existing physically based modelling techniques, and apply it to crush modelling. This capability can potentially increase the fidelity of analysis for composite energy absorbers and reduce the reliance on physical testing.

2.6.3 Obtaining material property data

A large range of material properties are required by the developed material model for accurate simulation results. These property values are measured using a range of standard and non-standard material characterisation tests. For the elastic properties, standards prescribing their measurements have been noted and discussed in Section 2.5. However, for properties that do not have standards governing their measurement, such as intralaminar critical energy release rates, the approaches found in the literature were briefly discussed in terms of the setup and the specimen required. Factors affecting the measured values were also highlighted.

As the energy absorbers are expected to be exposed to elevated rates of loading, the strain rate effect of the material may be of significance. The testing methods applicable for high rate testing were discussed and trends reported in the literature were also summarised.

Chapter 3
The Intralaminar Damage Model

3.1 Introduction

Existing techniques, discussed in Section 2.4, for numerically modelling the response of composite energy absorbing structures do not fully capture the detailed damage response. The developed Intralaminar Damage Model (IDM) will address the main shortcomings identified in the existing models through a physically based modelling approach.

Key features of the present model over existing methods include:

- The use of 3D solid elements in contrast to the 2D shell based models that are often used in modelling composite materials ([68], [70], [66]). This resolves issues associated with neglecting the out of plane stresses as the loading on a typical section of material in a crushing structure is highly complex and three-dimensional.

- A more generalised and accurate estimate of characteristic length based only on the fracture plane orientation and the nodal coordinates [76]. This improves flexibility in the mesh generation as the characteristic length is no longer dependent on the material coordinate system (MCS).

- A nonlinear shear response. Many current models ([6], [7]) neglect the experimentally observed nonlinearity in the shear response. This will have a significant impact as matrix damage under compressive and/or shear occurs via shear fracture.

- Greater interaction of different damage modes. Current approach mostly assumes damage due to loading on different axes are mutually independent ([68], [49]). However, experimental evidence suggests that this is not the case [11]. For example, both transverse compressive and shear loading contribute to shear cracking in the matrix. This issue is exacerbated by the highly complex 3D loading anticipated within a crush structure.

- Introducing isotropic hardening to deal with loading, unloading, reloading and/or load reversal ([12], [116]). This feature is necessary due to the softening nature of a CDM based model which causes load transfer from failing or failed structures to neighbouring regions.

- Accounting for load history effects in damage interaction due to load redistribution after material failure.

The reliance of currently available models on manipulation of input parameters against component level testing to achieve good accuracy reduces their usefulness in design analysis. The adopted approach allows the assessment of the crush response of a structure using only measured geometric and material property data. This process does not require physical testing of the component being analysed and thus is more suitable for use in the design process.

This chapter outlines the theory and implementation of the intralaminar damage model. The proposed model is based on using continuum damage mechanics (CDM) [59] as a mean of assessing microscopic damage in a material. Then the theory underpinning the model is explained. Aspects of the coding of the IDM using FORTRAN are discussed, including efforts to improve the legibility and performance of the resulting VUMAT. The IDM is used in combination with Abaqus inbuilt models which analyse contact between free surfaces as well as cohesive interaction between plies. This forms a complete and comprehensive modelling package. The theories underpinning these models are also described in this chapter.

3.2 Abaqus/Explicit with VUMAT

The IDM was implemented using the user-defined material response subroutine (VUMAT) within the Abaqus/Explicit package [6]. The Abaqus core provides the VUMAT with the current increment strain values as well as all state variables associated with the integration points at the previous increment. VUMAT then calculates and returns the stress state, as well as the state variables, of the current increment to Abaqus at each integration point. This process is repeated for each element in the model for every increment.

3.3   Quantifying damage using CDM

The intralaminar damage model is based on CDM for 3D stress states, proposed by Chaboche [16] and Lemaitre [17], as a method to determine the behaviour of a material under damage-inducing loads. Under the CDM framework, microscopic cracks and voids form within the material being loaded [17], before macroscopic fracture of the bulk material occurs. This causes a reduction in the effective load bearing area, which for the 1D case, can be quantified by a damage parameter:

$$d = \frac{A - \tilde{A}}{A} \tag{3.11}$$

where A is the pristine load bearing area and $\tilde{A}$ is the reduction in load bearing area in the presence of damage-induced microscopic cracks and voids as illustrated in Figure 3.1.
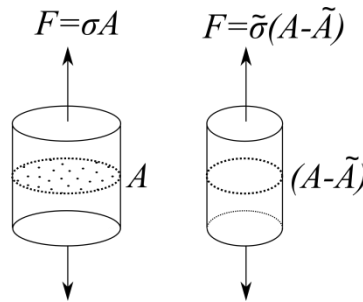
Figure 3.1: Specimen with damage induced micro-voids (left) idealised as a pristine specimen with a reduced load bearing area.

Thus, the damage parameter is a direct measure of the amount of damage in the material. Assuming that the remaining undamaged area has the same load bearing capacity as the pristine material, the damage parameter can be used to relate the stress in the damaged material, σ, to the effective stress, $\tilde{\sigma}$, which would have been experienced by the material, had damage not occurred.

$$\sigma = (1 - d)\tilde{\sigma} \tag{3.12}$$

Operating on the assumption of strain equivalence, the Young's modulus (E) of the damaged material may be expressed as:

$$E = (1 - d)\tilde{E} \tag{3.13}$$

Once damage has initiated, the damage parameter acts to soften the elastic modulus of the pristine material ($\tilde{E}$) to the damaged elastic modulus (E). Energy is required to create cracks and voids within the material as damage progresses. Hence, the load bearing capacity of the material is dependent on how much energy has already been dissipated in damage formation. The transmitted stress reduces to zero when the volumetric strain energy dissipated, g, reaches a critical value, signifying the complete failure of the material. This point is defined by the failure strain, $\varepsilon_{failure}$:

$$\int_0^{\varepsilon_{failure}} \sigma \, d\varepsilon = g \tag{3.14}$$

To be thermodynamically consistent, the IDM must be formulated so that the damage must be irreversible. Hence any damage parameter must be monotonically increasing. The physical interpretation of this is that once material is damaged, the strength will not recover regardless of loading condition. Damage mechanisms present within a unidirectional continuous fibre ply are captured by three damage parameters; two to account for the tension and compression in fibre-dominated damage and one for matrix-dominated damage. This is discussed in more detail in section 3.4. To capture the whole structural response to damage inducing loads on laminated composite structures, existing cohesive damage and contact models are utilised in conjunction with the developed intralaminar model.

3.4 IDM – theory and implementation

The developed IDM assesses damage in the two phases of a continuous fibre unidirectional composite ply. Fibre-dominated damage is primarily associated with loading along the fibre direction. The anticipated damage will occur in the form of net fibre breakage in tension and predominantly fibre kink band formation when loaded in compression. Matrix-dominated damage is primarily associated with transverse and shear loading, which leads to plasticity and formation of cracks in the matrix material. The use of a CDM based softening constitutive relationship necessitates the determination of

a characteristic length to correctly scale the critical energy density. Figure 3.2 outlines the structure of the IDM as implemented in the VUMAT.
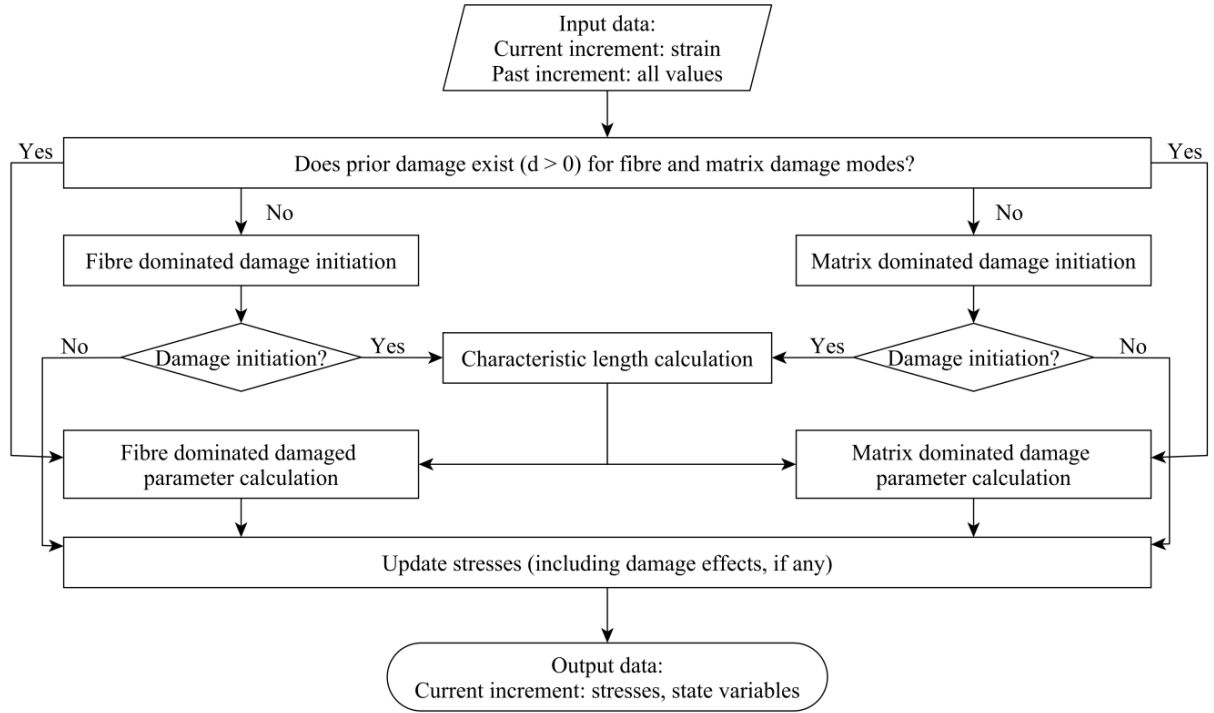
Figure 3.2: Flowchart showing the processes within the Intralaminar Damage Model.

3.4.1   Characteristic length calculations and implementation

The criterion for total failure of the material is when the strain energy density within an element exceeds g. After this point, it will no longer transmit loading. g is intrinsically linked to the critical energy release rate, G, the energy required to create a unit area of fracture surface, which can be measured experimentally. G and g are related by a characteristic length. Different fracture modes will exhibit different energy release rates. Each fracture mode will also have a corresponding characteristic length, l_{mode}, as the fracture surface formed will have different orientations. Through the characteristic length, g is scaled so that different mesh densities, as demonstrated in Figure 3.3, return the same total energy absorption at fracture.
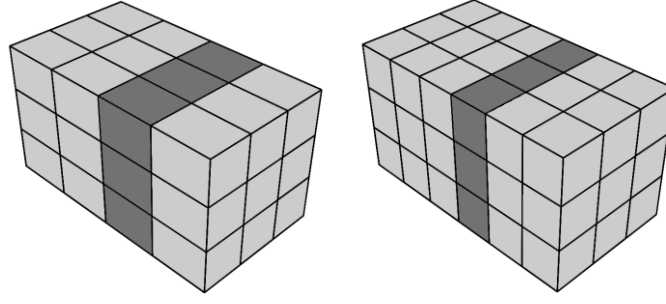
Figure 3.3: Two different meshes that represent the same failure case but with different failed volume.

Oliver [76] showed that by estimating the crack size within the element, a proper characteristic length (l_{mode}) can be deduced to scale the experimentally determined critical energy release rate (G_{mode}^{dir}) to the critical volumetric strain energy (g_{mode}^{dir}) for a given mode and direction:

$$g_{mode}^{dir} = \frac{G_{mode}^{dir}}{l_{mode}} \tag{3.15}$$

Oliver's analysis was performed on a 2D grid. The effective crack length was calculated according to how the crack partitions the element. From this, the characteristic length was calculated via a ratio between the area of the element and the effective crack length. This method was shown to be consistent with theoretical predictions for simple test cases. Generalising this concept to 3D yields:

$$l_{mode} = \frac{V}{A} \tag{3.16}$$

The elemental volume (V) can be obtained from the FE simulation. In calculating the crack area for an arbitrarily oriented crack surface (A), the orientation of the material coordinate system with respect to the element and the rotation of the fracture plane must be taken into consideration.

The fracture surface is defined by a unit normal vector $(\hat{n})$ in an arbitrary hexahedral element (Figure 3.4). This normal vector contains information about the material coordinate system as well as the fracture plane rotation.
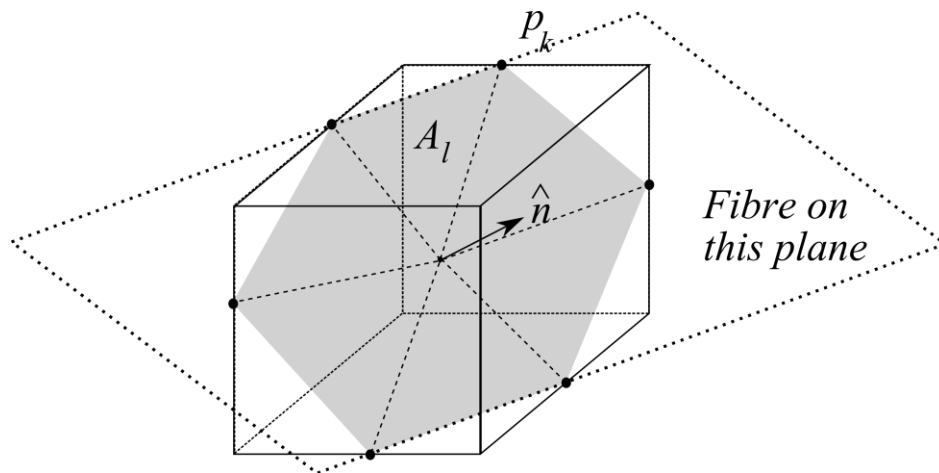
Figure 3.4: Definition of unit normal vector ($\hat{n}$) and points of edge intersection (p_k) for an arbitrary fracture plane (shaded) within a hexahedral element.

The algorithm determines the points (p_k) where the fracture plane intersects with the elemental boundary formed by connecting adjacent nodes. The triangular areas (A_l) enclosed by adjacent intersection points (p_k) and the centre are then determined. Summing these, the total fracture plane area is approximated. This calculation is completed for each element in the model.

This procedure requires material coordinate system information as well as initial nodal coordinates of the elements which are not provided by the VUMAT input/output interface. This is resolved by reading the input file itself in the pre-processing stage to extract this information. All elements in the model are assigned internal element numbers during the simulation process. An internal Abaqus utility routine (vgetinternal) was used to match the element data obtained from the input file to the correct element.

One of the major advantages of this method is that it is able to operate for models where the global, elemental and the material coordinate systems do not align, allowing greater freedom in how the structure is meshed. Additional flexibility comes from allowing each element to have an independent material coordinate system so that curved structures can be handled more accurately. It also enables the use of elements with a range of aspect ratios without significantly affecting accuracy.

Eight node linear reduced integration solid elements, with one integration point at the centroid, are used in Abaqus/Explicit. The use of reduced integration necessitates multiple elements in the through thickness direction to accurately represent bending. The fracture plane is assumed to pass through the centroid of each failed element. With further mesh refinement, an arbitrary macro-scale crack can be represented by a connected series of failed elements. It is also assumed that the element does not become concave. This is appropriate because built into the FE package [6] is a mechanism to prevent elements from becoming inverted.

3.4.2   Fibre-dominated damage

Fibre-dominated damage represents the damage which affects the longitudinal behaviour of a unidirectional prepreg (Figure 3.5).
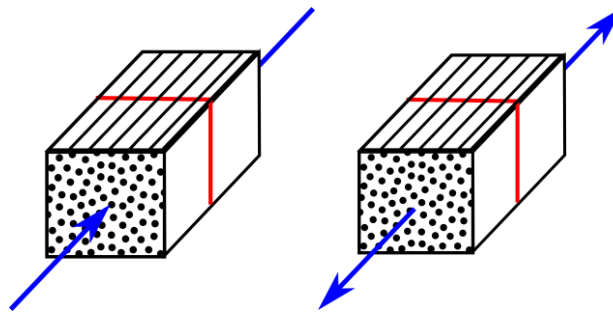
Figure 3.5: Fibre-dominated fracture with associated fracture plane.

In tension, this manifests as the breakage and pull out of fibres from the surrounding matrix. On the other hand, compressive damage causes the fibres to buckle and break in the formation of kink bands. The tensile and compressive characteristics are considerably different. Hence a separate damage parameter is defined for each mode. To determine the softening of the longitudinal modulus due to damage, the effects of tensile and compressive damage are combined. This approach is similar to that employed by other authors [12, 64, 116, 117].

3.4.2.1 Longitudinal elastic response

The VUMAT receives strains as input from the Abaqus code for each increment. This is used to calculate the elastic stress vector ($\{\bar{\sigma}\}$). This elastic stress (Eq. (3.17)) is determined by Hooke's law and represents the elastic response of the material before the application of the softening effect of damage.

$$\{\bar{\sigma}\} = [C]\{\varepsilon\} \tag{3.17}$$

where $[C]$ is the stiffness matrix of the orthotropic laminate, which is determined by the elastic properties in the fibre (11), transverse (22) and thickness (33) directions.

$$[C] = \begin{bmatrix} \dfrac{1-\nu_{23}\nu_{32}}{E_{22}E_{33}\,\Delta} & \dfrac{\nu_{21}-\nu_{23}\nu_{31}}{E_{22}E_{33}\,\Delta} & \dfrac{\nu_{31}-\nu_{21}\nu_{32}}{E_{22}E_{33}\,\Delta} & 0 & 0 & 0 \\ \dfrac{\nu_{21}-\nu_{23}\nu_{31}}{E_{22}E_{33}\,\Delta} & \dfrac{1-\nu_{13}\nu_{31}}{E_{11}E_{33}\,\Delta} & \dfrac{\nu_{32}-\nu_{12}\nu_{31}}{E_{11}E_{33}\,\Delta} & 0 & 0 & 0 \\ \dfrac{\nu_{31}-\nu_{21}\nu_{32}}{E_{22}E_{33}\,\Delta} & \dfrac{\nu_{32}-\nu_{12}\nu_{31}}{E_{11}E_{33}\,\Delta} & \dfrac{1-\nu_{12}\nu_{21}}{E_{11}E_{22}\,\Delta} & 0 & 0 & 0 \\ 0 & 0 & 0 & 2G_{12} & 0 & 0 \\ 0 & 0 & 0 & 0 & 2G_{23} & 0 \\ 0 & 0 & 0 & 0 & 0 & 2G_{13} \end{bmatrix} \tag{3.18}$$

$$\text{Where } \Delta = \frac{1-\nu_{12}\nu_{21}-\nu_{23}\nu_{32}-\nu_{13}\nu_{31}-2\nu_{21}\nu_{32}\nu_{13}}{E_{11}E_{22}E_{33}}$$

In order for the stiffness matrix, $[C]$, to remain positive-definite as damage progresses, the relationship in Eq. (3.19) must be maintained as the elastic moduli degrades due to damage. Consequently, the Poisson's ratios are also degraded concurrently.

$$\frac{\nu_{ij,\mathrm{d}}}{E_{ii,\mathrm{d}}} = \frac{\nu_{ij}(1-d_{ii})}{E_{ii}(1-d_{ii})} = \frac{\nu_{ji}(1-d_{jj})}{E_{jj}(1-d_{jj})} = \frac{\nu_{ji,\mathrm{d}}}{E_{jj,\mathrm{d}}} \tag{3.19}$$

This approach is consistent with the experimentally observed Poisson's ratio degradation that accompanies the progression of damage in composite materials [118].

3.4.2.2 Longitudinal damage initiation

The IDM treats the material as elastic until the initiation of damage. The point of damage initiation for the fibre-dominated mode is found by comparing the strain to the damage initiation strain (ε_{11}^{OT} and

ε_{11}^{OC} for tension and compression respectively). An initiation function (F_{11}^T and F_{11}^C for tension and compression respectively) is defined for both tensile and compressive loading as follows:

$$F_{fib}^{T/C} = \left(\frac{\varepsilon_{11}}{\varepsilon_{11}^{OT/OC}}\right)^2 \tag{3.20}$$

where the initiation strains are determined from the longitudinal elastic modulus (E_{11}) and strengths in tension and compression (X^T and X^C respectively).

$$\varepsilon_{11}^{OT/OC} = \frac{X^{T/C}}{E_{11}} \tag{3.21}$$

When the initiation function for any damage mode reaches unity, the initiation criterion is met and the damage begins to propagate.

3.4.2.3 Longitudinal damage progression

A bilinear response is assumed for both tensile (Figure 3.6) and compressive loading in the fibre direction. This was adopted due to the brittle nature of the material. A positive linear relationship describes the stress-strain behaviour prior to damage initiation. After damage initiation, the tangent modulus becomes negative due to the degradation of the elastic modulus by the damage parameter (d_{fib}) according to Eq. (3.13).
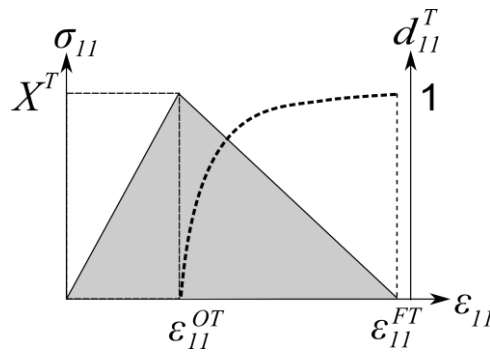
Figure 3.6: Bilinear stress-strain law (shaded area is the critical volumetric strain energy release rate g_{fib}^T) and associated damage parameter growth (bold dashed line).

The tensile fibre-dominated damage parameter (d_{11}^T) is found by comparing the current strain (ε_{11}) with the failure strain (ε_{11}^{FT}):

$$d_{11}^T(\varepsilon_{11}) = \frac{\varepsilon_{11}^{FT}}{\varepsilon_{11}^{FT} - \varepsilon_{11}^{OT}}\left(1 - \frac{\varepsilon_{11}^{OT}}{\varepsilon_{11}}\right) \tag{3.22}$$

The tensile failure strain (ε_{11}^{FT}) is formed by combining Eqs. (3.14) and Eq. (3.15), and is a function of the fibre-dominated tensile critical energy release rate (G_{fib}^T) and the corresponding characteristic length (l_{fib}).

$$\varepsilon_{11}^{FT} = \frac{2G_{fib}^T}{X^T \, l_{fib}} = \frac{2g_{fib}^T}{X^T} \tag{3.23}$$

The fibre tensile critical energy release rate (G_{fib}^T) is found experimentally, representing the energy consumed in creating an area of crack under uniaxial tensile loading in the longitudinal direction. Scaling G_{fib}^T with the characteristic length yields the corresponding critical volumetric energy density, g_{fib}^T, which represents the area under the constitutive relationship, at which point fracture should occur.

The same approach is applied for compressive loading, which leads to:

$$d_{11}^C(\varepsilon_{11}) = \frac{\varepsilon_{11}^{FC}}{\varepsilon_{11}^{FC} - \varepsilon_{11}^{OC}}\left(1 - \frac{\varepsilon_{11}^{OC}}{\varepsilon_{11}}\right) \tag{3.24}$$

$$\varepsilon_{11}^{FC} = \frac{2G_{fib}^C}{X^C \, l_{fib}} = \frac{2g_{fib}^C}{X^C} \tag{3.25}$$

Before initiation of damage, unloading and load reversal occur elastically for both tensile and compressive loading. After damage initiation, the damage caused by tensile and compressive loading interacts when the unloading and load reversal is introduced. It is assumed that the growth of damage in the tensile mode does not significantly affect the response in compression when the loading is reversed. Even though fibre breakage has occurred, it is assumed that the surrounding matrix material is still able to support the fibre when it experiences compressive loading, so the compressive modulus is maintained. The result is illustrated in Figure 3.7.
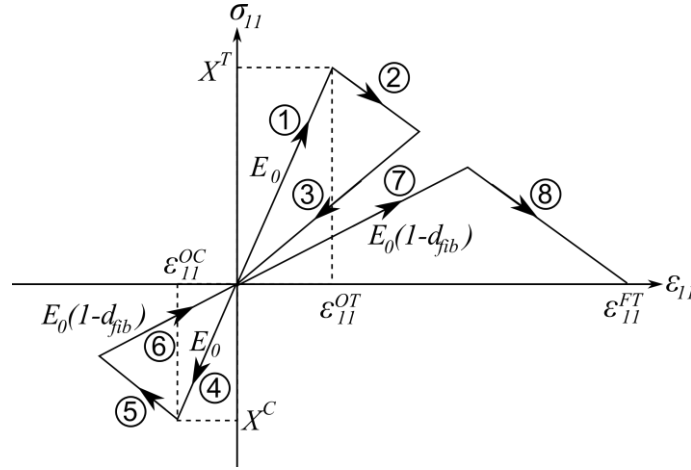
Figure 3.7: Stress-strain response during fibre direction loading/unloading: paths 1-2, tensile loading; 3, unloading; 4-5, loading in compression; 6-8, compressive unloading and tensile reloading until failure.

Unloading along paths 3 and reversing the load such that the material is now in compression will result in an initial elastic stiffness response represented by path 4. However, the reverse is not true. In compressive loading induced damage, fibre breakage occurs under kink band formation. Hence, the stiffness is reduced when the material is subsequently loaded in tension. Therefore, the growth in the compressive damage parameter will also cause the tensile damage parameter to grow and the stiffness to soften (paths 6 to 7).

To achieve the interaction shown in Figure 3.7, the modulus is reduced according to the longitudinal damage parameter defined as:

$$d_{fib} = \begin{cases} d_{11}^C & \varepsilon_{11} < 0 \\ d_{11}^T & \varepsilon_{11} \geq 0 \ and \ d_{11}^T > d_{11}^C \\ d_{11}^C & \varepsilon_{11} \geq 0 \ and \ d_{11}^T < d_{11}^C \end{cases} \tag{3.26}$$

Applying the damage parameter in Eq. (3.26) to the longitudinal component of Eq. (3.17), the damaged stress in the longitudinal direction can be determined by:

$$\sigma_{11} = \left(1 - d_{fib}\right)\bar{\sigma}_{11} \tag{3.27}$$

3.4.2.4 Mesh size limit for numerical stability

A necessary condition for the bilinear law to be physically sound is that the failure strain must be greater than the initiation strain. As a result, the characteristic length must satisfy

$$l_{fib} \leq \frac{2G_{fib}^{dir}}{X^{dir}\varepsilon_{fib}^{0,dir}} \qquad for \ dir = T \ and \ C \qquad (3.28)$$

for all elements in the mesh in order for the generated response to be valid. This criterion imposes an upper limit on the characteristic length, hence restricting the maximum coarseness of the mesh that is used to represent the composite ply.

3.4.3 Matrix-dominated damage

Matrix-dominated damage represents the damage sustained that affects the transverse behaviour (Figure 3.8).
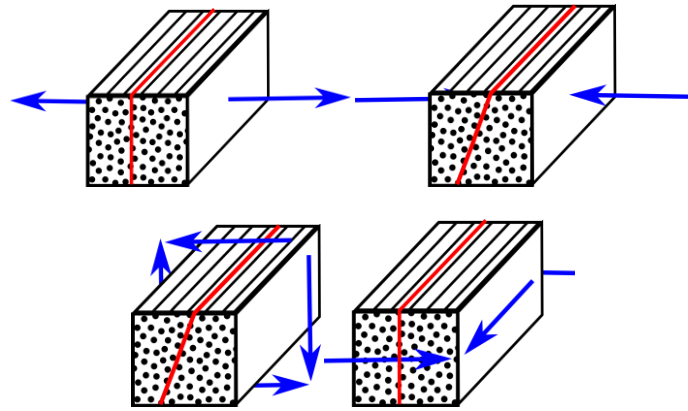
Figure 3.8: Matrix-dominated fracture with associated fracture plane.

In uniaxial tension, the fracture plane forms perpendicular to the principal loading direction. However, for compressive and shear loading, the fracture occurs via shear cracking along a rotated fracture plane. Puck and Schürmann [11] developed a set of damage initiation criteria that is based on this fracture plane, as defined by a rotation of θ about an axis parallel to the fibre direction shown in Figure 3.9.

66
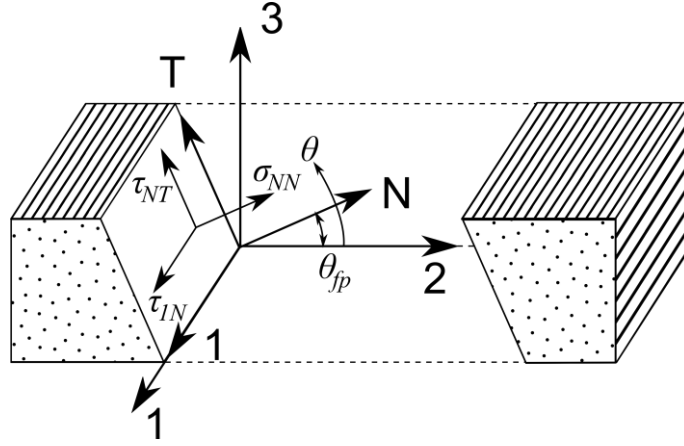
Figure 3.9: Coordinate system attached to the fracture plane (1,N,T) [11] relative to the material coordinate

system (1,2,3).

$$[T(\theta)] = \begin{bmatrix} 1 & 0 & 0 \\ 0 & cos(\theta) & sin(\theta) \\ 0 & -sin(\theta) & cos(\theta) \end{bmatrix} \tag{3.29}$$

$$\{\sigma_{FPCS}\} = \left[T(\theta_{fp})\right]\{\sigma_{MCS}\}\left[T(\theta_{fp})\right]^T \tag{3.30}$$

$$\{\varepsilon_{FPCS}\} = \left[T(\theta_{fp})\right]\{\varepsilon_{MCS}\}\left[T(\theta_{fp})\right]^T \tag{3.31}$$

The transformation matrix outlined in Eq. (3.29) is used to convert between the fracture plane

coordinate system (FPCS) and the material coordinate system (MCS), which is applied to both stress

and strain in tensor form (Eqs. (3.30) and (3.31)).

3.4.3.1 Transverse undamaged response

Experimental data shows the response of the composite under shear loading is nonlinear. Hence, a

cubic function (Eq. (3.32)) was used to describe the nonlinear behaviour of composites under shear

loading when damage has not yet initiated ($d_{mat} = 0$). The overall strain is divided between its

elastic and inelastic components (Eq. (3.33)).

$$\tau(\gamma_{ij}) = c_1\gamma_{ij}{}^3 - sgn(\gamma_{ij})c_2\gamma_{ij}{}^2 + c_3\gamma_{ij} \tag{3.32}$$

$$\gamma_{ij} = \gamma_{ij,el} + \gamma_{ij,in} \qquad i \neq j \tag{3.33}$$

With the inclusion of inelastic strain in the shear response, an isotropic hardening rule was used to

determine the undamaged response which is illustrated via the example in Figure 3.10, showing the

steps involved in determining the final load state. An initial stress state (γ^t, τ^t) is reached after partial

unloading along the shear modulus (G_{ij}). The stress state after subsequent reloading to $\gamma^{t+\Delta t}$ depends

on whether plastic yielding occurs. Initially, the stress is assumed to increase elastically to $\tau_E^{t+\Delta t}$.

Yielding occurs when $\tau_E^{t+\Delta t} > \tau(\gamma^t)$, which results in the increased inelastic strain of $\gamma_{in}^{t+\Delta t}$ and

reduced stress of $\tau^{t+\Delta t}$.
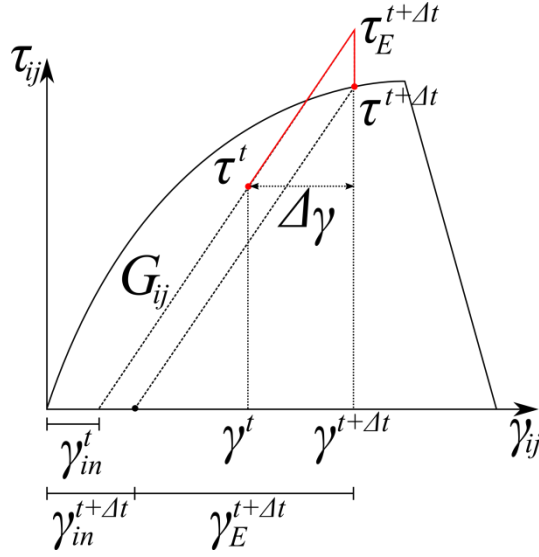
Figure 3.10: Calculating shear stress from shear strain using the elastic predictor method progressing from old

stress state τ_0 to τ in the present increment.

Alternatively, if $\tau_E^{t+\Delta t} < \tau(\gamma^t)$, yielding has not occurred so the inelastic strain remains constant and

$\tau_E^{t+\Delta t}$ is retained as the final stress state. The result is analogous to a "yield strength", initially zero,

which increases as the inelastic strain increase. Unloading and load reversal up to the "yield strength"

occur elastically and are characteristic of the isotopic hardening approach. An idealised cyclic loading

response with increasing amplitude and alternating sign is shown in Figure 3.11. This approach is

consistent with the inelasticity in the shear response experimentally observed by Donadon et al [64].
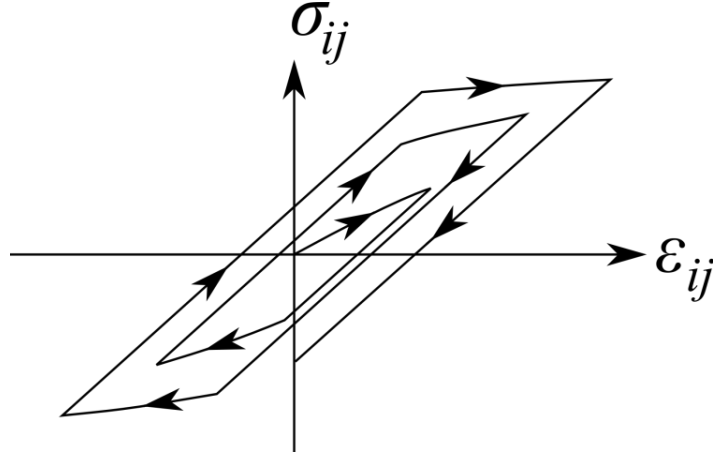
Figure 3.11: Cyclic loading under isotropic hardening, showing the increase in elastic unload/reload

range as "yield strength" increases.

Isotropic hardening only applies while the loading remains below the threshold of matrix damage

initiation. Once matrix damage initiates, unloading occurs along the damage shear modulus, similar to

the approach adopted in fibre-dominate damage.

3.4.3.2 Transverse damage initiation

Puck and Schürmann [11] noted that the brittle nature of failure in the matrix material would be better

captured using a Mohr circle based approach. They proposed that failure in the matrix phase is caused

by stresses on a fracture plane (the 1T plane in Figure 3.9), whose orientation is dependent on the

combination of loading on different axes, resulting in the matrix-dominated damage initiation

functions in Eqs. (3.34) and (3.35).

$$F_{mat}^{T} = \left(\frac{\sigma_{NN}}{Y^{T}}\right)^2 + \left(\frac{\tau_{NT}}{S_{23}^{A}}\right)^2 + \left(\frac{\tau_{1N}}{S_{12}}\right)^2 \quad \text{for } \sigma_{NN} > 0 \tag{3.34}$$

$$F_{mat}^{C} = \left(\frac{\tau_{NT}}{S_{23}^{A} - \mu_{NT}\sigma_{NN}}\right)^2 + \left(\frac{\tau_{1N}}{S_{12} - \mu_{1N}\sigma_{NN}}\right)^2 \quad \text{for } \sigma_{NN} \leq 0 \tag{3.35}$$

The damage initiation functions compare the loading against the resistance on the fracture plane

comprising of tensile and compressive transverse strengths (Y^{T} and Y^{C}), longitudinal and transverse

shear (S_{12} and S_{23}^{A}), friction coefficients (μ_{NT} and μ_{1N}) and the normal stress on the fracture plane

(σ_{NN}). However, the fracture plane angle (θ_{fp}) is not initially known for a general loading state. The

stresses ($\sigma_{NN}, \tau_{NT}, \tau_{1N}$) in the initiation functions (Eq. (3.34) and (3.35)) are a function of inclination

angle of the fracture plane (θ). The initiation functions must first be maximised with respect to θ.

Damage initiation occurs when the maximised initiation functions have a value greater than unity.

Once the angle is determined, it will not change for this element for the remainder of the simulation as

shear micro-cracking has occurred and any further fracture will preferentially occur on this plane.

Brent's algorithm [119] was used to efficiently determine the orientation of the fracture plane.

When $\sigma_{NN} > 0$, the damage initiation profile is defined by a semi-ellipse that intersects the stress axes

at the transverse tensile and shear strengths. When $\sigma_{NN} < 0$, the profile is defined by a line passing

through point A and the shear strength, where point A is derived from the observed fracture plane

angle (θ_f) of 53° for uniaxial transverse compression [11]. The damage initiation profile is

represented by the dashed curve in Figure 3.12.
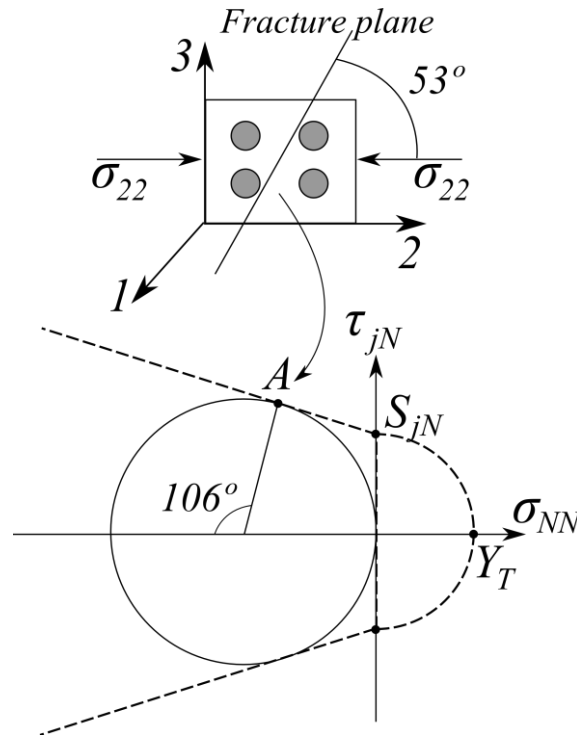
Figure 3.12: Defining the damage initiation profile (dashed line) via the material properties on the FPCS, where

j = 1, T, and inset represents the stress state at point A.

The transverse shear strength (S_{23}^A) is defined in terms of the transverse compressive strength [120], i.e.:

$$S_{23}^A = \frac{Y^C}{2\tan(\theta_f)} \tag{3.36}$$

The slope of the linear section of the damage initiation profile in Figure 3.12 can be interpreted as a friction coefficient that aids in resisting shear loading [120]:

$$\mu_{NT} = -\frac{1}{\tan(2\theta_f)} \tag{3.37}$$

The same analysis is repeated for the thickness direction response via:

$$\mu_{1N} = \frac{S_{12}}{S_{23}^A}\mu_{NT} \tag{3.38}$$

Combining both the transverse and thickness direction profiles using a quadratic relationship gives an overall damage initiation surface for matrix damage shown in Figure 3.13.
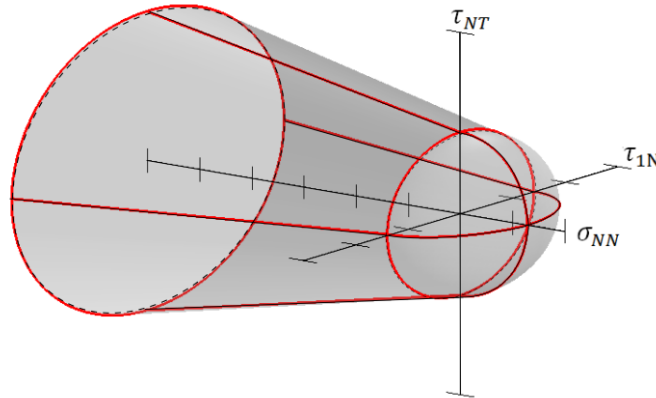
Figure 3.13: The surface of damage initiation in the stress space defined by the FPCS.

3.4.3.3 Transverse damage progression

The matrix damage parameter, d_{mat}, which controls the stiffness reduction due to matrix-dominated damage, is a function of both normal and shear stresses on the fracture plane. This is due to Puck and Schurmann's treatment of transverse damage, where these stresses on the fracture plane jointly

contribute to matrix cracking in a unidirectional ply [11]. Hence a resultant shear strain (γ_r) is defined

on the fracture plane [12] as the vector sum of the two planar shear components shown in Figure 3.9:

$$\gamma_r = \sqrt{\gamma_{NT}^2 + \gamma_{1N}^2} \tag{3.39}$$

The resultant failure strain, γ_r^{max}, is subsequently determined using the mixed mode critical energy

release rate, G_{mat}, and the total strain energy before damage initiation, A,

$$\gamma_r^{max} = \frac{2}{\sigma_r^O}\left(\frac{G_{mat}}{l_{mat}} - A\right) + \gamma_r^O \tag{3.40}$$

where σ_r^O and γ_r^O are the resultant damage initiation stress and strain respectively. The volumetric

strain energies associated with each stress component on the fracture plane, are combined using a

quadratic relationship,

$$A = A_{NN}\left(\frac{\langle \sigma_{NN} \rangle}{\sigma_r}\right)^2 + A_{1N}\left(\frac{\tau_{1N}}{\sigma_r}\right)^2 + A_{NT}\left(\frac{\tau_{NT}}{\sigma_r}\right)^2 \tag{3.41}$$

where the resultant shear stress (σ_r) is defined as the magnitude of the stresses on the fracture plane:

$$\sigma_r = \sqrt{\langle \sigma_{NN} \rangle^2 + \sigma_{1N}^2 + \sigma_{NT}^2} \tag{3.42}$$

The volumetric strain energy associated with each stress component, A_{ij}, is given by the integral in

Eq. (3.43).

$$A_{ij} = \int_{d_{mat}=0} \sigma_{ij}\, d\varepsilon_{ij} \quad, \quad where\ ij = NN, 1N, NT \tag{3.43}$$

The total strain energy release rate, G_{mat}, is given by:

$$G_{mat} = G_{mat}^C\left(\frac{\langle \sigma_{NN} \rangle}{\sigma_r}\right)^2 + G_{mat}^{12}\left(\frac{\sigma_{LN}}{\sigma_r}\right)^2 + G_{mat}^{23}\left(\frac{\sigma_{NT}}{\sigma_r}\right)^2 \tag{3.44}$$

and the matrix-dominated damage parameter, d_{mat}, is therefore:

$$d_{mat} = \frac{\gamma_r^{max}}{\gamma_r^{maz} - \gamma_r^O}\left(1 - \frac{\gamma_r^O}{\gamma_r}\right) \tag{3.45}$$

The shear stresses on the fracture plane are subsequently modified by the matrix-dominated damage parameter (d_{mat}) to create a softening effect:

$$\sigma_{LN} = (1 - d_{mat})\bar{\sigma}_{LN} \tag{3.46}$$

$$\sigma_{NT} = (1 - d_{mat})\bar{\sigma}_{NT} \tag{3.47}$$

$$\sigma_{NN} = \bar{\sigma}_{NN} - d_{mat} \langle \bar{\sigma}_{NN} \rangle \tag{3.48}$$

These stresses are transformed back to the material coordinate system to form the complete stress tensor of the damaged element. Once damage has initiated, unloading and reloading occurs along the damaged modulus from the fixed inelastic strain value as shown in path 3 in Figure 3.14.
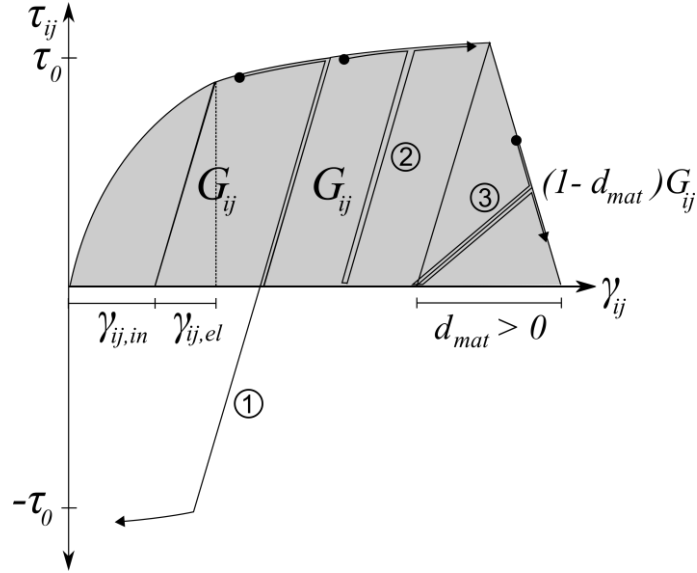
Figure 3.14: Shear stress-strain response with damage showing load reversal (1) and reloading (2) with kinematic hardening in the undamaged regime and reloading (3) in the damaged regime.

3.4.4 Deletion of elements with non-physical distortion

Element deletion was employed in this model due to the softening nature of the constitutive relationships. As damage progresses in the element, the stiffness of that element decreases. In the extreme case, when the damage parameter is unity, the element will not resist motion in the associated direction as there will be zero generated stress. Physically this represents an element that has completely failed. Consequently, it would be possible for infinite and/or unphysical distortions to

occur. This raises the possibility of causing the element to become concave and would cause the simulation to abort once detected.

Element deletion was employed to remove elements based on: (i) the damage parameter, or (ii) the determinant of the deformation gradient, $\det(F)$.

$$delete\ element\ when\ either \begin{cases} (i) & d_{11} > 0.99 \\ (ii) & 0.8 > \det(F)\ or\ \det(F) > 1.6 \end{cases} \tag{3.49}$$

Condition (i) in Eq. (3.49) represents the fibre-dominated failure mode. As the composite is strongest in the fibre direction, total failure can be assumed to occur when the fibres have failed. The maximum allowable damage was set to 0.99 to prevent the existence of elements with extremely low stiffness. On the other hand, condition (ii) is a measure of the change in volume of the element under deformation. Some change in volume is permitted in the material as the Poisson's ratios for composite materials are typically not 0.5. However, large volume changes are not permitted. This would be indicative of an element that has lost most of its stiffness and hence should be deleted. The parameters are chosen empirically aiming for a balance in allowing large deformations in the material to properly represent crush damage and avoiding abortion of the simulation due to numerical difficulties. Subsequent verification via compact tension/compression showed that the chosen values returns the correct energy dissipation.

3.5 Model assumptions and limitations

The proposed model assumed a homogenised composite ply (macro-mechanics approach). A macro-mechanics model, as opposed to a micro-mechanics model, is more suitable for use in structural modelling because the analysed structures are typically many orders of magnitude larger than the individual fibre and matrix constituents. Micro-cracking is assumed to be evenly smeared over the volume of the element. The lack of discontinuities within the element allows the application of conventional FE analysis rather than necessitating more exotic methods such as the extended finite element method [121]. Furthermore, the homogeneous nature does not differentiate between

unidirectional ply and woven fabric so the model can be used to represent both types of composite plies.

It is assumed that any damage that occurs is irreversible so the model is consistent with thermodynamic principles. Hence the damage parameters are constrained to be monotonically increasing for the entire model. This physically manifest in the behaviour of cracks. When a crack is created, subsequent loading that closes the crack will not cause the crack to disappear; only temporarily close.

Even though cyclic and repeated loading is included in the analysis, high cycle fatigue is ignored as this model is targeted towards application in the modelling of crushing structures. This is consistent with the intended applications of composite crush structure performance. Crush structures are designed to absorb energy sacrificially, after which, they would need to be discarded or replaced.

This model has been developed for use with linear hexahedral elements with reduced integration (Abaqus designation C3D8R). These elements offer a good combination of adequate accuracy with reduced computational demands by using a single integration point. It is important to note that in cases where there is significant bending, there are some drawbacks associated with the use of these elements. This is due to the integration point being at the centroid of the element, which, in pure bending of a single element thick ply, would lie on the neutral axis and form zero-energy modes. Results from the cantilever sensitivity study showed the best balance between accuracy and performance was be achieved by using 3 elements in the ply through thickness direction.

The IDM deals exclusively with intralaminar behaviour of the composite ply. Inter-ply behaviour is not considered by the current model. Behaviour such as delamination and friction must be captured separately. This is achieved using Abaqus' inbuilt cohesive surface and surface contact models.

3.6   Implementing the IDM into VUMAT

This section deals with the coding considerations when implementing the IDM into a VUMAT subroutine for use within Abaqus. The VUMAT subroutine is a feature built into Abaqus to allow for custom material response [6]. The VUMAT replaces internal Abaqus routines that calculate material response. The Abaqus solution process takes the nodal motion and calculates the incremental strains. This is passed into the VUMAT so the stress can be calculated. This output stress is then translated into nodal forces which drives nodal motion in the next increment. This process is summarised in Figure 3.15.
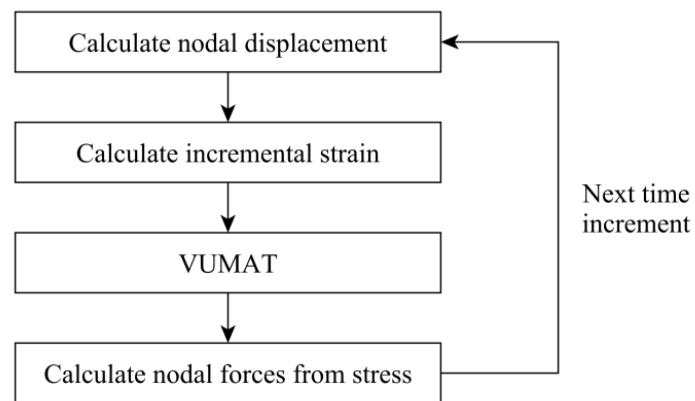
Figure 3.15: VUMAT within the Abaqus solution process.

3.6.1   Interfacing with Abaqus/Explicit

An interface allows the exchange of information between the main Abaqus routine and VUMAT. The variables passing through the interface is predefined explicitly to ensure VUMAT's compatibility with the rest of Abaqus. All input and outputs must pass through this interface as defined in the documentation [6]. The VUMAT takes the following variables as input:

- Current simulation time,
- Current step time,
- Current time increment,
- List of material properties,

- List of elements to be processed and their:

    - Current midpoint coordinate,

    - Current characteristic length,

    - Current density,

    - Current incremental strain,

    - Deformation gradient in the past increment,

    - Stress state in the past increment,

    - State variables in the past increment.

The outputs of the VUMAT, which are the current stress state and state variables, are calculated from these inputs for each element.

3.6.2 Obtaining nodal coordinates for characteristic length calculations

Calculating the characteristic length requires the initial nodal coordinates which are not included in the VUMAT interface. The nodal coordinates can be extracted from the input files. The element numbers that identify a particular element in the input file are, in general, not the same as the global element numbers used in the VUMAT subroutine. This is a result of (i) using part labels in the input files and (ii) using division of the mesh into numerous sub-domains. The use of part labels in the input file improves readability. Domain division occurs so that multiple instances of VUMAT can be created to work on these domains simultaneously to achieve reduction in overall computational time. A utility routine, vgetinternal [6], is used to translate the input file element number into the global element number used by VUMAT in processing. The nodal coordinates for each element extracted from the input file during the initialisation process were stored in an array with the respective global element number. During the simulation, an "undocumented" feature is required to extract the global element number from the VUMAT interface [122]. The parameter nblock is actually an array of pointers which is used as though it was a single value to preserve backwards-compatibility. The first pointer points to nblock which is the number of elements processed in this instance of VUMAT. The fifth pointer points to an array which contains the global element numbers for all the elements being

processed in this instance of VUMAT. By separating nblock and using the pointers separately, the global element numbers for all the elements can be found. Knowing the global element number of the element being processed allows the corresponding nodal coordinates to be accessed from the array created during initialisation. These nodal coordinates, in combination with the fracture plane orientation, are then used to calculate the characteristic length.

3.6.3 Modular implementation of code

The source code was brought to FORTRAN 90 standards. This allowed the incorporation of object-oriented programming approaches which improved the ease of development and maintenance of the source code. The source code is composed of distinct objects, each performing a set function on associated data. Data flow between objects is limited to only what is strictly necessary for the object to perform its designated function. In essence, each object is self-contained and can afford many advantages. This improves the readability of the source code as each object will have only one goal and all the code in this object would have been written to achieve this goal. Consequently, debugging and trouble-shooting is also simplified.

A modular approach also improves the ease of development for the source code. Each object can be developed largely in isolation with respect to the other objects. As the objects are self-contained, there is no mechanism for changes to one object to affect another, except when explicitly defined in the interfaces. The requirement to explicitly define interface ensures that the flow of data between objects is transparent to the developer. Changes and extensions can be made efficiently by replacing the affected object with a new one without significant change to the rest of the source code. To reduce the complexity of the interfaces, a module was defined to contain global parameters which are accessible by all objects.

Data is also stored in a modular manner to simplify the input and output interfaces between different objects. "Structures" are used to store related variables so that they can be passed through the interface as a complete package. "Structures" are only allocated storage when incoming data is about

to populate them and then discarded when the data is not required any more. This dynamic allocation process minimises memory requirements of the simulation process.

3.6.4 Optimisation techniques to improve computational efficiency

The VUMAT was developed for Abaqus/Explicit which utilises an explicit integration scheme. The characteristic of such a scheme is the use of the state of the system at the current time to directly calculate the state at a later time. Hence, the equation of motion for each node is in the form of:

$$\dot{u}(t + \Delta t) = F\big(\dot{u}(t), \ddot{u}(t)\big)$$
$$u(t + \Delta t) = G\big(u(t), \dot{u}(t)\big)$$

(3.50)

As a result, an upper limit is placed on the time increment that can be used in the integration. The central difference integration method is conditionally stable given the time increment is:

$$\Delta t \leq \frac{2}{\omega_{max}}$$

(3.51)

where ω_{max} is the highest frequency of the system [6]. As results of the high stiffness in typical composite materials, the maximum allowable time increment is very small. Even with the addition of mass scaling to increase time increment length, a simulation spanning one second of real time would require on the order of 10^6 increments. As the VUMAT is called for every increment, optimising the performance of the VUMAT can mean significant reduction in the total computation resources required.

3.6.4.1 Use of pre-calculated results in loops

Repeatedly required quantities are calculated and then saved for future use. Using this approach, only one calculation is done, rather than every time the value is needed. For example, the matrix damage initiation and progression calculations involve repeated use of trigonometric functions of the fracture plane angle. The use of pre-calculation reduces the calls to trigonometric functions by an order of magnitude.

3.6.4.2 Brent's algorithm

Finding the maxima for Eq. (3.34) and Eq. (3.35) to obtain the fracture plane angle can be computationally expensive. An optimisation based on Brent's algorithm [119] was used for maximising the damage initiation function to obtain the fracture plane angle. This method combines the robustness of a golden section search with the speed of quadratic interpolation by alternating between the two methods.

The efficiency gain is most found away from the maxima, where the quadratic interpolation allows the solution to advance rapidly towards the desired maxima as shown in Figure 3.16 (left). The golden section search provides the robustness that ensure that the solution is found. This approach is superior to a series of function evaluations on possible fracture plane angles [119] when taking into consideration the need to achieve a good accuracy while minimising the runtime required.
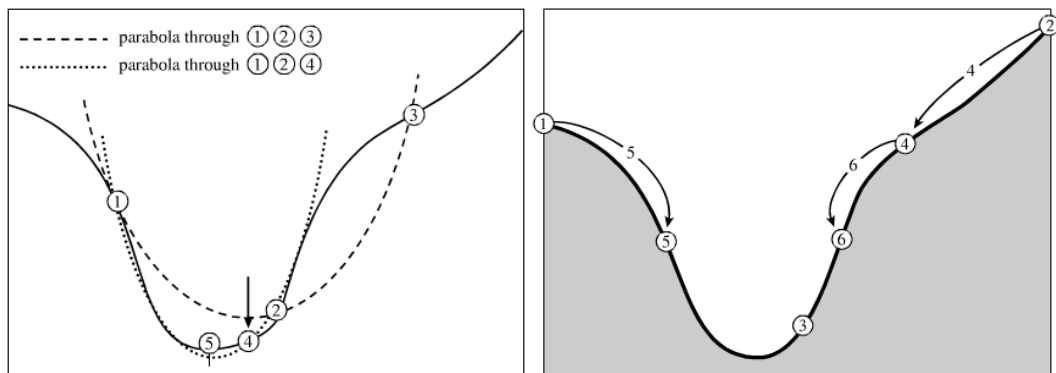
Figure 3.16: Quadratic interpolation (left) and golden section search (right) for extrema search [119].

3.6.4.3 Bounding box estimation

Even with the help of Brent's algorithm, this process is still computationally expensive; hence there is a need to reduce unnecessary evaluations of the damage initiation function. A bounding box was introduced to quickly check whether a particular loading state was well below that needed to achieve damage initiation. This bounding box was created to encompass the set of all possible stress states in the 1NT coordinate system due to rotation of the fracture plane. Figure 3.17 shows the blue curve which represents the possible stresses at different fracture plane angles contained within a blue box in

the 1N-NN, NT-NN and 1N-NT-NN stress spaces respectively. The red curve/surface represents damage initiation curve/surface in the respective stress spaces, which the bounding box is compared against.
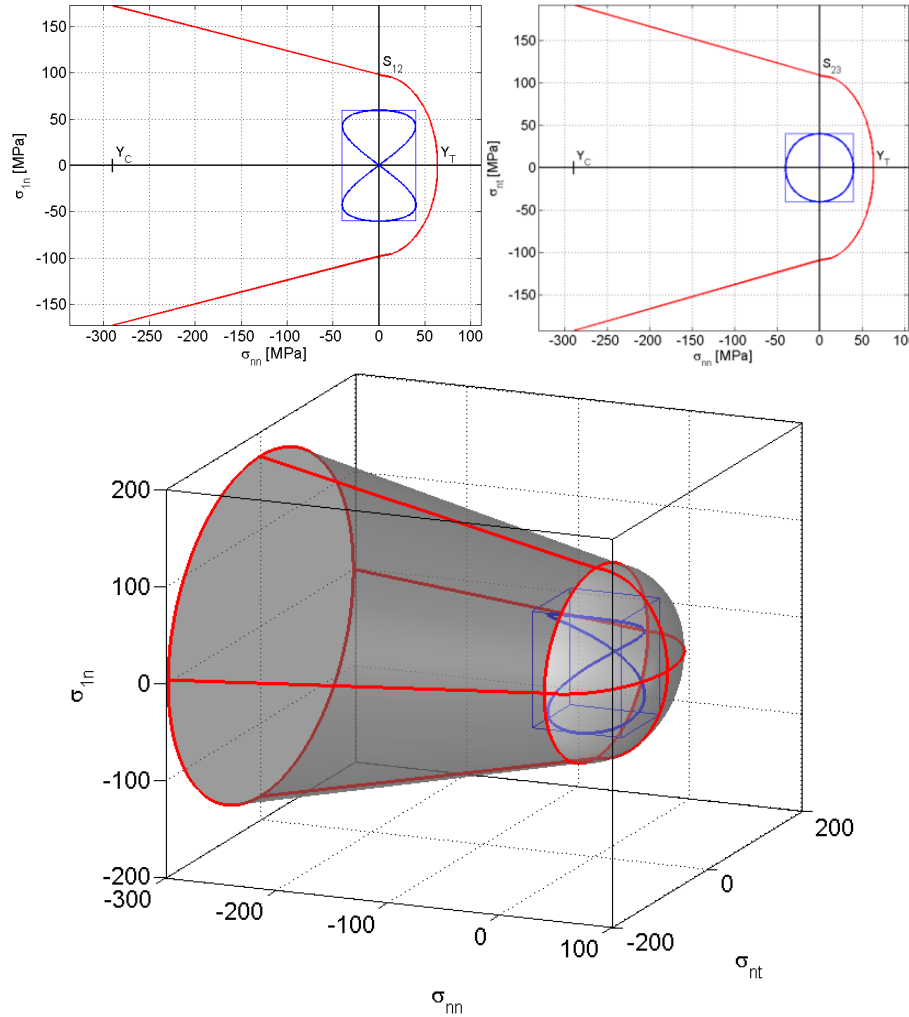
Figure 3.17: Bounding box over the set of stress states possible due to rotation of the fracture plane as shown in the 1N-NN, NT-NN and 1N-NT-NN stress spaces (clockwise from top left).

If the bounding box is entirely within the damage initiation surface (as shown in Figure 3.17), then this stress state cannot initiate damage. Hence, the routine which maximises damage initiation functions to identify the inclination of the fracture plane does not need to be executed. With this arrangement, only the elements nearing damage initiation are assessed. As the crush zone that is

actively causing damage generally represents a small portion of the overall structure, significant saving in computational costs were realised.

3.7 Abaqus models used in conjunction with the IDM

The IDM provides detailed intralaminar response of the composite structure. This is combined with established algorithms to capture the interactions between two different plies or a ply and another object to yield the complete behaviour of composite structures under crushing loads. An energy-based cohesive surfaces algorithm is used to capture delamination of the laminate and a penalty-based general contact algorithm to deal with contact between various surfaces, including ply surfaces created by delamination.

3.7.1 Cohesive surfaces

Cohesive surfaces [6] provide a framework for a general traction-separation relationship to be defined between two surfaces. The surface-based approach is adopted as it is able to represent a negligibly small thickness interface region. Delamination, which has a well-defined traction-separation behaviour (Figure 3.18), is well captured by these surfaces.
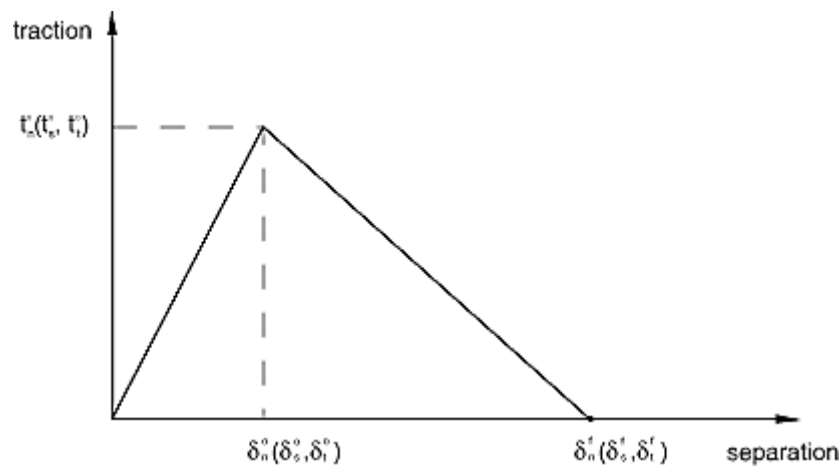
Figure 3.18: Typical traction separation response for delamination.

The tractive stress follows a bilinear response. A damaging constitutive model is adopted. Damage initiation is controlled by the interlaminar strengths in the normal (N) and shear (S, T) directions respectively. Damage initiates when the initiation function (Eq. (3.52)) reaches unity.

$$F_{interlaminar} = \left(\frac{\langle t_N \rangle}{t_N^o}\right)^2 + \left(\frac{t_S}{t_S^o}\right)^2 + \left(\frac{t_T}{t_T^o}\right)^2 \tag{3.52}$$

After initiation, a scalar damage variable (D) is used to represent the overall damage in the interface. Similar to intralaminar damage parameters, it grows from zero to unity and acts to reduce the transmissible loading. This parameter is also monotonically increasing and does not recover after crack closure.

$$t_N = \begin{cases} (1-D)\bar{t}_N & \bar{t}_N > 0 \\ \bar{t}_N & otherwise \end{cases} \tag{3.53}$$

$$t_s = (1-D)\bar{t}_S \tag{3.54}$$

$$t_s = (1-D)\bar{t}_S \tag{3.55}$$

where $\bar{t}_N, \bar{t}_S$ and $\bar{t}_T$ are the contact traction components predicted by the elastic traction-separation behaviour for the current separations without damage. The point of complete delamination is determined by a quadratic interaction of the ratio of current strain energy in the interface and the critical fracture energy for the normal and shear directions:

$$\left(\frac{G_N}{G_N^C}\right)^2 + \left(\frac{G_S}{G_S^C}\right)^2 + \left(\frac{G_T}{G_T^C}\right)^2 = 1 \tag{3.56}$$

Cohesive surfaces are defined between adjacent piles. Once delamination has occurred, the plies fall back as per contact behaviour detailed in section 3.7.2, in which the two surfaces are treated as two free surfaces in contact.

3.7.2 Contact behaviour between surfaces

Contact behaviour broadly falls under two categories: normal and tangential behaviour. Both must be defined for each contacting surface pair.

The "hard" contact condition (Figure 3.19) is used to characterise normal direction behaviour between contacting surfaces. The aim is to prevent that the contacting surfaces from penetrating each other.
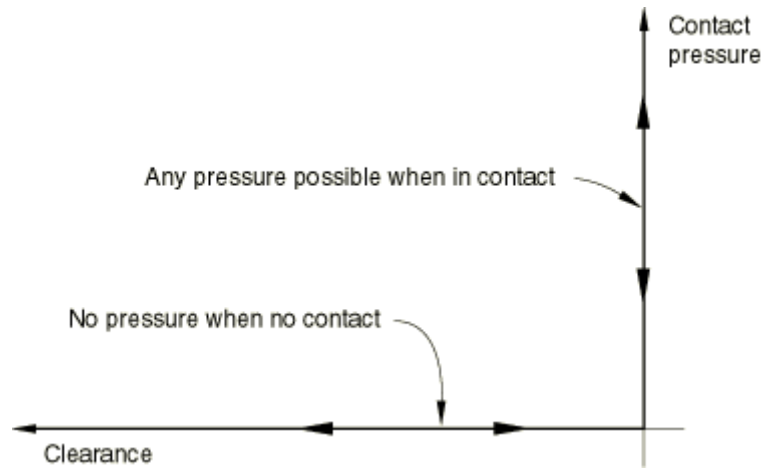
Figure 3.19: Idealised relationship between penetration distance and contact pressure exerted on the contacting surfaces[6].

This condition is enforced through penalty forces, which are generated through penetration of nodes through the contact surfaces. Using penalty contact [6] allows the kinetic energy to be preserved during an impact event. This is important, as energy absorption is a critical metric in determining crush structure performance. Furthermore, this flexible approach can handle multiple contacts per node and contact involving rigid bodies. This allows contact to be defined between loading surfaces, which are typically modelled as rigid. The algorithm searches for any instances of penetration between the assigned contact surfaces and applies a force to oppose the penetration. A stiffness constant is used to relate the forces generated this way to the penetration distance. This stiffness is automatically generated, balancing the need to have a very high stiffness to minimise penetration and the effect of a very high stiffness on reducing the allowable time increment in the progression of simulation. This stiffness is calculated based on a representative stiffness of the underlying elements. Due to the enforcement method, some penetration is observed. However, this effect is only significant on elements that are close to failure due to their extremely low stiffness. Typically, these elements are subsequently deleted.

Coulomb friction [6] is used to characterise tangential contact behaviour. The coefficient of friction (μ) and the contact pressure is used to determine whether slip occurs (Figure 3.20).
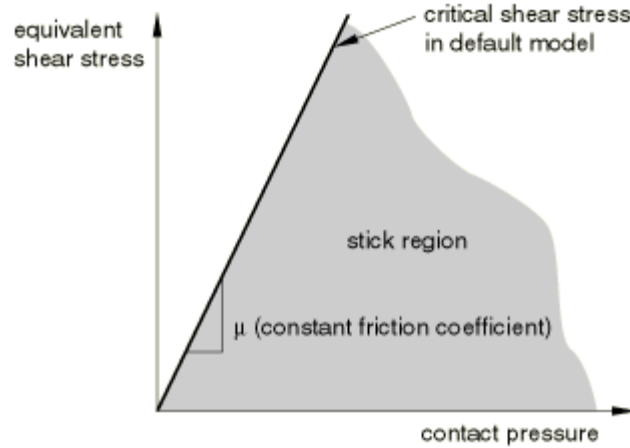
Figure 3.20: Tangential response with friction: determining whether slip occurs[6].

Figure 3.21 shows the shear stress incurred as slipping occurs. Due to the penalty method of contact enforcement, the stiffness (κ) must be finite. The algorithm will ensure that when the surfaces are sticking (i.e., the grey area in Figure 3.20), that the magnitude of the sliding is under sticking friction (within the linearly sloped region in Figure 3.21). Hence once slipping initiates, the proper slipping friction is recovered.
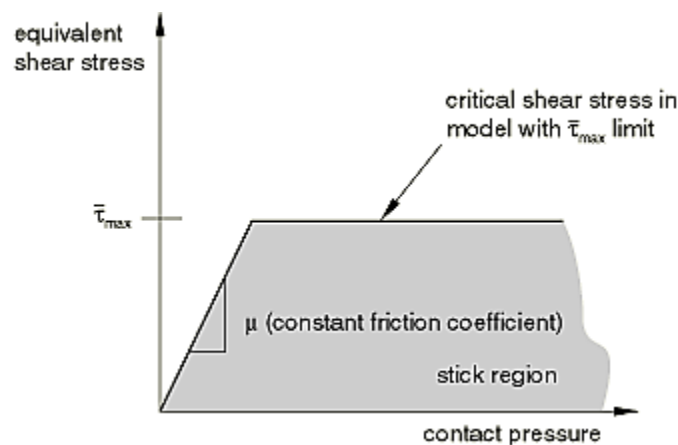
Figure 3.21: Tangential response with friction: shear stress while slipping [6].

3.8 Summary

An intralaminar damage model was developed using a physically based damage modelling approaches. This model combines a range of novel and established techniques to accurately capture the material response under damaging loads. Key features of the model include:

- A 3D formulation for solid elements to account for multi-axial loading

- An energy-based method, based on continuum damage mechanics, to control damage progression, and,

- A unified matrix damage mechanism with load-adjusted critical strain energy release rate along the fracture plane.

Key improvements over existing approaches include:

- A novel, robust method for characteristic length calculations that maintains accuracy for any mesh and damage mode,

- A novel, nonlinear, inelastic shear response more consistent with experimental observations, and,

- A novel, improved physically based mechanism for damage interaction which includes load history effects.

The developed material damage model was combined with established interlaminar and contact models to form a complete modelling package able to predict the crush response of composite structures.

In contrast to the more empirical approaches dominant in commercially available damage models, the developed model provides greater fidelity in the modelling of composite structures due to its physically based nature. Another advantage of the presented approach is its predicative capability as no calibration would be required. All model inputs are physical, such as the geometry of the structure, the orientations of the layup and the material properties of the composite ply.

The implementation of the damage model in Abaqus was outlined in this chapter. The interface between the developed model and Abaqus was summarised in terms of the input and output variables. Modelling the complex damage modes was computationally expensive. The optimisation methods utilised to reduce the computation resources required were also discussed, such as pre-calculation, Brent's algorithm and the bounding box.

Chapter 4
Verification and sensitivity study of the intralaminar damage model

4.1   Introduction

This chapter details the work completed on examining the performance of the proposed intralaminar damage model. There are two main sections. The first section outlines the verification of the model through a variety of test cases. The second section describes the sensitivity studies done and their implications.

The developed intralaminar damage model was examined to ensure the expected performance was achieved. A set of benchmark models was developed to assess key aspects of the intralaminar damage model (IDM). This verification is designed to ensure that the theory has been correctly implemented. These tests check each aspect of the implanted model and ensure that the behaviour is consistent with theoretical expectations.

Furthermore, the sensitivities of the model to different inputs were also probed. A range of different sensitivities was examined, particular attention has been paid to input that either varies throughout the structure or difficult to measure and simulation parameters that affect simulation performance. The implications of these sensitivities (or lack thereof) are discussed.

4.2   Benchmark verification

There are three main categories of benchmark tests developed. The first focuses on the characteristic length, which include whether the IDM correctly process the elements within the model and ascertain that mesh independence has been achieved. The second category is single element performance. There are two parts in this category. The first gauges whether the theory has been adequately implemented in terms of the stress response in each direction of loading. The second checks that the damage interaction is properly captured. In the third category, larger models are used to check for expected macroscopic features. Both the coalescence of microscopic damage into macroscopic cracks and the associated energy absorption are benchmarked. This series of verification ensures that the IDM

performs as expected. To achieve this, aspects of the IDM implementation is verified against theoretical expectations. These include:

1. Characteristic length calculations is accurate;

2. Normal damage response is bilinear;

3. Shear response is cubic, followed by linear degradation;

4. Damage is interactive;

5. Fracture plane is formed properly; and

6. Energy consumption is correct.

Parts 2 to 4 above were verified using single element models while parts 1, 5 and 6 were completed using multi-element models. The details of these will be described in detail in the following sections.

4.2.1 Characteristic length calculations

The IDM is expected to deal with meshes that are composed of multiple parts with different material coordinate systems. A 4-part model was created to check that the characteristic lengths are correctly calculated for all elements belonging to different parts.

This model covers the different cases encountered when calculating the characteristic length. The implemented code must correctly deal with all listed scenarios. These include:

- Material coordinate system (MCS) not aligning with the global or local coordinate system (CS),

- Local CS offset from global CS,

- Local CS rotated with respect to global CS, and

- Local CS offset and rotated with respect to global CS.

The larger elements had unit length sides and the small elements had one side reduced to 1/3. The MCS used in the model are illustrated in Figure 4.1 (left) with the blue line showing the fibre direction and (right) shows the characteristic lengths for fibre-dominated damage. A characteristic

length of unity (red) was recovered on the left and bottom sides as the fibre direction align with one side of the element. The other two sides returned a characteristic length of $\frac{1}{\sqrt{2}}$ (blue) as the fibre direction forms a 45° angle with the element side. Both were consistent with expectation.
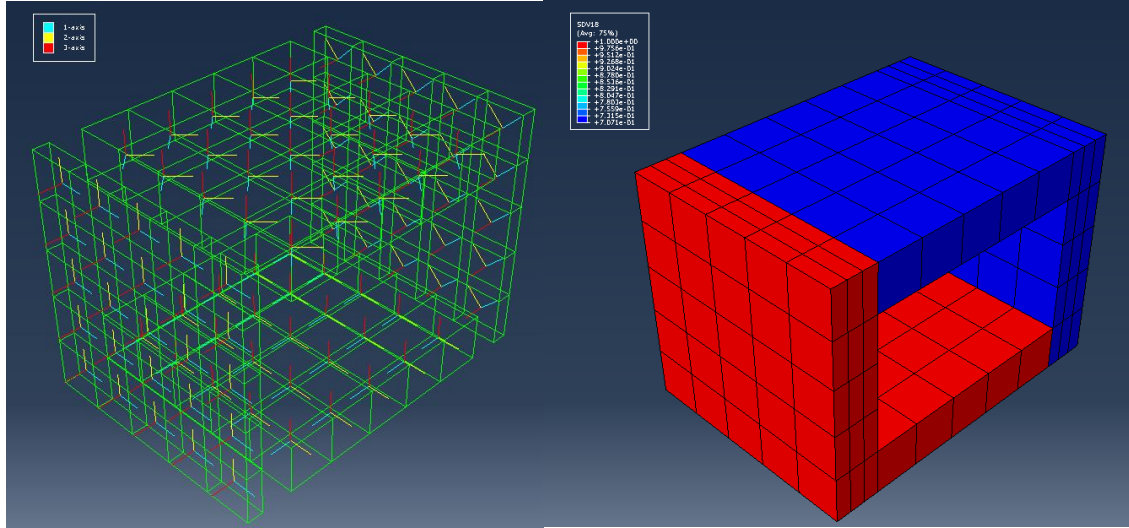
Figure 4.1: Model consisting of 4 different parts showing the different material orientation (left) and the corresponding fibre-dominated characteristic length (right, where 1-axis is fibre direction).

4.2.2 Single element performance evaluation

Single element benchmarks were developed to assess the correct implementation of the IDM theory. In particular, the longitudinal, transverse and shear responses were examined on a single element with the appropriate loading. The models were set up with appropriate loading and boundary conditions that allows uniaxial loading in the direction of interest. The aim was to ascertain the correct behaviour is achieved. The input properties used have been altered to highlight specific features being verified.

4.2.2.1 Uniaxial loading

For the longitudinal tensile and compressive directions as well as the transverse tensile direction, the behaviour should be bilinear. This was confirmed by the response in Figure 4.2 for both longitudinal compression and tension. The small drop-off at failure was due to the adoption of 0.99 as the maximum allowable damage value for fibre-dominated damage for improved numerical stability.
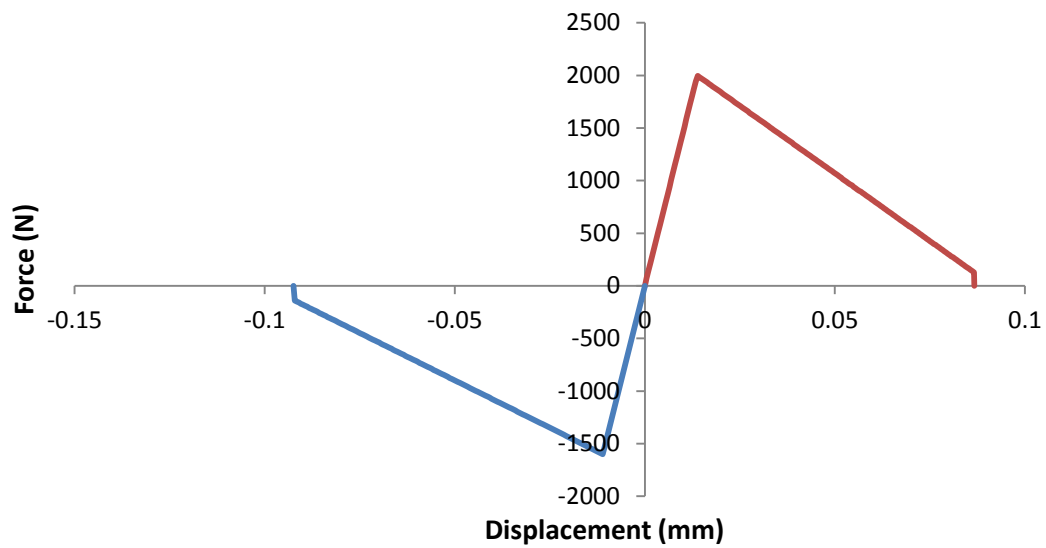
Figure 4.2: Force-displacement curve for longitudinal loading as described in Figure 3.6.

The expected bilinear response was captured in the tensile direction. The pre-damaged transverse compressive response should be linear with a nonlinear damaging response, caused by the damage manifesting in the reduction of shear loading on the fracture plane. Figure 4.3 shows the benchmark model was able to capture all the above features.
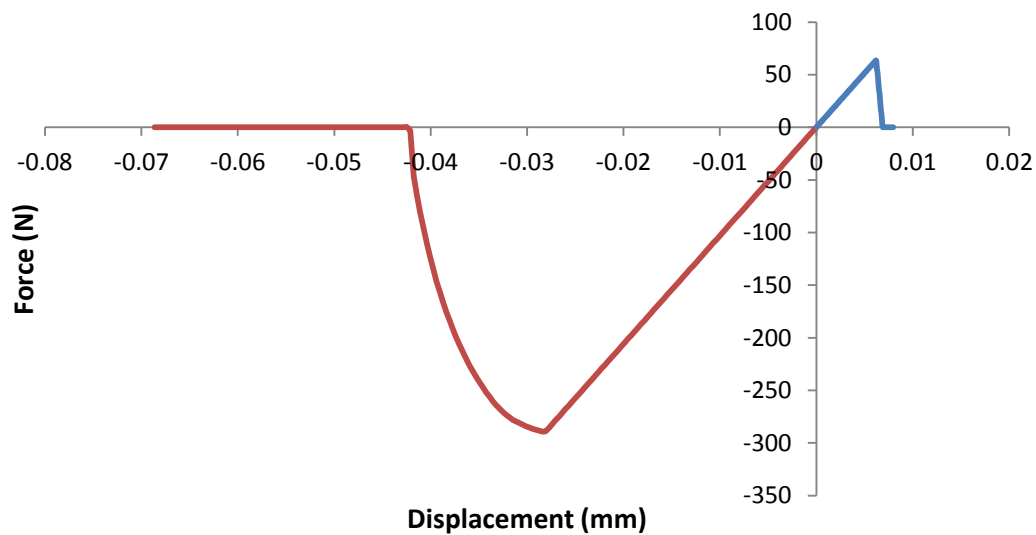
Figure 4.3: Force-displacement curve for transverse loading as described in Figure 3.6.

The shear response should be initially cubic then becoming linear as damage is initiated. The cubic shear response was clearly shown by the benchmark result in Figure 4.4. The subsequent damaged force response was linear and in line with the utilised theoretical model.
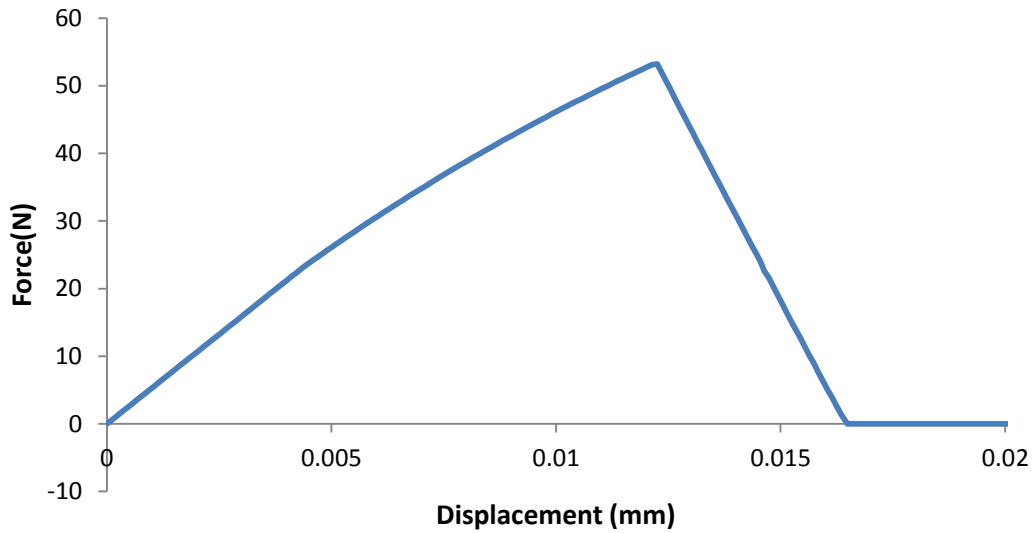
Figure 4.4: Force-displacement curve for shear loading as described in Figure 3.10.

4.2.2.2 Cyclic loading

Repeated loading is an important consideration in crush modelling due to material softening and failure. This series of tests gauge the response of the IDM in the presence of unloading and load reversal. This series of verifications were performed on the same mesh as section 4.2.2.1 with the same material properties. For cyclic loading, the load was applied via an oscillating end displacement with increasing magnitude, where the loading direction was constant. For load reversal, this displacement was oscillating with increasing amplitude, with successive peaks of alternating signs. The load displacement amplitudes are shown in Figure 4.5.
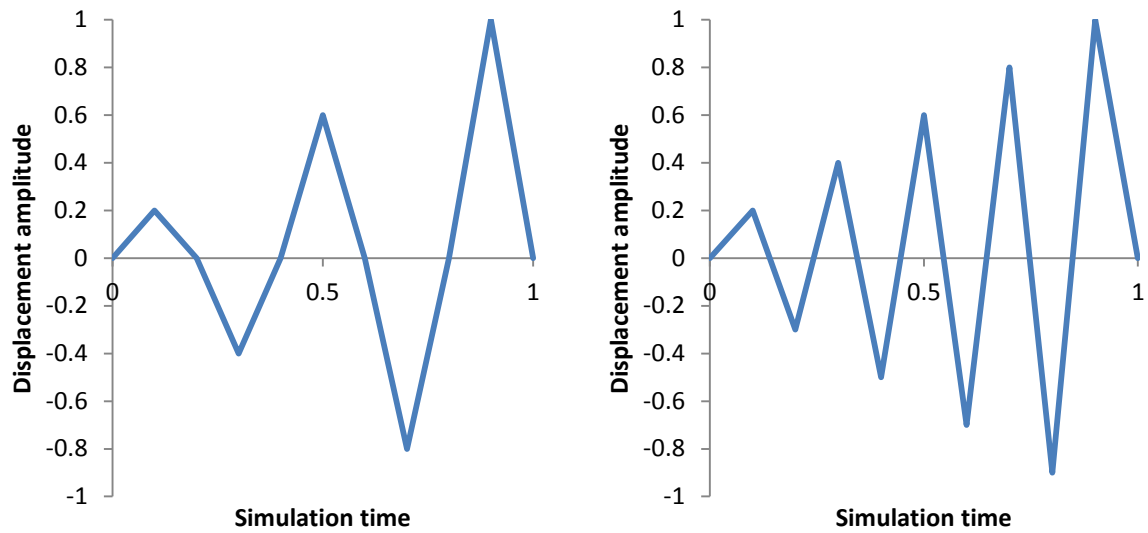
Figure 4.5: Cyclic loading amplitude for longitudinal tensile (left) and shear (right).

In the normal direction, cyclic loading is elastic; i.e., unloading and reloading occurs at the current stiffness (which included the effect of damage, if any). The longitudinal tensile test with load reversal yield the damage interaction as described in Figure 4.5.

The unloading and reloading paths in Figure 4.6 follows the damage degraded stiffness as expected during the damage process.
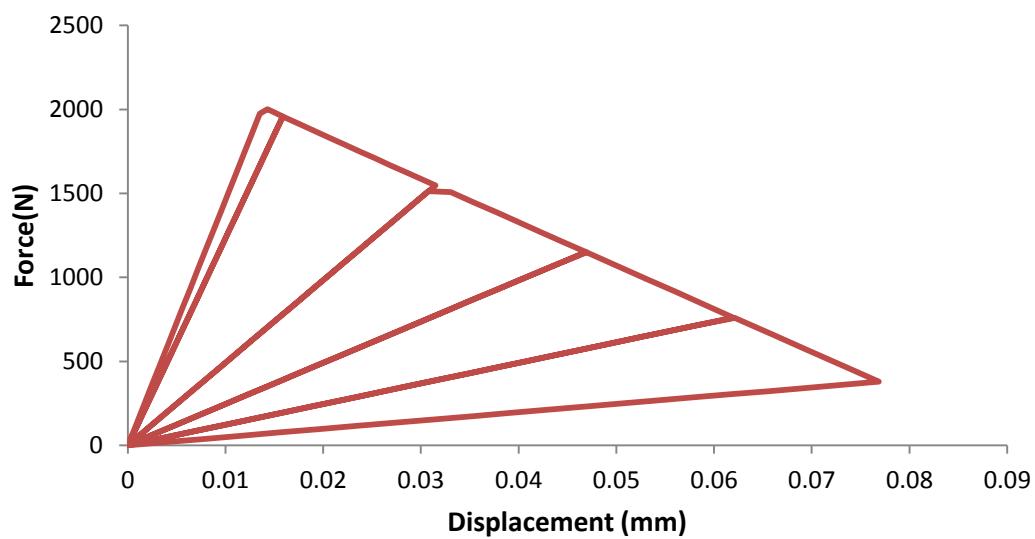
Figure 4.6: Force-displacement curve for longitudinal tensile cyclic loading.

94

Figure 4.7 demonstrates the increase in tensile damage with increasing compressive damage whereas increase in tensile damage does not increase compressive damage. This is consistent with the damage mechanism as described in Figure 3.7.
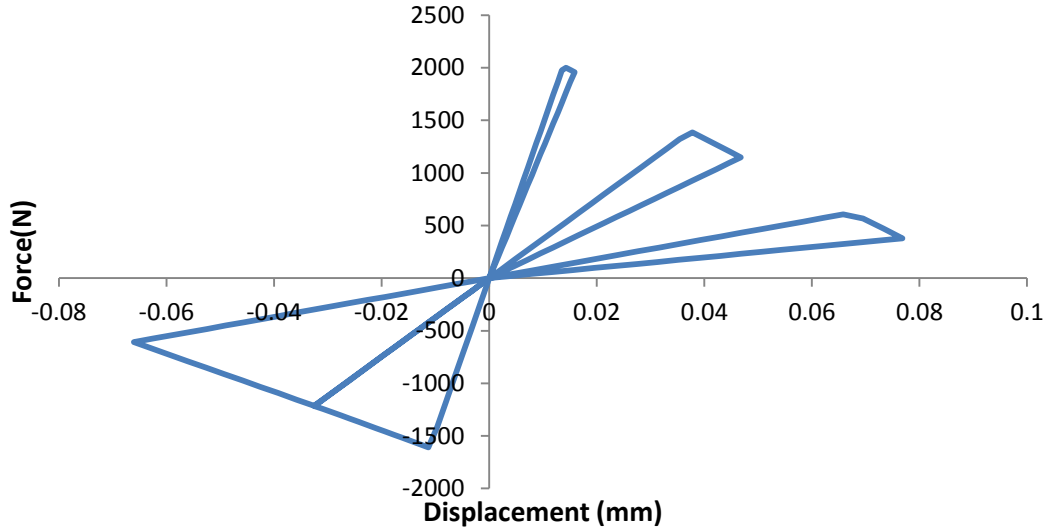
Figure 4.7: Force-displacement curve for longitudinal tensile cyclic loading with load reversal, realising the interaction described in Figure 3.7.

The shear response in Figure 4.8 showed unloading and reloading within the envelope defined by the cubic function. The unloading and reloading path was along the current shear modulus which included damage effects, if any. The non-zero fully unloaded strain is the inelastic strain. The increase of inelastic strain during the undamaged regime was demonstrated, with the inelastic strain reaching a maximum when damage initiates.
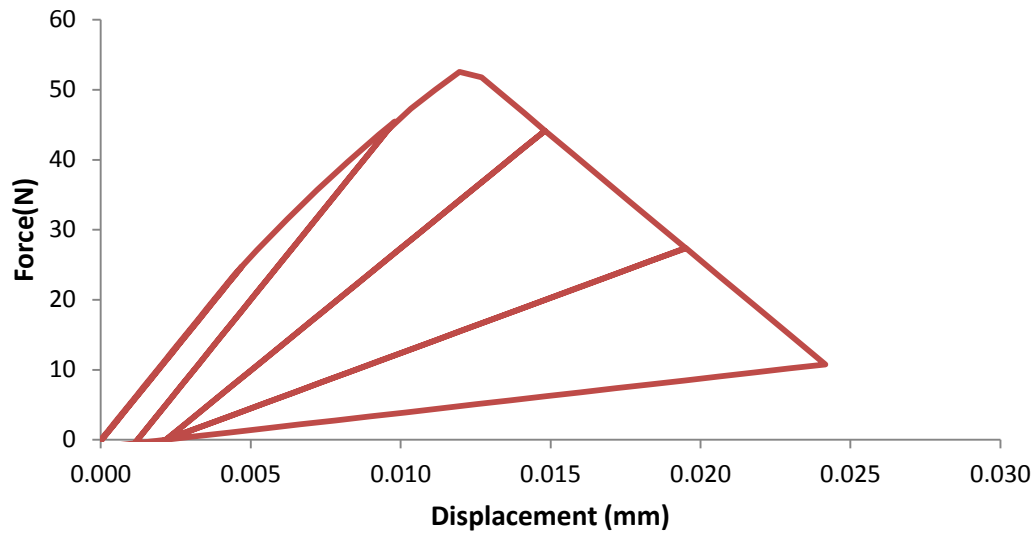
Figure 4.8: Force-displacement curve for shear cyclic loading, realising the interaction described in Figure 3.10.

The unloading-load reversal path in Figure 4.9 was a constant equal to the pristine shear modulus as the damage has not initiated. The increasing "yield" stress that is characteristic of the kinematic hardening method used was also observed as per theory.
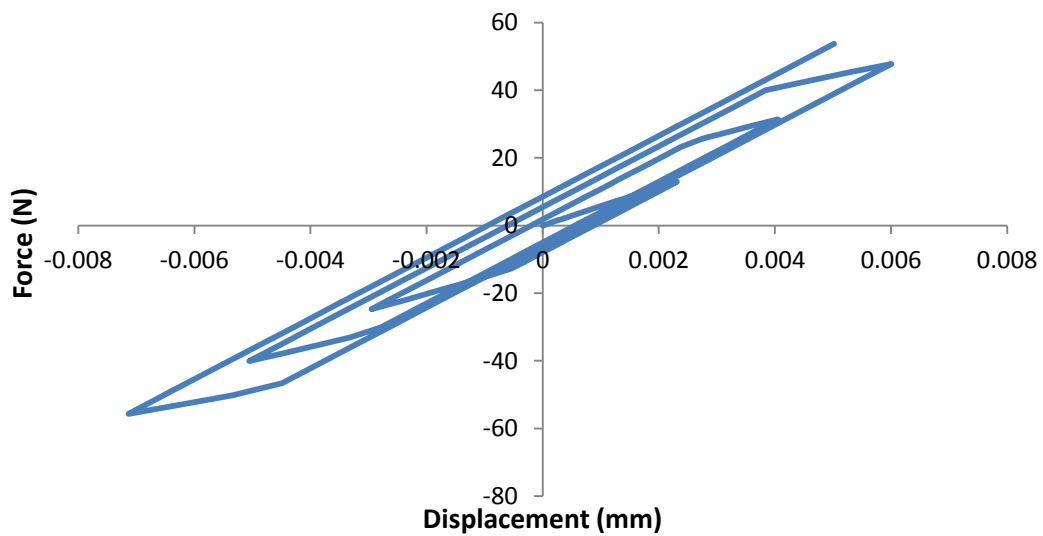
Figure 4.9: Force-displacement curve for shear cyclic loading with load reversal, realising the interaction

described in Figure 3.11.

4.2.3 Large model performance evaluation

The IDM also contain features that cannot be observed in single elements. In order to verify these features, larger models were constructed. These models are representative of actual coupon test parts and the results can be directly compared against experimental observations.

4.2.3.1 Transverse compression

One feature of the IDM is that it is able to capture the macroscopic shear cracking on the fracture plane resulting from a combination of shear and transverse compressive loading which was observed experimentally [112]. A small virtual coupon was loaded in transverse compression to verify this behaviour.

Figure 4.10 (top left) shows the idealised fracture plane which forms as a result of compressive and/or shear loading in the transverse directions. The fracture morphology of the numerical model shown in Figure 4.10 (top right) bore close resemblance to theoretical predictions.
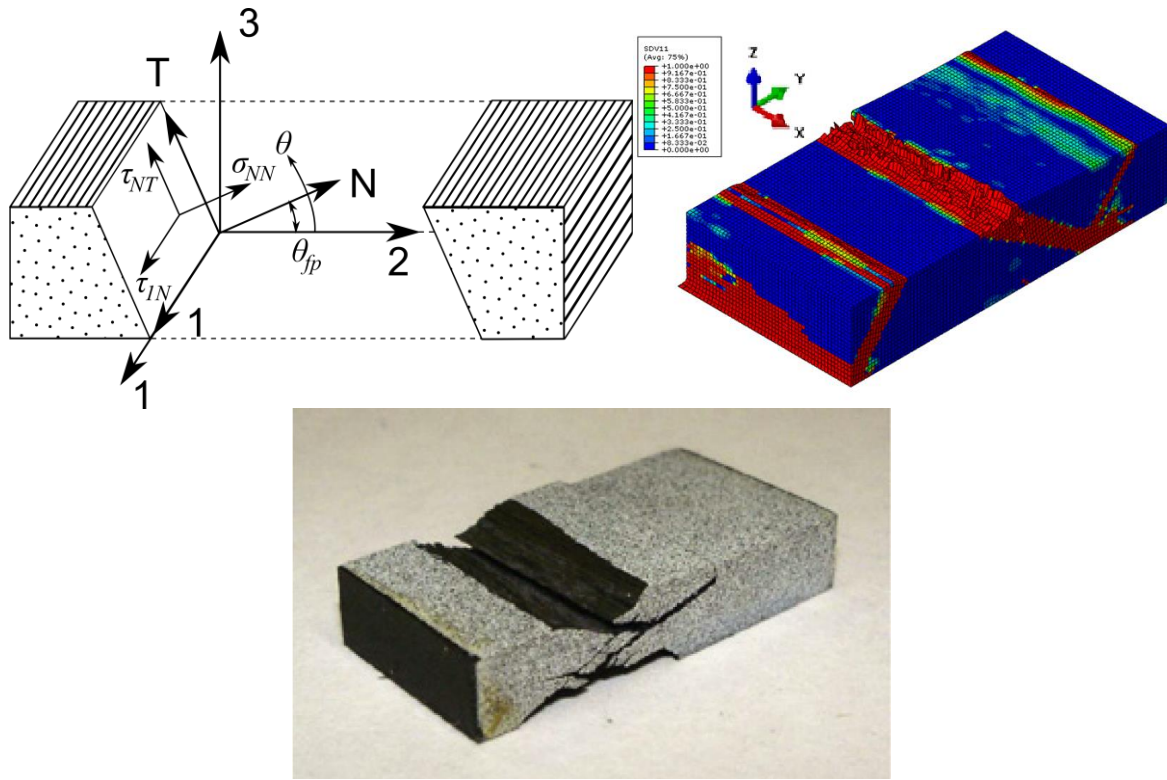
Figure 4.10: Theoretical fracture plane formation (top left), of a laminate with fibres parallel to the x direction, is well captured by the virtual coupon (top right) which correspond to experimental observations [112] (bottom).

The occurrence of multiple points of fracture initiation was observed. The fracture initiation points were not artificially triggered but a natural result of the loading coupled with variations due to floating point arithmetic. This is analogous to what happens experimentally where initiation points are localised weak points in the material. These localised weaknesses can be microscopic defects, voids or damage due to manufacturing. Fractures grow from these points of initiation and coalesce into macroscopic fractures in Figure 4.10 (top left). Formation of multiple fracture surfaces observed experimentally was also captured by the virtual coupon. The inclination of the macroscopic fracture plane was consistent with an expected value of approximately 53° [11] for pure transverse compression. The model returned a transverse compressive strength of 290 MPa which is consistent with input properties derived from experimental value presented in Ref [112].

4.2.3.2 Compact tension and compact compression

The fracture strain energy release rate controls the damage evolution in the IDM. Compact tension (CT) and compact compression (CC) tests (Figure 4.11) are used to obtain the fibre dominated fracture energy release rates [95]. Therefore a virtual CT and a virtual CC specimen were constructed to verify the model strain energy release rate returned by the IDM.
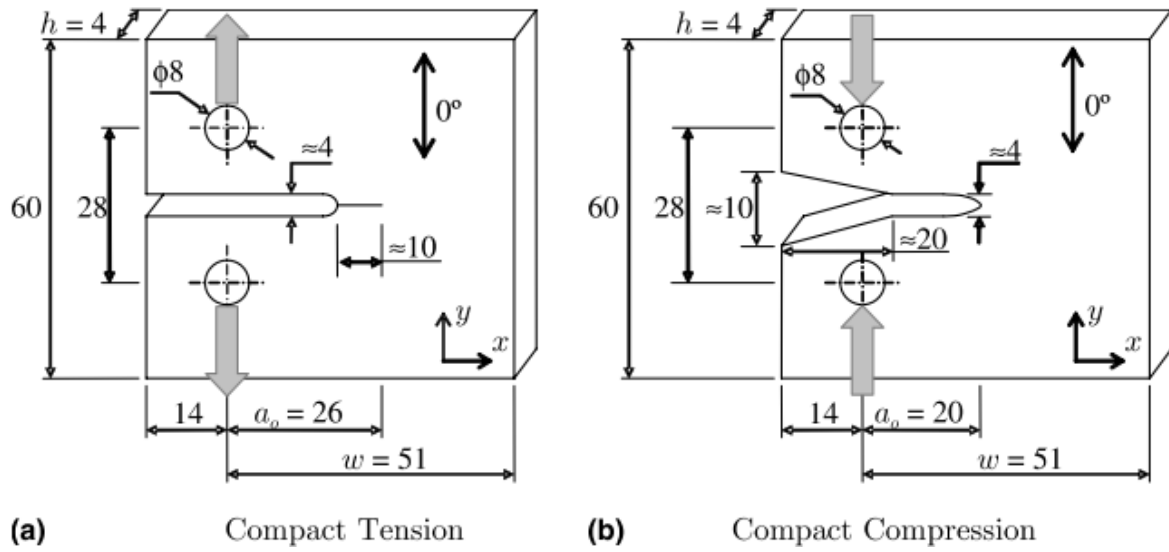
Figure 4.11: Geometry of CT (a) and CC (b) specimen [95].

The virtual specimen is constructed based on tests done by Pinho et al., with the fibres running parallel to the loading direction (Y direction in Figure 4.12). Fibre tensile and compressive critical energy release rates were verified using these virtual specimens. The model geometry is shown in Figure 4.12. The model was meshed using C3D8R elements. The material properties used are shown in Table 4.1.
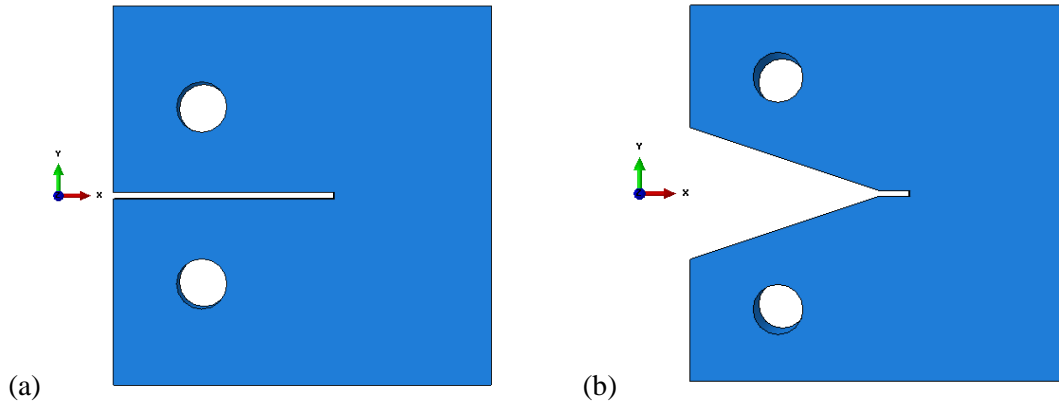
Figure 4.12: CT (a) and CC (b) virtual specimen.

Table 4.1: Intralaminar material property inputs for T700/M21.

Intralaminar properties	Value	Intralaminar properties	Value
E_{11}	142 GPa [123]	G_{fib}^{T}	108 Nmm [FYP]
E_{22}	8.4 GPa [123]	G_{fib}^{C}	58.4 Nmm [FYP]
E_{33}	8.4 GPa [123]	G_{mat}^{T}	0.331 Nmm [124]
ν_{12}	0.32 [123]	G_{mat}^{C}	1.1 Nmm [12]*
ν_{23}	0.32 [123]	G_{mat}^{12}	0.443 Nmm [124]
ν_{13}	0.32 [123]	G_{mat}^{23}	0.443 Nmm [124]
G_{12}	4.80 GPa [123]	G_{mat}^{13}	0.443 Nmm [124]
G_{23}	3.95 GPa [123]	$c_{1,12}$	34.238 GPa [125]
G_{13}	4.80 GPa [123]	$c_{2,12}$	15.061 GPa [125]
X^{T}	2.282 GPa [123]	$c_{3,12}$	2.189 GPa [125]
X^{C}	1.465 GPa [126]	$c_{1,23}$	34.238 GPa [125]
Y^{T}	65 MPa [123]	$c_{2,23}$	15.061 GPa [125]
Y^{C}	290 MPa [12]*	$c_{3,23}$	2.189 GPa [125]
S_{12}	105 MPa [123]	$c_{1,13}$	34.238 GPa [125]
		$c_{2,13}$	15.061 GPa [125]
property taken from *HTA/6376C		$c_{3,13}$	2.189 GPa [125]

The area method (Eq. (4.57)) was used to calculate the fracture energy release rate (G). Crack formation in these specimens was unsteady, with successive bouts of crack growth which happened almost instantaneously.

$$G = \frac{\partial W}{\partial A} \approx \frac{\Delta W}{\Delta A} \tag{4.57}$$

ΔW is the energy consumed in the creation of crack surface, derived from the area under the force-displacement curve at the loading pins during crack growth. ΔA is the change in crack area, approximated by the summation of cross sectional areas of the newly failed elements on the damage plane. The measured G was compared against the input value.

The energy release rates measured from the virtual specimens were in agreement with input values. The numerical description of the compact tension or compression tests introduces some errors into this measurement as shown in Table 4.2.

Table 4.2: Comparison of numerically measured and input energy release rate.

Critical fracture energy release rate (mJ/mm^2)	CC	CT
Input	58.4	108.0
Numerical	63.0	114.7
Difference	8%	6%

The virtual compact tension/compression specimens suffered from many of the same difficulties that were observed experimentally. The root cause stems from the measurement of crack area in the specimen. When an element has been deleted, a crack is said to have formed. Crack propagation in the virtual specimen is not uniform. The crack front in the virtual specimen is not always perpendicular to the direction of crack propagation. To account for this, the crack area was obtained by summing the elemental volumes of deleted elements and then dividing by the thickness of the damage band. This gives a good estimate of the crack area formed in the test. However, since the damage in the material is monotonically increasing, from initiation to final fracture, counting only the deleted elements will overestimate the energy that has been dissipated. Elements adjacent to the crack front will also sustain damage and hence dissipate energy. However, these damaged, but not yet failed, elements do not contribute to the crack area. The net result of this approach overestimates critical fracture energy release rate.

Furthermore, the discretisation of the body through meshing also affects the accuracy of the crack area measurement as the smallest crack surface that can be resolved is the size of one element. This

was particularly significant in the initial stages where the ΔA measured were small compared with the resolution of crack area. As crack propagation is very unsteady, the time interval between simulation outputs must also be of sufficient refinement to capture accurately the time history of crack propagation. Despite these issues, the numerical CC and CT models did return the correct energy release rates, demonstrating that the implementation correctly captures the consumption of energy by the damaged elements.

4.3   Model sensitivity material property variations and simulation options

Accurate measurement of some of the required input material properties was difficult and in some cases simplifying assumptions had been employed. Hence the sensitivity of the response to these parameters needed to be assessed. The affected parameters included transverse strengths and friction coefficients.

Different simulation options also presented a challenge, as their effect on the material model was unknown. This section also evaluated the effect of common simulation parameters, such as mesh sensitivity, distortion and hourglass controls. Furthermore, the developed model is very computationally intensive. Mass scaling is a very effective method to reduce the number of increments required in a given problem at the expense of accuracy. Determination of an appropriate level of scaling is essential.

4.3.1   Sensitivity to matrix strength variations

The transverse material properties have been shown to be dependent to the local layup orientations [87]. However, to simplify the model, in-situ effects had been neglected. To ensure that this assumption is valid, the effect of the variation in the input property parameters needed to be assessed. The sensitivity of the value of transverse strengths was investigated using a model of a simple

chamfered flat plate undergoing crushing against a rigid surface. The variation in peak force (Figure 4.13) and SEA (Figure 4.14) with variations to the input transverse properties was compared.
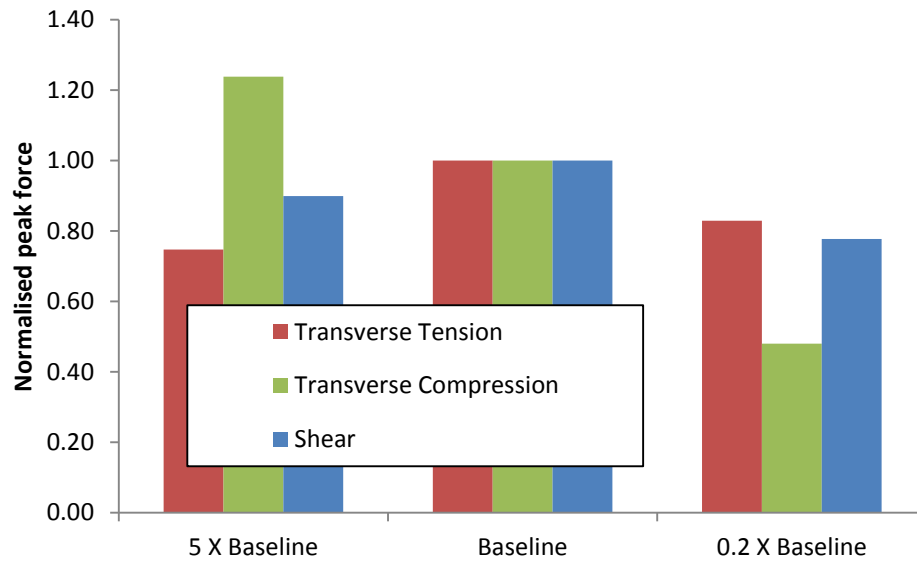
Figure 4.13: Sensitivity of peak force to transverse properties.
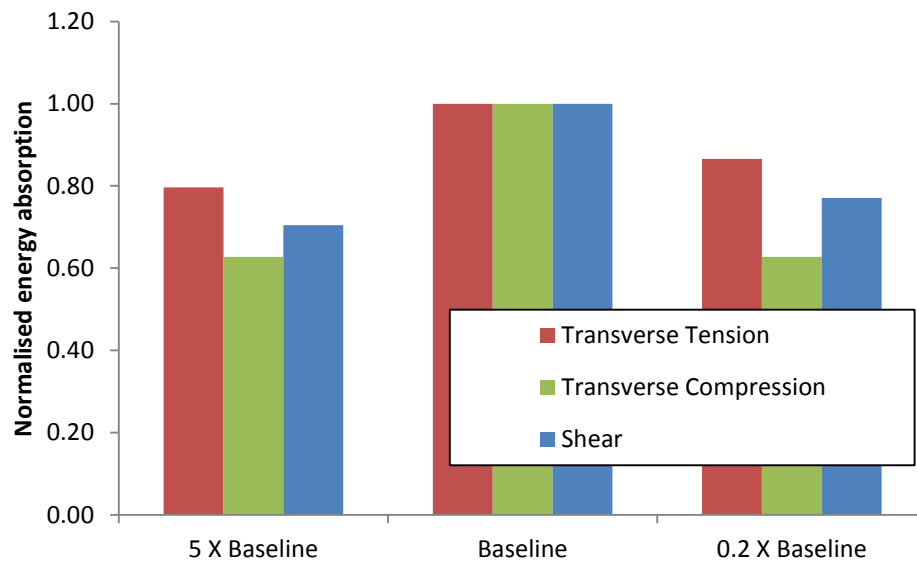
Figure 4.14: Sensitivity of total energy absorption to transverse properties.

As expected, decreasing the transverse tensile, compressive and shear strengths to 20% of the baseline values resulted in a reduced peak force. On the other hand, a fivefold increase in the transverse tensile and shear strengths led to failure via buckling away from the crush front, resulting in a decreased

overall peak force. The increase in transverse compressive strength caused an expected increase in peak force. Overall, the simulation demonstrated that the SEA was not very sensitive to the variation in these transverse properties. A 500% change in the transverse property caused a maximum of 60% and 40% change in the peak force and the SEA respectively, meaning that the results were not very sensitive to changes in the transverse properties. This phenomenon was likely the result of the low energy associated with matrix damage as the primary energy dissipation was expected to be through fibre-dominated damage mechanisms. These results suggested that in-situ variations can be safely neglected.

4.3.2 Sensitivity to inter-ply friction

Friction is an important input parameter for the simulation. Schön [127] showed experimentally that contact between plies with different orientations results in different friction coefficient, showing that the ply interface plays a substantial role in the sliding behaviour. However, these interfaces are often poorly characterised due to experimental constraints such as the variability of the surfaces in contact. Furthermore, one value cannot adequately represent the variety of different interfacial conditions between two contacting surfaces in a crush simulation. This variability is due to the changes in the ply surface as the crushing progresses. Three different general interface conditions will need to be captured. The first condition occurs between the ply and the platen during the early stages of trigger consumption. At this point, there is little debris and the plies have sustained relatively little damage. This condition is well approximated by the experimental measurement of the friction coefficient through simple sliding tests. However, as damage progresses, debris is generated and the interface property is altered by this. The resulting friction property will depend on the shape and amount of debris generated as well as the rate of removal of this debris. The final interfacial condition is the most complex and occurs between delaminated plies. The ply interface formed from delamination is a function of the potential for bridging of fibres, size and shape of the generated debris, the surface roughness of the delaminated surfaces and many other interactions. The characterisation of friction for this interface is difficult and unreliable.

As a result, there was a need to determine the sensitivity of a typical specimen to variations in the friction coefficient. A sensitivity analysis was completed using the chamfered cylindrical tube as the test case. The total energy absorption of the structure under crushing was examined for a range of different friction coefficients. Figure 4.15 shows that, in terms of total energy absorption, there was a distinct change between zero and non-zero friction coefficient. However, the difference in energy absorption for friction coefficients between 0.10 and 0.30 was small. These results suggest that the effect of changes in frictional coefficient was small and an approximate value can be safely used as long as the interface was not assumed to be frictionless.
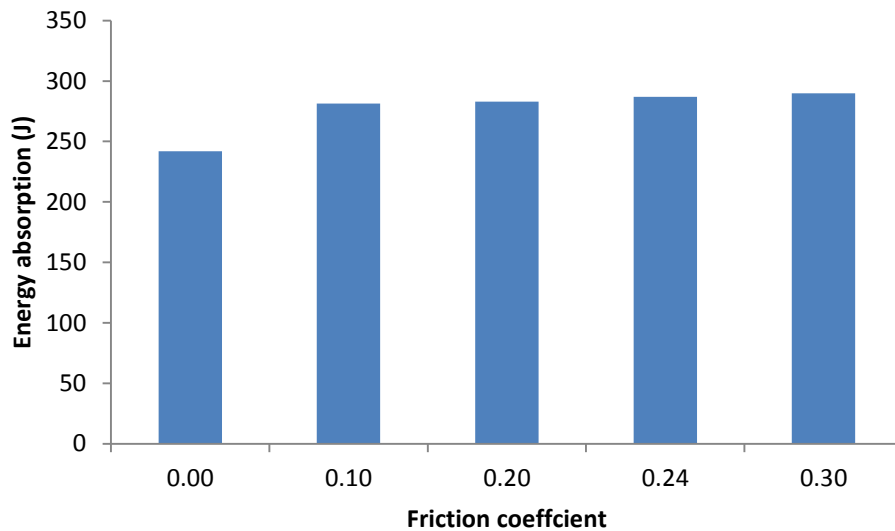
Figure 4.15: Sensitivity of total energy absorption to friction coefficient.

4.3.3   Sensitivity to mesh density

The developed constitutive model softens the material locally as damage progresses. This leads to the localisation of damage, which is strongly mesh dependent. This is resolved through the use of a characteristic length to ensure the overall energy dissipation is consistent between different mesh configurations. A mesh sensitivity study, on a 2 mm sided cube loaded in longitudinal tension, was performed with 1^3, 2^3, 3^3, 4^3 and 5^3 elements respectively. The models were loaded in tension

longitudinally until destruction. These models had uniform material properties and no artificial stress concentrators were included to encourage damage initiation at a pre-defined location.

The expected planar damage formation was well captured, as shown in Figure 4.16, for all of the test cases. Damage localisation was also confirmed as the damage planes were single element thick.
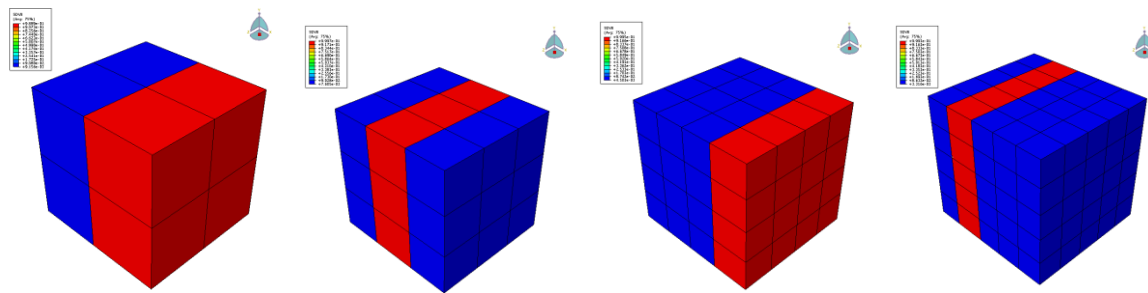
Figure 4.16: Plot showing damaged elements (red) in the mesh sensitivity study.

The response in Figure 4.17 confirmed the mesh independence of the proposed model as the force-displacement curve of the different meshes were in alignment except near the point of complete failure. Consequently, the mesh independence of the damage energy dissipation was shown for small strains.
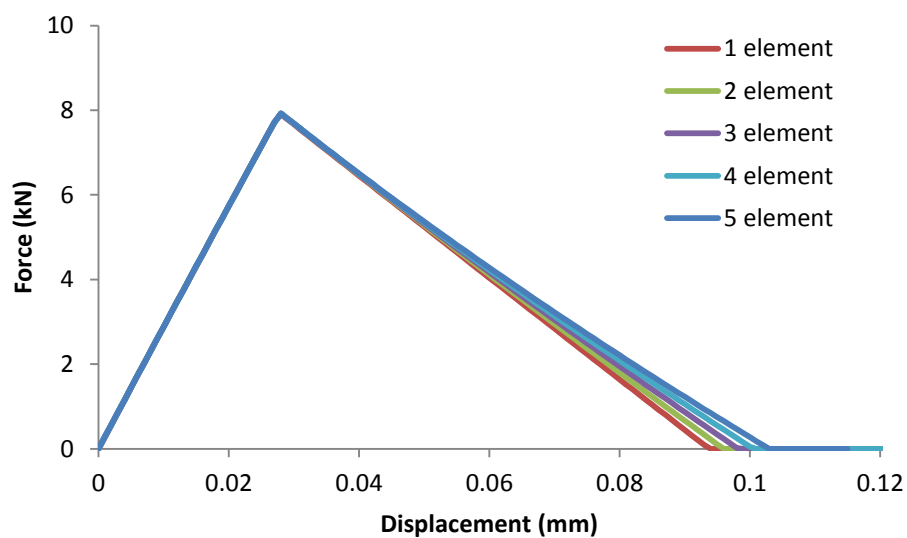
Figure 4.17: Force-displacement curve for cube model with different mesh densities.

Summation of the incremented strains yielded the total strain used in the calculations. The deviation near complete failure is caused by the difference between the infinitesimal strain used in the model and the finite deformation formulation used in the FE package. This difference is only significant where there are large strains experienced by small elements nearing complete failure. The failure strain of the element was inversely proportional to the characteristic length. The characteristic length was dependent on the elemental geometry as well as the fracture plane orientation. This led to a large strain for finely meshed elements nearing failure. Strain values of beyond 0.5 were observed. These were too large for the infinitesimal strain condition to apply, causing some mesh dependence. This places a lower limit on the fineness of the mesh. An optimal mesh is somewhere between this limit and the upper limit imposed by Eq. (4.58), which is found by equating the fracture energy with the strain energy in the element just before failure.

$$l_{fib} \leq \frac{2G_{fib}^{dir}}{X^{dir}\varepsilon_{fib}^{0,dir}} \tag{4.58}$$

This analysis showed mesh-size independent when the mesh was within these prescribed limits.

The effect of mesh sizing on larger models was also explored. The element deletion algorithm in the implemented material model caused undesirable numerical noise in the simulated response. This effect was assessed using models with cylindrical tube geometry meshed using different seed sizes. Figure 4.18 shows the force response of specimens meshed using 0.6 mm, 1 mm and 2 mm target mesh spacing, with a thickness of approximately 0.06 mm due to the need for 3 element per ply in the thickness direction.
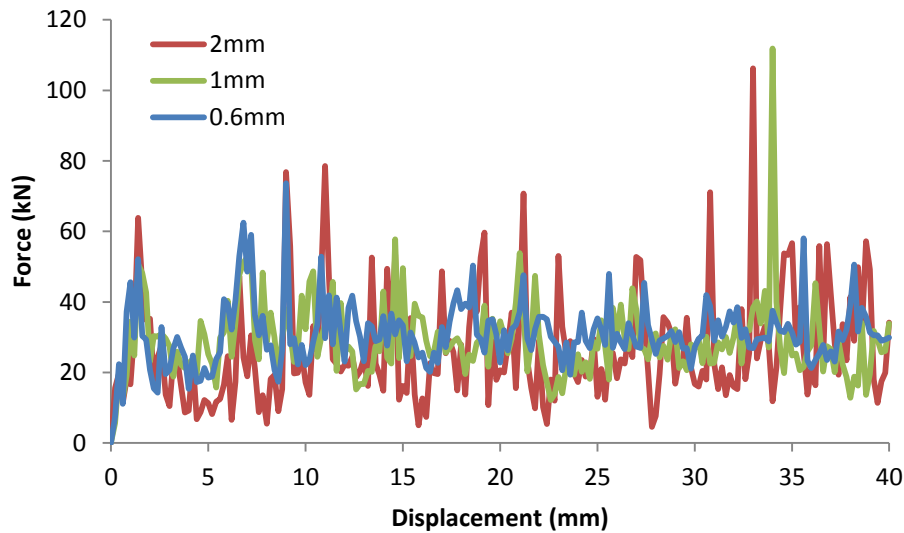
Figure 4.18: Effect of mesh sensitive on a typical tube specimen.

These results clearly show that the finer mesh gives a smoother force curve. This matches

observations by McCarthy et al [45]. This was consistent with expectation, as the coarser mesh would

cause larger discontinuities in the structure and hence a more jagged response due to the larger

elements being removed. However, care must be taken to ensure that the mesh is not too fine so that

the large failure strain begins to affect the accuracy of the results. For models similar to the cylindrical

tube tested here, the target mesh dimension in the in-plane directions was set to approximately 1 mm.

4.3.4   Sensitivity to hourglass and distortion controls

The material model was designed for use with reduced integration linear (C3D8R) elements. However,

the reduced integration element is inherently prone to hourglass effects. Hourglass effects are caused

by the reduced integration formulation not being able to detect deformation in certain modes and the

strain energy in these modes cannot be accounted for. This results in a lack of resistance to motion in

these modes, which can propagate readily through a mesh, resulting in the characteristic hourglass-

like shapes. Abaqus has inbuilt controls [6] for the suppression of these modes which can be used.

The strain softening model presents challenges to the stability of the simulation. As elements are

damaged, they lose stiffness and the ability to resist motion. This can result in the appearance of badly

distorted elements. If an element is sufficiently distorted, the simulation could be terminated. Abaqus has a distortion control feature [6] which stops the element from inverting or distorting excessively by enforcing a penalty constraint on motion of nodes towards the centre of the element that will create a non-convex element.

A cylindrical test case was used to gauge the effect of hourglass and distortion controls on C3D8R elements. Comparison between reduced and full integration elements was impractical as substantial redevelopment of the code was required. The effect of each control on the controlling unphysical distortions is assessed. Four different configurations were tested:

- NDH – neither distortion nor hourglass control.

- DC – distortion control only.

- HG – enhanced hourglass control only.

- D+H – both distortion and hourglass control.

The resulting element distortion was compared in Figure 4.19.
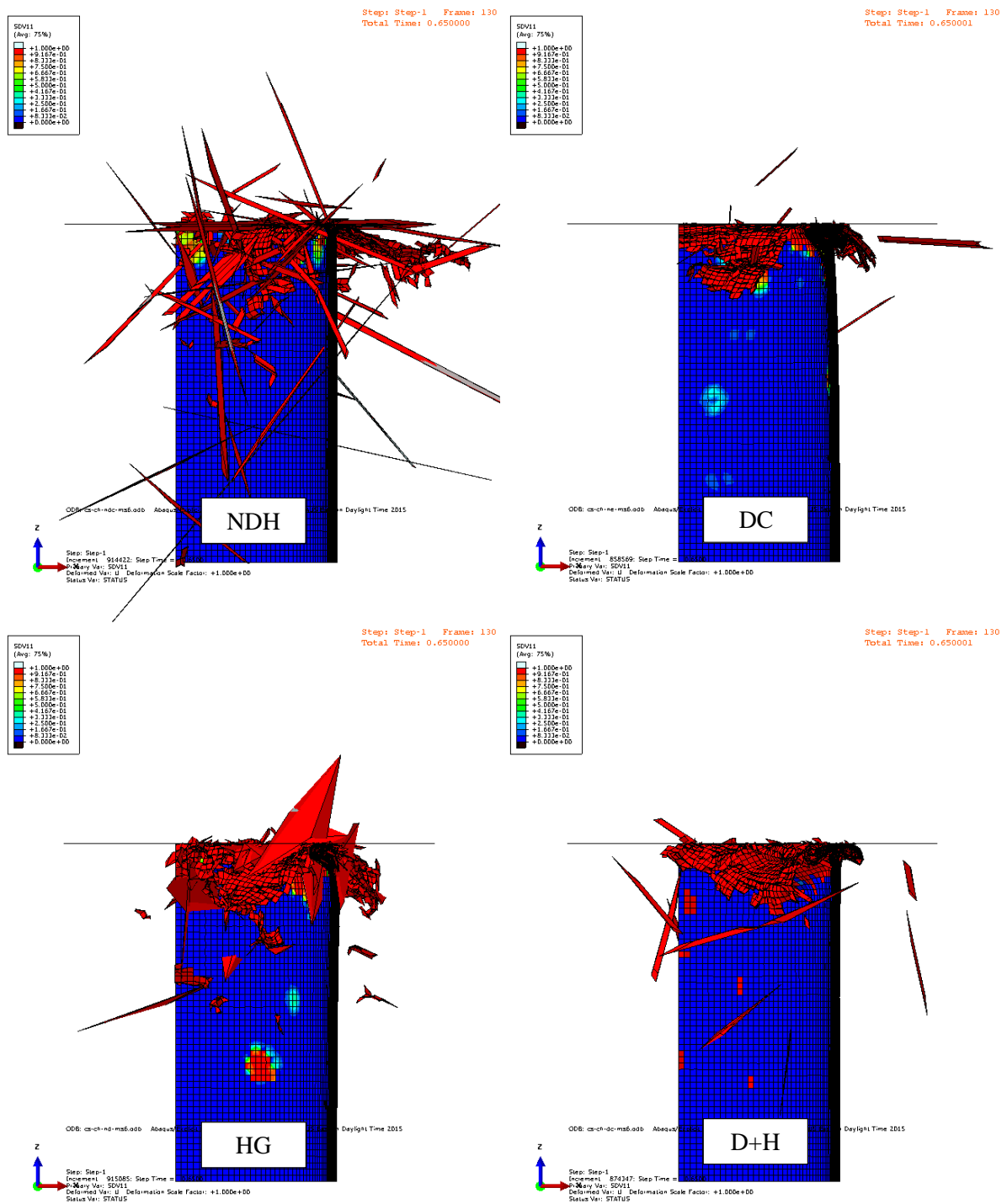
Figure 4.19: Effect of hourglass (HG) and distortion (DC) controls on overall deformation.

The NDH test case clearly demonstrated the proliferation of severely distorted elements when no numerical controls had been applied. Numerous large lance-like elements obscured the crush front. The HG test case represented a significant improvement in suppressing severely distorted elements.

Only a small number of severely distorted elements were observed. Furthermore, these distorted elements were generally still attached to the main structure and affecting the overall response. The DC test case showed results similar to the D+H test case in terms of suppression of excessive distortion.

This can also be indirectly observed in the force response as unphysical distortion is often accompanied by large numerical noise. The force responses are shown in Figure 4.20.
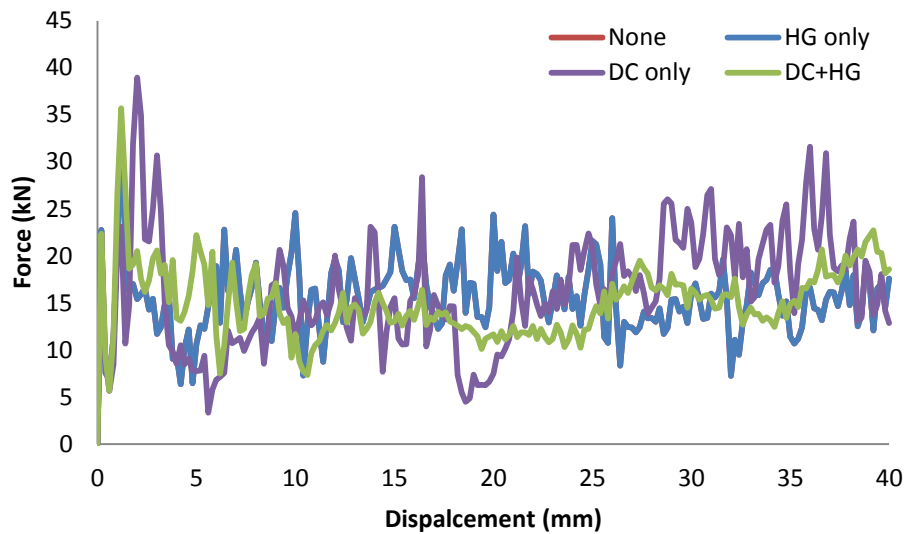
Figure 4.20: Effect of hourglass (HG) and distortion (DC) controls on force response.

The use of hourglass controls on its own was ineffective. The responses overlapped with the model with no controls. The use of distortion control only was not very effective in suppressing the numerical noise. When both hourglass and distortion controls are activated, the numerical noise was well suppressed. This was particularly prominent in the relatively flat force response during the steady-state crushing of the tube body.

Table 4.3 shows that the use of these numerical controls has a negligible effect on the overall runtime of the simulation. It was likely that the computing resources required to implement these controls were offset by detrimental effect of severely distorted elements on the time increment. As a result, it is recommended that both hourglass and distortion control be used with the proposed material model.

Table 4.3: Effect of hourglass and distortion control on simulation runtime.

Simulation time relative to NDH case	NDH	HG	DC	D+H
	1.000	1.026	0.970	0.993

4.3.5 Sensitivity to mass scaling

Mass scaling is an effective tool in speeding up the FE analysis by increasing the mass of elements. The stability limit for the time increment (Δt) size is shown in Eq. (4.59) and represents the time it takes for a stress wave to traverse the element.

$$\Delta t < \frac{L_{min}}{c_{waev}} \tag{4.59}$$

This limit is dependent on the size of the element (L_{min}) and the dilatational wave speed (c_{wave}) of the material. The wave speed is dependent on the elastic modulus (E) and the density (ρ) via Eq. (4.60).

$$c_{wave} = \sqrt{\frac{E}{\rho}} \tag{4.60}$$

By increasing the density of the element, a larger time increment can be used without violating the time increment size stability limit. However, this increase in time increment size is at the cost of solution accuracy.

The damage-softening nature of the material model adds an extra level of complexity to the application of mass scaling. Variable mass scaling struck the best balance for increased time increment with minimal increase in model mass. Using this method of mass scaling, the model was periodically scanned and the need for mass scaling was determined on a per element basis. Only elements with a time increment lower than a predefined target were scaled. As the simulation progress, the elements near the crush front deformed due to loading. When these elements deformed, the time for the propagation of a stress wave through the element changed according to Eq. (4.59). Thus, mass scaling was expected to be concentrated near the crush front where the deformation

caused a reduction in the critical time increment. This region was also where deletion of excessively distorted elements occurred as damage reduced the element's ability to resist further deformation. Logically, a significant portion of mass scaled elements would also be deleted and removed from the simulation. This had a net effect of reducing the overall mass scaling applied to the model as the remainder of the model was unaffected.

A test case was created using a cylindrical tube geometry to test the convergence of results with decreasing mass scaling as represented via the target time increment. Figure 4.21 shows that the results converged well. The models with a target time increment size of 1 μs and 0.1 μs had almost identical response. This gives confidence that mass scaling can be used with the material model without significantly affecting the accuracy. For structures similar to the tested tube, a mass scaling of 1 μs can be used.
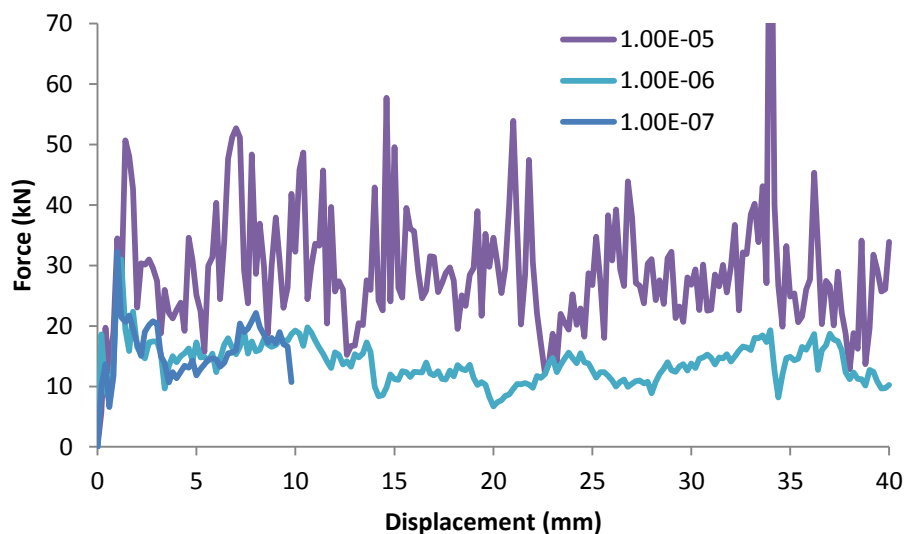
Figure 4.21: Effect of mass scaling on response.

4.4 Summary

The developed material model had been verified through a series of different tests. The characteristic length calculation was verified on a mesh containing elements that have different MCS. Single element tests confirmed the bilinear normal response as well as the cubic shear response. Cyclic

113

loading and load reversal were also demonstrated. Formation of a macroscopic fracture surface in transverse compression was observed at the correct inclination with respect to the loading direction. The total energy absorption was captured with good accuracy. All of the tests indicated that the implementation correctly reproduced the expected theoretical responses. The large model performance shows that experimentally observed features are well captured by this model.

The sensitivity of the proposed model was explored for a range of different parameters. The transverse strengths and friction coefficient can vary in value throughout the simulation. However, sensitivity studies suggest that changes in these values do not have a significant effect on the final energy dissipation of the composite structure. Mesh independence was also confirmed as long as the element size was within prescribed limits. Sensitivity of parameters controlling the simulation was also investigated. It was shown that the numerical noise associated with element deletion could be reduced through mesh refinement. The effect of hourglass and distortion control was also examined. Finally, it was shown that mass scaling can be used with this material model without significantly affecting accuracy. This sensitivity information aids the setup and use of the proposed damage model.

Chapter 5
Crushing of tulip-triggered cylindrical tube – an experimental study

5.1   Introduction

An experimental study was completed as a part of this project. This study served two main purposes. The data gathered in this experimental study was used to validate the efficacy of the IDM in predicting the crush response of composite structures. The tested specimen was modelled numerically using the present material model and the result was benchmarked against the experimental results obtained in this study:

- Quantitatively via the comparison of various metrics including forces experienced and energy absorption.

- Qualitatively via the comparison of post-crush deformation and damage distribution throughout the structure.

This experimental program also sought to establish the strain rate dependence of the chosen material and structure combination. This is driven by the dynamic nature of crash events which these energy absorbing structures are expected to provide protection against. Hence, it was vital to establish whether an increase in the test rate correlates to a change in structural response.

The details of the experimental program are outlined in this chapter. The rationale for the chosen specimen configuration is specified. The manufacturing method, developed to ensure the consistency in the produced specimens and hence crush performance, is also described. The specimens were tested at different nominal strain rates. The obtained results, both quantitative as well as qualitative, are presented and analysed.

5.2   Experimental study

The chosen specimen used for validation of the proposed model must be representative of typical configurations encountered during the design of a composite energy absorber. A large variety of different designs had been reported in the literature as outlines in Chapter 2. A purely composite design (no foams or honeycomb structures) will be considered here so that the composite intralaminar

damage model can be validated. The specimen configuration has been chosen from trends in the literature to maximise performance. In choosing the configuration of the representative energy absorber specimen, the following characteristics were taken into account:

- Whether the specimen will crush progressively or catastrophically,

- Specific energy absorption achieved,

- Crush efficiency achieved, and

- Consistency in the force response.

5.2.1 Specimen choice

The primary objective in the design of the test specimen is to maximise its energy absorption during the crushing process while minimising the peak force transmitted through the structure. The specimen geometry was chosen to be a cylindrical tube with tulip triggers along the top surface. The laminate configuration was $[0/90/0/90]_s$. The material system used was Hexcel Hexply M21/35%/UD268/T700, which was a high strength, intermediate modulus carbon fibre embedded in a toughened epoxy matrix. The material was available in the form of unidirectional prepreg plies. The dimensions of the specimen are given in Figure 5.1.
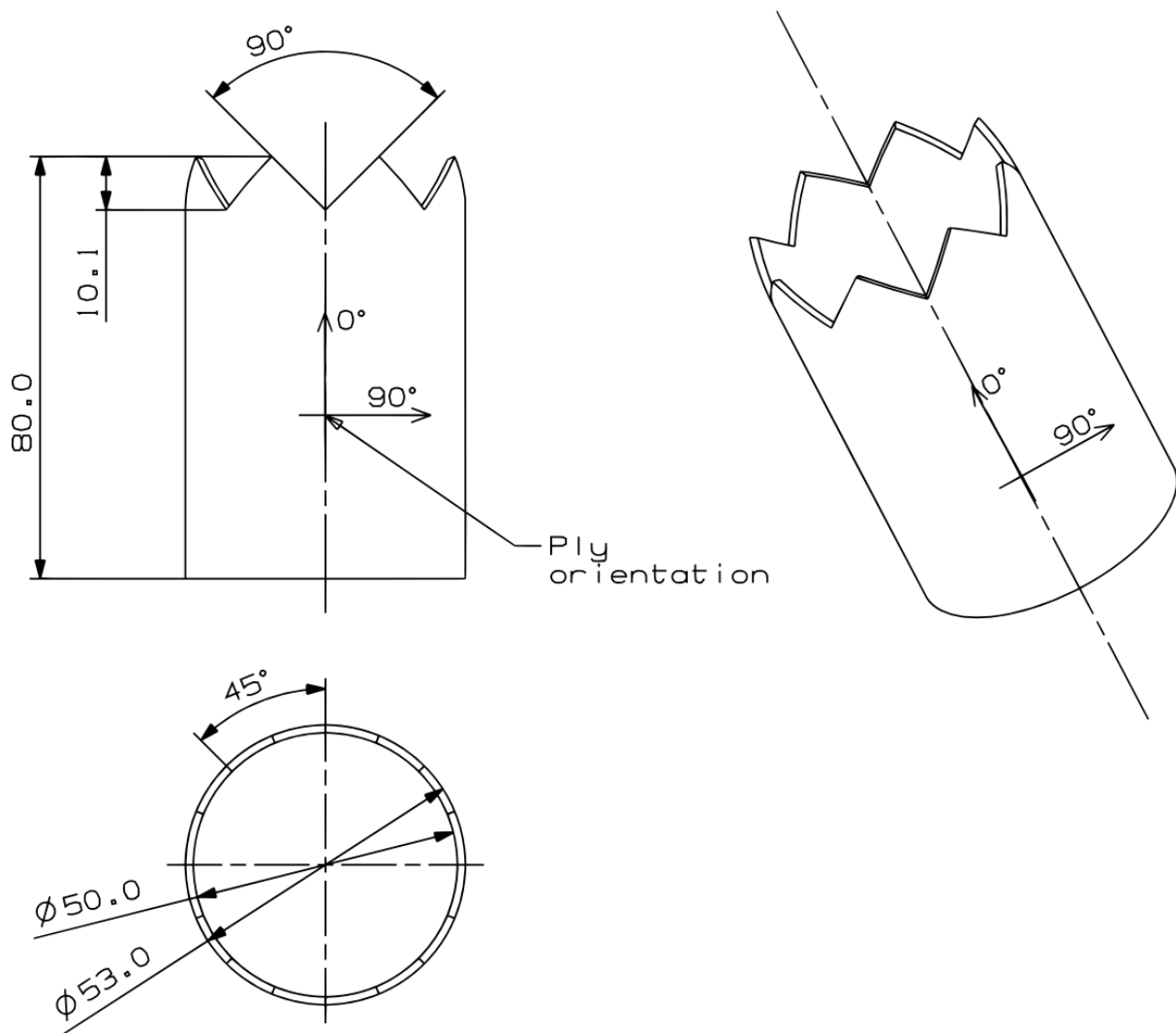
Figure 5.1: Test specimen: Cylindrical tube topped with tulip triggers.

A circular cross-section was chosen because the published literature [5, 22, 46] are in agreement that it is superior to a square or rectangular cross-section. The lack of stress concentrations allows crush damage to be evenly distributed over the entire cross-section. In contrast, the tubes of square or rectangular cross-sections with straight sides tend to fail by buckling, which is less energy absorbent than localised crush failure of cylindrical tubes [22], as progressive crushing damages more material than global buckling. A circular cross-section is also self-supporting so no additional support structure is required, which is more practical than simpler structures such as a flat plate. The self-supporting nature of the circular geometry also provides resistance to global buckling, which, again, promotes progressive crushing. Conical structures are conducive to a more stable and progressive crushing but

their energy absorbing capability are lower than that of triggered cylindrical tubes [46]. Other

geometries such as tubes with an hourglass contour were also considered. It was shown that the

increasing difficulty in manufacturing these geometries do not bring an increase in the energy

absorbing capability [43] when compared with a triggered cylindrical tube.

Triggering is vital in the design of energy absorbing devices. The role of the trigger is to initiate

damage in a controlled manner so that it leads to progressive damage accumulation rather than a

single catastrophic damage event. A series of tulip peaks cut into the composite tube is adopted as the

trigger mechanism for this study, see Figure 5.1. Compared with hourglass [43], crown and chamfer

[27] triggers, the triangular tulip trigger leads to a crushing response with a higher steady-state crush

load [22]. The tulip trigger is also more stable as the cross-sectional area of the sample being crushed

is continuous with respect to the crushing process. This leads to a greater energy absorption capability

than similar structures with different triggers [22, 46]. Furthermore, the tulip trigger can span over a

larger range of displacement, which can increase the displacement span of region I of the typical crush

response. Consequently, the initial growth in load occurs over a longer timeframe. The lengthening of

the trigger region helps to reduce the initial force spike, which is a typical phenomenon in an impact

situation. Spreading the dissipated energy over a larger displacement contributes directly to improved

crashworthiness by reducing the transmitted force [5]. The ability to vary the angle of the tulip trigger

and/or number of triggers along the cross-section improves the flexibility of this design as the

displacement span of region I can be tailored to the expected crash load profile for a suitable amount

of cushioning to alleviate the initial force spike on impact.

The $[0/90/0/90]_s$ layup configuration was chosen for its balanced nature and improved lateral support.

Jacob et al.[5] noted that by providing lateral support to fibres and increasing the number of fractured

fibre parallel to the loading direction, the overall energy absorption is increased. Commercially

available filament wound tubes were not considered due to a lack of fibres parallel to the loading

direction.

5.2.2 Manufacturing the specimen

The literature has shown that there was a significant amount of spread that is inherent in experimental responses of energy absorbing devices [32]. This is particularly relevant for specimens with a complex geometry [43]. Furthermore, visual inspections of photographs of many specimens used in the literature show the existence of manufacturing variations. For example, Figure 5.2 shows that circular tube not manufactured through filament winding is prone to developing creases and undulations on the free surfaces during curing [27]. Furthermore, the layup of dry fibre fabric was also problematic, as fibre alignment cannot be guaranteed due to wrinkling and fraying of the fabric [52]. A set of manufacturing processes were developed to minimise the possibility of variation in the produced specimens so that consistent resulting responses can be achieved.

Figure 5.2: Specimens showing manufacturing defects: creases along a seam (B-1) and wrinkling of the ply (C-1 and C-2).

The specimens used in the tests were produced in-house. Each tube was laid up manually between an aluminium core mandrel and outer mould (Figure 5.3). The cylindrical aluminium mandrel had a diameter of 50 mm and a length of 200 mm. The outer mould was a pair of aluminium half-pipes with a 54 mm internal diameter and 150 mm length.

(a)   (b)
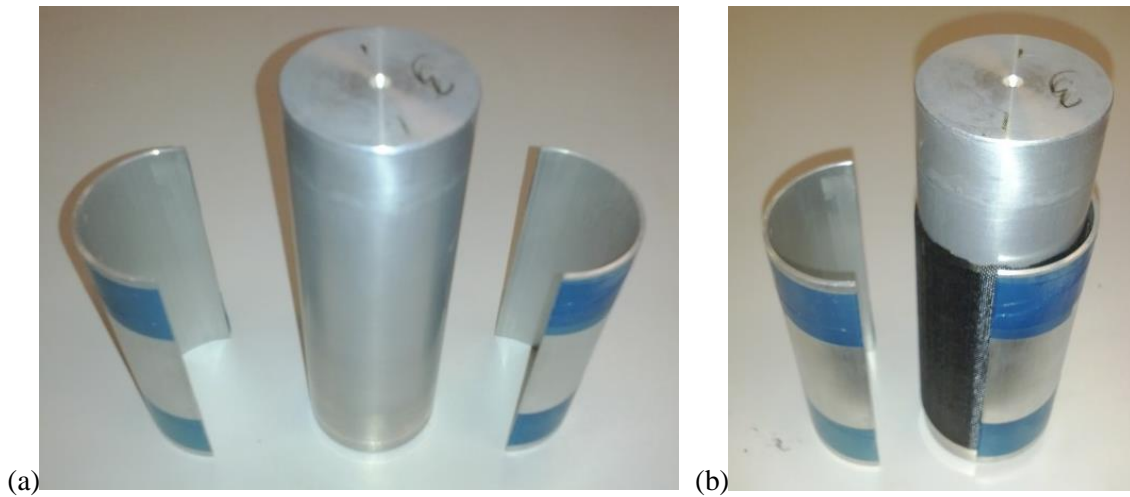
Figure 5.3: Mandrel and mould: without specimen (a) and with specimen (b).

It was necessary to use both an inner mandrel and a pair of outer moulds to ensure that a defect-free specimen of the correct geometry can be achieved consistently. A smooth and rigid inner surface was provided by the mandrel to ensure the correct inner diameter was achieved after debulking and curing. The semi-circular outer moulds prevent the occurrence of wrinkling of the composite tube during curing which was observed in initial testing. This wrinkling would cause the fibres to be out of line with the loading direction and introduce thickness variations, which become points of weakness that might trigger unintended damage mechanisms. With the inclusion of the outer moulds, the pressure is applied on the mould rather than directly on the curing tube so that the outer surface of the tube takes on the geometry of the mould's inner surface.

Before layup, the mandrel was cleaned using acetone. Once the mandrel was clean, three coats of Marbocote TRE75 ECO semi-permanent release agent liquid were applied and allowed to dry. Two reference lines were carefully marked on the opposite sides of the mandrel, ensuring the lines were vertical with respect to the cylinder to provide an accurate reference to orient the 0 and 90° plies (Figure 5.4).
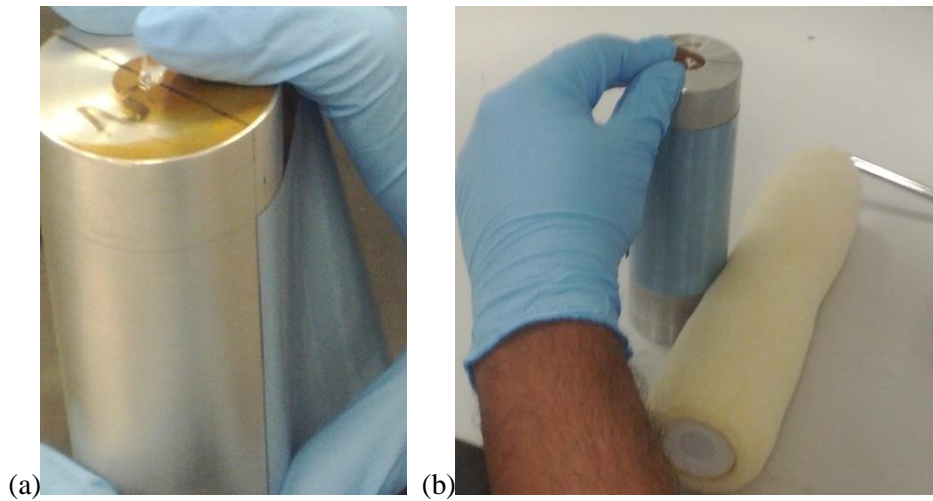
Figure 5.4: Lining up the ply with reference (a) and removing possible voids (b).

Prepreg ply sheets were cut to size, taking into consideration the changing circumference as plies were built up. These were laid on the mandrel carefully to avoid wrinkle formation. A debulking process was performed for the 1st, 2nd, 7th and 8th plies. Debulking is the compacting and removal of air and volatile gases within plies of prepreg laminates under low heat and vacuum (Figure 5.5). This process promotes adhesion between the laid plies as well as significantly reducing wrinkling and other deformation during the curing process. Debulking was done via rolling over the plies in the fibre direction using a soft roller after low heat was applied via a hair dryer. This was followed by vacuum bagging for about 30 seconds.

Figure 5.5: Debulking in vacuum bag after applying low heat.

The 8 plies form a circular tube. Each successive ply would have its seam offset from the previous ply by 90 degrees around the circle to minimise their effect. After layup, the part was wrapped with a Nylon peel ply (stitch ply A Gurit). It was then wrapped using a perforated release film (A2200 P31251.3 red), followed by a layer of breather material (Airbleed 120 breather/bleeder woven polyester) and finally a layer of non-perforated release film (A6000 BNP Teflon) (Figure 5.6).

The perforated release film allowed excess resin to drain away though the breather cloth. The breather cloth created a pathway for gases to escape. The non-perforated release film prevented any excess resin from adhering onto the outer mould.

(a)   (b)
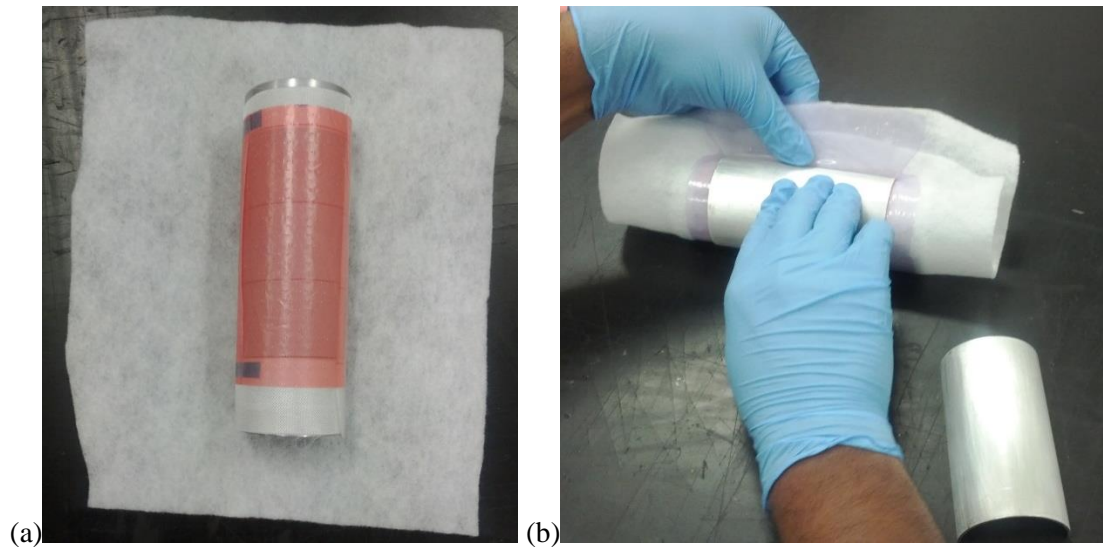
Figure 5.6: Applying perforated release film, breather cloth, non-perforated release film (a) and then the outer mould to the specimen (b).

The half-pipe outer moulds were then put over the top and taped closed (Figure 5.7). Another layer of breather was placed on top to ensure airflow path was unobstructed.
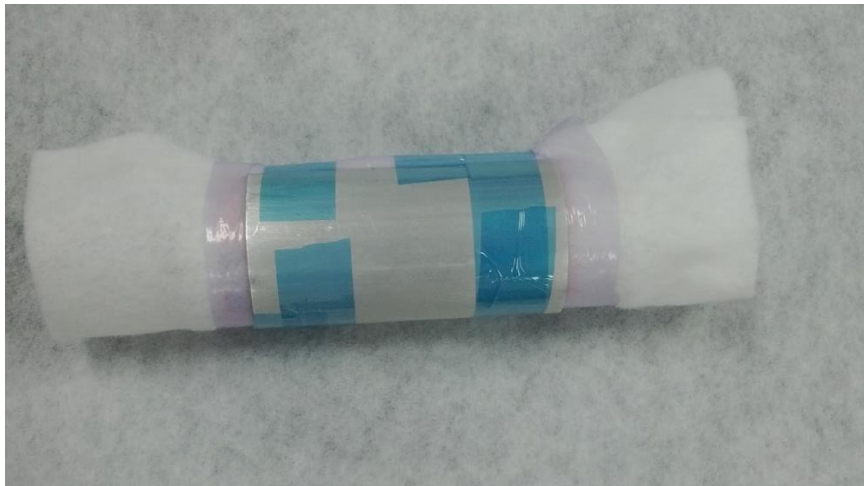
Figure 5.7: Applying perforated release film, breather cloth, non-perforated release film then outer mould.

The entire assembly was then sealed inside a vacuum bag, ensuring that there was a continuous loop for gas flow between the vacuum ports and the part. The SM5143 sealant (yellow) was used to seal the vacuum bag. Curing was completed in an autoclave (Figure 5.8).

Figure 5.8: Autoclave used in manufacture.

The vacuum ports provide a -1 bar pressure to the vacuum bag while the autoclave was pressurised to 4.5 bars (the recommended 7 bars was not used due to autoclave limitations). A heating rate of

2°C/min was applied until the part reached 180°C as measured by temperature probes placed near the part. The cure time was 120 min at 180°C. The entire assembly was allowed to cool naturally. The applied pressure was vented when the part cooled down.

Figure 5.9: Cured specimen.

After curing, the composite tubes were machined to the geometry specified in Figure 5.1. The tubes were fitted over a sacrificial mandrel in preparation for machining. The sacrificial mandrel minimise undesired damage to the composite tube during the machining process by supporting the composite as it is being cut. This minimises the tearing and delamination that often occurs when cutting composite laminates. Soft packing was used to prevent the lathe chuck from causing local damage to the composite. The cylinder was cut to 80 mm using a high speed side turning tool. Care was taken to ensure that the top and the bottom surfaces of the tube were parallel. Ample water-based lubricant was used during the cutting process. In addition to its lubricating effect, the liquid also carried away the heat generated in the cutting process to keep the temperature within the tolerance range of the epoxy matrix. The tulip trigger was then cut using a high speed steel end-mill with lubricant. The specimen (Figure 5.10) was removed from the sacrificial mandrel after cutting and the edges lightly sanded to remove any fragments that may still be attached.

Figure 5.10: Finished specimen.

With this process, a series of reliable samples was produced. As the layup and curing conditions were tightly controlled, there was little variation in the quality of the composite produced. A total of three batches of identical specimens were produced: two batches for low rate tests and one for high rate testing.

5.2.3 Test matrix for the experimental study

The chosen specimens were tested at a range of different test rates as detailed in Table 5.1. The number of associated specimens for each test is also listed.

Table 5.1: Test matrix.

	Low rate tests Screw driven testing machine		High rate tests Hydraulic testing machine		
Nominal strain rate	$2\times10^{-4}\,\varepsilon$/s	0.2 ε/s	30 ε/s	60 ε/s	100 ε/s
Nominal platen speed	1.7×10^{-5} m/s	0.016 m/s	2.4 m/s	4.8 m/s	8.0 m/s
Number of specimens	9	8	4	5	7

The maximum test speed was limited to 8m/s for the test machine used. The low speed study consists of two test speeds: 1.7×10^{-5} and 0.016 m/s, with a nominal strain rate of $2\times10^{-4}\,\varepsilon$/s and 0.2 ε/s respectively. Three test speeds, 2.4, 4.8 and 8.0 m/s, were chosen for the dynamic study. This corresponds to a nominal strain rate of 30, 60 and 100 ε/s respectively for a specimen with an 80mm length in the loading direction.

A series of drop tests, performed on a representative fuselage section at NASA [33] were performed against rigid, water and soft soil surfaces at 11.7, 7.6 and 11.4 m/s respectively on 508mm long energy absorber section which corresponded to a nominal strain rate of between 15 and 23 /s. This represented the expected strain rates in a crash situation. Data in JSSG-2010-7 [3] indicates that survivable impacts were typically below approximately 15m/s, which correspond to a strain rate of 30 ε/s for the NASA specimens. Hence, 100 ε/s is a suitable upper limit of the strain rates likely to be encountered during a crash situation.

A number of specimens were tested at each nominal strain rate to obtain a large sample size. This was done to provide a meaningful estimate of the variation in the specimen response, which allows for the estimation of spread present in the test configuration. A significant spread was observed in Palanivelu's [43] low speed tests which becomes more pronounced when the specimen geometry becomes increasingly complex. This variability is compounded by the dynamic nature of the high speed tests [32].

5.2.4 Testing method for the experimental study

The low rate tests ($2\times10^{-4}\ \varepsilon$/s and 0.2 ε/s) were performed on a screw-driven testing machine (Figure 5.11(a)). The specimens were rested freely on a steel platen while another steel platen descended on the specimen at the designated speed. The force measurement was recorded from the load cell attached to the top platen and the displacement was obtained from the moving crossbar. Examinations of the crushed specimens were post-test to determine the overall damage mechanism within the specimen during the crushing process. The crush stroke was set to be 40mm. This arrangement allowed the steady state crushing to be fully developed after the consumption of the trigger mechanism.

(a)   (b)

Figure 5.11: Screw-driven (a) and hydraulic testing machine (b) used in this study.

The high rate tests (2.4, 4.8 and 8.0 m/s) were completed on a hydraulic testing machine (Figure 5.11(b)). In contrast to the screw-driven testing machine, the hydraulic testing machine has a fixed upper platen with attached load cell while the bottom platen moves upwards to crush the specimen in between. The specimen was fixed on the bottom platen with a small amount of adhesive. During the test, the platen was accelerated to the desired test speed along with the test specimen. The purpose of the adhesive was to hold the specimen to the platen as they accelerated to the test speed. The crush stroke was nominally set to 40mm. This was the region where the platen speed was kept

constant where possible. The platen then progressed approximately another 20 mm. This was required so that the hydraulic system to bring the piston and attached platen to a complete stop at the end of the test. This means that the platen speed at the beginning of the test was higher than the speed when the 40 mm of nominal stroke has almost been completed. In order to achieve the correct test speed over as much of the test stroke as possible, a velocity profiler was used. The velocity profiler takes the resulting speed profile of the previous test and compares that against the desired speed. This comparison was then used to adjust the drive parameters for the hydraulic system to achieve a better match between the desired and actual speed. Despite the use of profiler, variation in the platen speed was observed but this did not have a significant bearing on the results obtained. The selected sampling frequency of the recorded displacement and load history data was increased to compensate for the increasing rates of loading.

The screw-driven testing machine yields a precise and constant test speed in comparison with the hydraulic driven testing machine. The force and displacement history data obtained from the hydraulic testing machine was truncated to ensure that all data were captured at a test speed that was within a reasonable range of the target test speed. The speed range that applies to each set of results is shown in Table 5.2.

Table 5.2: Platen speed range for the performed tests.

	Low rate tests Screw driven testing machine		High rate tests Hydraulic testing machine		
Actual test speed	1.7×10^{-5} m/s	0.016 m/s	2.6-2.0 m/s	5.0-4.0 m/s	8.3-5.5 m/s
Valid test data sets	6	6	4	5	7

5.3   Experimental results

5.3.1   Low strain rate tests

All tests were conducted at room temperature. Prior to testing, the geometry of each specimen was measured and recorded (see Appendix). Results show that the manufacturing method was effective and the reference geometry was achieved in almost all specimens. The standard deviations of the thickness and outer diameter in specimens without identified defects were less than 3% and 1% respectively. Pre-test visual inspections of the specimens were also conducted to check for defects and imperfections. The outer and inner surfaces of the tube free from ripples in general. Machining damage was found to be confined to a small region immediately adjacent to the machined surface.

Some manufacturing defects were detected in the low rate samples and Figure 5.12 shows the effect of different manufacturing defects on the performance of the specimen. A resin rich cure leaves extra matrix material in the specimen so the designated fibre volume fraction was not achieved. These resin rich specimens had a thickness of 1.21 mm in contrast to the 1.14 mm average. The extra resin caused an increased in the outer diameter as well as the appearance of minor undulations to be present on the surface of the tube. An increase in the plateau force, due to the thicker specimen, was observed from the results.
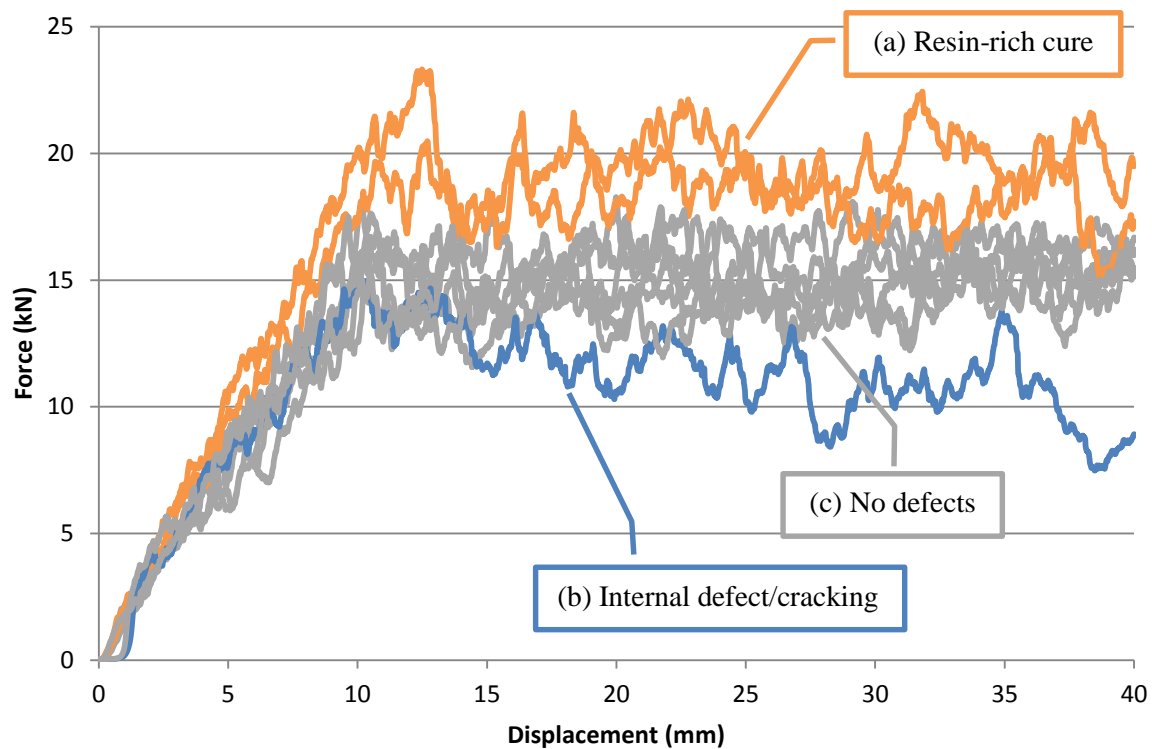
Figure 5.12: Comparing responses of specimens (a and b) with identified defects and (c) without defects.

Another potential defect was the internal weakness or cracking which accompanied a reduced thickness (1.09 mm). These defects were not readily visible as they were embedded inside the laminate and non-destructive evaluation methods such as C-scan were required to detect these. The defect cause rapid unsteady damage growth which can be heard as loud cracks during the test. The expected decrease in plateau force magnitude as a result of the defect was clearly visible in the results.

5.3.1.1 Typical low strain rate response

Figure 5.13 shows a typical response of an energy absorber being tested at quasi-static or low nominal strain rate. The response curves of the low rate tests were very similar. The general shape of the response curves was consistent with expectation (Fig 2.2), consisting of a trigger region followed by a force plateau.
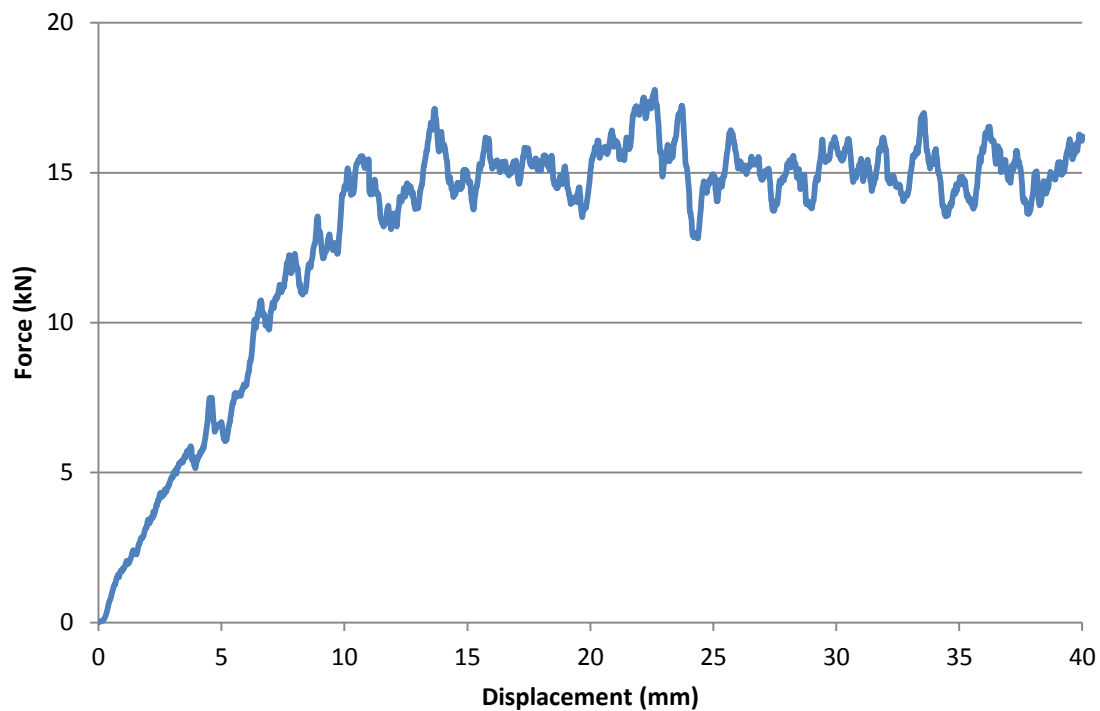
Figure 5.13: Typical force-displacement curve for low rate tests.

During the initial stage of the test (less than 10mm displacement), the trigger mechanism was being crushed. This region is characterised by an almost linear increase in load with respect to displacement. This is indicative of the gradual and progressive consumption of the trigger as desired.

When the displacement was between 7 and 15 mm, the transition from crushing of the trigger region to the crushing of the bulk tube occurs. This transition occurs very smoothly as no sudden peaks were observed in the force trace. The lack of a distinct peak force is evidence for the effectiveness of the trigger mechanism. The overall peak load is very close to the average plateau load. This is advantageous in crashworthiness terms as the bulk of the energy is absorbed at or near the peak force. In this case, crash protection is limited by the energy absorbing capability rather than the peak force. This leads to a more efficient absorption of crash energy compared with designs that have a significantly higher peak load than the average plateau load. By optimising the trigger in Design A in Figure 5.14, a lower peak force was achieved and a design with higher energy absorbing capacity can

be used where the design is constrained by a maximum allowable load dictated by tolerances of the
human body.
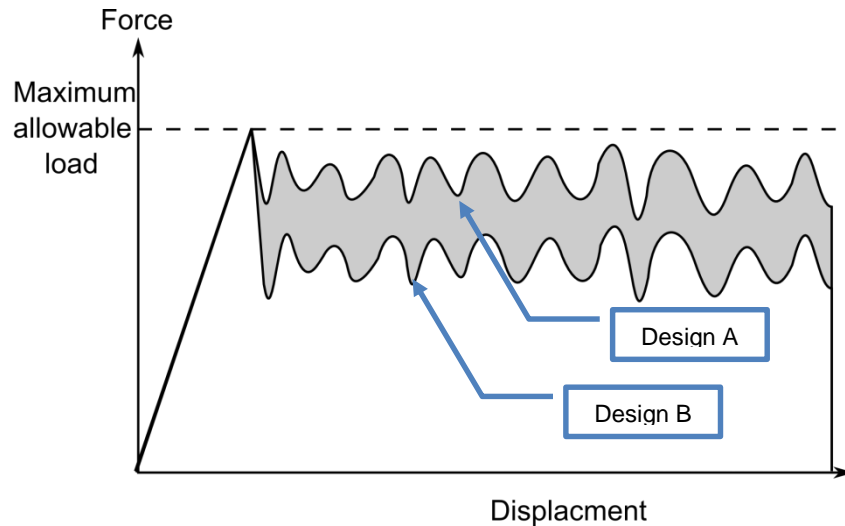
Figure 5.14: Increase in energy absorbed (grey region) when the plateau load approaches the peak load for a

given allowable peak load.

Beyond 15mm displacement, the specimen enters a progressive crushing stage where the force
plateaus. The oscillation in loading was relatively small compared to the overall force magnitude. The
lack of spikes and troughs indicates that there were no catastrophic damage events, suggesting that the
bulk tube is being consumed progressively. Consequently, the energy absorption was spread over a
large displacement interval, which acts to cushion the impact event. The test was completed when the
displacement reached 40mm so that the test specimen does not disintegrate. Since the energy absorber
is designed to absorb the impact energy before bottoming out, the behaviour past this region is not
important.

5.3.1.2 Typical low strain rate damage pattern

Figure 5.15 and Figure 5.16 show the energy absorbing specimen at various stages of crushing.

(a)   (b)
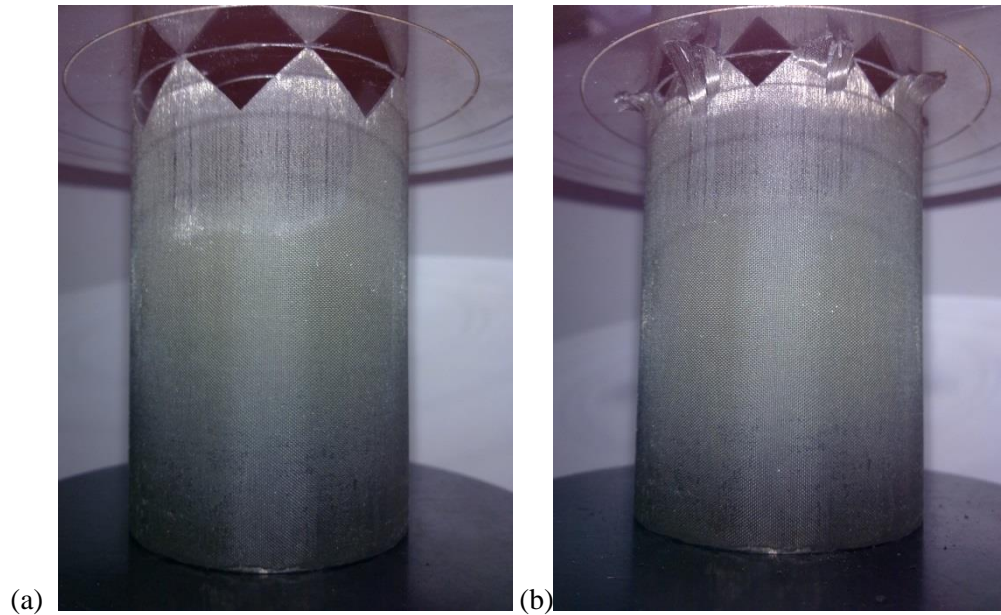
Figure 5.15: Specimen at the start of test (a) and when half the trigger had been consumed (b).

Figure 5.15 (a) shows a very early initiation of damage. The sharp tip of the tulip trigger splits very easily, creating a reliable pathway for damage to progress through the structure. The trigger region performs as expected, slowing increasing the damage region from the eight tulip peaks to covering the entire circumference of the tube. Figure 5.15 (b) shows the advance of delamination that occurs throughout the test. The outer plies separate from the bulk of the tube, with delamination extending a significant distance past the crush front where most of the damage to the internal plies occurs. The splaying of the outer-most ply prompts splitting to occur parallel to the fibre direction. The lengths of these splits are closely related to the amount of delamination currently experienced by the ply.
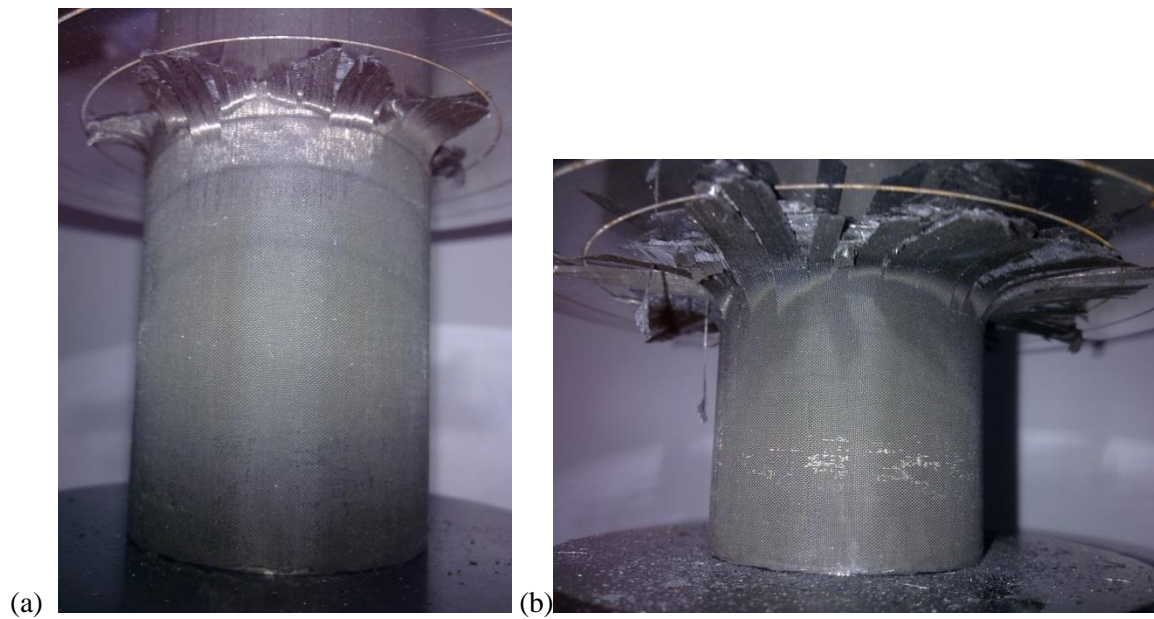
Figure 5.16: Specimen after the trigger has been completely consumed (a) and during steady state crushing of

the bulk tube (b).

The damage pattern before and after the end of the trigger region is similar, indicating a smooth

transition from the trigger region and the bulk tube (Figure 5.16). The debris is mainly trapped

between the platen and the tube. The debris is mostly held in place by the outer-most ply, which

undergoes significantly less damage than other plies. As the damage progresses, more debris

accumulates between the tube and the platen. Smaller pieces of debris begin to fall through the gaps

opened as the outer ply splits (Figure 5.16 (b)).

The outer-most 0 degree ply remains relatively undamaged throughout the test as shown in

Figure 5.17. As the matrix material between the fibres is much weaker, they are preferentially

damaged. As a result of the formation of cracks parallel to the fibres, the outer ply is allowed to bend

away from the platen and avoids further damage. This was mirrored by the inner-most 0 degree ply in

Figure 5.18 (1). The inner ply undergoes more significant bending due to the available internal space

is taken up by the debris generated. These two plies support the layer of debris and hold them in place

between the platen and the specimen.
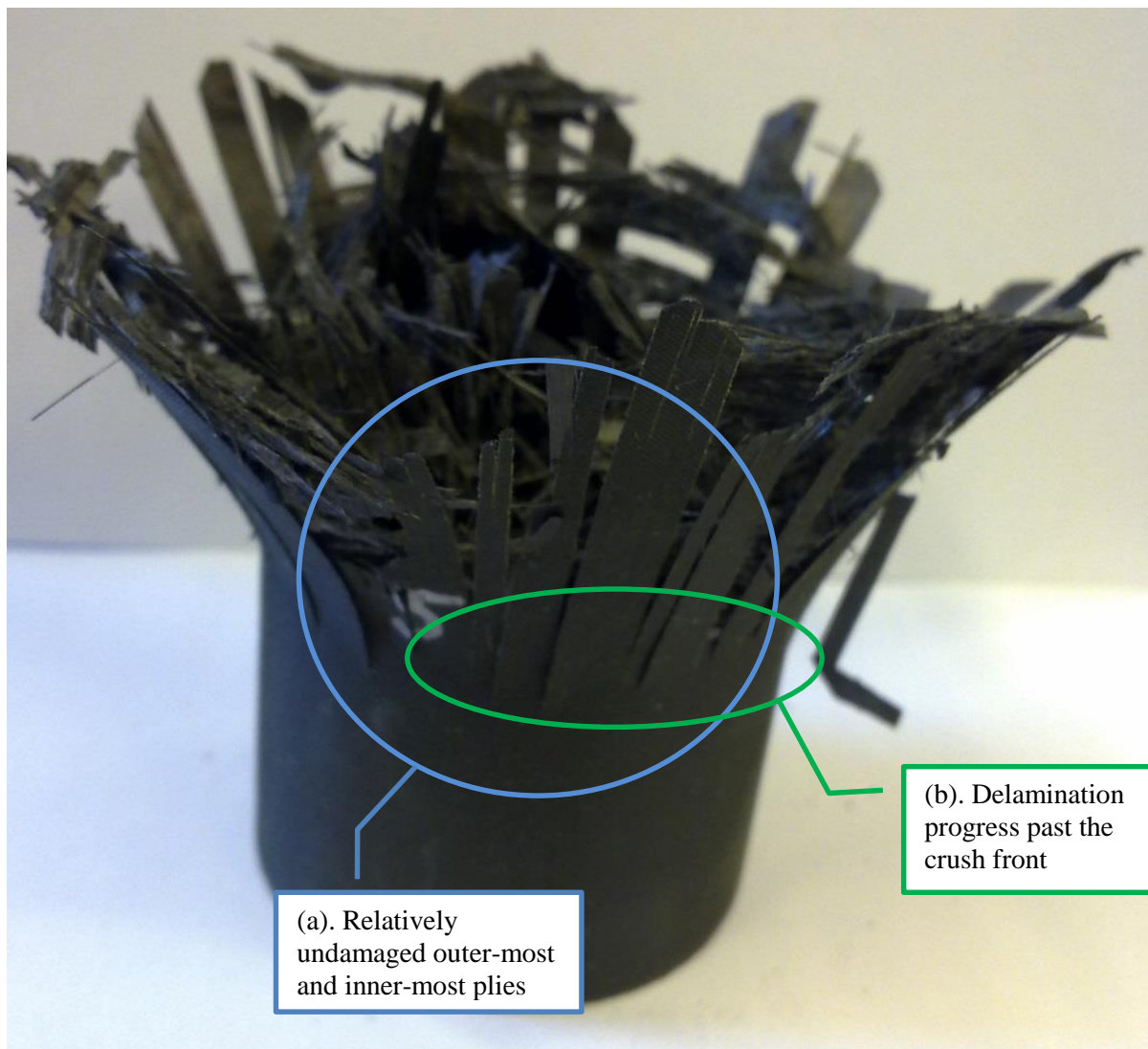
Figure 5.17: Post-test side view of specimen showing debris held in place by the outer-most ply.
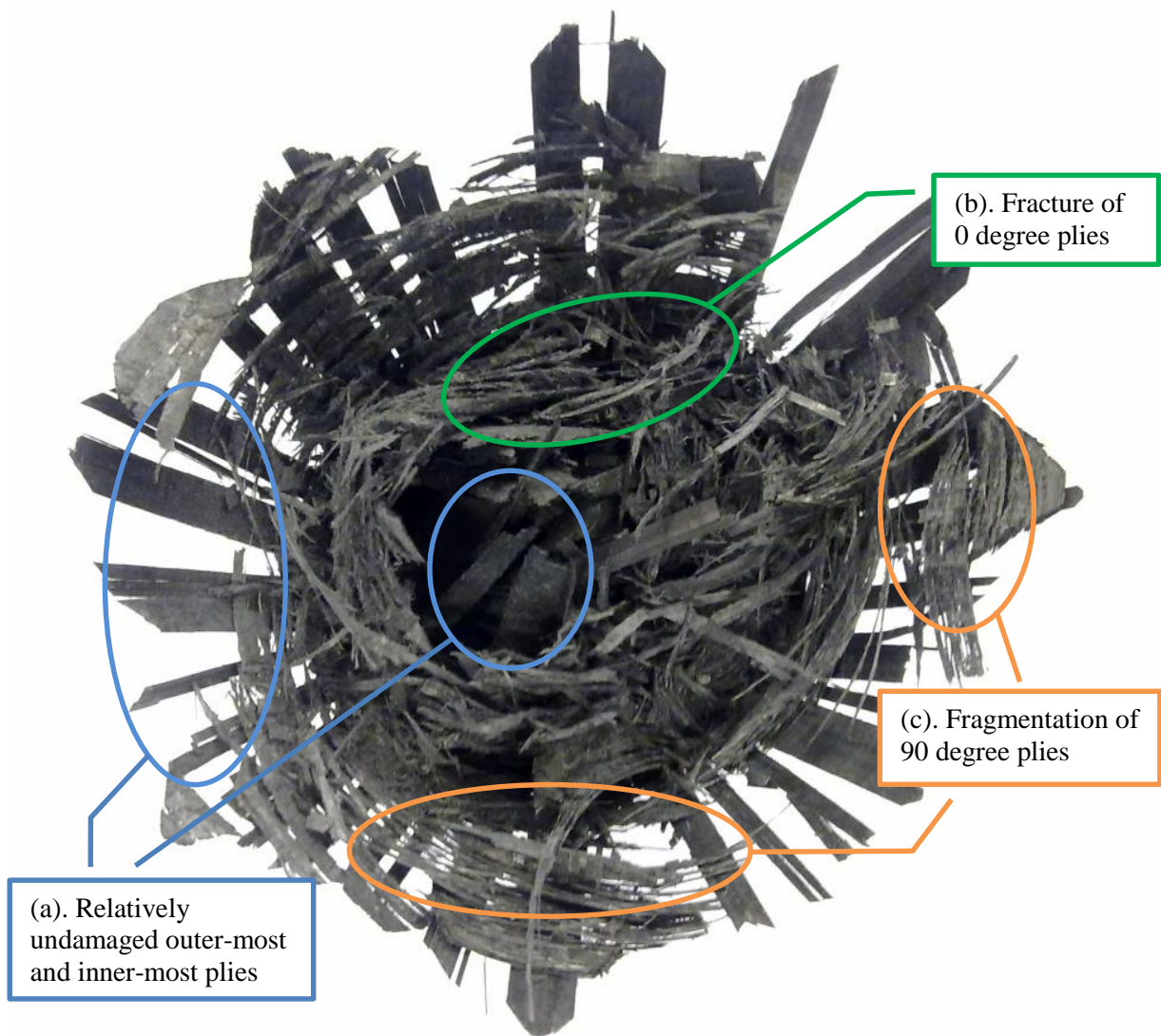
Figure 5.18: Post-test top view of specimen showing difference damage mechanisms.

Internal plies, regardless of whether the orientation was at 0 degree or 90 degree with respect to the

loading direction, suffered significant damage. Complete crushing of the internal plies was observed

in Figure 5.18 with the resulting debris bearing little resemblance to the original plies. Significant

differences were observed in the damage between the different orientations. The fibres in the 0 degree

plies tended to break into smaller pieces (Figure 5.18 (b)). These fragments were typically short and

wide. In comparison, the fibres in the 90 degree plies, which originally ran the circumference of the

tube, tended to split into 3 to 4 segments and form thin tendril-like pieces (Figure 5.19).

137

Figure 5.19: Close-up of fragmentation of the internal plies.

The difference in the damage morphology can be explained via the different damage mechanism triggered by the loading conditions. In the 0 degree plies, the main form of damage was brittle fibre breakage accompanied by matrix shearing as fibres give way as illustrated in Figure 5.20. The majority of loading is borne by the fibre. Longitudinal loading causes bending in the fibres and this is resisted by the matrix material connecting the fibres. This axial instability is amplified when the matrix fails, which in turn cause fibre breakage.
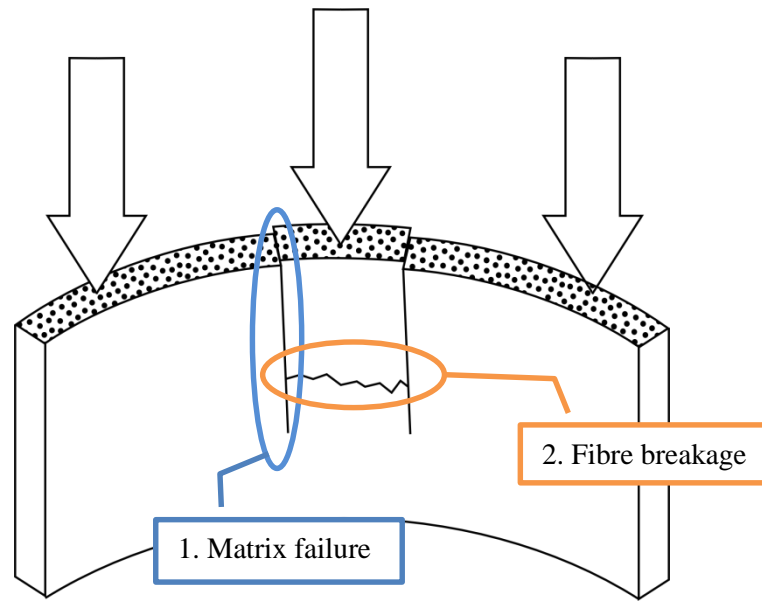
Figure 5.20: Idealised 0 degree ply damage mechanism.

On the other hand, the main form of damage in the 90 degree plies were shear matrix cracking parallel to the fibre with limited amount of fibre breakage due to hoop stresses as illustrated in Figure 5.21. In this instance, the load is predominately borne by the matrix material. Vertical loading loads the matrix in compression. The associated failure mode is shear crack formation parallel to the fibres. When the material detach from the bulk tube, the increase in hoop stress cause fibre breakage in the detached rings of material.
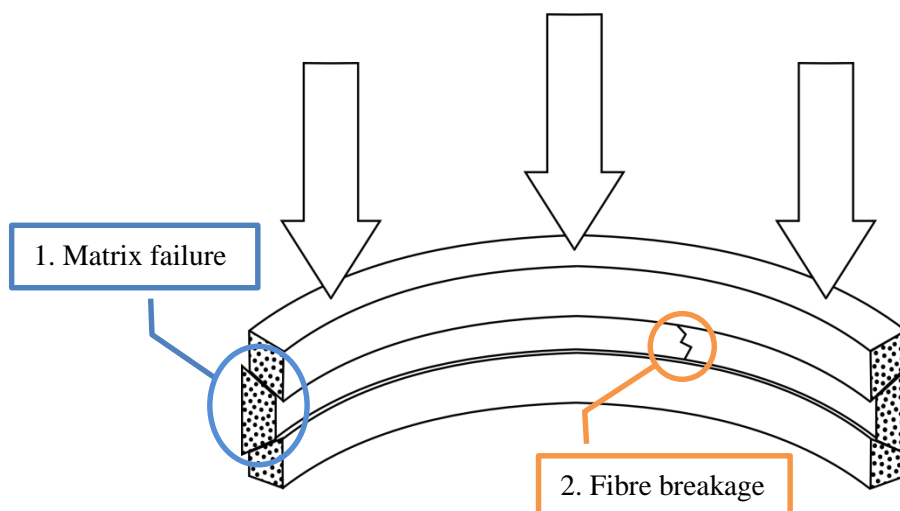
Figure 5.21: Idealised 90 degree ply damage mechanism.

The obtained damage distribution compares well with similar tests previously published in the literature. Huang et al.[65] performed static crush test on a pair of chamfered composite tubes made with unidirectional prepreg. Figure 5.22 shows the damage distribution of Huang's specimen. A significant portion of the 0 degree plies sustained relatively little damage, consisting mainly of splitting along the fibre and subsequent splaying. The 90 degree plies also formed thin segments which were hidden behind the 0 degree plies due to the layup used. The smaller the overall size of the fragmentation is likely due to higher fibre volume fraction of the prepreg used in the present experimental study. The comparatively resin rich samples in Huang et al.[65] were better at holding the fibres together during the crushing process.
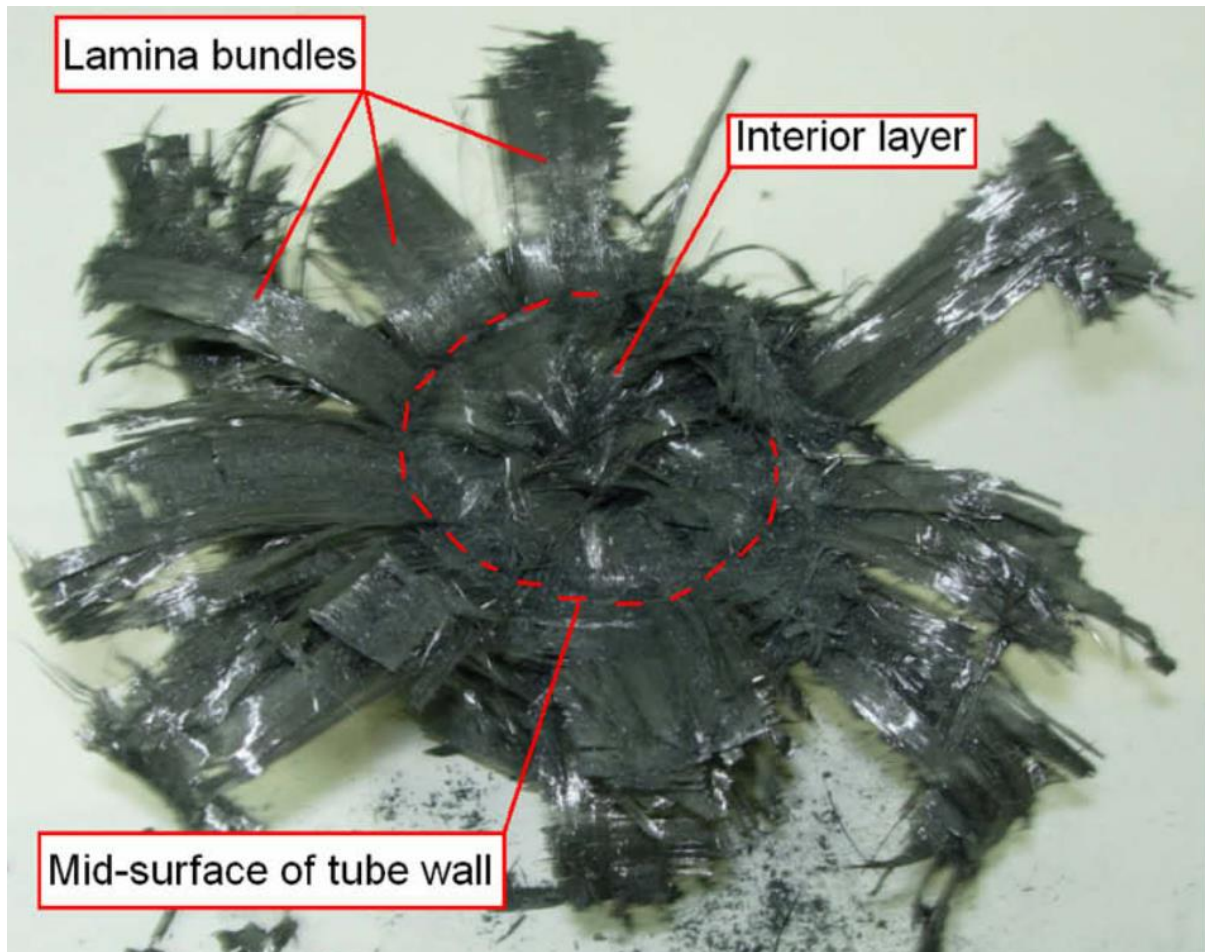
Figure 5.22: Damage pattern of a statically crushed cylindrical tube [65].

140

Similarities in the damage pattern can also be observed in the progressive crushing of specimens with different geometry and composition. Splaying and fragmentation similar to those observed in this experimental study was reported by Jackson et al.[54].

Jackson et al. used a woven material in contrast to the unidirectional plies used in the present study, which caused the fragments in Figure 5.23 to be more interweaved, forming a mat like structure. Despite this difference, the C-shaped specimens exhibited clear splaying of plies that are adjacent to the surface of the laminate, with splits running down the length of the splayed plies. The general size of the fragmentation debris was also similar.
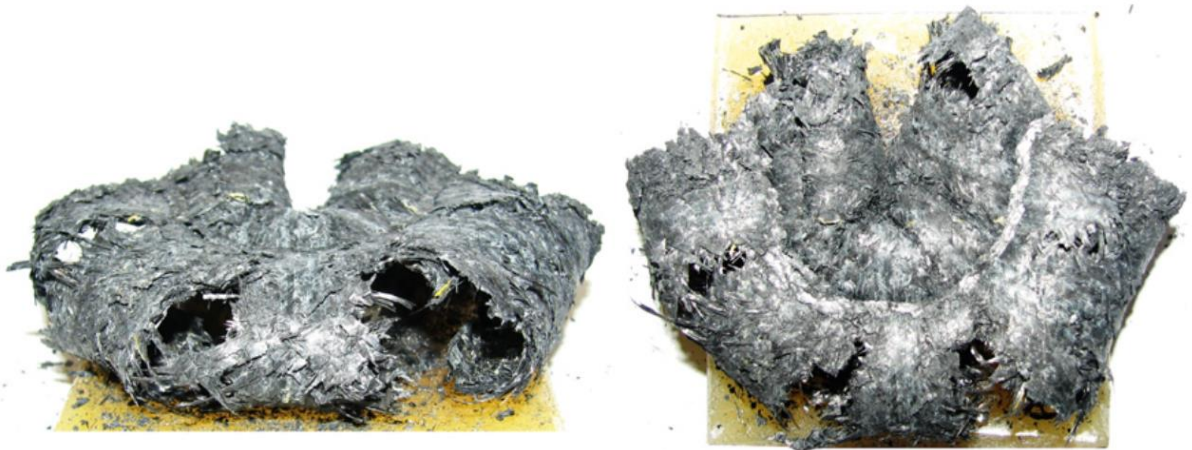
Figure 5.23: Damage pattern of a statically crushed C-section [54].

5.3.1.3 Overall low strain rate results

Once the results with known defects were removed, the overall responses of these specimens were very consistent. The responses of specimen tested at 1.7×10^{-5} m/s are shown in Figure 5.24. The variation observed between different specimens during steady state crushing was approximately the same as the force variation of a single specimen during steady state crushing. The same trend and consistency was observed in the specimens tested at 0.016m/s (Figure 5.25).
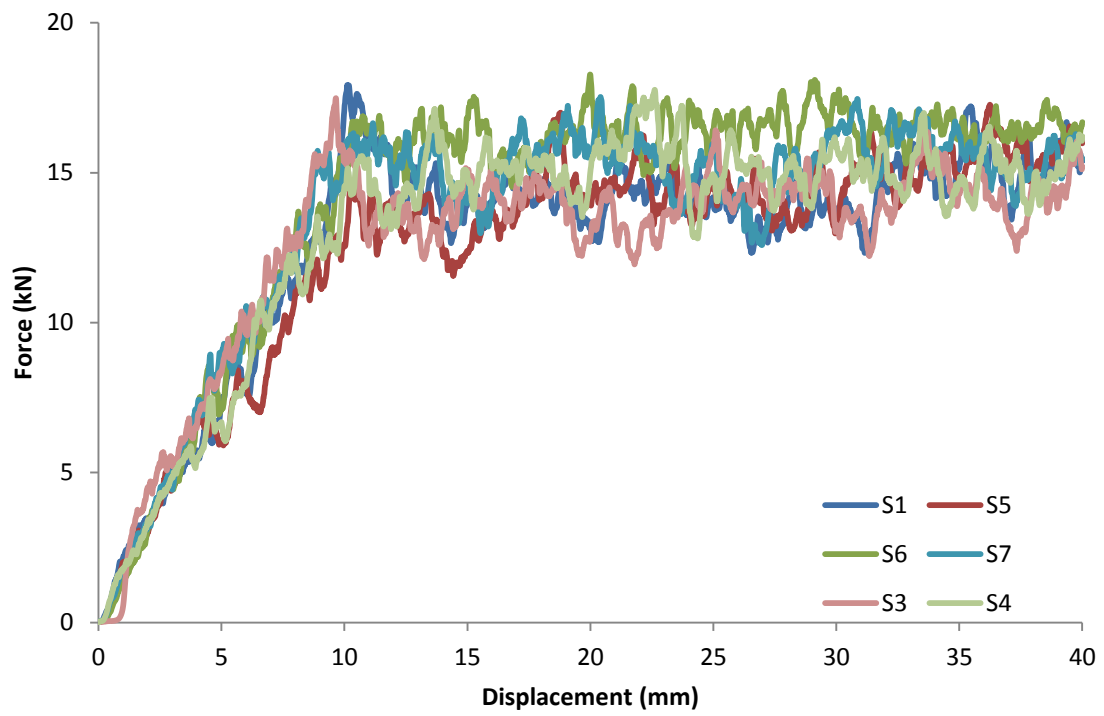
Figure 5.24: Force-displacement curves for quasi-static tests.
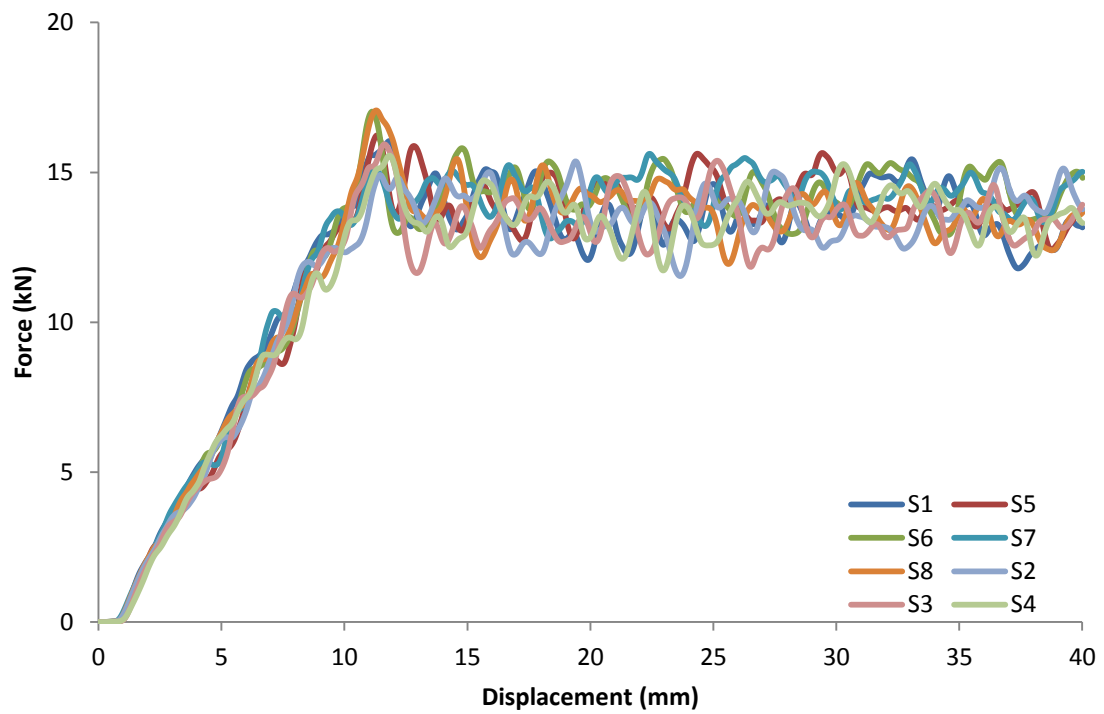
Figure 5.25: Force-displacement curves for 0.2 ε/s tests.

5.3.2 High strain rate tests

5.3.2.1 Typical high strain rate specimen response

The observed force-displacement curve (Figure 5.26) is very similar in overall shape to those seen in the low rate tests. Likewise, the trigger regions in the specimens of the dynamic tests performed within expectation to produce a nearly linear rise in force before coming to a plateau was observed. A force plateau was also observed during the progressive crushing of the bulk tube. In comparison with the low rate tests, the higher test rates have increased the magnitude of noise in the force data over the steady state crushing zone.

In contrast to the low rate tests, where the peak force is expected to occur during the transition from triggering to steady state crushing, the peak force was generally observed during force fluctuations in the steady-state crushing region. This effect was a due to the combination of the smoothing effect of the trigger mechanism sometimes delays the onset and the magnitude of peak force and the increasing oscillatory noise during steady-state crushing.
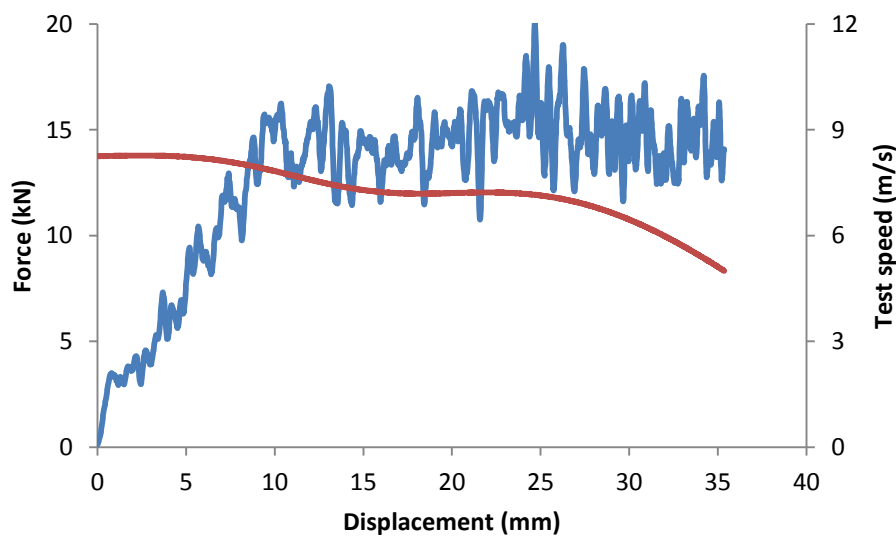
Figure 5.26: Typical specimen response (blue) at 8.0m/s with the actual velocity profile (red).

143

Despite the use of an adhesive to hold the specimen to the accelerating platen, some specimens detached from the platen during the acceleration phase. This caused the specimen to hit the upper platen prematurely, resulting in the response curve in Figure 5.27. The first small force peak occurs at first contact between the detached specimen and platen, after which the accelerating platen catches back up to the specimen, forming the main force response curve. Both the force gradient during the consumption of the trigger region and the magnitude of the peak and steady-state forces compared well with specimens that did not detach. The amount of noise and vibration in the plateau region was also similar. The detachment had little impact on the total energy absorption of the specimen. Hence, once the specimen settles between the platen, the crush performance of detached specimens is indistinguishable from the response of undetached specimens at the same stage of crushing.
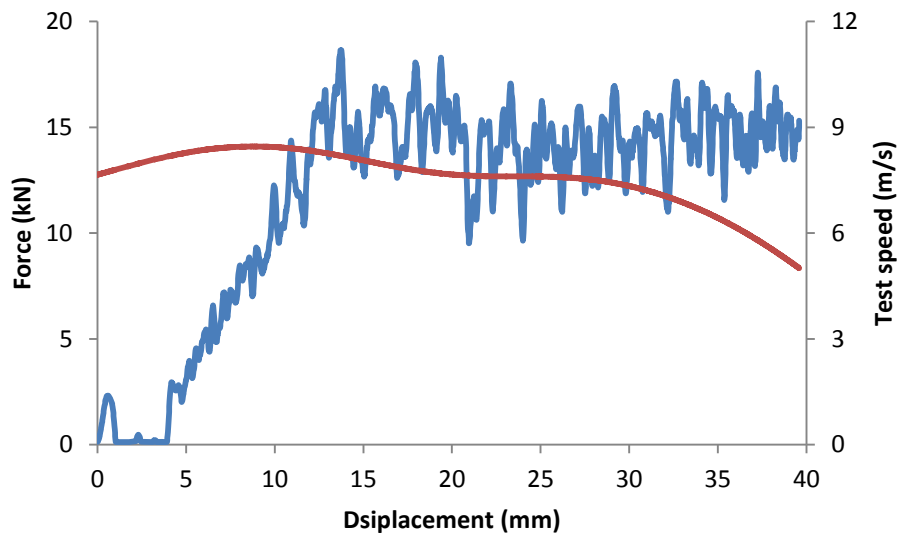
Figure 5.27: Typical specimen response with detached sample (blue) at 8.0m/s with the actual velocity profile (red).

5.3.2.2 Typical high strain rate damage pattern

Figure 5.28 shows the specimen during various stages of crushing in a dynamic test.
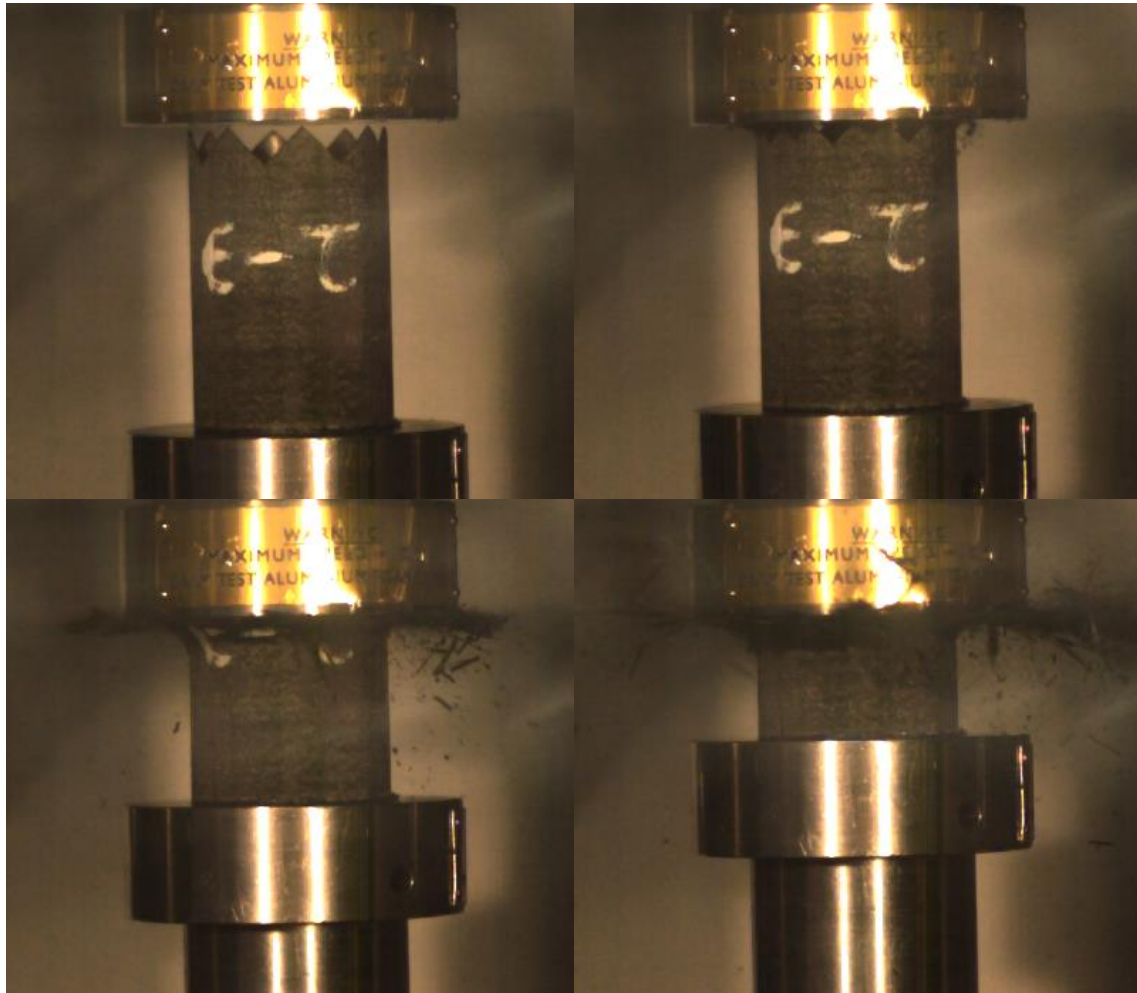
Figure 5.28: Progression of dynamic crush test (clockwise from top left).

Despite the increased tests rate, the crush progression was very similar to that of the low rate tests.
There was also comparatively little damage done to the outer-most ply. The fibres of the outer ply
remained mostly intact. The ply was split along the fibre direction at multiple locations to produce the
splaying observed in Figure 5.29 and Figure 5.30. Significant delamination of this outer ply was also
observed to extend past the crush front. Similarly, the damage done to the inner-most ply was
concentrated in cracks running parallel to the fibres with little fibre breakage. The debris formed from
the internal plies was held in place by the outer-most and the inner-most plies.
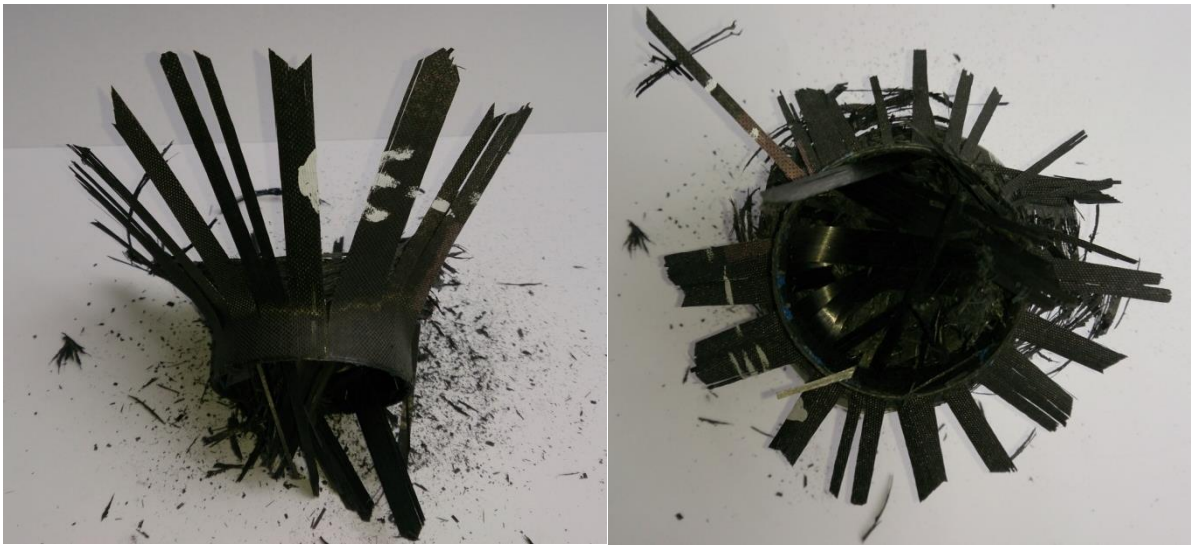
Figure 5.29: Post-test view of dynamic specimen showing the relatively intact outer-most and inner-most plies.

Figure 5.30: Post-test view of dynamic specimen showing concentration of debris near the centre.

Debris formation was similar to that in the low rate tests. Both short and wide fragments from the 0

degree plies and long tendril-like debris from the 90 degree plies were observed in the specimens.

Damage mechanisms described in Figure 5.20 and Figure 5.21 are also applicable here. The higher

146

strain rate has caused the debris to be concentrated in the central region, whereas the debris in the low

strain rate tests remained spread over the splayed outer ply. This is likely to be a result of the debris

not having sufficient time to move radially along with the splaying ply in the high rate tests.

5.3.2.3 Overall high strain rate results

The test speed profile was improved over a few iterations using the velocity profiler (Figure 5.31 to

Figure 5.33). The change was especially apparent at the beginning of the test. As nominated test speed

increased, there was an increased reliance on the profiler to provide the tuning to hydraulic drive

parameters in order to achieve the nominated test speed over the test displacement.
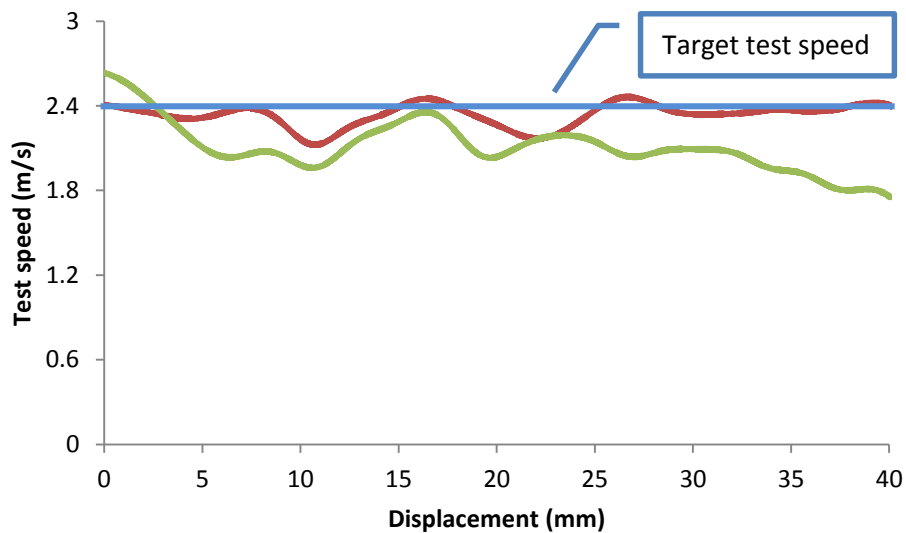
Figure 5.31: Speed profile of the first (green) and last (red) 2.4 m/s test.
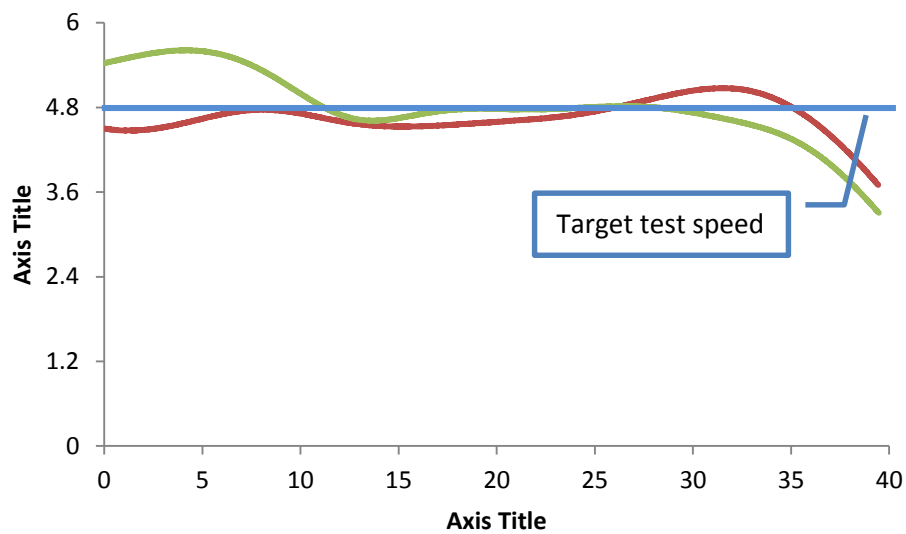
Figure 5.32: Speed profile of the first (green) and last (red) 4.8 m/s test.

The drop in tests speed during the final 5 to 10 mm of test stroke that is particularly noticeable in Figure 5.32 and Figure 5.33 were an indication of the limitation of the testing machine. This drop in test speed was caused by the need to decelerate the platen to a rest at the end of the test. The platen needs to be stopped before the entire specimen has been crushed. This allows the uncrushed "base" of the structure holds the debris in place so the damage pattern can be observed. The length limit of the specimen means that the deceleration process sometimes begins before the designated crush stroke has been completed.
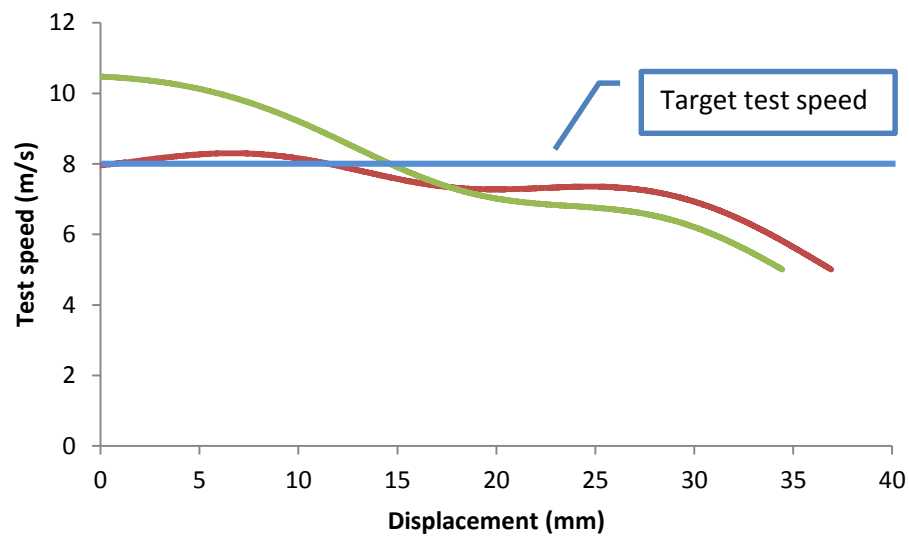
Figure 5.33: Speed profile of the first (green) and last (red) 8.0 m/s test.

The force responses obtained from the different specimens for a given test speed were very consistent (Figure 5.34 to Figure 5.36). The overall amplitude of the noise in the plateau region increased with increasing test speed. A noticeable increase in overall oscillation can be observed in the 8.0 m/s tests. This increased noise caused a larger spread in results than the low rate tests. However, the shape of the overall response was indistinguishable from that observed in low rate tests.
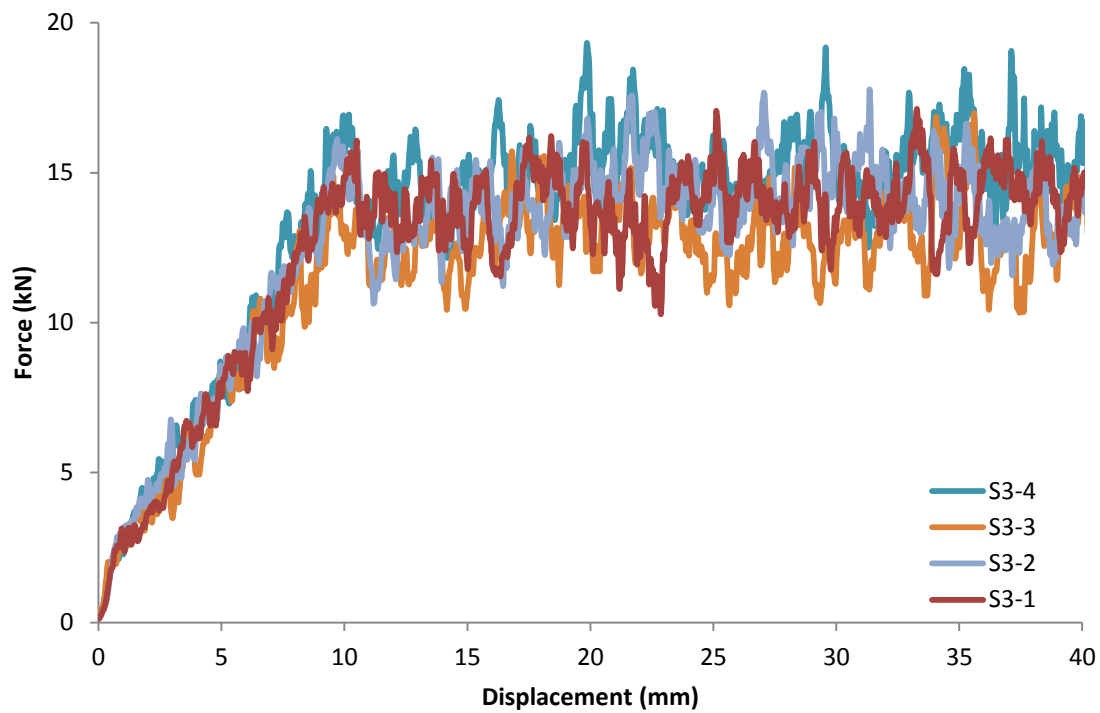
Figure 5.34: Force-displacement curves for 2.4m/s tests.

For one specimen in the 4.8m/s and three specimens in the 8.0m/s, the adhesive used was insufficient to hold the specimens on the accelerating platen, causing premature contact with the upper platen. A likely cause of this detachment issue was the adhesive was not given sufficient time to set before the test was run. The close resemblance between the overall responses of the specimens, regardless of whether the specimens detach from the bottom platen is shown in Figure 5.35 and Figure 5.36.
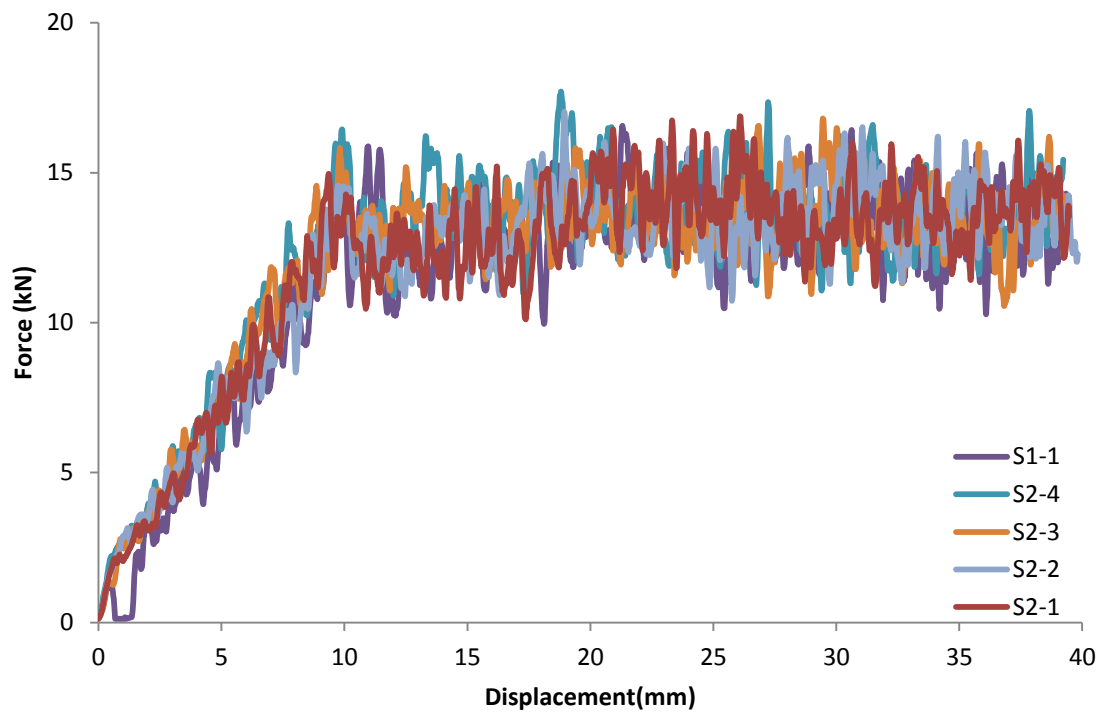
Figure 5.35: Force-displacement curves for 4.8m/s tests.
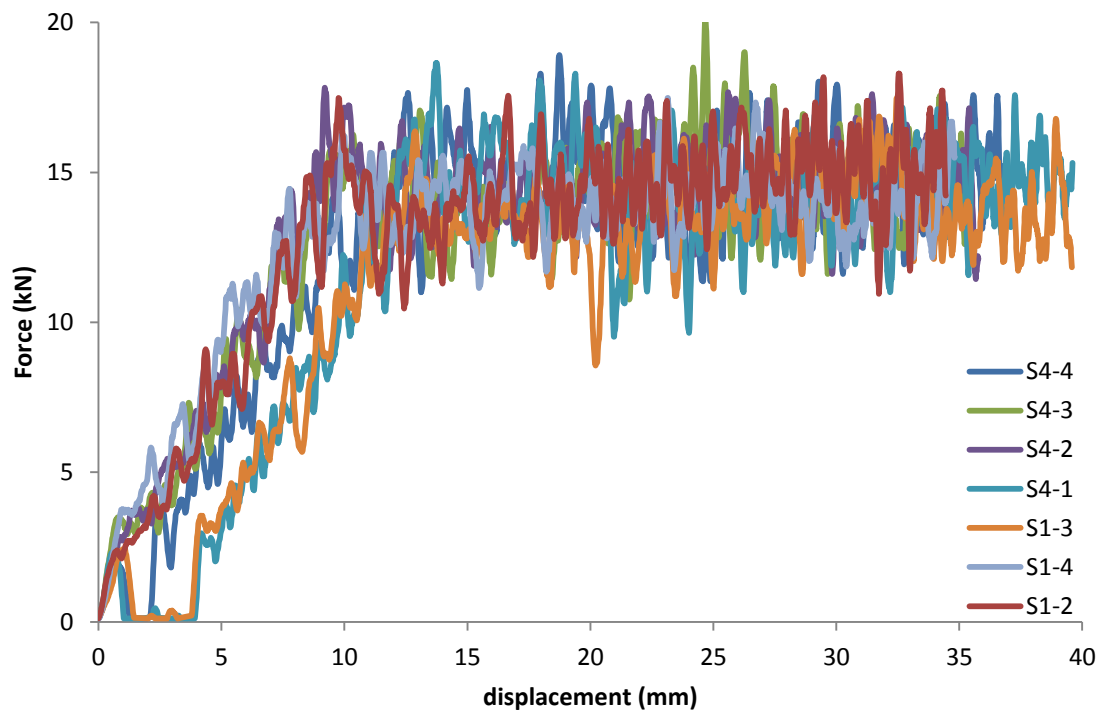
Figure 5.36: Force-displacement curves for 8.0m/s tests.

Significant oscillatory noise was also recorded for both the high rate tests. The average amplitude of the oscillations are summarised in Table 5.3. A clear increase in the amplitude of these oscillations with the increase in test rate was observed.

Table 5.3: Oscillation amplitude during steady-state crushing.

	Low rate tests Screw driven testing machine		High rate tests Hydraulic testing machine		
Nominal strain rate	$2\times10^{-4}\ \varepsilon/s$	$0.2\ \varepsilon/s$	$30\ \varepsilon/s$	$60\ \varepsilon/s$	$100\ \varepsilon/s$
Average oscillation amplitude (kN)	4.7	3.4	7.0	6.6	8.1

5.4   Discussion

5.4.1   Data reliability

Experimental results in the literature generally only test a small number of specimens for each configuration and hence are unable to measure the amount of spread associated with each configuration. As shown in the low rate tests, defects in composite structures significantly affect performance and may not necessarily be detectable upon visual inspection. This can skew observed results. A large sample size (between 4 to 7 samples for each test configuration) used in this program allows the spread to be measured that mitigate the risk of variation in results. This is in contrast to many authors ([53], [55], [23], [32]) tested only one specimen per test configuration in a bid to maximise the number of different configurations that can be tested.

Consistency and repeatability is a good indicator of the reliability of obtained results. There was little variation in the responses observed between different samples within a batch. The magnitudes of one standard deviation were less than 8% of the mean value for every metric measured under the different test rates.

The responses observed between different samples within a batch for each testing condition was also very consistent in terms of the damage pattern and underlying damage modes. Two typical specimens in the low rate test (Figure 5.37) show this consistency.
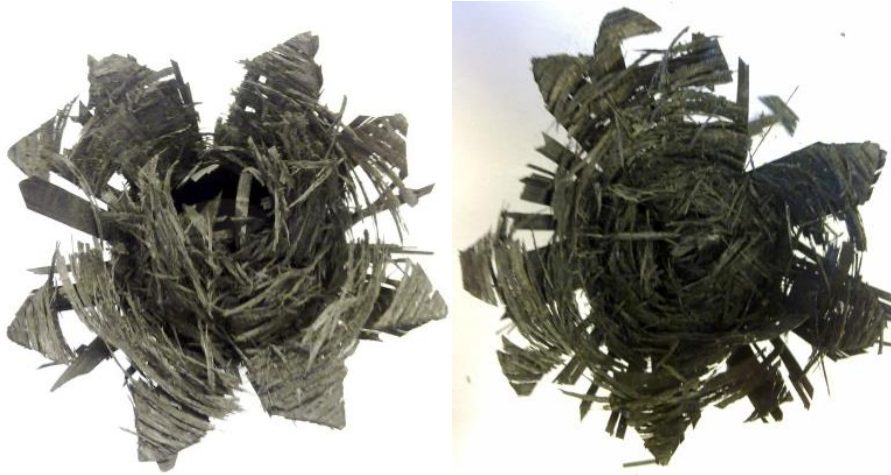
Figure 5.37: Similarity of laminate damage modes between two specimens from the 1.7×10^{-5} m/s test.

As a result, the small scatter in the measured metrics and the consistency in the observed damage modes give weight to the conclusions drawn.

5.4.2 Tulip triggered tube as a representative energy absorber

The chosen tulip triggered tube configuration exhibit characteristics that would allow it to perform well in a crash protection application. These include:

- Reliable crush response,

- Stable damage initiation and progression,

- Comparable SEA to those in the literature,

- Progressive crushing, and

- High crush efficiency.

As these characteristics are common to optimal energy absorber designs, the results from the current study is suitable for use as a representative energy absorber specimen against which the developed material model can be benchmarked. A model capable of reproducing the force response and damage

distribution pattern of this specimen is likely to be able to do the same with other composite energy absorber designs intended for crashworthiness applications.

5.4.3   Effect of strain rate on specimen response

A comparison between key metrics used to determine energy absorber performance between the different loading rates is used to assess whether the structural response is rate dependent. The average value was taken of all the specimens tested at the same nominal strain rate. The error bars were indicative of one standard deviation away from the mean.

The steady-state crush load occurs after the triggering and represents the force experienced during crushing of the bulk tube. This value did not vary significantly with the test rate (Figure 5.38).
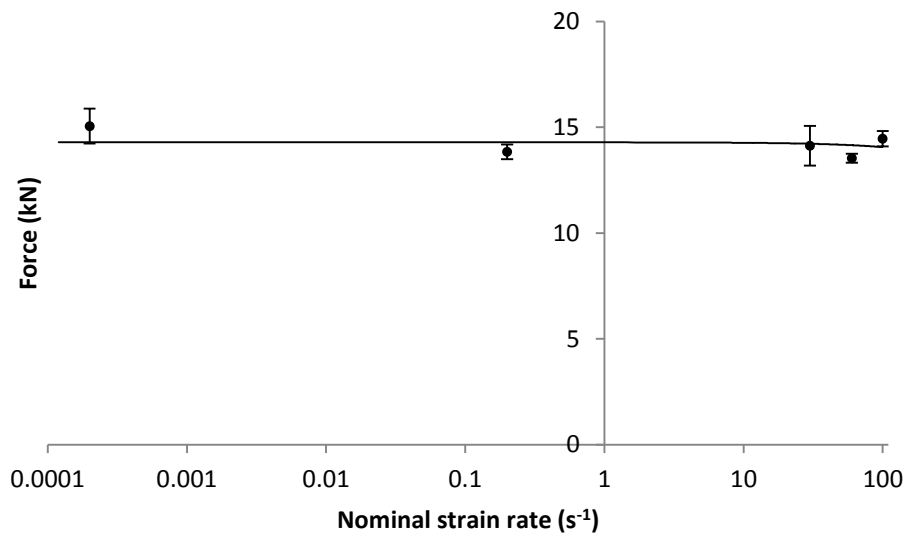
Figure 5.38: Steady-state crush load during progressive crushing.

The peak force is the maximum force experienced during the entire crushing process. The peak forces displayed a slight upwards trend with increasing testing rate, as shown in Figure 5.39.
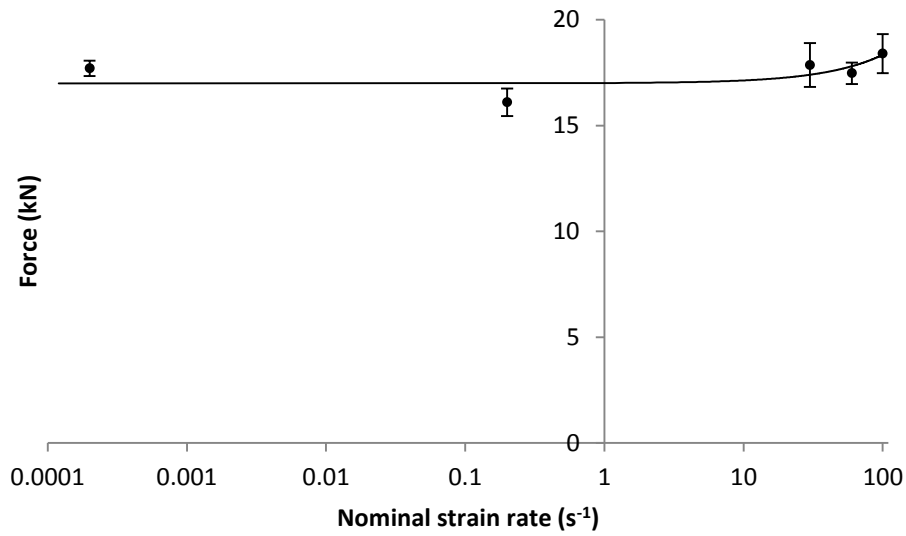
Figure 5.39: Peak load.

The crush efficiencies, defined as the ratio of steady-state to peak force, formed two distinct groups (Figure 5.40). The low rate tests had efficiencies that were a few percent higher than that of high rate tests. However, the standard deviations were noticeably higher for the low rate tests.
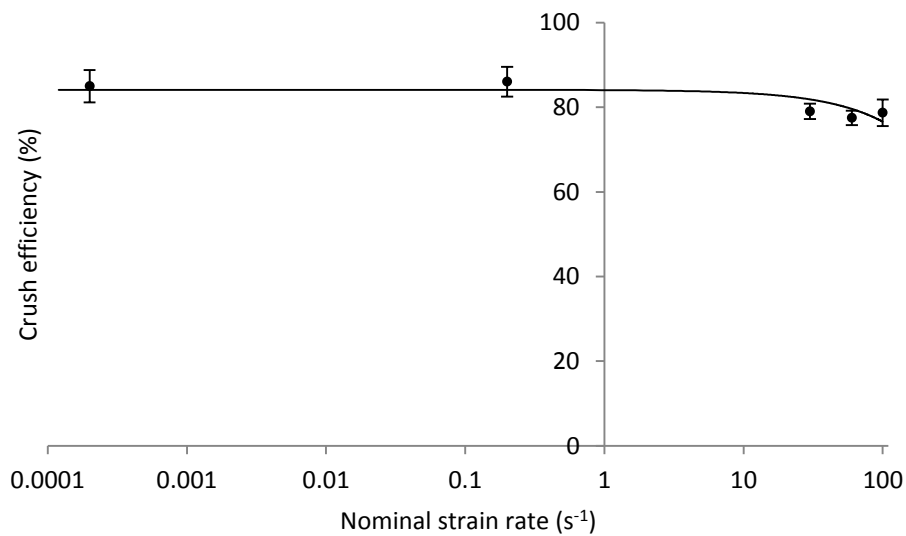
Figure 5.40: Crush efficiency.

The specific energy absorption, which is the energy absorption per mass of structure crushed, (Figure 5.41) also did not appear to vary appreciably with test rate.
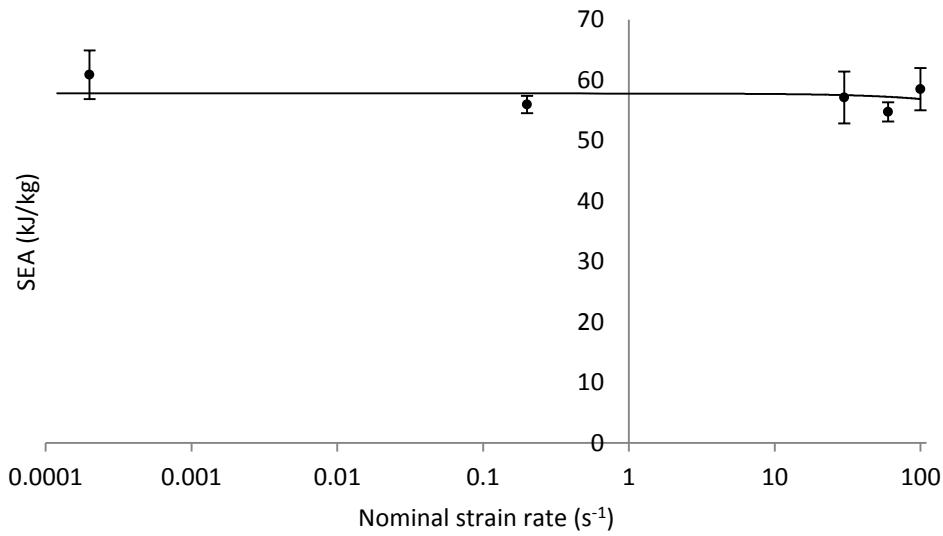
Figure 5.41: Specific energy absorption.

To quantify the observed trends in the data, linear regression was performed on the steady-state crush load, the peak load, the crush efficiency and the specific energy absorption. The results are summarised in Table 5.4.

Table 5.4: Results of linear regression performed on calculated metrics.

	SEA	F_{peak}	F_{SS}	CE
Regression gradient	-0.0092	0.0151	-0.0008	-0.0008
Std. error in gradient	0.0317	0.0041	0.0034	0.0002
Change over 100 s^{-1}	2.6%	9.0%	0.6%	8.9%

The regression gradient of the specific energy absorption and the steady-state force with respect to the nominal strain rate were small. More importantly, the standard errors of the gradients were many times greater than the magnitude of the gradient, suggesting that these two quantities were rate independent. On the other hand, the peal force had a slight upwards trend with respect to nominal strain rate. The increase in peak force with increase in test rate was caused by an increase in the observed oscillatory noise. The average amplitude of these high frequency oscillations increased from 4.7 kN for the $2\times10\ s^{-1}$ test to 8.1 kN for the $100\ s^{-1}$ test, which matched the apparent increase in the peak force. This suggests that the increase in peak was not due to an inherent change in the material

response but rather a result of the vibrations in experimental testing. This notion is further supported by the crush efficiency forming two groups depending on the testing machine used for testing.

Furthermore, no change in damage mechanism exhibited with increasing test rate was observed within the rage of rates tested. The damage pattern was indistinguishable between specimen from the low and high rate tests (Figure 5.42). This further substantiates the notion that the response of this structure is not dependent on rate of loading for the range of nominal strain rate being considered.
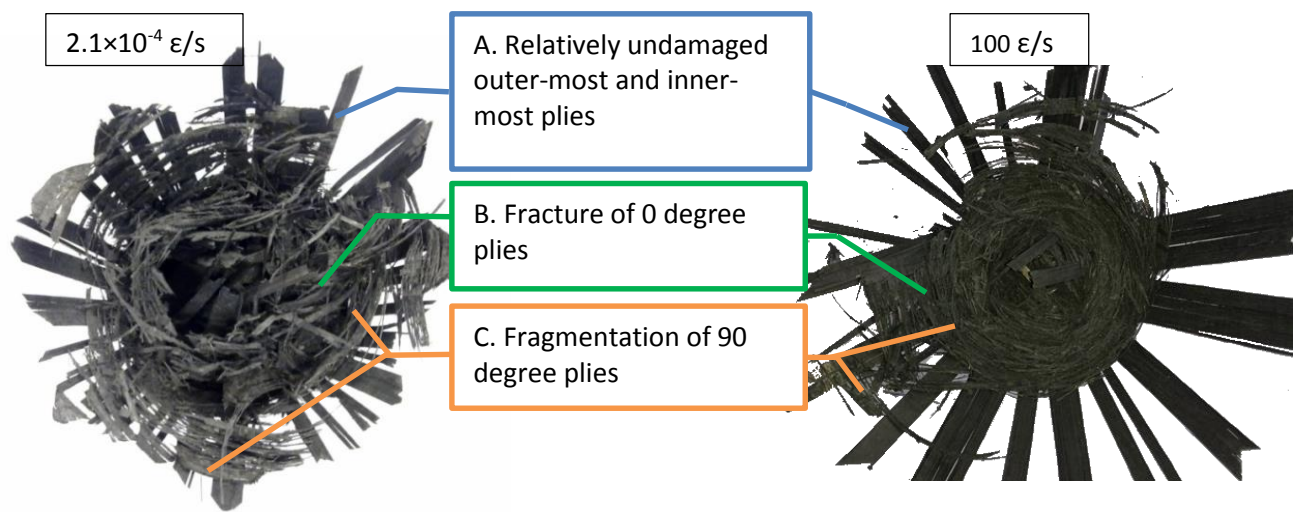
Figure 5.42: Low and high rate test specimens showing identical damage modes.

The ply cross-section was also examined for loading rate sensitivity. The tested specimens were potted in a clear epoxy resin and the cut to reveal the ply cross-section near the crush front. The cuts were subsequently polished and examined under a low power optical microscope. The role of the epoxy was to stabilise the specimen through the cutting and polishing process so that the features are properly preserved.

Figure 5.43 shows a comparison of features present in the cross-section view of the laminate at low and high test rate respectively. The meso-scale damage morphology was highly consistent between the two observed specimens. The fragments generated in the two specimens were highly similar. The fragments in both cases were short and segmented as a result of fibre breakage. A substantial amount of these fragments was contained both 0 and 90 degree plies. Fragments up to three plies thick were

observed. There is evidence that a significant amount of the cracking occurred within the interior of the ply rather than at the ply interface through delamination. A relatively flat crush front was also observed in both cases. The delamination of the outer ply advanced ahead of the crush front due to the splaying of the ply.
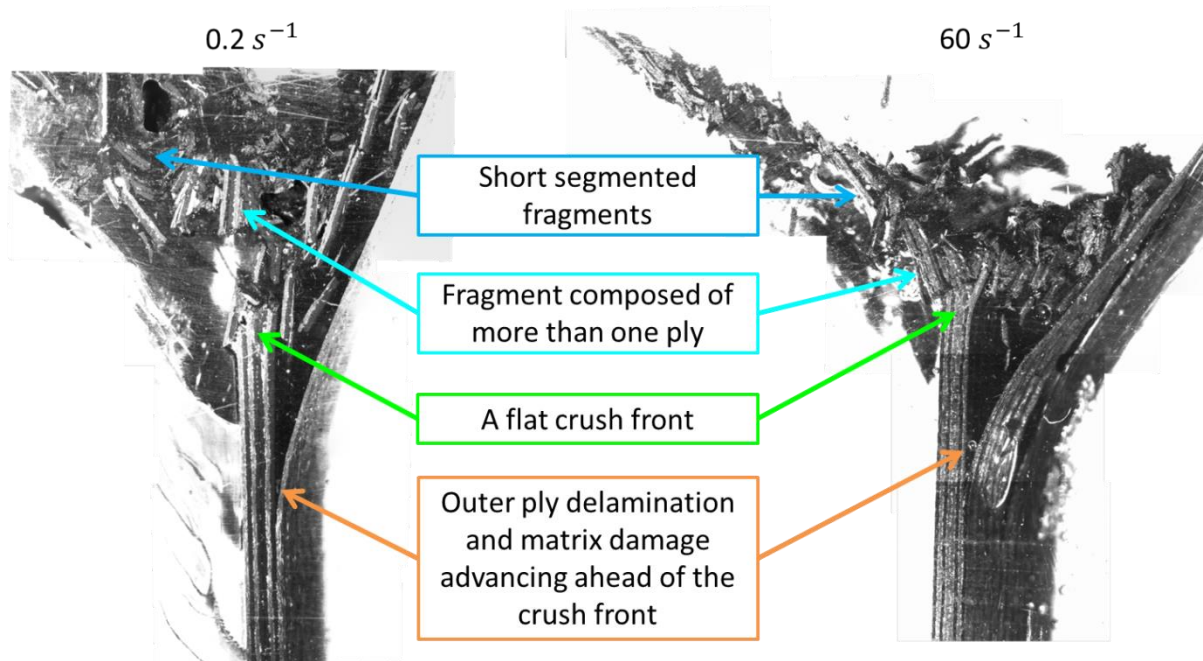
Figure 5.43: Low and high rate test specimens showing identical crush front morphology.

Both the quantitative and qualitative data suggested that the strain rate dependence of the tested CFRP material was negligible for the range of speeds tested in this experimental program.

There are few comparisons between statically and dynamically tested energy absorbers in the existing literature and a consensus has not be reached over the effect of loading rate on structural response. Palanivelu et al.[23] reported that energy absorption capability of cylindrical tubes are not sensitive to increasing test speeds (Figure 5.44). This is consistent with observations in the present experimental study.
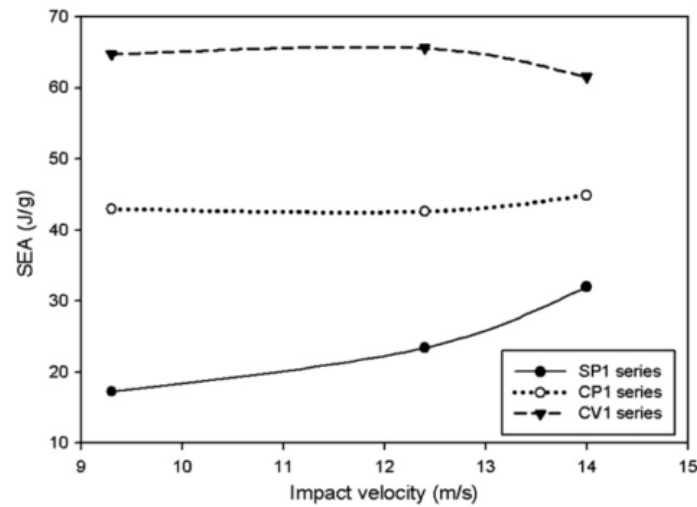
Figure 5.44: Effect of crush velocity on SEA for square (SP1) and circular tubes (CP1/CV1) [23].

However, Palanivelu also observed test speed dependence in the response of square tubes. Given that the CP and SP series of tubes have the same composition; this raises the possibility that loading rate effects may not be purely a material property. This can have significant ramifications in how strain rate sensitivity is dealt with in crashworthiness applications. A substantially more comprehensive experimental program is required to develop a more complete understanding of this phenomenon and would be outside the scope of this study.

Berthe et al.[128] conducted high rate coupon testing on the T700GC/M21 material used in this study. It was found that the shear modulus increased by 40% when the loading rate was increased from 1 $\mu\varepsilon$/s to 88 ε/s but no discernible change in the transverse modulus, suggesting that the material itself is not strain rate independent and that laminate configuration may play a role.

While the literature has not reached a consensus over the effect of strain rate on the material response of composite materials [111], there have been evidence to suggest that strain rate dependence is driven by the polymer matrix phase of the composite laminate [129]. The properties most affected by changes in loading rate tended to be matrix-dominated properties such as transverse and shear stiffness and strengths, which supports this idea. For example, Koerber et al. have shown matrix-dominated material properties, for a carbon-toughened epoxy material system, were rate dependent

[112]. However, the fibre-dominated longitudinal compressive modulus was not [113]. If loading rate sensitivity is driven by the matrix material, then this may explain the apparent rate insensitivity of the tested specimens in the present study.

Two aspects of this study cause the strain sensitivity of the matrix material to be minimised. Firstly, the fibre volume fraction of the T700/M21 prepreg is a relatively high at 57% due to its unidirectional nature. This means that the fibre properties dominate the overall properties of the [0/90/0/90]$_s$ laminate and minimising any effect of the rate dependency in the matrix material. Furthermore, the transverse and shear stiffness, strengths as well as the critical energy release rates are all significantly lower than that in the longitudinal direction. For the T700/M21 material used, the fibre-dominated critical energy release rate is 108 N/mm and 58.4 N/mm in tension and compression respectively. This is significantly higher than the 0.331 N/mm and 1.1 N/mm for transverse tension and compression as well as 0.443 N/mm in shear. The laminate was composed of equal amount of 0 and 90 degree plies. Therefore, when a given volume of laminate is crushed, the majority of the energy absorption is attributed to the fibre-dominated failure modes as they consume the most energy. Again, a change in matrix-dominated energy release rate will have a relatively small effect on the overall energy absorption capability of the laminate.

5.4.4 Implications for energy absorber design

This result may have a substantial impact on the design process of composite energy absorbers. Jacob et al.[5] has identified that an increase in the amount of fibre fracture leads to increased energy absorption. This is consistent with the fact that critical energy release rate attributed to fibre-dominated damage is significantly higher than that attributed to matrix-dominated damage. Hence, increasing fibre fracture would be one of the goals in the design of energy absorbers. Coupled with weight constraints, designs would tend towards having the vast majority of the crash energy absorbed through fibre fracture damage modes. The present results suggest that this fibre-dominated nature allows rate dependence of the composite material to be ignored for intermediate rates of loading similar to that used in the test program.

The analysis process for CFRP energy absorber design can be significantly sped up if the material can be assumed to be strain rate independent. Under this assumption, dynamic material properties are not required. These properties are typically difficult to obtain, as their measurement require special equipment such as the hydraulic press and the split Hopkinson bar. The use of rate independent constitutive equations reduces the complexity and the computational resources required for solution. Rate independence also allow the use of time scaling to speed up finite element solutions as the material response is not time dependent.

5.5 Summary

An extensive experimental program was completed on a representative crush energy absorber specimen. A series of crush tests were conducted at five different nominal strain rates ranging from $2 \times 10^{-4}\,\varepsilon$/s to $100\,\varepsilon$/s. The specimens' responses were recorded both qualitatively (mode and distribution of damage through the structure) and quantitatively (force-displacement response). The collected data will be used at a later stage to validate the proposed material model.

Between four to seven data sets were collected for each nominal strain rate, giving a good estimate of the spread inherent in the tests. It was found that the results were very consistent as indicated by the small standard deviation in each measured metric. This gives confidence in the correctness of the results.

Comparisons between responses measured at the different test rates were made and no rate dependence was found for tests up to $100\ \varepsilon$/s. The observed damage patterns were indistinguishable between samples tested at different rates. The four metrics, used to gauge performance of the energy absorbing structure, did not display any statistically significant trends with respect to the nominal strain rate. As a result, the T700/M21 material can be considered to be strain rate independent within the range of strain rates tested. The high fibre content of the prepreg used and the high fibre-dominated fracture energy release rates in comparison to those of matrix-dominated fracture were likely causes of the observed rate independence.

As a consequence of this result, subsequent study of composite energy absorber design using this material can be simplified by neglecting material property rate dependence. Furthermore, this assumption can be extended to ply configurations where the majority of the energy is expected to be absorbed through the fibre-dominated fracture modes. This can significantly simplify the analysis process by reducing the amount of material property data required for input as well as allowing the analysis to be performed with static assumptions. Furthermore, rate effect was neglected in the material model presented in the previous chapter in light of these results.

Chapter 6
Evaluation of model performance via experimental test cases

6.1   Introduction

This chapter details the application of the developed material model to the simulation of several experimental test cases. In order to demonstrate the effectiveness of the material model as a virtual testing tool, its performance in predicting the response of a range of different energy absorber structure configurations must be evaluated against experimental data.

Four test cases were selected for this purpose. These test cases represent a range of different structures likely to be encountered in crashworthiness applications. The test cases were selected to evaluate different aspects of the model.

For each test case, the structure being considered was modelled numerically with appropriate meshing and boundary conditions. All inputs to the model are physical, measurable properties, including elastic moduli, strengths and critical energy release rates. As the model is heavily dependent on material property values, every effort has been made to ensure the correct values are obtained from testing or the literature. As the material model requires a number of inputs, some of which cannot be measured easily, this process is not trivial. Material properties that are not available were estimated based on those for similar material systems.

The simulated results were compared against experimental observations. The force displacement response between the simulation and experiment was compared. Particular attention has been placed on energy absorption as well as peak and steady-state forces. The damage morphology and the structural deformation were examined and compared with experimental observations. The successful prediction of the quantitative and qualitative responses for these test cases gives confidence in the utility of the model for its intended purpose.

6.2   Test case selection

Four different test cases were selected for this study: a chamfer triggered cylinder, a tulip triggered cylinder, a steeple triggered hat section as well as a corrugated web section. These specimens contain

a range of features commonly found in composite energy absorbers. All of the geometries chosen were self-supporting under axial crush loading.

Two closed cross-sections were considered. The chamfered cylinder [27] is a very common choice for construction of energy absorbing structures due to its tendency to undergo progressive crushing as well as its ease of manufacture [46]. This test case is representative of a simple but well understood design, which assesses the overall capability of the model to capture crush damage and deformation. The tulip triggered cylinder [48] represents a more complex design. This test case assesses the model's ability to handle multiple sites of damage initiation and then subsequent merging of the damaged regions. These two cases represent possible stand-alone designs for composite energy absorbers.

The study also examined two open cross-sections. The hat shaped structures [49]are already used to stiffen large panels as well as beam sections [130]. This test case explores the effect of stress concentrations arising from bends in the material on the overall crush behaviour, particularly their effect on the advancing crush front. The semi-circular corrugated web is also used to provide energy absorbing capacity in various aviation [45] and automotive [40] platforms. This configuration gives rise to a more complex local loading condition as well as possible contact between adjacent splaying plies, which will test the model's ability to handle these complexities.

6.3   Chamfered cylinder

The chamfered cylindrical tube was chosen as it is one of the simplest designs for a freestanding composite energy absorbing structure and has been studied extensively [46]. This test case utilises experimental data from Huang and Wang [27]. The tested chamfered cylinders were made from T700/QY8911 unidirectional prepreg with [+45/-45/90/0/0/90/0]$_\text{S}$ layup. The specimen is made from a cylindrical tube with a 50 mm inner diameter. The top edge of the tube has a 45° chamfer to act as a trigger. The tube has an approximate height of 100 mm. Figure 6.1 shows the specimens as they were manufactured.
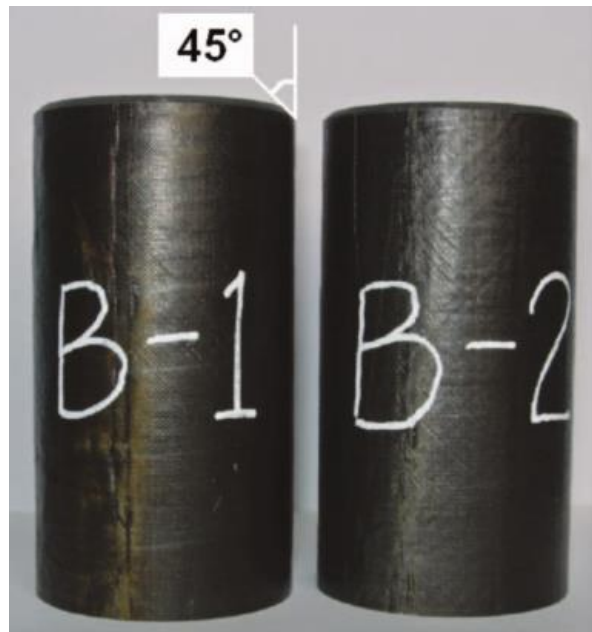
Figure 6.1: Specimen geometry from Huang and Wang [27].

6.3.1 Numerical model setup

The tube was meshed in Abaqus to create a numerical model. In order to reduce the computational resources required to run the simulation, the specimen was approximated as having quarter symmetry, i.e., only one quarter of the tube was modelled. The model consisted of 78 thousand C3D8R reduced integration solid hexahedral element. Each ply was meshed using elements of approximately 1 mm in the axial and circumferential directions and three elements thick (~0.06 mm element thickness) in the thickness direction for each ply (Figure 6.2 (right)). The plies were held together using cohesive surfaces which also accounts for the delamination as well as contact behaviour. The tube is aligned with the z axis. The bottom of the mesh is fixed and symmetric boundary conditions were imposed on the two side edges of the quarter symmetric model (Figure 6.2 (left)).

The crush loading is provided by a flat rigid surface that descends on the specimen during the simulation. The force response and displacement is measured from this surface. This loading surface is constrained to motion only in the axial crush (z) direction without rotation.

The hourglass and distortion control were applied to the mesh representing the ply to manage non-physical deformations. Mass scaling with a target time increment of 10^{-6} s was also used as per the results of the sensitivity study presented in Section 4.3.5. A friction coefficient of 0.10 was assumed due to the observed lubricating effect [131] of the debris generated by the damage process.
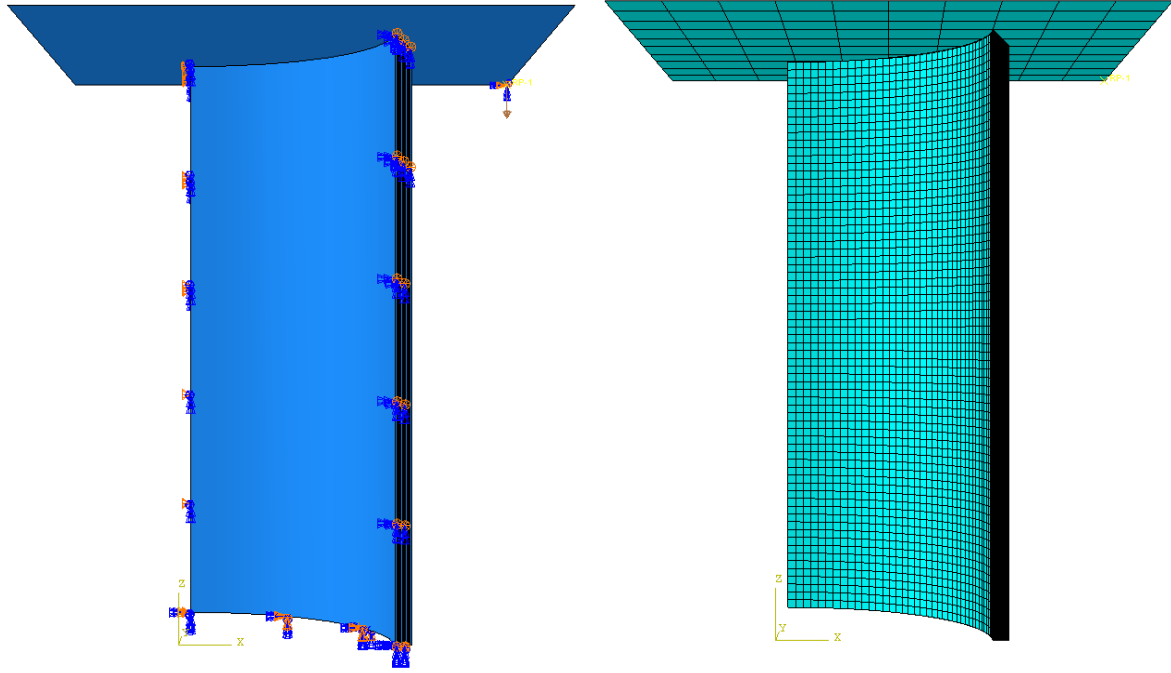
Figure 6.2: Boundary condition (left) and mesh (right) of the chamfered cylinder specimen.

The material properties of the mesh were mostly obtained from Huang and Wang's paper [27] (Table 6.1 and Table 6.2). These values were used without modification in this simulation. Some material properties (such as some energy values and the shear profile) were unavailable and thus were estimated using properties of similar carbon-epoxy material systems.

Table 6.1: Intralaminar material property inputs for T700/QY8911.

Intralaminar properties	Value	Intralaminar properties	Value
E_{11}	135 GPa [27]	G_{fib}^{T}	108 Nmm [FYP]*
E_{22}	9.12 GPa [27]	G_{fib}^{C}	58.4 Nmm [FYP]*
E_{33}	9.12 GPa [27]	G_{mat}^{T}	0.425 Nmm [132]
ν_{12}	0.31 [27]	G_{mat}^{C}	1.1 Nmm [12]*
ν_{23}	0.31 [27]	G_{mat}^{12}	0.587 Nmm [132]
ν_{13}	0.31 [27]	G_{mat}^{23}	0.587 Nmm [132]
G_{12}	5.67 GPa [27]	G_{mat}^{13}	0.587 Nmm [132]
G_{23}	5.67 GPa [27]	$c_{1,12}$	34.238 GPa [125]*
G_{13}	5.67 GPa [27]	$c_{2,12}$	15.061 GPa [125]*
X^{T}	2.326 GPa [27]	$c_{3,12}$	2.189 GPa [125]*
X^{C}	1.236 GPa [27]	$c_{1,23}$	34.238 GPa [125]*
Y^{T}	51 MPa [27]	$c_{2,23}$	15.061 GPa [125]*
Y^{C}	209 MPa [27]	$c_{3,23}$	2.189 GPa [125]*
S_{12}	87.9 MPa [27]	$c_{1,13}$	34.238 GPa [125]*
		$c_{2,13}$	15.061 GPa [125]*
Property taken from *T700/M21		$c_{3,13}$	2.189 GPa [125]*

Table 6.2: Interlaminar material property inputs for T700/QY8911.

Interlaminar properties	Value	Interlaminar properties	Value
Normal strength	80 MPa [9]	Normal fracture energy	0.425 Nmm [132]
Shear strength (1)	60 MPa	Shear (1) fracture energy	0.587 Nmm [132]
Shear strength (2)	60 MPa	Shear (2) fracture energy	0.587 Nmm [132]

The solution time for the simulation was 12.2 hr on an Intel Xeon based compute node with 16 cores for a total of 195 CPU.hr.

6.3.2 Results comparison between simulation and experiment

Figure 6.3 shows the measured force response was very well captured by the simulations.
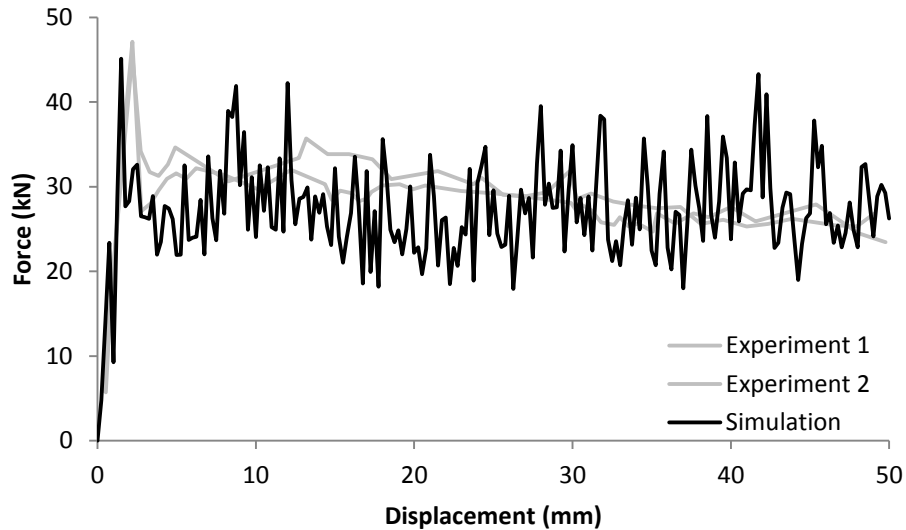
Figure 6.3: Comparison of experimentally measured (grey) and simulated (black) force response of chamfered

cylindrical tube [27].

The experimentally observed initial peak (47 kN) was accurately reproduced by the numerical

simulation which yielded a value of 45 kN. A selective, frequency-based filtering method was used to

remove high frequency noise generated by the numerical simulation (Figure 6.4). Figure 6.3 clearly

shows there was substantial noise during the simulation of the steady-state crush process. This noise

was numerical in nature and thus should be filtered. A low-pass Butterworth filter was used. An

appropriate cutoff frequency was determined by balancing the minimising numerical noise while

retaining expected features. This same approach had been applied to subsequent test cases where

necessary. Despite this filtering, some lower frequency oscillations are present in the steady-state

crush region of the numerical response (Figure 6.4). In contrast, the experimental steady-state force

region was substantially flatter.

Figure 6.4: Comparison of experimentally measured (grey) and filtered, simulated (black) force response of

chamfered cylindrical tube [27].

Steady-state crushing occurred as expected after the initial peak force, resulting in a relatively

constant force. The steady-state crushing force was also well captured by the numerical model and

found to be in agreement with the experimental steady state force of approximately 30 kN. The

numerically predicted total energy absorption was 1.37 kJ, which compared well with energies of 1.44

kJ and 1.40 kJ respectively for the two tests conducted.

The predicted deformation of the specimen was highly consistent with observations. Multiple "lamina

bundles" forming from the splitting of the ply along the axial direction was observed in the

simulation. Substantial splitting in both inwards and outwards splaying plies was evident in

consecutive elements deleted in the axial directions (Figure 6.5). A clear V-shaped trench marked the

mid-surface of the laminate by the splaying plies. The laminate was split along the mid-surface as

expected. Substantial amount of partially attached fragments observed experimentally was also

reproduced in the simulation. A range of fragments of different sizes was formed.
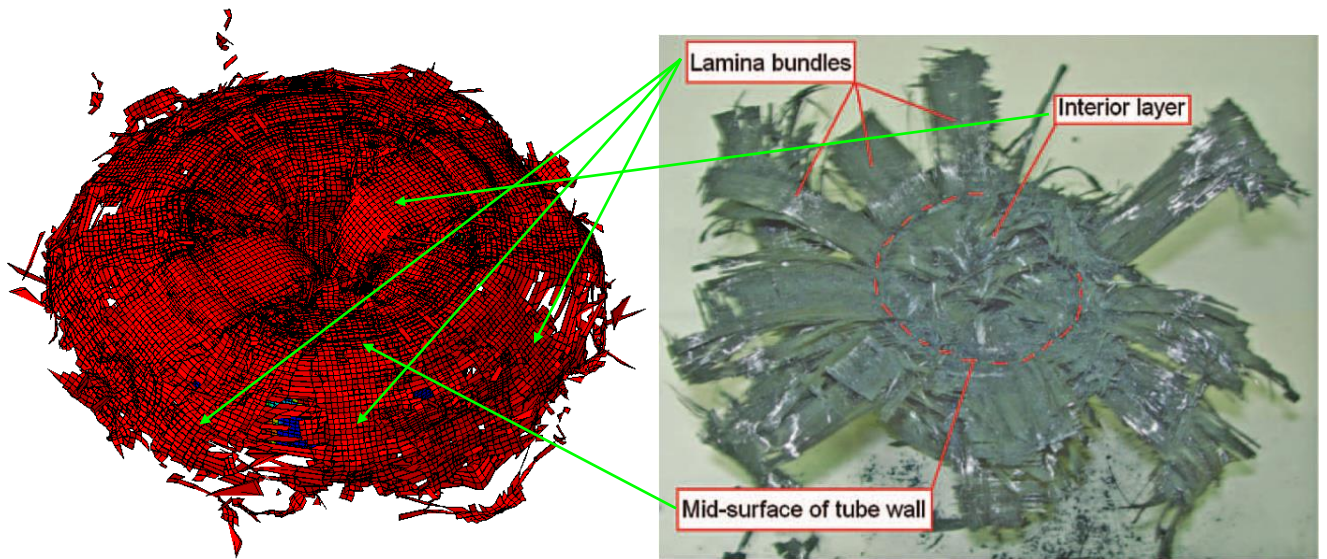
Figure 6.5: Comparison of damage morphology between simulated result (left) and experimental observation

(right).

6.4   Tulip triggered cylinder

The inclusion of a tulip trigger in cylindrical tubes represents a more flexible design where the initial

force response can be tailored to the expected load profile. The experimental study completed on the

tulip triggered cylinders was previously presented in Chapter 5. The data extracted from the low rate

tests (16mm/s) was used in this test case. This test case assesses the ability of the model to initiate

damage independently and to handle the subsequent coalescing of the damage zones. The force

response and damage morphology observed in the testing program conducted by the authors [48] was

used in this comparison.

The material system used to manufacture the specimens was T700/M21in the form of unidirectional

prepreg sheets which were laid up in a $[0/90/0/90]_s$ configuration. Figure 5.1 shows the specimen

geometry and dimensions. The specimens' specification and manufacturing method had been detailed

in Chapter 5. The manufactured specimen is shown in Figure 5.10.

6.4.1 Numerical model setup

Similar to the chamfered tube, the tulip triggered specimen was meshed using quarter symmetry. A total of 91 thousand C3D8R solid elements were used. The trigger region of the ply was meshed using elements of approximately 1 mm in the fibre and transverse directions and three elements thick in the thickness direction per ply (Figure 6.6 (right)). The bulk tubular region constrained elements that were up to 2 mm in the axial direction. Interlaminar interactions were captured through cohesive surfaces. The tube is aligned with the z axis. The mesh is fixed at the bottom and symmetric boundary conditions were imposed on the two side edges of the symmetric model (Figure 6.6 (left)).

The crush loading is again provided by a flat rigid surface that descends on the specimen during the simulation. The force response and displacement was measured from this surface. This loading surface is constrained to move down at the prescribed speed. Hourglass and distortion control were applied to the meshed plies. Mass scaling with a target time increment of 10^{-6} s was also used as per the results of the sensitivity study presented in Section 4.3.5.
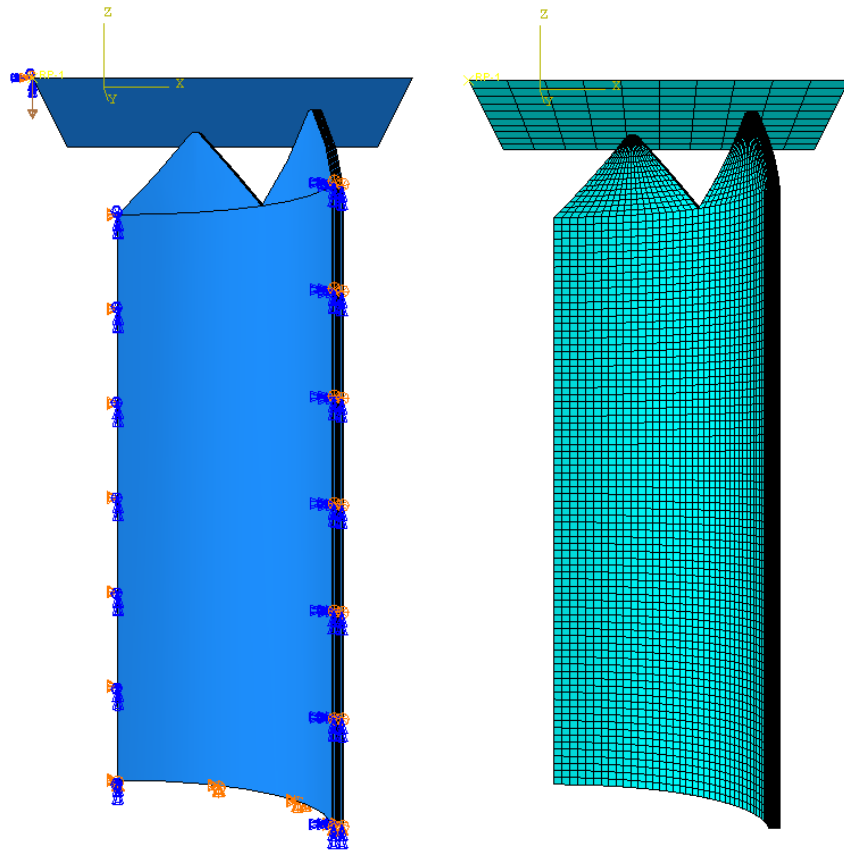
Figure 6.6: Boundary condition (left) and mesh (right) of the tulip triggered cylinder specimen.

The material properties used in the simulation were obtained from the literature. They are presented in

Table 6.3 and Table 6.4.

Table 6.3: Intralaminar material property inputs for T700/M21.

Intralaminar properties	Value	Intralaminar properties	Value
E_{11}	142 GPa [123]	G_{fib}^{T}	108 Nmm [FYP]
E_{22}	8.4 GPa [123]	G_{fib}^{C}	58.4 Nmm [FYP]
E_{33}	8.4 GPa [123]	G_{mat}^{T}	0.331 Nmm [124]
ν_{12}	0.32 [123]	G_{mat}^{C}	1.1 Nmm [12]*
ν_{23}	0.32 [123]	G_{mat}^{12}	0.443 Nmm [124]
ν_{13}	0.32 [123]	G_{mat}^{23}	0.443 Nmm [124]
G_{12}	4.80 GPa [123]	G_{mat}^{13}	0.443 Nmm [124]
G_{23}	3.95 GPa [123]	$c_{1,12}$	34.238 GPa [125]
G_{13}	4.80 GPa [123]	$c_{2,12}$	15.061 GPa [125]
X^{T}	2.282 GPa [123]	$c_{3,12}$	2.189 GPa [125]
X^{C}	1.465 GPa [126]	$c_{1,23}$	34.238 GPa [125]
Y^{T}	65 MPa [123]	$c_{2,23}$	15.061 GPa [125]
Y^{C}	290 MPa [12]*	$c_{3,23}$	2.189 GPa [125]
S_{12}	105 MPa [123]	$c_{1,13}$	34.238 GPa [125]
		$c_{2,13}$	15.061 GPa [125]
property taken from *HTA/6376C		$c_{3,13}$	2.189 GPa [125]

Table 6.4: Interlaminar material property inputs for T700/M21.

Interlaminar properties	Value	Interlaminar properties	Value
Normal strength	60 MPa [133]	Normal fracture energy	0.331Nmm [124]
Shear strength (1)	60 MPa [133]	Shear (1) fracture energy	0.443 Nmm [124]
Shear strength (2)	60 MPa [133]	Shear (2) fracture energy	0.443 Nmm [124]

The solution time for the simulation was 42.7 hr on an Intel Xeon based compute node with 16 cores

for a total of 683 CPU.hr.

6.4.2 Results comparison between simulation and experiment

Figure 6.7 shows the comparison between the experimentally observed response of the tulip-triggered

cylinder and the filtered simulated response. The simulated response closely followed the linearly

increasing force response during the consumption of the tulip trigger. The subsequent plateauing of the force response during steady-state crushing was also reproduced. The simulated energy absorption of 470 J agreed very well with those measured experimentally (between 465 J and 495 J).
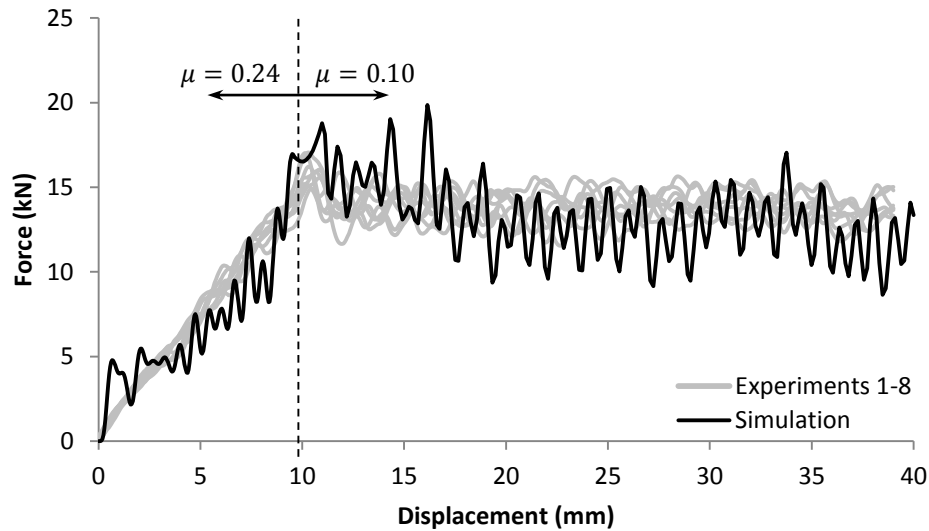
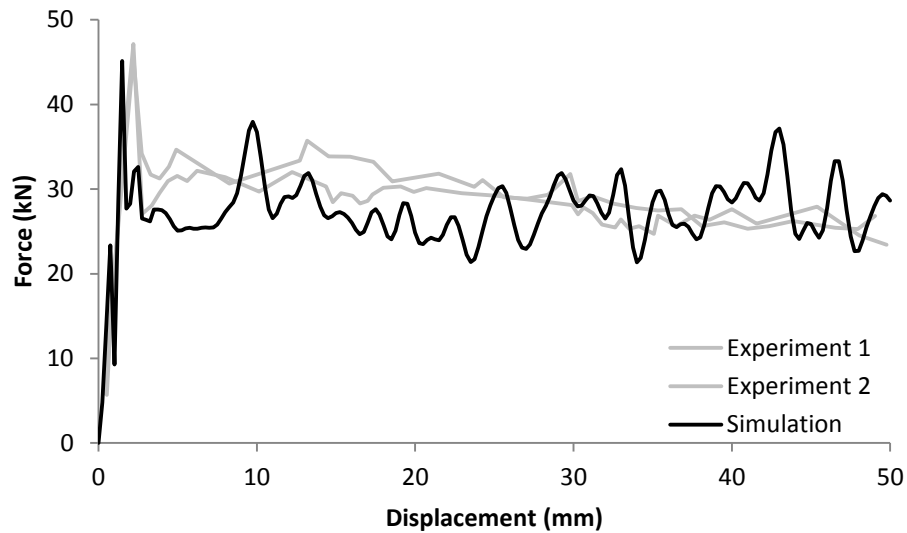
Figure 6.7: Comparison of experimentally measured (grey) and filtered simulated (black) force response of tulip triggered cylindrical tube.

However, oscillatory noise was observed in this specimen throughout the simulation despite the use of selective filtering. The noise was likely a result of the element deletion algorithm, which removes failed elements. Furthermore, two substantial peak regions were observed in the unfiltered numerical results. The first occurred when the specimen first made contact with the platen and the second was caused by the requirement for a new simulation step to enable the change in friction coefficient to simulate the effect of accumulating composite debris. Both these effects were artificial and numerical in origin. For example, moving back to a single step removed the second peak.

The deformation and the spread of the different damage modes through the specimen was also successfully predicted by the numerical model (Figure 6.8). Damage initiated at the tips and spread with the crush front as expected. The simulation produced debris pieces in the same manner as observed experimentally. The completeness of the damage to the 90° plies was evident by the red

colour in the simulated specimen, which represents matrix-dominated damage. The multiple splitting

of the inner-most and outer-most 0° plies were also evident in the simulation.
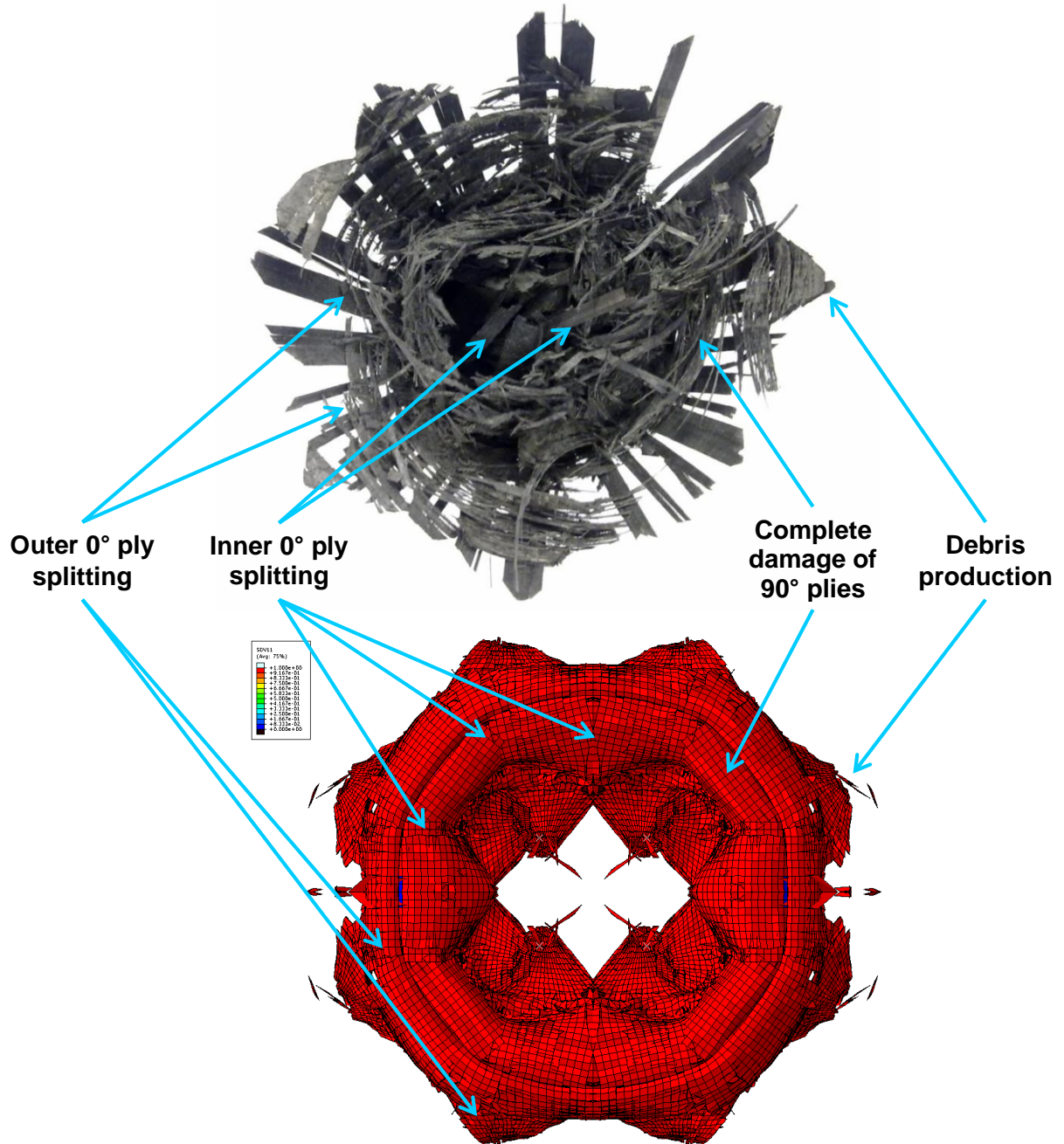
Figure 6.8: Top view comparison of simulated (left) and experimental (right) damage morphology.

In particular, the simulation was able to resolve the meso-scale damage morphology present within

the laminate near the crush front observed through microscopy of the experimental specimen.

Figure 6.9 shows a range of damage at this length scale, including: (1) debris formation with

176

widespread matrix damage; (2) a flat crush front and (3) outer ply delamination and matrix damage advancing ahead of the crush front.
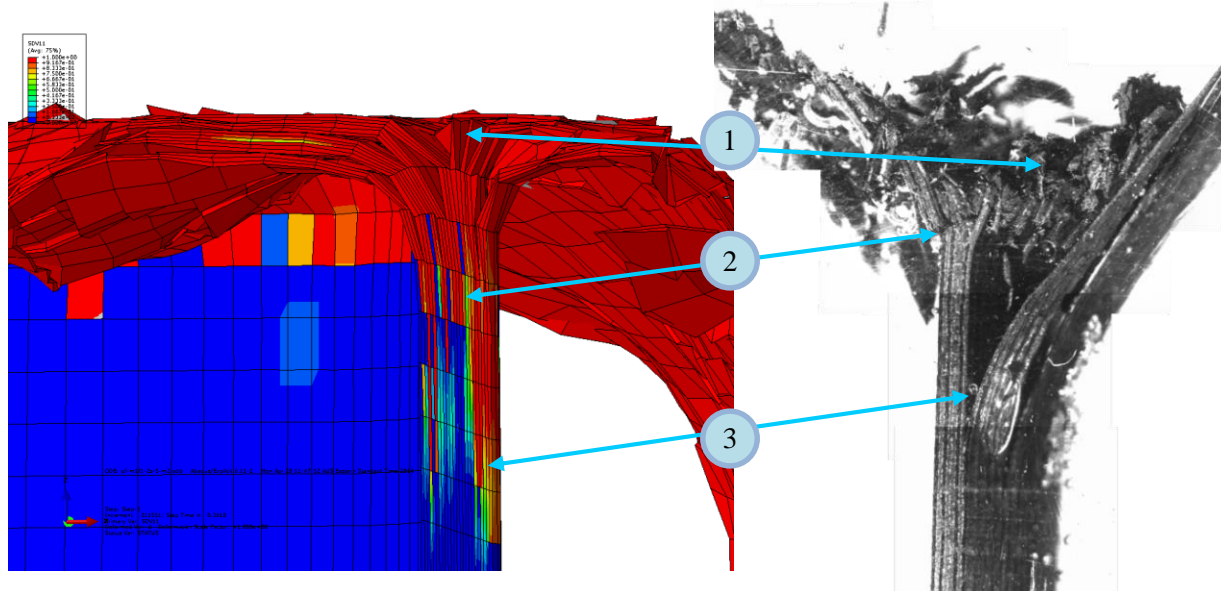
Figure 6.9: Cross-sectional view of the laminate near the crush front in the simulated (left) and experimental (right) specimen.

6.5   Hat shaped open section

A popular stiffener configuration has a hat shaped cross-section [130]. This specimen will gauge the ability to handle structures with fewer constraints as well as the presence of stress concentrations. Experimental data from Joosten et al. [49] for a hat-shaped crush element was used for comparison with the simulated response.

The specimens were made with woven T300/970 carbon-epoxy prepreg with a $[0/90]_8$ stacking sequence. Figure 6.10 shows the geometry and dimensions of the hat shaped specimen tested by Joosten et al. [49]. The testing configuration is shown in Figure 6.11. Testing was performed by Joosten et al. [49] at 5 mm/min initially and then increased to 25 mm/min.
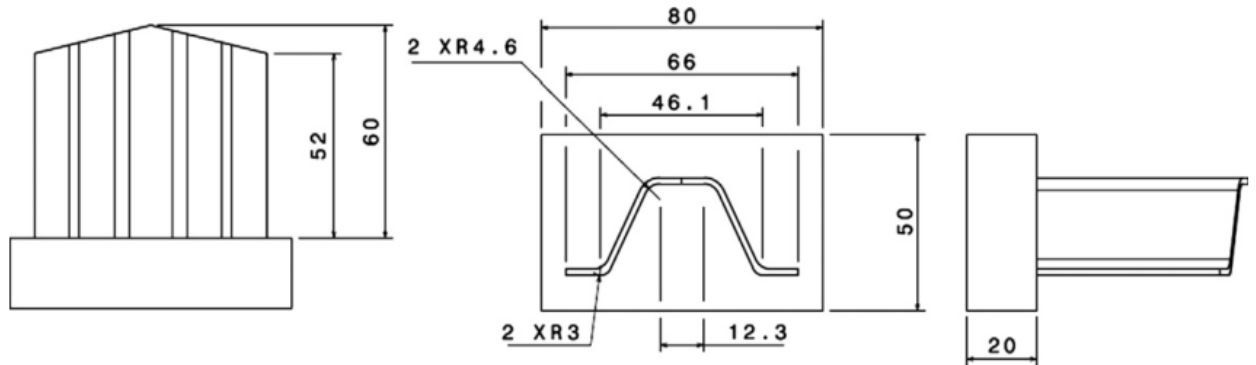
Figure 6.10: Geometry of steeple triggered hat shaped specimen from Joosten et al.[49].
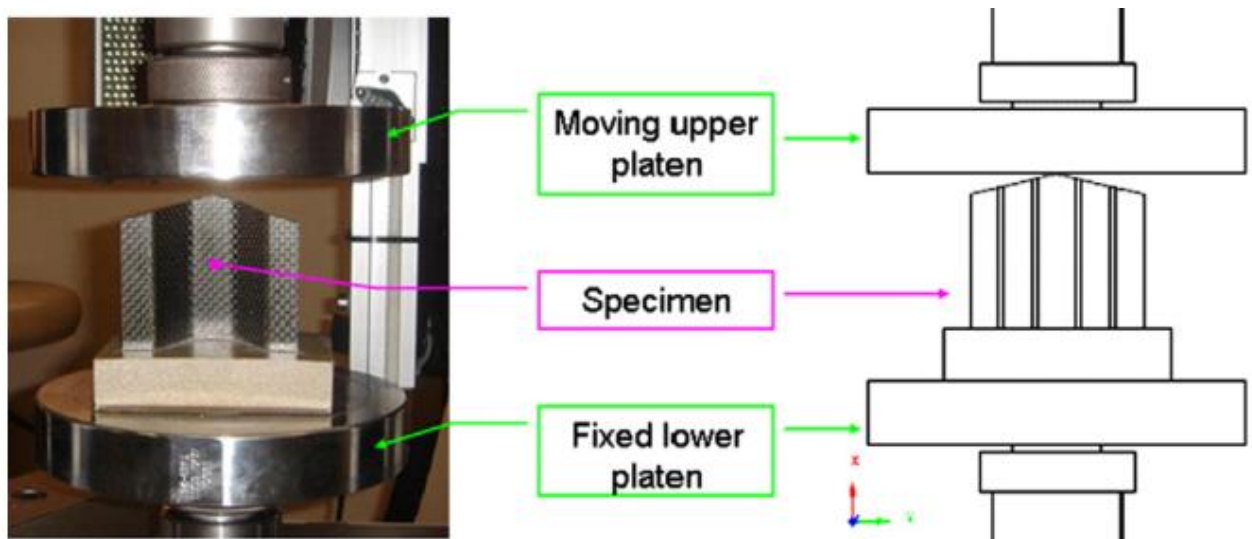
Figure 6.11: Steeple triggered hat section test setup [49].

6.5.1   Numerical model setup

The hat section was meshed utilising half symmetry using C3D8R solid elements. A total of 73 thousand elements were used. The plies were meshed using elements of approximately 1 mm in the fibre and transverse directions and three elements thick in the thickness direction per ply (Figure 6.12 (right)). Care was taken during mesh generation to ensure that sufficient number of elements to approximate the curved joints of the specimen, causing the elements at the curved sections to be slightly smaller. The mesh is fixed at the bottom and symmetric boundary conditions were imposed on the two side edges of the symmetric model (Figure 6.12 (left)).

The crush loading is again provided by a flat rigid surface that descends on the specimen during the simulation. The force response and displacement was measured from this surface. This loading surface is constrained to move down at the prescribed speed. Hourglass and distortion control were applied to the mesh representing the ply. Again, a mass scaling with a target time increment of 10^{-6} s was used as per the results of the sensitivity study presented in Section 4.3.5. A friction coefficient of 0.10 was also assumed in the absence of data.

Figure 6.12: Boundary condition (left) and mesh (right) of the hat section specimen.

Table 6.5 and Table 6.6 presents the material property values used in this test case. These values were obtained from the literature. Values for unidirectional T300/970 plies were used as input and combined to form the fabric values needed.

Table 6.5: Intralaminar material property inputs for T300/970.

Intralaminar properties	Value	Intralaminar properties	Value
E_{11}	138 GPa [134]	G_{fib}^T	91 Nmm [134]
E_{22}	8.42 GPa [134]	G_{fib}^C	79 Nmm [134]
E_{33}	8.42 GPa [134]	G_{mat}^T	0.15 Nmm [134]
ν_{12}	0.257 [134]	G_{mat}^C	0.45 Nmm [134]
ν_{23}	0.387 [134]	G_{mat}^{12}	2.5 Nmm [134]
ν_{13}	0.257 [134]	G_{mat}^{23}	2.5 Nmm [134]
G_{12}	3.93 GPa [134]	G_{mat}^{13}	2.5 Nmm [134]
G_{23}	3.03 GPa [134]	$c_{1,12}$	636.33 GPa [9]*
G_{13}	3.93 GPa [134]	$c_{2,12}$	97.193 GPa [9]*
X^T	1.496 GPa [134]	$c_{3,12}$	5.517 GPa [9]*
X^C	1.026 GPa [134]	$c_{1,23}$	636.33 GPa [9]*
Y^T	90 MPa [134]	$c_{2,23}$	97.193 GPa [9]*
Y^C	211 MPa [134]	$c_{3,23}$	5.517 GPa [9]*
S_{12}	77 MPa [134]	$c_{1,13}$	636.33 GPa [9]*
		$c_{2,13}$	97.193 GPa [9]*
property taken from *plain weave fabric		$c_{3,13}$	5.517 GPa [9]*

Table 6.6: Interlaminar material property inputs for T300/970.

Interlaminar properties	Value	Interlaminar properties	Value
Normal strength	64 MPa [9]	Normal fracture energy	0.15 Nmm [9]
Shear strength (1)	70 MPa [9]	Shear (1) fracture energy	2.5 Nmm [9]
Shear strength (2)	80 MPa [9]	Shear (2) fracture energy	2.5 Nmm [9]

The solution time for the simulation was 3.4 hr on an Intel Xeon based compute node with 16 cores for a total of 54.4 CPU.hr.

6.5.2 Results comparison between simulation and experiment

Figure 6.13 shows that the filtered simulated force response of the hat section specimen was consistent with that of the experimental response. The triggering and steady-state crushing were both successfully captured by the numerical model.
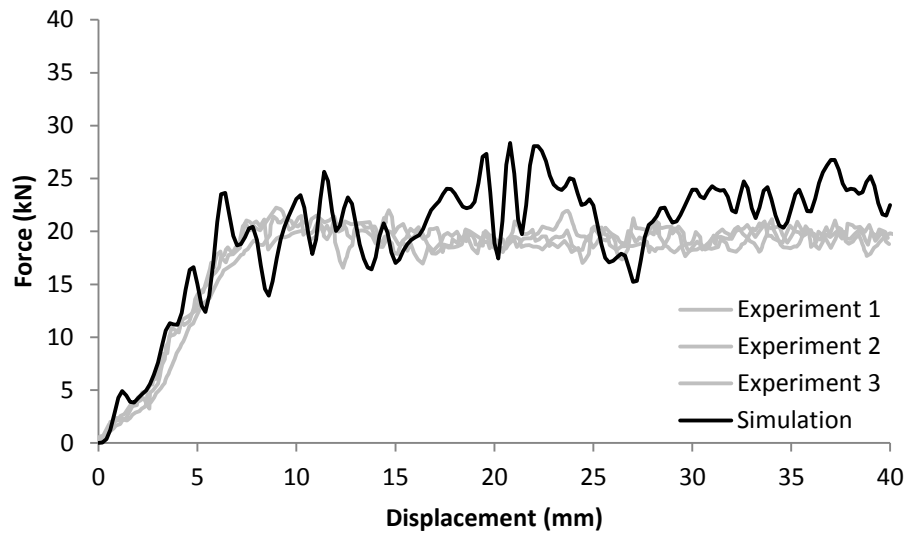
Figure 6.13: Numerical prediction (black) overlaying filtered experimental results (grey).

The simulated energy absorption of 794 J was higher than the experimental average of 704 J. This increased energy absorption was caused by as small but consistent over-prediction of the force response. Some low frequency undulations were evident in the force response, which corresponded to the slight buckling behaviour of the unconstrained flanges. These are likely the results of instability inherent in the open section. The accuracy of the material properties can also contribute to this difference. In particular, measurement of the critical energy release rate can have significant scatter [96], potentially affecting both intra- and interlaminar behaviour.

The simulated specimen (Figure 6.14(left)) shared many similarities with experimental observation. The damage progression of the simulated specimen was smooth and gradually spreading from the crush front with the advancing loading surface. Stress concentrations were well captured as evident in the pronounced failure of ply in these locations. Large petals were produced from the crushing of the flat surfaces, consistent with reality.
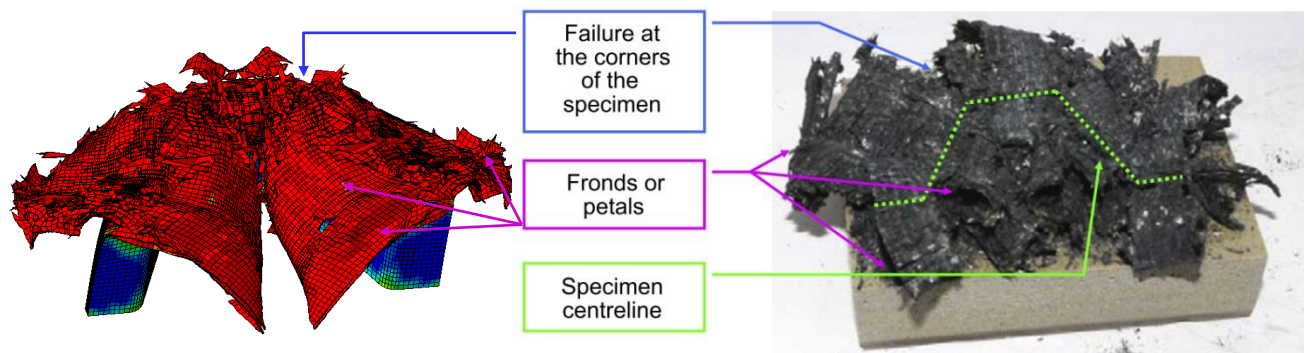
Figure 6.14: Comparison of ply damage between simulation (left, red denoting matrix-dominated damage) and experiment [49] (right).

However, the simulation produced larger petals that are more intact than what was observed. The separation of plies along the stress concentrations have been suppressed, likely due to the more extensive delamination seen in the simulation, which reduced the stresses on the plies.

6.6   Semi-circular corrugated web

The corrugated web geometry has already been used in energy absorbing structures for various aviation [45] and automotive [40] applications. Testing this specimen assess performance of the model on a geometry used currently used in energy absorber design and one which is somewhat more complex in terms of expected interactions. The experimental data from Feroboli [40] were used in this test case.

A semi-circular corrugated web specimen made using unidirectional T700/2510 carbon-epoxy prepreg with a $[0/90]_{3S}$ layup. The geometry and dimensions are shown in Figure 6.15. The web is manufactured through press moulding using aluminium tools. A $45°$ chamfer was cut into the top surface to act as a trigger mechanism. Figure 6.16 shows the web specimen that is ready for testing.
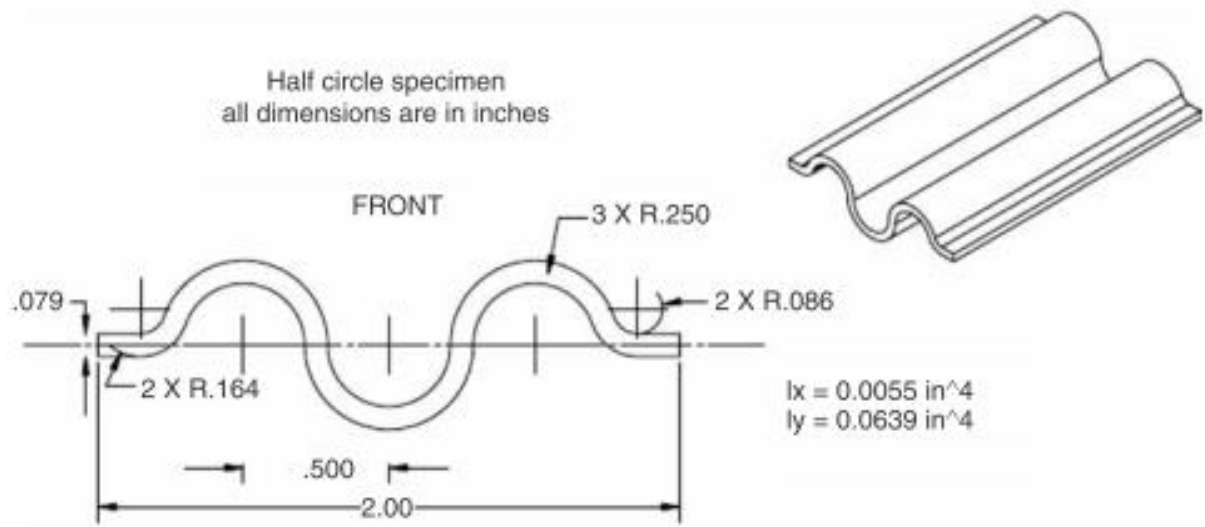
Figure 6.15: Geometry of semi-circular corrugated web specimen [40].
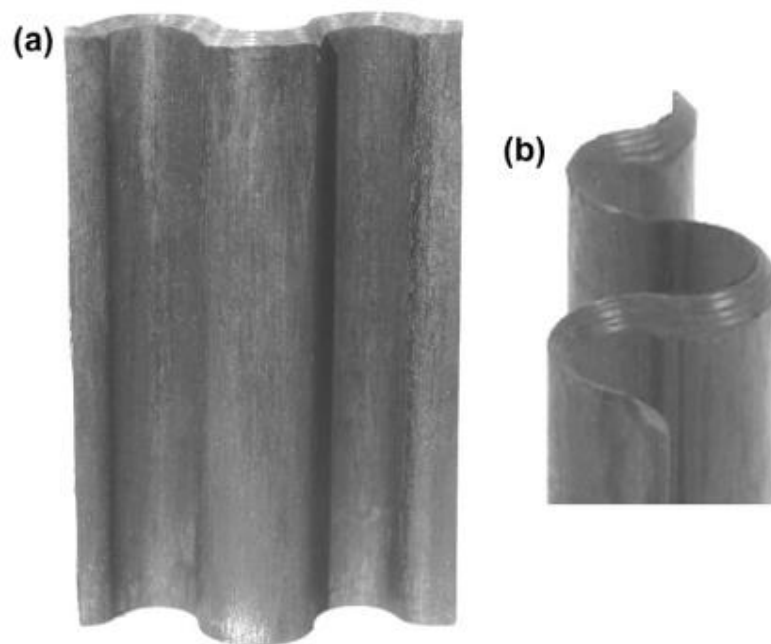
Figure 6.16: The semi-circular corrugated web specimen as manufactured [8].

6.6.1 Numerical model setup

The corrugated section was meshed using a total of 176 thousand C3D8R solid elements. The plies were meshed using elements of approximately 1 mm in the fibre and transverse directions and three elements thick in the thickness direction per ply (Figure 6.17 (right)). Care was taken during mesh generation to ensure that the elements of adjacent plies are not staggered. As a result the elements at

the inside edge of the curved sections were slightly smaller. The mesh is fixed at the bottom and symmetric boundary conditions were imposed on the two side edges of the symmetric model (Figure 6.17 (left)).

The crush loading is again provided by a flat rigid surface that descends on the specimen during the simulation. The force response and displacement is measured from this surface. This loading surface is constrained to move down at the prescribed speed. Hourglass and distortion control were applied to the mesh representing the ply. Mass scaling with a target time increment of 10^{-6} s was also used for consistency. A friction coefficient of 0.10 was assumed due to its similarity with the T700/M21 material system.
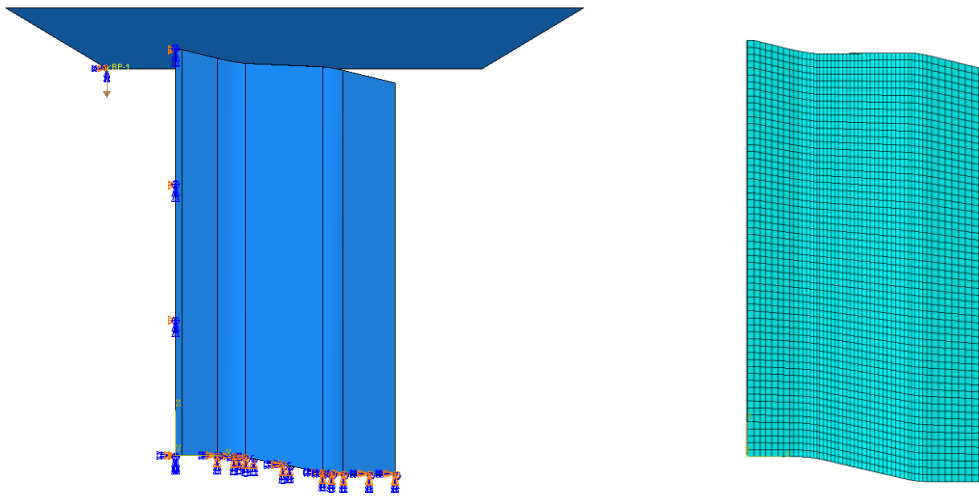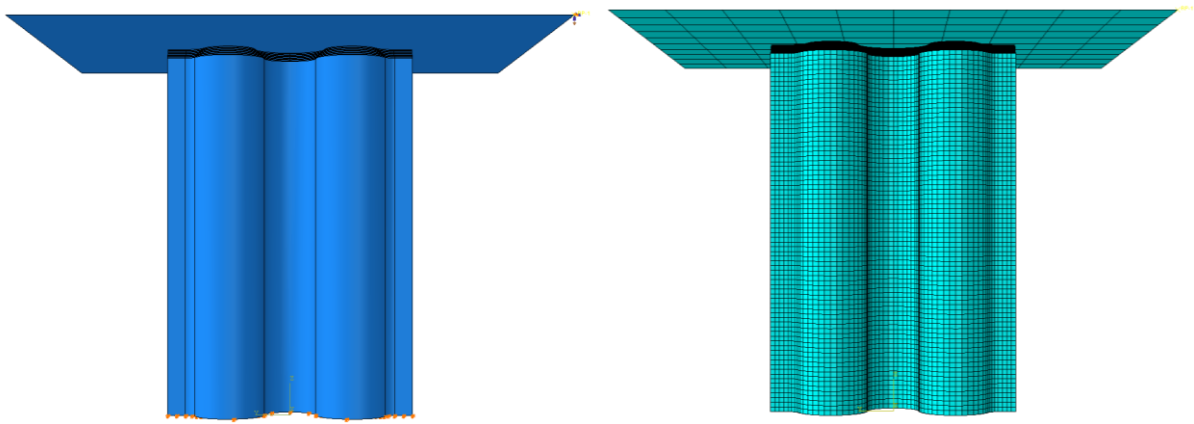

Figure 6.17: Boundary condition (left) and mesh (right) of the hat section specimen.

Table 6.7 and Table 6.8 presents the material property values, obtained from the literature, that were used in this test case.

Table 6.7: Intralaminar material property inputs for T700/2510.

Intralaminar properties	Value	Intralaminar properties	Value
E_{11}	127 GPa [8]	G_{fib}^T	108 Nmm [FYP]
E_{22}	8.41 GPa [8]	G_{fib}^C	58.4 Nmm [FYP]
E_{33}	8.41 GPa [8]	G_{mat}^T	0.504 Nmm [77]
ν_{12}	0.309 [8]	G_{mat}^C	1.1 Nmm [12]^
ν_{23}	0.309 [8]	G_{mat}^{12}	1.566 Nmm [77]
ν_{13}	0.309 [8]	G_{mat}^{23}	1.566 Nmm [77]
G_{12}	4.21 GPa [8]	G_{mat}^{13}	1.566 Nmm [77]
G_{23}	4.21 GPa [8]	$c_{1,12}$	34.238 GPa [125]*
G_{13}	4.21 GPa [8]	$c_{2,12}$	15.061 GPa [125]*
X^T	2.20 GPa [8]	$c_{3,12}$	2.189 GPa [125]*
X^C	1.47 GPa [8]	$c_{1,23}$	34.238 GPa [125]*
Y^T	48.9 MPa [8]	$c_{2,23}$	15.061 GPa [125]*
Y^C	199 MPa [8]	$c_{3,23}$	2.189 GPa [125]*
S_{12}	154 MPa [8]	$c_{1,13}$	34.238 GPa [125]*
		$c_{2,13}$	15.061 GPa [125]*
property taken from ^HTA/6376C,*T700/M21		$c_{3,13}$	2.189 GPa [125]*

Table 6.8: Interlaminar material property inputs for T700/2510.

Interlaminar properties	Value	Interlaminar properties	Value
Normal strength	54 MPa [77]	Normal fracture energy	0.504 Nmm [77]
Shear strength (1)	70 MPa [77]	Shear (1) fracture energy	1.566 Nmm [77]
Shear strength (2)	70 MPa [77]	Shear (2) fracture energy	1.566 Nmm [77]

The solution time for the simulation was 29.5 hr spread over three AMD Opteron based compute nodes with 12 cores each for a total of 1062 CPU.hr.

6.6.2 Results comparison between simulation and experiment

Figure 6.18 shows the simulation yielded almost identical steady-state force response in comparison with experimental measurements. In contrast, the numerical peak force was over-predicted. The

experimental peak was much narrower and had a reduced height. This increased initial peak has

resulted in an increased energy absorption (674 J) of the numerical model in comparison with the

experimentally measured 631 J. Low level oscillatory noise was also present, with occasional higher

amplitude spikes. However, filtering was not deemed to be necessary as the amplitude of numerical

oscillations was small.
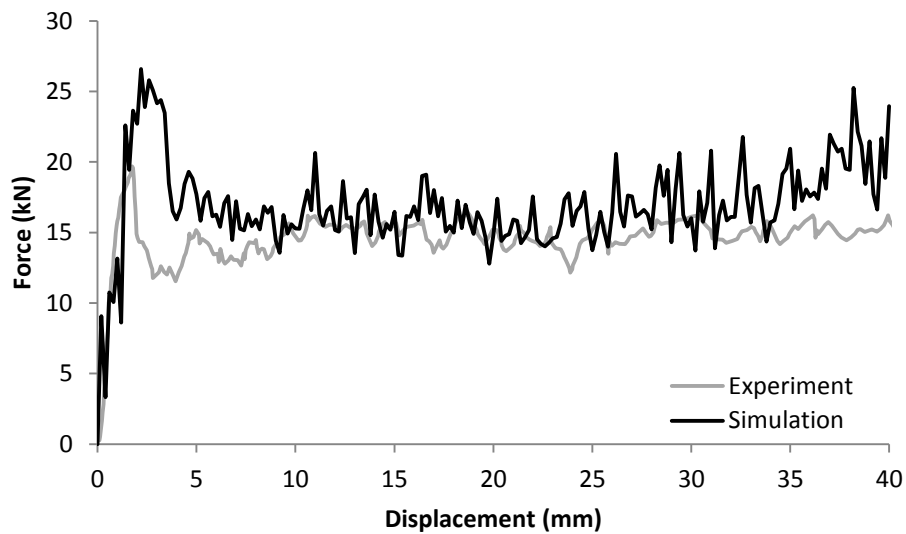
Figure 6.18: Comparison of experimentally measured [8] (grey) and simulated (black) force response of the

corrugated web.

The finite element process meshing process uses linear line segments to approximate the specimen

geometry and this process is limited by the mesh density. This can have an impact on the accurate

reproduction of the trigger region behaviour. The trigger is more susceptible to these geometric

deviations due to the small size (approximately four or five elements long) of the chamfer region. This

may have been a factor in the 28% over-prediction of the peak force in the corrugated web specimen.

Initiation of damage in the mesh occurs on a per-elements basis which is slightly delayed as the strain

energy needs to accumulate sufficiently to damage an entire element. Furthermore, the initial bending

of the ply may not be well captured because effectively, only a few linear segments are used to

capture the theoretical parabolic curve. Both of these issues diminished quickly as the crushing

progressed. Furthermore, the inaccuracy of the delamination fracture energies can be significant [135] and thus contribute to this difference.

The simulated response closely matched the ply damage and debris generation observed in the experimental tests (Figure 6.19). Delamination and subsequent splaying of constituent plies was the main form of deformation in both the simulated and experimental response. The roughness of the splayed plies shows the extensive matrix-dominated damage in this region, which was also captured numerically. The variety of different sized debris generated during the splaying process was also mirrored in the simulated results.
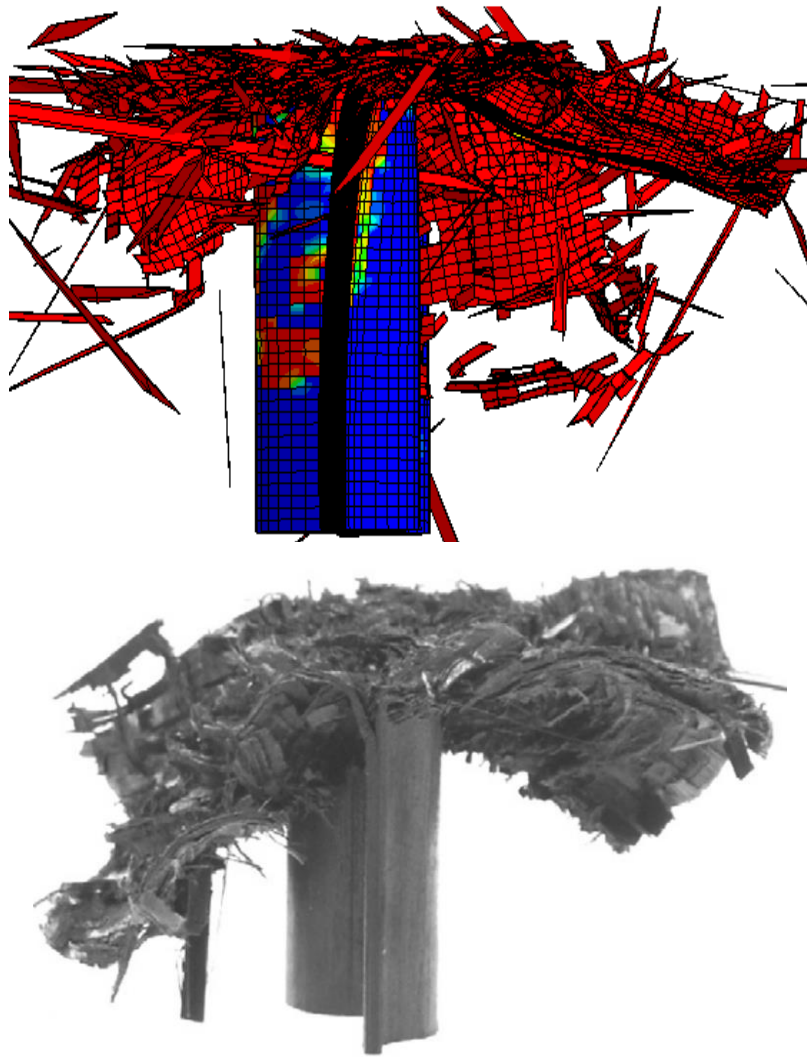
Figure 6.19: Comparison of ply damage and debris generation between simulation (left, red denoting matrix-dominated damage) and experiment [8] (right).

6.7   Discussions

6.7.1 Predicting force responses and energy absorption

The simulated force histories showed that the numerical model was able to accurately predict the force response of each specimen in general. However, there was a tendency to over-predict the peak load (Figure 6.20) at the initiation of widespread damage. This was likely the result of the mesh size used in the simulation not having enough resolution to capture the true behaviour of the trigger region.
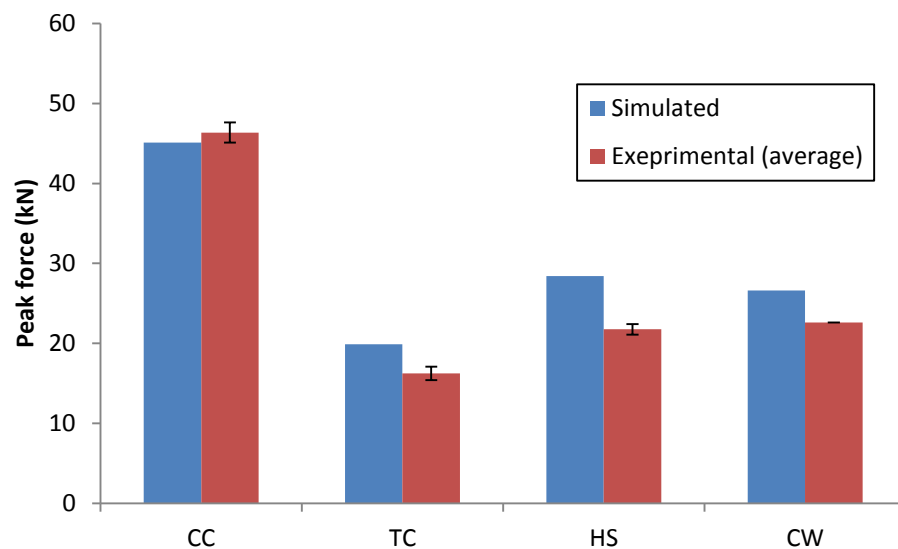
Figure 6.20: Comparison of peak force experienced.

The steady-state force responses (Figure 6.21), which accounts for the majority of the crush stroke, were generally well captured. This has led to a good assessment of the total energy absorption during the crushing process.
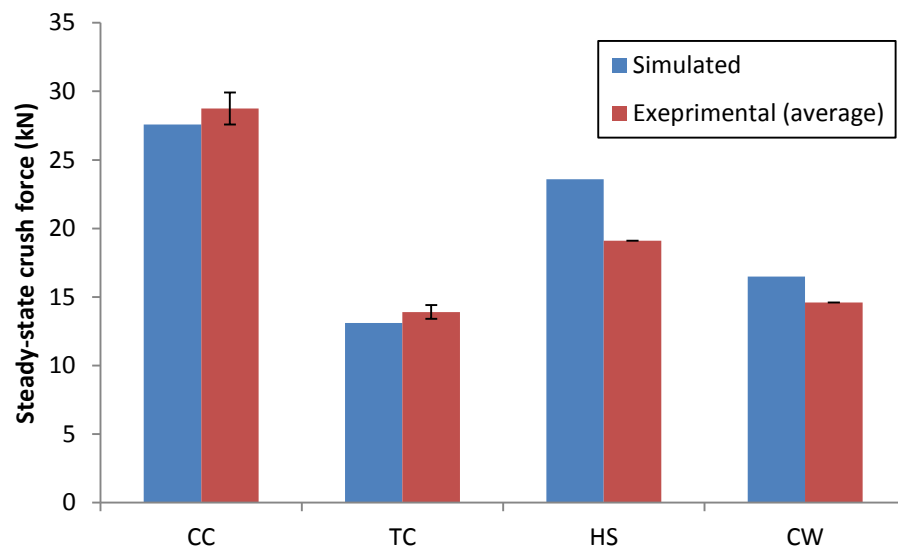
Figure 6.21: Comparison of steady-state crush force.

From the force response, the total energy absorption can be calculated. The energy absorption

returned by the simulated closely matched experimental observation as shown in Figure 6.22.
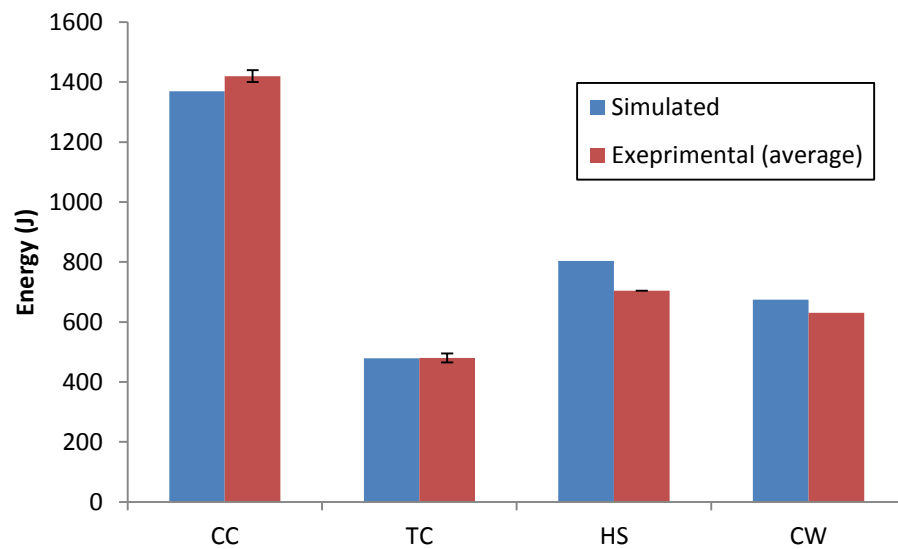
Figure 6.22: Comparison of total energy absorption.

The two cylindrical sections yielded the best results, with a < 4% difference between simulated and

experimental results. This is followed by the corrugated web, which has a 6% difference. The hat-

section yielded a larger 11% difference, which may be a result of the lack of constraint and hence a

lack of rigidity on the flat outer flanges of the hat sections. The large flanges on the sides were prone to global bending instead of splaying which changed the active damage mode locally. The change in damage mode resulted in a slightly different resultant energy absorption. The simulated SEA (Figure 6.23) also compared well to the experimental measurements, particularly for the tubular specimens.
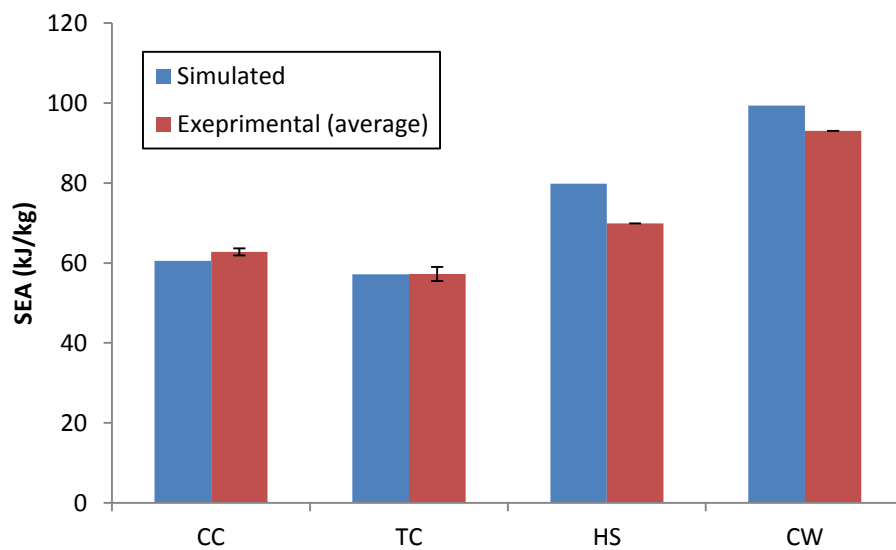
Figure 6.23: Comparison of specific energy absorption.

The crush efficiency (Figure 6.24) was also well captured with the exception of the tulip triggered tube.
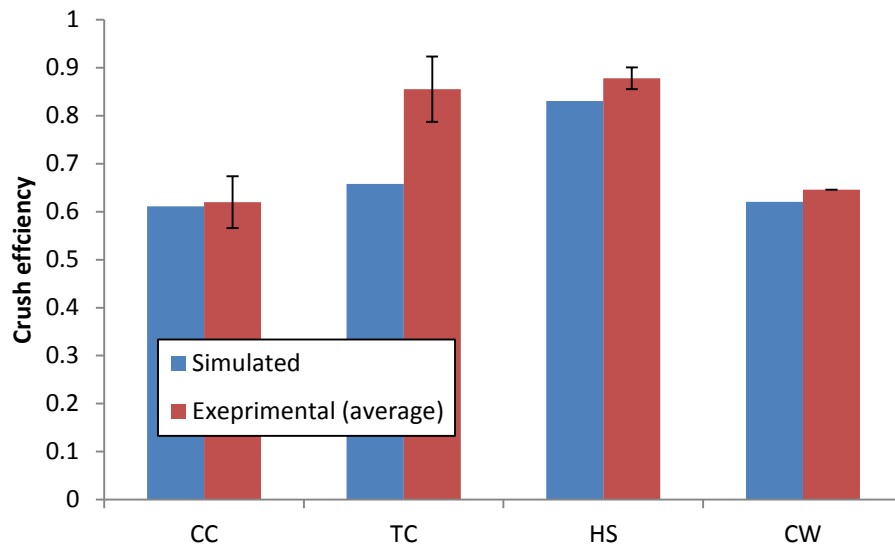
Figure 6.24: Comparison of crush efficiency.

6.7.2 Issues in predicting damage response

Oscillatory noise spikes were present in the force responses of these specimens, which may have been a result of the deletion algorithm for severely degraded elements. This noise could have an impact on the total energy absorption. This oscillatory noise was caused by the deletion of elements which became severely damaged. The removal of these elements also removed the resistive forces that they provided. This caused the loading surface to drop onto the next layer of elements, forming the trough as well as the remaining structure to spring back to hit the loading surface some time later, causing a peak. This issue was be alleviated through increasing the mesh density at the expense of increased computational requirement. For example, moving from 2 mm to 1 mm sided elements for the chamfered cylinder reduced the average magnitude of oscillatory noise by approximately 50%, which is consistent with sensitivity study results in Chapter 4. Alternatively, randomising the mesh could also result in a positive impact by spreading the deletion of elements over a wider range of conditions. Despite the use of a regular mesh, the present model did not experience the deletion of entire rows of elements which could cause the force to drop to zero (Figure 6.25) which caused issues for some existing models.
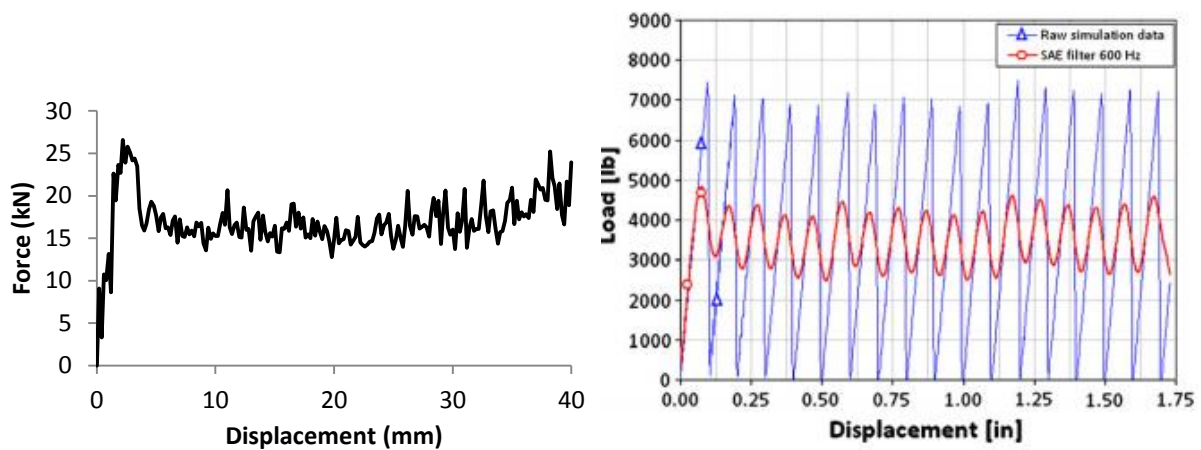
Figure 6.25: Comparison of raw simulated response of a corrugated web using the present model (left) and LS-

DYNA [8]

The different geometries were generally well handled as the experimentally observed damage

morphologies were well predicted in the simulations. A large variety of different features were

successfully reproduced numerically. These features range in size from large sheets of petalling plies

to small debris pieces being ejected from the main body. The splitting and splaying of the composite

laminate under crush loading, which is a critical feature of the damage process, was very well

reproduced. Each ply was modelled individually, allowing the meso-scale effects to be adequately

captured.

However, the stiffness of the damaged laminate was somewhat lower than what was observed in

reality, as demonstrated by the limp appearance of the splayed laminate sections in the chamfered and

tulip-triggered tubes. This phenomenon was a result of the CDM formulation, which approximate the

numerous intralaminar fractures and voids as a softening of the ply element. Very sharp geometric

features such as the peaks of the tulip triggers and chamfered edges sometimes caused numerical

spikes in the force response. The sharp tips caused the over-prediction of force response during the

first millimetre of crush stroke in the tulip-triggered specimen. This was a result of using degraded

and deleted elements to represent damage, which means damage can only be resolved to the size of

one element. This issue should diminish as the damage zone increases in size. Increasing mesh density

will also improve the response in this regard by reducing the area of the smallest resolvable region of damage.

6.7.3   Variability in material parameters

A number of material parameters are required to produce the correct response. In particular, the intralaminar critical energy release rates for each damage mode underpin the response of the composite structure. Laffan et al. [98] noted variability in the experimentally measured intralaminar critical energy release rates due to the difficulty in ensuring that only the desired damage mode is being activated in the production of the crack. Variability in these values can adversely affect the performance of the model and degrade its predictive power. It is expected that the fibre-dominated value would have the greatest effect and hence its accurate assessment is crucial. Material characterisation tests should be repeated to understand the distribution of values so that a more representative value can be used in the simulation.

Another important parameter is the friction coefficient between different surfaces that come into contact. As crushing progresses, debris is generated which alters the properties of the contact interface. This changing contact condition plays a role in the overall crush response of the structure by changing the local forces acting on the ply. This change can be captured by separating the simulation into steps with different contact properties in each. However, there is a risk that the transition between simulation steps can cause numerical artefacts in the response. As shown in an earlier chapter, a small change in the friction coefficient does not create a significant change in the overall force response if the specimen. Understanding the magnitude of change in friction coefficient through experimental testing on different surface conditions should guide the decision on whether this change should be modelled.

6.8 Summary

A 3D intralaminar damage model was developed to predict the behaviour of composite structures under crush loading. This damage model demonstrated, through comparison with experimental results, to have the capacity to simulate composite structures under crush loading with satisfactory results. Additionally, only the geometry and measured material properties of the structure were required for accurate results.

This evaluation consisted of four test cases where the experimental results were either obtained through testing done in this project or the literature. The four test cases containing geometries representative of typical composite energy absorbing structures were chosen: a chamfered cylindrical tube, a tulip-triggered cylindrical tube, a hat shaped section and a semi-circular corrugated web. This enables the assessment of the developed model for the variety of conditions likely to be encountered in analysis of composite energy absorber structures.

The force response was well predicted by the simulation and the total energy absorption in the crushing process compared well with experimental measurements. The total energy absorptions were in good agreement with observations. The predicted deformation and damage morphology of the specimens were also highly consistent with experimental observations. The main features of the damage progression through the structures were effectively captured. These results demonstrate the suitability of the model to form part of a virtual testing method for analysis of composite structures under crushing loads.

Chapter 7
Conclusions

7.1   Conclusions

This project aimed to enhance current capabilities to improve the design process for composite energy absorbing structures. A predictive damage model for composite laminates has been developed and implemented in Abaqus. This model integrated physically based damage mechanisms and interactions to achieve an accurate solution. An experimental program was conducted on a set of representative energy absorbing specimens to assess the strain rate dependence of crush structures. The results provided information for the development of composite energy absorbing structures. The experimental data was also used in subsequent validation. The capability of the proposed model was demonstrated by validating the prediction with experimental data in various test cases which represent a variety of configurations potentially encountered in composite energy absorbers. Therefore the developed damage model can be incorporated into virtual testing methodologies for the analysis and design of composite energy absorbing structures.

7.1.1   Development of comprehensive modelling capability for composite structures

Due to the inherent complexity of composite structures, the design process of energy absorbing composite structures currently relies on extensive testing at the subcomponent level to analyse their performance. Virtual testing can reduce the reliance on costly and time consuming physical testing. However, deficiencies exist in currently available numerical models which do not adequately provide the modelling predictive capability required for use in virtual testing. The current work addressed these through the development of a predictive, physically based damage model.

The developed damage model offers substantial advantages over current approaches through its physically based modelling approach. The model combines novel and existing modelling techniques to fully capture the damage behaviour of composite structures. The following summarises the main features of the developed damage model:

- A 3D formulation for solid elements which accounts for multi-axial loading;

- A novel and robust method for characteristic length calculations so allow for greater flexibility when meshing;

- A continuum damage mechanics based damage response, which incorporates energy dissipation through strain softening of the material with damage progression;

- A non-linear, inelastic shear response to account for the experimentally observed matrix behaviour, particularly for larger deformations;

- An improved physically based mechanism for damage interaction to handle the loading-unloading-reloading caused by large formation and failure of adjacent material; and

- A unified matrix damage mechanism with load-adjusted critical strain energy release rate along the fracture plane to accurately represent the experimentally observed failure mode.

This model is implemented in Abaqus/Explicit for use with solid reduced integration linear hexahedral elements. The developed model was combined with existing delamination and contact models to form a complete modelling package. These characteristics allow the model to predict the crushing of the composite structure with high accuracy down to the ply level. In particular, the physical nature of the presented model requires only physically measureable inputs, such as geometry, material properties and loading conditions, to achieve an accurate solution. Empirical calibration and manipulation of input parameters was not required. This gives the model predictive power which is essential in any virtual testing techniques.

The model was benchmarked to ensure the desired response was properly captured through a series of single element and coupon sized tests. Certain material parameters, such as transverse strengths, vary substantially with local configurations and the sensitivity of the model to changes in these values was explored. It was found that the model was not sensitive to these changes. Furthermore, the sensitivity of the model to various simulation parameters, such as numerical damping and scaling, was also assessed to reach an optimal simulation configuration.

7.1.2 Strain rate effect on a representative energy absorbing specimen

An in-depth experimental study was completed to explore the effect of rate dependence of a composite structure dynamically loaded in crushing, where the literature is currently in disagreement. Conflicting behaviours have been reported for a range of different composite structures under crush loading. A representative energy absorbing specimen was designed and tested to understand the rate behaviour as well as to explore the mechanisms driving these effects.

A set of tulip-triggered cylindrical tubes made from unidirectional carbon-epoxy prepreg was prepared and tested at $2 \times 10^{-4} \ s^{-1}, 0.2 \ s^{-1}, 30 \ s^{-1}, 60 \ s^{-1}$ and $100 \ s^{-1}$ under crushing loads. A number of specimens were tested at each speed with very little observed scatter, suggesting that the measured trend was reliable. Both the force response and the damage morphologies were carefully examined. The four different metrics, specific energy absorption, peak and steady-state force as well as the crush efficiency, were calculated and averaged for each tested rate. Regression analysis of these metrics shows that the tested configuration was strain rate independent. The observed damage modes did not change with increased test speed either. These results confirm the rate independence of the tested configuration.

The apparent rate insensitivity is likely a result of the fibre-dominated nature of the tested configuration. Major factors contributing to the fibre-dominance in the performance of the specimen include:

- Unidirectional prepreg with a large fibre volume fraction,
- [0/90/0/90]s layup causing overall laminate properties to be fibre-dominated,
- Measured critical energy release rates for fibre-dominated damage are up to 2 orders of magnitude larger than that of matrix-dominated damage.

Optimising crush energy absorption leads to increased proportion of energy absorbed through fibre-dominated damage mode due to its high critical energy release rate. Hence, these results showed that

strain rate sensitivity can be neglected for design of composite structures for crash protection purposes using materials similar to those investigated in this work.

7.1.3 Validation of damage model against experimental data

The damage model was shown to be capable of predicting the damage response of composite structures under crush loading to a high degree of accuracy. Model performance was evaluated against experimental data obtained from the testing done as a part of this project as well as from the literature. Four representative composite energy absorbing structures were chosen as test cases: a chamfered cylindrical tube, a tulip-triggered cylindrical tube, a hat shaped section and a semi-circular corrugated web. These test cases cover a range of different features found in composite energy absorbers, including:

- Various open and closed cross-sections,

- Various trigger configurations,

- Curved and straight sections.

Finite element meshes of the test cases were created and simulated under crush loading. Material properties were obtained from the literature and used without modifications. The predicted forces corresponded well with the experimentally measured force responses of the four test cases. The calculated total energy absorption of the different test cases was also in agreement with the experimental results. For the two closed section geometries, the simulated energy dissipations were predicted to within 4% of experimental averages, whereas the hat section and corrugated web sections were within 12% of experimental values. Differences in accuracy appear to be associated with the degree of constraint applied to the sections.

The damage morphology was very well predicted by the numerical modelling. Different damage behaviour was well reproduced. These phenomena include:

- Splitting and subsequent splaying of the plies during petal formation,

- Crack formation near the crush front,

- Debris formation and ejection.

Overall, the simulated deformation of the damaged structure correlates closely with experimental observations. The model has sufficient resolution to capture meso-scale features within the ply cross-section such as the flat crush front.

This study has shown that this damage model has the capacity to simulate composite structures under crush loading with satisfactory results and thus suitable for use as a part of a validated virtual testing methodology.

7.1.4 Summary

The three main research aims for this project have been successfully achieved:

1. A reliable, comprehensive and predictive composite material damage model was developed and implemented for Abaqus/Explicit;

2. An experimental program was completed, showing loading rate independence for a representative energy absorber specimen;

3. Evaluation of the developed material damage model against experimental data showed it was able to predict the experimentally observed force response and structural deformation to a high degree of accuracy without the need for manipulation.

7.2 Contributions to analysis of composite energy absorbers

This work serves to aid the design of energy absorbing structures by providing a validated method to predict the crushing response. The use of the developed modelling capability can substantially reduce the requirement for physical tests during the initial and optimisation stages of the design process. By conducting the analysis numerically rather than through physical testing, the design process becomes easier and requires less support. As a result, a greater range of design configurations can be explored and/or the design can be completed with less time and money.

The experimental program also shed light on the strain rate effect on the overall response of composite structures under elevated loading rates. This work suggests that for configurations where the performance is dominated by fibre damage mechanism, strain rate effects can be safely neglected. This simplifies the analysis process for the response of the composite structure.

7.3   Recommendations for future work

The success of the developed model opens new doors to a variety of different applications. The detailed and physically based nature of the model allows it to be used as a general constitutive model for composite structures. A study of the utility of this material model for other load cases can substantially improve virtual testing capability in those areas. Potentially suitable applications include:

1. Performance of damaged composite structures.
    a. Assess the performance of structures after damage.
    b. Assess tolerance to damage and set safe limits for load bearing structures.
2. Damage in composite joints.
    a. Joint design analysis, particularly those with mechanical fasteners.
    b. Transfer of loading across a joint, particularly damaging loads.

The apparent strain rate independence also warrants further investigation to quantify the contribution of each contributing factor, including:

- Fibre volume fraction,
- Laminate layup configuration,
- Relative stiffness of fibre and matrix material,
- Relative critical energy release rates of fibre and matrix material.

As a result of the measured strain rate independence, rate effects were not included in the presented damage model. The modular construction of the implementation allows rate effect to be readily included in the model once the mechanisms behind the rate effects were better understood.

The observed numerical oscillation is another area where improvements can be made. A deeper understanding of the interaction between the progression of damage and the deletion of distorted elements can potentially smooth the simulated response and eliminate the need for filtering.

Finally, moving the present model towards a finite strain formulation can allow continued mesh refinement without having to consider whether the resulting large failure strain will cause deviations from theoretical expectations as seen in Figure 4.17.

References

[1]   Kaw, A.K., *Mechanics of composite materials*. 1997: CRC Press.

[2]   Company, T.B., *Advanced composite use*. 2008, The Boring Company: http://www.newairplane.com/787/#/design-highlights/visionary-design/composites/advanced-composite-use/.

[3]   JSSG-2010-7, *DEPARTMENT OF DEFENSE JOINT SERVICE SPECIFICATION GUIDE - CREW SYSTEMS CRASH PROTECTION HANDBOOK*. 2002, US Department of Defence.

[4]   MIL-STD-1290A(AV), *MILITARY STANDARD LIGHT FIXED AND TOTARY-WING AIRCRAFT CRASH RESISTANCE*. 1988, US Department of Defence.

[5]   Jacob, G.C., J.F. Fellers, S. Simunovic, and J.M. Starbuck, *Energy Absorption in Polymer Composites for Automotive Crashworthiness.* Journal of Composite Materials, 2002. **36**(7): p. 813-850.

[6]   SIMULIA, *Abaqus Documentation version 6.11*. 2011: SIMULIA (Dassault Systems).

[7]   Hallquist, J.O., *LS-DYNA theory manual*. 2006, Livermore: Livermore Software Technology Corporation.

[8]   Feraboli, P., B. Wade, F. Deleo, M. Rassaian, M. Higgins, and A. Byar, *LS-DYNA MAT54 modeling of the axial crushing of a composite tape sinusoidal specimen.* Composites Part A: Applied Science and Manufacturing, 2011. **42**(11): p. 1809-1825.

[9]   Joosten, M.W., *Experimental and Numerical Investigation of Triggered Composite Energy Absorbing Structures*, in *School of Mechanical and Manufacturing Engineering*. 2011, University of New South Wales: University of New South Wales, Sydney, NSW, 2052, Australia.

[10]   Garnich, M.R. and V.M.K. Akula, *Review of Degradation Models for Progressive Failure Analysis of Fiber Reinforced Polymer Composites.* Applied Mechanics Reviews, 2009. **62**(1): p. 010801-33.

[11]   Puck, A. and H. Schürmann, *Failure analysis of FRP laminates by means of physically based phenomenological models* Composites Science and Technology, 1998. **58**(7): p. 1045-1067.

[12]   Faggiani, A. and B.G. Falzon, *Predicting low-velocity impact damage on a stiffened composite panel.* Composites Part A: Applied Science and Manufacturing, 2010. **41**(6): p. 737-749.

[13]   Maimí, P., P.P. Camanho, J.A. Mayugo, and C.G. Dávila, *A continuum damage model for composite laminates: Part I – Constitutive model.* Mechanics of Materials, 2007. **39**(10): p. 897-908.

[14]   Donadon, M.V., S.F.M. de Almeida, M.A. Arbelo, and A.R. de Faria, *A Three-Dimensional Ply Failure Model for Composite Structures.* International Journal of Aerospace Engineering, 2009. **2009**.

[15]   *AIRWORTHINESS STANDARDS: NORMAL, UTILITY, ACROBATIC, AND COMMUTER CATEGORY AIRPLANES*, in *14 CFR Part 23*, Federal Aviation Authority, Editor.

[16]   *AIRWORTHINESS STANDARDS: TRANSPORT CATEGORY AIRPLANES*, in *14 CFR Part 25*, Federal Aviation Authority, Editor.

[17]   *AIRWORTHINESS STANDARDS: NORMAL CATEGORY ROTORCRAFT*, in *14 CFR Part 27*, Federal Aviation Authority, Editor.

[18]   *AIRWORTHINESS STANDARDS: TRANSPORT CATEGORY ROTORCRAFT*, in *14 CFR Part 29*, Federal Aviation Authority, Editor.

[19]   Desjardins, S.P., *The evolution of energy absorption systems for crashworthy helicopter seats.* Journal of the American Helicopter Society, 2006. **51**(2): p. 150-163.

[20]   Heimbs, S., F. Strobl, and P. Middendorf, *Integration of a Composite Crash Absorber in Aircraft Fuselage Vertical Struts.* International Journal of Vehicle Structures & Systems, 2011. **3**(2): p. 87-95.

[21]   Waimer, M., D. Kohlgrüber, D. Hachenberg, and H. Voggenreiter, *Experimental study of CFRP components subjected to dynamic crash loads.* Composite Structures, 2013. **105**(0): p. 288-299.

[22]   Garner, D.M. and D.O. Adams, *Test methods for composites crashworthiness: A review.* Journal of Advanced Materials, 2008. **40**(4): p. 5-26.

[23]   Palanivelu, S., W. Van Paepegem, J. Degrieck, J. Van Ackeren, D. Kakogiannis, D. Van Hemelrijck, J. Wastiels, and J. Vantomme, *Experimental study on the axial crushing behaviour of pultruded composite tubes.* Polymer Testing, 2010. **29**(2): p. 224-234.

[24]   Abedrabbo, N., R. Mayer, A. Thompson, C. Salisbury, M. Worswick, and I. van Riemsdijk, *Crash response of advanced high-strength steel tubes: Experiment and model.* International Journal of Impact Engineering, 2009. **36**(8): p. 1044-1057.

[25]   Pitarresi, G., J.J. Carruthers, A.M. Robinson, G. Torre, J.M. Kenny, S. Ingleton, O. Velecela, and M.S. Found, *A comparative evaluation of crashworthy composite sandwich structures.* Composite Structures, 2007. **78**(1): p. 34-44.

[26]   Taher, S.T., E. Mahdi, A.S. Mokhtar, D.L. Magid, F.R. Ahmadun, and P.R. Arora, *A new composite energy absorbing system for aircraft and helicopter.* Composite Structures, 2006. **75**(1-4): p. 14-23.

[27]   Huang, J. and X. Wang, *On a new crush trigger for energy absorption of composite tubes.* International Journal of Crashworthiness, 2010. **15**(6): p. 625 - 634.

[28]   Swaminathan, N. and R.C. Averill, *Contribution of Failure Mechanisms to Crush Energy Absorption in a Composite Tube.* Mechanics of Advanced Materials and Structures, 2006. **13**(1): p. 51 - 59.

[29]   Elgalai, A.M., E. Mahdi, A.M.S. Hamouda, and B.S. Sahari, *Crushing response of composite corrugated tubes to quasi-static axial loading.* Composite Structures, 2004. **66**(1-4): p. 665-671.

[30]   Ghasemnejad, H., B.R.K. Blackman, H. Hadavinia, and B. Sudall, *Experimental studies on fracture characterisation and energy absorption of GFRP composite box structures.* Composite Structures, 2009. **88**(2): p. 253-261.

[31]   Xiao, X., *Modeling Energy Absorption with a Damage Mechanics Based Composite Material Model.* Journal of Composite Materials, 2009. **43**(5): p. 427-444.

[32]   Mamalis, A.G., D.E. Manolakos, M.B. Ioannidis, and D.P. Papapostolou, *On the response of thin-walled CFRP composite tubular components subjected to static and dynamic axial compressive loading: experimental.* Composite Structures, 2005. **69**(4): p. 407-420.

[33]   Jackson, K.E., Y.T. Fuchs, and S. Kellas, *Overview of the National Aeronautics and Space Administration Subsonic rotary wing aeronautics research program in rotorcraft crashworthiness.* Journal of Aerospace Engineering, 2009. **22**(3): p. 229-239.

[34]   Kellas, S. and K.E. Jackson, *Deployable System for Crash---Load Attenuation.* Journal of the American Helicopter Society, 2010. **55**(4): p. 042001-14.

[35]   Mamalis, A.G., D.E. Manolakos, M.B. Ioannidis, and D.P. Papapostolou, *On the experimental investigation of crash energy absorption in laminate splaying collapse mode of FRP tubular components.* Composite Structures, 2005. **70**(4): p. 413-429.

[36]   Feraboli, P., *Development of a Modified Flat-plate Test Specimen and Fixture for Composite Materials Crush Energy Absorption.* Journal of Composite Materials, 2009. **43**(19): p. 1967-1990.

[37]   Johnson, A.F. and M. David, *Failure Mechanisms and Energy Absorption in Composite Elements under Axial Crush.* Key Engineering Materials, 2012. **488-489**: p. 638-641.

[38]   Feraboli, P., B. Wade, F. Deleo, and M. Rassaian, *Crush energy absorption of composite channel section specimens.* Composites Part A: Applied Science and Manufacturing, 2009. **40**(8): p. 1248-1256.

[39]   Johnson, A.F. and M. David, *Failure mechanisms in energy-absorbing composite structures.* Philosophical Magazine, 2010. **90**(31): p. 4245 - 4261.

[40]   Feraboli, P., *Development of a Corrugated Test Specimen for Composite Materials Energy Absorption.* Journal of Composite Materials, 2008. **42**(3): p. 229-256.

[41]   McCarthy, M.A., C.G. Harte, J.F.M. Wiggenraad, A.L.P.J. Michielsen, D. Kohlgrüber, and A. Kamoulakos, *Finite element modelling of crash response of composite aerospace sub-floor structures.* Computational Mechanics, 2000. **26**(3): p. 250-258.

[42]   Zhang, J., P. Supernak, S. Mueller-Alander, and C.H. Wang, *Improving the bending strength and energy absorption of corrugated sandwich composite structure.* Materials & Design, 2013. **52**(0): p. 767-773.

[43]   Palanivelu, S., W.V. Paepegem, J. Degrieck, J. Vantomme, D. Kakogiannis, J.V. Ackeren, D.V. Hemelrijck, and J. Wastiels, *Crushing and energy absorption performance of different geometrical shapes of small-scale glass/polyester composite tubes under quasi-static loading conditions.* Composite Structures, 2011. **93**(2): p. 992-1007.

[44]   Jackson, K.E. and E.L. Fasanella, *Development of a Scale Model Composite Fuselage Concept for Improved Crashworthiness.* Journal of Aircraft, 2001. **38**(1): p. 95-103.

[45]   McCarthy, M.A. and J.F.M. Wiggenraad, *Numerical investigation of a crash test of a composite helicopter subfloor structure.* Composite Structures 2001. **51**(4): p. 345-359.

[46]   Lau, S.T.W., M.R. Said, and M.Y. Yaakob, *On the effect of geometrical designs and failure modes in composite axial crushing: A literature review.* Composite Structures, 2012. **94**(3): p. 803-812.

[47]   Kakogiannis, D., S. Chung Kim Yuen, S. Palanivelu, D. Van Hemelrijck, W. Van Paepegem, J. Wastiels, J. Vantomme, and G.N. Nurick, *Response of pultruded composite tubes subjected to dynamic and impulsive axial loading.* Composites Part B: Engineering, 2013. **55**(0): p. 537-547.

[48]   Chiu, L.N.S., B.G. Falzon, D. Ruan, S. Xu, R.S. Thomson, B. Chen, and W. Yan, *Crush responses of composite cylinder under quasi-static and dynamic loading.* Sumbitted to Composite Structures.

[49]   Joosten, M.W., S. Dutton, D. Kelly, and R. Thomson, *Experimental and numerical investigation of the crushing response of an open section composite energy absorbing element.* Composite Structures, 2011. **93**(2): p. 682-689.

[50]   Siromani, D., G. Henderson, D. Mikita, K. Mirarchi, R. Park, J. Smolko, J. Awerbuch, and T.-M. Tan, *An experimental study on the effect of failure trigger mechanisms on the energy absorption capability of CFRP tubes under axial compression.* Composites Part A: Applied Science and Manufacturing, 2014. **64**(0): p. 25-35.

[51]   Farley, G.L., *The Effects of Crushing Speed on the Energy-Absorption Capability of Composite Tubes.* Journal of Composite Materials, 1991. **25**(10): p. 1314-1329.

[52]   Brighton, A., M. Forrest, M. Starbuck, D. Erdman, and B. Fox, *Strain Rate Effects on the Energy Absorption of Rapidly Manufactured Composite Tubes.* Journal of Composite Materials, 2009. **43**(20): p. 2183-2200.

[53]   Thornton, P.H., *Energy Absorption in Composite Structures.* Journal of Composite Materials, 1979. **13**(3): p. 247-262.

[54]   Jackson, A., S. Dutton, A.J. Gunnion, and D. Kelly, *Investigation into laminate design of open carbon–fibre/epoxy sections by quasi–static and dynamic crushing.* Composite Structures, 2011. **93**(10): p. 2646-2654.

[55]   David, M., A. Johnson, and H. Voggenreiter, *Analysis of Crushing Response of Composite Crashworthy Structures.* Applied Composite Materials, 2013. **20**(5): p. 773-787.

[56]   Talreja, R., *Damage mechanics of composite materials.* Composite materials series. 1994, Amsterdam [The Netherlands]; New York: Elsevier.

[57]   Griffith, A.A., *The Phenomena of Rupture and Flow in Solids.* Philosophical Transactions of the Royal Society of London. Series A, Containing Papers of a Mathematical or Physical Character, 1921. **221**(582-593): p. 163-198.

[58]   Anderson, T.L., *Fracture Mechanics: Fundamentals and Applications, Third Edition.* 2005: Taylor & Francis.

[59]   Chaboche, J.-L., *Continuous damage mechanics - A tool to describe phenomena before crack initiation.* Nuclear Engineering and Design, 1981. **64**(2): p. 233-247.

[60]   Lemaitre, J., *A Continuous Damage Mechanics Model for Ductile Fracture.* Journal of Engineering Materials and Technology, 1985. **107**(1): p. 83-89.

[61] Talreja, R., *Transverse Cracking and Stiffness Reduction in Composite Laminates.* Journal of Composite Materials, 1985. **19**(4): p. 355-375.

[62] Bathe, K.J., *Finite element procedures.* 1996: Prentice Hall.

[63] Zienkiewicz, O.C., R.L. Taylor, and J.Z. Zhu, *The finite element method: its basis and fundamentals.* 2005: Elsevier Butterworth-Heinemann.

[64] Donadon, M.V., L. Iannucci, B.G. Falzon, J.M. Hodgkinson, and S.F.M.d. Almeida, *A progressive failure model for composite laminates subjected to low velocity impact damage.* Computers and Structures, 2008. **86**(11-12): p. 1232-1252.

[65] Huang, J. and X. Wang, *Numerical and experimental investigations on the axial crushing response of composite tubes.* Composite Structures, 2009. **91**(2): p. 222-228.

[66] Chang, F.-K. and K.-Y. Chang, *A Progressive Damage Model for Laminated Composites Containing Stress Concentrations.* Journal of Composite Materials, 1987. **21**(9): p. 834-855.

[67] Tsai, S.W. and E.M. Wu, *A General Theory of Strength for Anisotropic Materials.* Journal of Composite Materials, 1971. **5**(1): p. 58-80.

[68] Matzenmiller, A., J. Lubliner, and R.L. Taylor, *A constitutive model for anisotropic damage in fiber-composites.* Mechanics of Materials, 1995. **20**(2): p. 125-152.

[69] Ladeveze, P. and E. LeDantec, *Damage modelling of the elementary ply for laminated composites.* Composites Science and Technology, 1992. **43**(3): p. 257-267.

[70] Hashin, Z., *Failure Criteria for Unidirectional Fiber Composites.* Journal of Applied Mechanics, 1980. **47**(2): p. 329-334.

[71] Williams, K.V., R. Vaziri, and A. Poursartip, *A physically based continuum damage mechanics model for thin laminated composite structures.* International Journal of Solids and Structures, 2003. **40**(9): p. 2267-2300.

[72] Raimondo, L., L. Iannucci, P. Robinson, and P.T. Curtis, *A progressive failure model for mesh-size-independent FE analysis of composite laminates subject to low-velocity impact damage.* Composites Science and Technology, 2012. **72**(5): p. 624-632.

[73] Shi, Y., T. Swait, and C. Soutis, *Modelling damage evolution in composite laminates subjected to low velocity impact.* Composite Structures, 2012. **94**(9): p. 2902-2913.

[74] Egan, B., M.A. McCarthy, R.M. Frizzell, P.J. Gray, and C.T. McCarthy, *Modelling bearing failure in countersunk composite joints under quasi-static loading using 3D explicit finite element analysis.* Composite Structures, 2014. **108**: p. 963-977.

[75] Bažant, Z. and B. Oh, *Crack band theory for fracture of concrete.* Materials and Structures, 1983. **16**(3): p. 155-177.

[76] Oliver, J., *A consistent characteristic length for smeared cracking models.* International Journal for Numerical Methods in Engineering, 1989. **28**(2): p. 461-474.

[77] Sokolinsky, V.S., K.C. Indermuehle, and J.A. Hurtado, *Numerical simulation of the crushing process of a corrugated composite plate.* Composites Part A: Applied Science and Manufacturing, 2011. **42**(9): p. 1119-1126.

[78] Israr, H.A., S. Rivallant, C. Bouvet, and J.J. Barrau, *Finite element simulation of 0°/90° CFRP laminated plates subjected to crushing using a free-face-crushing concept.* Composites Part A: Applied Science and Manufacturing, 2014. **62**(0): p. 16-25.

[79] Hongkarnjanakul, N., C. Bouvet, and S. Rivallant, *Validation of low velocity impact modelling on different stacking sequences of CFRP laminates and influence of fibre failure.* Composite Structures, 2013. **106**(0): p. 549-559.

[80] Bouvet, C., S. Rivallant, and J.J. Barrau, *Low velocity impact modeling in composite laminates capturing permanent indentation.* Composites Science and Technology, 2012. **72**(16): p. 1977-1988.

[81] Johnson, A.F., *Modelling fabric reinforced composites under impact loads.* Composites Part A: Applied Science and Manufacturing, 2001. **32**(9): p. 1197-1206.

[82] McGregor, C., R. Vaziri, and X. Xiao, *Finite element modelling of the progressive crushing of braided composite tubes under axial impact.* International Journal of Impact Engineering, 2010. **37**(6): p. 662-672.

[83] McGregor, C.J., R. Vaziri, A. Poursartip, and X. Xiao, *Simulation of progressive damage development in braided composite tubes under axial compression.* Composites Part A: Applied Science and Manufacturing, 2007. **38**(11): p. 2247-2259.

[84]   ASTM, *D3039 / D3039M – 08* in *Standard Test Method for Tensile Properties of Polymer Matrix Composite Materials*. 2007, ASTM International, West Conshohocken, PA.

[85]   ASTM, *D3410 / D3410M – 03* in *Standard Test Method for Compressive Properties of Polymer Matrix Composite Materials with Unsupported Gage Section by Shear Loading*. 2003, ASTM International, West Conshohocken, PA.

[86]   Chang, F.-K. and M.-H. Chen, *The In Situ Ply Shear Strength Distributions in Graphite/Epoxy Laminated Composites*. Journal of Composite Materials, 1987. **21**(8): p. 708-733.

[87]   Camanho, P.P., C.G. Dávila, S.T. Pinho, L. Iannucci, and P. Robinson, *Prediction of in situ strengths and matrix cracking in composites under transverse tension and in-plane shear*. Composites Part A: Applied Science and Manufacturing, 2006. **37**(2): p. 165-176.

[88]   ASTM, *D3518 / D3518M – 94* in *Standard Test Method for In-Plane Shear Response of Polymer Matrix Composite Materials by Tensile Test of a ±45° Laminate*. 2001, ASTM International, West Conshohocken, PA.

[89]   ASTM, *D4255 / D4255M - 01*, in *Standard Test Method for In-Plane Shear Properties of Polymer Matrix Composite Materials by the Rail Shear Method*. 2001, ASTM International, West Conshohocken, PA.

[90]   ASTM, *D7078 / D7078M - 05*, in *Standard Test Method for Shear Properties of Composite Materials by V-Notched Rail Shear Method*. 2005, ASTM International, West Conshohocken, PA.

[91]   ASTM, *D5379 / D5379M - 05*, in *Standard Test Method for Shear Properties of Composite Materials by the V-Notched Beam Method*. 2005, ASTM International, West Conshohocken, PA.

[92]   ASTM, *E399 – 09* in *Standard Test Method for Linear-Elastic Plane-Strain Fracture Toughness KIc of Metallic Materials*. 2009.

[93]   ASTM, *E1820 – 01* in *Standard Test Method for Measurement of Fracture Toughness*. 2001.

[94]   ASTM, *D1922 – 03a* in *Standard Test Method for Propagation Tear Resistance of Plastic Film and Thin Sheeting by Pendulum Method*. 2003, ASTM International, West Conshohocken, PA.

[95]   Pinho, S.T., P. Robinson, and L. Iannucci, *Fracture toughness of the tensile and compressive fibre failure modes in laminated composites*. Composites Science and Technology, 2006. **66**(13): p. 2069-2079.

[96]   Laffan, M.J., S.T. Pinho, P. Robinson, and L. Iannucci, *Measurement of the in situ ply fracture toughness associated with mode I fibre tensile failure in FRP. Part I: Data reduction*. Composites Science and Technology, 2010. **70**(4): p. 606-613.

[97]   Laffan, M.J., S.T. Pinho, P. Robinson, and L. Iannucci, *Measurement of the in situ ply fracture toughness associated with mode I fibre tensile failure in FRP. Part II: Size and lay-up effects*. Composites Science and Technology, 2010. **70**(4): p. 614-621.

[98]   Laffan, M.J., S.T. Pinho, P. Robinson, and A.J. McMillan, *Translaminar fracture toughness testing of composites: A review*. Polymer Testing, 2012. **31**(3): p. 481-489.

[99]   ASTM, *D5528 – 01*, in *Standard Test Method for Mode I Interlaminar Fracture Toughness of Unidirectional Fiber-Reinforced Polymer Matrix Composites*. 2007, ASTM International, West Conshohocken, PA.

[100] ASTM, *D6617 / D6617M - 06*, in *Standard Test Method for Mixed Mode I-Mode II Interlaminar Fracture Toughness of Unidirectional Fiber Reinforced Polymer Matrix Composites*. 2006, ASTM International, West Conshohocken, PA.

[101] ASTM, *D4762 - 04*, in *Standard Guide for Testing Polymer Matrix Composite Materials*. 2004, ASTM International, West Conshohocken, PA.

[102] Sierakowski, R.L., *Strain Rate Effects in Composites*. Applied Mechanics Reviews, 1997. **50**(12): p. 741-761.

[103] Kolsky, H., *An Investigation of the Mechanical Properties of Materials at very High Rates of Loading*. Proceedings of the Physical Society. Section B, 1949. **62**(11): p. 676-700.

[104] Li, G. and D. Liu, *A Testing Technique for Characterizing Composite at Strain Rates up to 100/s*, in *Dynamic Behavior of Materials, Volume 1*, B. Song, D. Casem, and J. Kimberley, Editors. 2014, Springer International Publishing. p. 73-79.

[105] Vural, M. and G. Ravichandran, *Transverse Failure in Thick S2-Glass/ Epoxy Fiber-Reinforced Composites.* Journal of Composite Materials, 2004. **38**(7): p. 609-623.

[106] Hosur, M.V., S.M. Waliul Islam, U.K. Vaidya, A. Kumar, P.K. Dutta, and S. Jeelani, *Dynamic punch shear characterization of plain weave graphite/epoxy composites at room and elevated temperatures.* Composite Structures, 2005. **70**(3): p. 295-307.

[107] Shokrieh, M.M. and M.J. Omidi, *Compressive response of glass-fiber reinforced polymeric composites to increasing compressive strain rates.* Composite Structures, 2009. **89**(4): p. 517-523.

[108] Cantwell, W.J. and M. Blyton, *Influence of loading rate on the interlaminar fracture properties of high performance composites - A review.* Applied Mechanics Reviews, 1999. **52**(6): p. 199-212.

[109] Sun, C.T. and C. Han, *A method for testing interlaminar dynamic fracture toughness of polymeric composites.* Composites Part B: Engineering, 2004. **35**(6–8): p. 647-655.

[110] Hsiao, H.M. and I.M. Daniel, *Strain rate behavior of composite materials.* Composites Part B: Engineering, 1998. **29**(5): p. 521-533.

[111] Jacob, G.C., J.M. Starbuck, J.F. Fellers, S. Simunovic, and R.G. Boeman, *Strain rate effects on the mechanical properties of polymer composite materials.* Journal of Applied Polymer Science, 2004. **94**(1): p. 296-301.

[112] Koerber, H., J. Xavier, and P.P. Camanho, *High strain rate characterisation of unidirectional carbon-epoxy IM7-8552 in transverse compression and in-plane shear using digital image correlation.* Mechanics of Materials, 2010. **42**(11): p. 1004-1019.

[113] Koerber, H. and P.P. Camanho, *High strain rate characterisation of unidirectional carbon-epoxy IM7-8552 in longitudinal compression.* Composites Part A: Applied Science and Manufacturing, 2011. **42**(5): p. 462-470.

[114] Shokrieh, M.M. and M.J. Omidi, *Tension behavior of unidirectional glass/epoxy composites under different strain rates.* Composite Structures, 2009. **88**(4): p. 595-601.

[115] Shokrieh, M.M. and M.J. Omidi, *Investigating the transverse behavior of Glass-Epoxy composites under intermediate strain rates.* Composite Structures, 2011. **93**(2): p. 690-696.

[116] Falzon, B.G. and P. Apruzzese, *Numerical analysis of intralaminar failure mechanisms in composite structures. Part I: FE implementation.* Composite Structures, 2011. **93**(2): p. 1039-1046.

[117] Falzon, B.G. and P. Apruzzese, *Numerical analysis of intralaminar failure mechanisms in composite structures. Part II: Applications.* Composite Structures, 2011. **93**(2): p. 1047-1053.

[118] Van Paepegem, W., I. De Baere, E. Lamkanfi, and J. Degrieck, *Monitoring quasi-static and cyclic fatigue damage in fibre-reinforced plastics by Poisson's ratio evolution.* International Journal of Fatigue, 2010. **32**(1): p. 184-196.

[119] Press, W.H., S.A. teukolsky, W.T. Vetterling, and B.P. Flannery, *Numerical recipes in Fortran 2nd Ed.* 1992, Cambridge: Cambridge University Press.

[120] Pinho, S.T., L. Iannucci, and P. Robinson, *Physically-based failure models and criteria for laminated fibre-reinforced composites with emphasis on fibre kinking: Part I: Development.* Composites Part A: Applied Science and Manufacturing, 2006. **37**(1): p. 63-73.

[121] Liu, P.F. and J.Y. Zheng, *Recent developments on damage modeling and finite element analysis for composite laminates: A review.* Materials and Design, 2010. **31**(8): p. 3825-3834.

[122] Gross, M.J. *Element number in vumat*. 2008 14/8/2012]; Available from: http://imechanica.org/node/2540.

[123] Torres Arellano, M., L. Crouzeix, F. Collombet, B. Douchin, and Y.-H. Grunevald, *Mechanical Characterization of an Alternative Technique to Embed Sensors in Composite Structures: The Monitoring Patch.* Applied Composite Materials, 2012. **19**(3-4): p. 379-391.

[124] Falzon, B.G., S.C. Hawkins, C.P. Huynh, R. Radjef, and C. Brown, *An investigation of Mode I and Mode II fracture toughness enhancement using aligned carbon nanotubes forests at the crack interface.* Composite Structures, 2013. **106**(0): p. 65-73.

[125] Preetamkumar, M., L. Gilles, L. Pierre, and G. Ana-cristina, *Validation of Intralaminar Behaviour of the Laminated Composites by Damage Mesomodel*, in *50th AIAA/ASME/ASCE/AHS/ASC Structures, Structural Dynamics, and Materials Conference*. 2009, American Institute of Aeronautics and Astronautics.

[126]   Caminero, M.A., M. Lopez-Pedrosa, C. Pinna, and C. Soutis, *Damage monitoring and analysis of composite laminates with an open hole and adhesively bonded repairs using digital image correlation.* Composites Part B: Engineering, 2013. **53**(0): p. 76-91.

[127]   Schön, J., *Coefficient of friction of composite delamination surfaces.* Wear, 2000. **237**(1): p. 77-89.

[128]   Berthe, J., M. Brieu, E. Deletombe, G. Portemont, P. Lecomte-Grosbras, and A. Deudon, *Consistent Identification of CFRP Viscoelastic Models from Creep to Dynamic Loadings.* Strain, 2013. **49**(3): p. 257-266.

[129]   Jacob, G.C., J.M. Starbuck, J.F. Fellers, S. Simunovic, and R.G. Boeman, *The effect of loading rate on the fracture toughness of fiber reinforced polymer composites.* Journal of Applied Polymer Science, 2005. **96**(3): p. 899-904.

[130]   Kassapoglou, C., *Design and Analysis of Composite Beams*, in *Design and Analysis of Composite Structures*. 2013, John Wiley & Sons Ltd. p. 189-236.

[131]   Liu, Z., J. Yang, F. Grey, J.Z. Liu, Y. Liu, Y. Wang, Y. Yang, Y. Cheng, and Q. Zheng, *Observation of Microscale Superlubricity in Graphite.* Physical Review Letters, 2012. **108**(20).

[132]   Ye, Q. and P. Chen, *Prediction of the cohesive strength for numerically simulating composite delamination via CZM-based FEM.* Composites Part B: Engineering, 2011. **42**(5): p. 1076-1083.

[133]   Ilyas, M., F. Lachaud, C. Espinosa, and M. Salaün, *Dynamic delamination of aeronautic structural composites by using cohesive finite elements*, in *17th International Conference on Composite Materials (ICCM-17)*. 2009: Edinburgh, Scotland.

[134]   Chishti, M., C.H. Wang, R.S. Thomson, and A.C. Orifici, *Characterising fibre compression fracture toughness of composites using bearing tests.* Composites Part A: Applied Science and Manufacturing, 2012. **43**(10): p. 1775-1782.

[135]   Brunner, A.J., *Experimental study of delamination in cross-ply laminates*, in *Delamination behaviour of composites*. 2008, Woodhead Publishing Limited. p. 281-309.